

MECHANISMS OF DAMAGE TOLERANCE AND ARREST IN PRESSURIZED COMPOSITE CYLINDERS

by

Haryanto T. Budiman

B.S., Aerospace Engineering, Texas A&M University (1990)

M.S., Engineering Mechanics, Virginia Polytechnic Institute & State University (1991)

Submitted to the Department of Aeronautics and Astronautics in Partial Fulfillment of the
Requirements for the Degree of

DOCTOR OF PHILOSOPHY

in

STRUCTURES TECHNOLOGY

at the

MASSACHUSETTS INSTITUTE OF TECHNOLOGY

September 1996

© 1996 Massachusetts Institute of Technology

All rights reserved

Signature of Author _____
Department of Aeronautics and Astronautics
August 12, 1996

Certified by _____
Professor Paul A. Lagace
Thesis Supervisor, Professor of Aeronautics and Astronautics & MacVicar Faculty Fellow

Certified by _____
Professor John W. Hutchinson
Gordon McKay Professor of Applied Mechanics, Harvard University

Certified by _____
Professor Subra Suresh
Richard P. Simmons Professor of Metallurgy and Professor of Mechanical Engineering

Certified by _____
Professor Hugh L. N. McManus
Class of 1943 Assistant Professor of Aeronautics and Astronautics

Accepted by _____
Professor Jaime Peraire
Chairman of the Department Graduate Committee

MASSACHUSETTS INSTITUTE
OF TECHNOLOGY

OCT 15 1996

LIBRARIES

ARCHIVES

MECHANISMS OF DAMAGE TOLERANCE AND ARREST IN PRESSURIZED COMPOSITE CYLINDERS

by

Haryanto T. Budiman

Submitted to the Department of Aeronautics and Astronautics on August 19, 1996 in Partial Fulfillment of the Requirements for the Degree of Doctor of Philosophy in the Area of Structures Technology

ABSTRACT

Work was conducted to understand the mechanisms of damage tolerance and arrest in pressurized composite cylinders. The damage state considered in the present work was a through-thickness slit oriented along the longitudinal direction of the cylinder. The two structural responses relevant to *damage growth initiation* and *arrest* in such a cylinder (bulging and flapping) were studied using a unified analytical, numerical, and experimental approach. In the *damage growth initiation* work, the effects of geometric nonlinearity (due to bulging) on the response and failure of such cylinders were investigated in a general way. It was shown that the nonlinear membrane stress intensification factor depends on *two* nondimensional parameters: a *geometrical parameter*, which depends on the cylinder radius, thickness, and slit length; and a *loading parameter*, which depends on the pressure, material (structural) stiffness, and radius-to-thickness ratio. The nonlinear effects on the failure of smaller, laboratory-scaled specimens were shown to be relatively insignificant with differences between the linear and nonlinear predictions being typically less than 15%. However, more significant effects (on the order of 50% or greater) were predicted in larger cylinders resembling real fuselages, suggesting that a one-to-one (linear) scaling is not possible. An engineering estimation scheme, based solely on the two nondimensional parameters, was proposed to assess the nonlinear effects in any quasi-isotropic and isotropic cylinders and to allow proper scaling. Nonlinear pressure-strain responses were also identified numerically and experimentally and were shown to be (local) manifestations of the nonlinear effects in the form of membrane-stiffening. Work on damage growth and arrest on the stiffened cylinders also predicted the existence of an interaction between geometric nonlinear behavior and stiffening bands. Such an interaction is a likely contributor to the phenomenon of bifurcation in a stiffened cylinder and is related to the ratio of bending stiffnesses of the stiffened and unstiffened regions. It was also shown (from some preliminary numerical results) that nonlinearity may play a role in the observed damage bifurcation in an unstiffened cylinder. The combined effects of longitudinal and hoop stiffeners on the subsequent damage propagation in the hoop direction after bifurcation was also studied. Using a simple engineering method, it was shown that the damage growth initiation and arrest phenomena in pressurized composite cylinders are governed by two different scaling/loading parameters. The propagation prior to damage bifurcation is governed by the *hoop stress* which depends on the pressure, cylinder radius, and thickness. After bifurcation, the proper scaling parameter is the so-called *bending parameter* which depends on the pressure at rupture, longitudinal stiffener spacing, and base cylinder thickness. For a laboratory-scaled specimen scaled for *hoop stress*, the magnitude of the *bending parameter* can be one order of magnitude higher than that in a full-scale fuselage. It is therefore difficult, if not impossible, to completely satisfy both parameters in a single laboratory-scaled specimen in order to model both the damage propagation and arrest characteristics of a full-scale fuselage. A scheme to show a possibility of damage arrest in laboratory-scaled specimens is proposed. Further work in all these related areas, involving both numerical analyses and experiments, are identified.

Thesis Supervisor: Professor Paul A. Lagace

Title: Professor of Aeronautics and Astronautics and MacVicar Faculty Fellow

Acknowledgments

There are many people who have helped me go through my nine years of study at four different universities (Texas A&M University, Virginia Tech, Harvard University, and MIT). During that time, I met some really good and caring individuals. I would like to take this opportunity to thank them.

First, I would like to express my sincere respect and deep appreciation to my teacher/advisor/mentor/friend, Professor Paul A. Lagace, for his constant support, encouragement, guidance, and for the time he spent with me on this project and on my thesis. I have spent slightly more than four years working with Paul and it has been a truly enjoyable experience. I would also like to acknowledge my thesis committee members: Profs. John W. Hutchinson (Division of Applied Sciences, Harvard University), Subra Suresh (Materials Science & Engineering, MIT), and Hugh L. N. McManus (Aeronautics & Astronautics, MIT). I am extremely grateful to Prof. Hutchinson for his willingness to serve on my committee and for his teaching, support, exemplary character, caring, continuous guidance, and constant interest in my work and future plan. I thank Prof. Suresh for his caring and for being such an excellent teacher and mentor. I also thank Profs. Dugundji and Spearing for many stimulating discussions/chats I had and for just being there when I needed someone to talk to. Last, but not least, I would like to thank my Master's thesis advisor, Dr. John Morton, who is now the Director of the Structural Materials Center at the Defense Research Agency (DRA) Farnborough, United Kingdom. It was a very pleasant experience for me to have Dr. Morton as my mentor at Virginia Tech. Dr. Morton was the one who encouraged me to pursue my doctoral education at MIT. It is therefore fair to

say that I would not have been at MIT without Dr. Morton's encouragement and confidence in me.

I would like to thank the TELAC staff members: Al Supple, who was always willing to help me with my experiments; Ping Lee who helped me get through the (sometimes) confusing MIT administrative procedures and for all the weekly grocery coupons for the past four years; and Debbie Bowser for helping me keep track of my advisor. I also thank Robin Lagace for her hospitality for the past four years.

Equally important is the support that I received from all TELAC graduate (Brian, Lauren, Mark, Ronan, Sharath, Chris, Steve, Kuo-Shen, Bari, Bethany, and others) and undergraduate students past and present. My six outstanding UROPers (Michael, Janeen, Laura, Doug, Peter, and Barbara) deserved a lot of credits for what I have accomplished here. Special thanks go to my best friend, David Shia, who is currently pursuing a Ph.D. degree at Cornell University. I wish him my very best in his study and future endeavor. My dear friends, David & Dawn-Ann Wilson and James & Rita Bruton and their family in Texas, also deserve special thanks. They all have been very supportive to me since my freshman year at A&M back in 1987. Their friendship and hospitality will always be remembered.

Finally, I would like to thank my beloved family for their long-distance support and for their constant confidence, support, and positive encouragement for the past nine years. I would also thank my brothers (Benny, Lingga and Henry) for providing me with constant encouragement and inspiration and for all the fun we had together. Also, I would like to thank my dear Grandma (Grandma Tan) for her support and confidence in me. I do hope I haven't missed anybody and I thank you all again ! It has been fun to have known every single one of you !

DEDICATION

To my parents, Mr. and Mrs. Hendra Budiman, for their love, caring, support, encouragement, and prayer that make all this possible.

FOREWORD

This investigation was conducted in the Technology Laboratory for Advanced Composites (TELAC) of the Department of Aeronautics and Astronautics at the Massachusetts Institute of Technology. This work was sponsored by NASA Grant NAG-1-991 from NASA Langley Research Center.

Table of Contents

List of Figures	10
List of Tables	19
Nomenclature	21
1. INTRODUCTION	26
2. PREVIOUS WORK	31
2.1 Damage Tolerance of Pressurized Cylinders	31
2.2 Damage Arrest in Pressurized Cylinders	45
3. APPROACH	50
3.1 Problem Definition	50
3.2 Objectives	52
3.3 Overview of Work	53
3.3.1 Analytical and Numerical Work	54
3.3.2 Experimental Work	63
4. ANALYTICAL AND NUMERICAL METHODS	74
4.1 Derivation of the Nondimensional Parameters	74
4.2 Numerical Solution	78
5. ANALYTICAL AND NUMERICAL RESULTS	83
5.1 Verification of Numerical Solutions	83
5.2 Use of Nondimensional Parameters	89
5.3 Simulation of Damage Growth	100
5.3.1 Simulation of Damage Growth in the Unstiffened Cylinders	101
5.3.2 Simulation of Damage Growth in Stiffened Construction	118

6. EXPERIMENTAL PROCEDURES	139
6.1 Cylinder Manufacture	139
6.2 Slit Construction	157
6.3 Specimen Sealing Procedure	161
6.4 Instrumentation	167
6.5 Testing	168
7. EXPERIMENTAL RESULTS	181
7.1 Strain Responses	181
3	
7.1.1 Unstiffened Case (<i>Type-1</i> Cylinder)	183
7.1.2 Circumferentially-Stiffened Cylinder (<i>Type-2</i> Cylinder)	198
7.2 Failure	204
7.3 Damage Path of the <i>Type-3</i> Cylinders	206
8. DISCUSSION	220
8.1 Strain Response	220
8.2 Failure	248
8.3 Damage Arrest	262
8.3.1 Damage Bifurcation	263
8.3.2 Implications of the Results from Damage Arrest Experiments	273
8.4 Final Notes	282
9. CONCLUSIONS AND RECOMMENDATIONS	288
9.1 Conclusions	288
9.2 Recommendations	291
References	294

Appendix A	Derivation of the Nondimensional Parameters using the Sanders Nonlinear Shell Theory	304
Appendix B	Derivation of the Iso-Error Chart	315
Appendix C	Predicted and Experimental Strain Data	320
Vita		346

List of Figures

Figure 2.1	Illustration of bulging of the crack face in an axially-cracked cylinders (the out-of-plane deformations are magnified 20 X).	33
Figure 2.2	Comparison between the Folias formula and the numerical solution of Erdogan and Kibler [18] for the membrane stress intensification.	35
Figure 2.3	Illustration of notch-sensitive and notch-insensitive behavior.	38
Figure 2.4	Two general configurations involved in the development of the failure prediction methodology: (<i>left</i>) flat coupon and (<i>right</i>) pressurized cylindrical shell.	41
Figure 3.1	Illustration of generic geometry of a longitudinally-cracked cylindrical shell under internal pressure.	55
Figure 3.2	Geometry of a longitudinally-cracked, unstiffened, laboratory-scaled cylinder investigated in the present work.	59
Figure 3.3	Geometry of a circumferentially-stiffened cylinder analyzed in the present investigation.	62
Figure 3.4	Geometry of the cylinder stiffened in the longitudinal and circumferential directions.	69
Figure 3.5	Illustrations of two different stiffener configurations investigated (half of cylinder configuration shown).	71
Figure 4.1	Illustration of the finite element mesh topology near a crack tip necessary to use the Nodal Release Technique: crack tip, (<i>left</i>) initially at position (j); (<i>right</i>) is moved to position (j+1).	80
Figure 5.1	Geometry of a large center-cracked panel loaded perpendicular to the crack plane.	84
Figure 5.2	Illustration of the symmetry that exists in a cylindrical shell with a longitudinal crack/slit.	87
Figure 5.3	Typical finite element mesh for a notched cylinder (the case shown is cylinder with R=1.52 m, h=1.4 mm, and	88

$2a=0.62$ m): (*upper*) entire one-half cylinder model, and blow-up of region near slit tip.

- Figure 5.4 Plot of the linear membrane stress intensification versus the geometrical parameter as computed using STAGS code and the Nodal Release Technique and using the Erdogan & Kibler numerical solution. 90
- Figure 5.5 Dependence of the membrane stress intensification factor (K^{eff}) on the internal pressure for different cylindrical configurations with the geometrical parameter, λ , equal to 3. 92
- Figure 5.6 Dependence of the membrane stress intensification factor (K^{eff}) on the loading parameter η for different cylindrical configurations with the geometrical parameter, λ , equal to 3. 93
- Figure 5.7 Dependence of the membrane stress intensification factor (K^{eff}) on the loading parameter η for cylinders with different values of the geometrical parameter λ . 94
- Figure 5.8 Iso-nonlinear plot showing the percentage difference between the linear and nonlinear membrane stress intensification as functions of the two nondimensional parameters. 97
- Figure 5.9 Iso-error plot showing the percentage error of the predicted failure pressures using linear and nonlinear methodologies for the (0/45)_s AW370-5H/3501-6 fabric cylinders. 99
- Figure 5.10 Typical finite element mesh for a laboratory-scaled, unstiffened specimen (the case shown is cylinder with $R=152$ mm, $h=1.4$ mm, and $2a=104$ mm): (*upper*) entire one-half cylinder model, and (*lower*) blow-up of region near slit tip. 102
- Figure 5.11 Effects of different skin configurations and thus bending properties on the nonlinear membrane stress intensification factors for cylinders with a longitudinal slit length of 104 mm. 105
- Figure 5.12 Total longitudinal strains on the top surface of the (0/45)_s cylinder with a longitudinal slit length of 104 mm at 1 MPa internal pressure. 107

Figure 5.13	Total hoop strains on the top surface of the (0/45) _s cylinder with a longitudinal slit length of 104 mm at 1 MPa internal pressure.	108
Figure 5.14	Total longitudinal strains on the top surface of the (45/0) _s cylinder with a longitudinal slit length of 104 mm at 1 MPa internal pressure.	109
Figure 5.15	Total hoop strains on the top surface of the (45/0) _s cylinder with a longitudinal slit length of 104 mm at 1 MPa internal pressure.	110
Figure 5.16	Membrane longitudinal strain distributions of a (0/45) _s cylinder with a longitudinal slit length of 104 mm at 1 MPa internal pressure predicted from linear and nonlinear analyses.	112
Figure 5.17	Bending longitudinal strain distributions on the top surface of a (0/45) _s cylinder with a longitudinal slit length of 104 mm at 1 MPa internal pressure predicted from linear and nonlinear analyses.	113
Figure 5.18	Membrane hoop strain distributions of a (0/45) _s cylinder with a longitudinal slit length of 104 mm at 1 MPa internal pressure predicted from linear and nonlinear analyses.	114
Figure 5.19	Bending hoop strain distributions on the top surface of a (0/45) _s cylinder with a longitudinal slit length of 104 mm at 1 MPa internal pressure predicted from linear and nonlinear analyses.	115
Figure 5.20	Cross-sections of the unstiffened and stiffened regions.	120
Figure 5.21	Typical finite element mesh for a laboratory-scaled, stiffened specimen (the case shown is cylinder with R=152 mm, h=1.4 mm, and 2a=104 mm): (<i>upper</i>) entire one-half cylinder model, and (<i>lower</i>) blow-up of region near slit tip.	121
Figure 5.22	The evolution of the nonlinear membrane stress intensification factors for cylinders with a longitudinal slit length of 312 mm corresponding to the ψ/a -ratio of 0.13.	125
Figure 5.23	Linear and nonlinear total longitudinal strain distributions for the stiffened (0/45) _s cylinders with a longitudinal slit length of 312 mm at 1 MPa internal pressure (total strains are computed on the top surface of the stiffener in the stiffened region and on the top surface of the skin in the unstiffened region).	126

Figure 5.24	Linear and nonlinear total hoop strain distributions for the stiffened (0/45) _s cylinders with a longitudinal slit length of 312 mm at 1 MPa internal pressure (total strains are computed on the top surface of the stiffener in the stiffened region and on the top surface of the skin in the unstiffened region).	127
Figure 5.25	Nonlinear total longitudinal strain distributions for the unstiffened and stiffened (0/45) _s cylinders with a longitudinal slit length of 312 mm at 1 MPa internal pressure (total strains are computed on the top surface of the stiffener in the stiffened region and on the top surface of the skin in the unstiffened region).	130
Figure 5.26	Nonlinear total hoop strain distributions for the unstiffened and stiffened (0/45) _s cylinders with a longitudinal slit length of 312 mm at 1 MPa internal pressure (total strains are computed on the top surface of the stiffener in the stiffened region and on the top surface of the skin in the unstiffened region).	131
Figure 5.27	Membrane and bending longitudinal strain distributions in a stiffened (0/45) _s cylinder with a longitudinal slit length of 312 mm at 1 MPa internal pressure (bending strains are computed on the top surface of the stiffener in the stiffened region and on the top surface of the skin in the unstiffened region).	133
Figure 5.28	Nonlinear membrane and bending hoop strain distributions in a stiffened (0/45) _s cylinder with a longitudinal slit length of 312 mm at 1 MPa internal pressure (bending strains are computed on the top surface of the stiffener in the stiffened region and on the top surface of the skin in the unstiffened region).	134
Figure 5.29	Nonlinear membrane and bending (long.) strain distributions in an unstiffened (0/45) _s cylinder with a longitudinal slit length of 312 mm at 1 MPa internal pressure (bending strains are computed on the top surface of the skin).	135
Figure 5.30	Nonlinear membrane and bending (hoop) strain distributions in an unstiffened (0/45) _s cylinder with a longitudinal slit length of 312 mm at 1 MPa internal pressure (bending strains are computed on the top surface of the skin).	136

Figure 6.1	Illustrations of motorized tubewinder and mandrel.	140
Figure 6.2	Illustration of cylinder layup procedure and terminology.	142
Figure 6.3	Illustrations of the $(0/45)_8$ cylinder ply dimensions and orientations utilized in [34, 37].	144
Figure 6.4	Illustration of the $(0/45)_8$ cylinder ply dimensions and orientations utilized in the present work.	145
Figure 6.5	Illustration of the alignment and placement of the hoop stiffener on the <i>type-2</i> cylinders and <i>type-3</i> cylinder with the <i>type-A</i> stiffener configuration.	147
Figure 6.6	Illustration of the alignment and placement of stiffener on the <i>type-3</i> cylinder with the <i>type-B</i> stiffener configuration.	150
Figure 6.7	Curing assembly for graphite/epoxy cylinder.	153
Figure 6.8	Standard cure cycle for the AW370-5H/3501-6 graphite/epoxy cylinders.	154
Figure 6.9	Grid on a cylinder for fracture path identification.	156
Figure 6.10	Illustration of cylinder slit-cutting setup.	158
Figure 6.11	Illustrations of aluminum cylinder endcaps.	162
Figure 6.12	Photograph of a cylinder with its endcaps bonded ready for testing.	164
Figure 6.13	Illustrations of rubber pieces for cylinder bladder.	165
Figure 6.14	Schematic of the strain gage locations in the <i>type-1</i> (unstiffened) cylinders.	169
Figure 6.15	Schematic of the strain gage locations in the <i>type-2</i> (circumferentially stiffened) cylinders.	170
Figure 6.16	Photograph of the gage region in a <i>type-1</i> cylinder.	171
Figure 6.17	Photograph of the gage region in a <i>type-2</i> cylinder.	172
Figure 6.18	Test setup of a cylinder inside the blast chamber.	177
Figure 6.19	Schematic of the blast chamber setup for cylinder testing.	179

Figure 7.1	Characteristic types of strain responses (predicted and measured) in the <i>type-1</i> and <i>type-2</i> cylinders.	182
Figure 7.2	Predicted and experimental strain responses for gages 1 to 3 in the unstiffened (0/45) _s cylinder with a longitudinal slit length of 104 mm.	184
Figure 7.3	Predicted and experimental strain responses for gages 4 to 6 in the unstiffened (0/45) _s cylinder with a longitudinal slit length of 104 mm.	185
Figure 7.4	Predicted and experimental strain responses for gages 7 to 9 in the unstiffened (0/45) _s cylinder with a longitudinal slit length of 104 mm.	186
Figure 7.5	Predicted and experimental strain responses for gages 10 to 12 in the unstiffened (0/45) _s cylinder with a longitudinal slit length of 104 mm.	187
Figure 7.6	Predicted and experimental strain responses for gages 1 to 3 in the unstiffened (45/0) _s cylinder with a longitudinal slit length of 104 mm.	192
Figure 7.7	Predicted and experimental strain responses for gages 4 to 6 in the unstiffened (45/0) _s cylinder with a longitudinal slit length of 104 mm.	193
Figure 7.8	Predicted and experimental strain responses for gages 7 to 9 in the unstiffened (45/0) _s cylinder with a longitudinal slit length of 104 mm.	194
Figure 7.9	Predicted and experimental strain responses for gages 10 to 12 in the unstiffened (45/0) _s cylinder with a longitudinal slit length of 104 mm.	195
Figure 7.10	Predicted and experimental strain responses for gages 1 to 3 in the stiffened (0/45) _s cylinder with a longitudinal slit length of 104 mm.	199
Figure 7.11	Predicted and experimental strain responses for gages 4 and 5 in the stiffened (0/45) _s cylinder with a longitudinal slit length of 104 mm.	200
Figure 7.12	Predicted and experimental strain responses for gages 1 to 3 in the stiffened (45/0) _s cylinder with a longitudinal slit length of 104 mm.	202

Figure 7.13	Predicted and experimental strain responses for gages 4 and 5 in the stiffened (45/0) _s cylinder with a longitudinal slit length of 104 mm.	203
Figure 7.14	Illustration of the presentation of the damage path in the <i>type-3</i> cylinder.	207
Figure 7.15	Fracture path of cylinder 1 stiffened with four layers of 0° tape (hoop) and 8 layers of 0° tape (longitudinal).	208
Figure 7.16	Fracture path of cylinder 2 stiffened with two layers of continuous (<i>type-B</i>) 0° fabric layers.	210
Figure 7.17	Photograph showing damage bifurcation (~40° - 50° turn) within the hoop stiffener (arrows indicate the locations of bifurcation points) in cylinder 2.	211
Figure 7.18	Close-up photograph of the "triangular" region near the bifurcation point in cylinder 2.	212
Figure 7.19	Fracture path of cylinder 3 stiffened with four layers of continuous (<i>type-B</i>) 0° fabric layers.	214
Figure 7.20	Photograph showing damage bifurcation (~90° turn) at the edge of hoop stiffener (arrows indicate the locations of bifurcation points) in cylinder 3.	215
Figure 7.21	Close-up photograph of the "triangular" region near the bifurcation point in cylinder 3.	216
Figure 7.22	Fracture path of cylinder 4 stiffened with four layers of continuous (<i>type-B</i>) 45° fabric layers.	217
Figure 7.23	Fracture path of cylinder 5 stiffened with four layers of continuous (<i>type-B</i>) 0° fabric layers and four additional continuous 0° fabric layers in the longitudinal direction.	218
Figure 8.1	Evolution with increasing pressure of the longitudinal total strain distribution on the top skin surface.	222
Figure 8.2	Evolution with increasing pressure of the longitudinal membrane strain distribution on the top skin surface.	223
Figure 8.3	Evolution with increasing pressure of the longitudinal bending strain distribution on the top skin surface.	224
Figure 8.4	Evolution with increasing pressure of the normalized longitudinal total strain distribution on the top skin	225

surface (normalized by the corresponding far-field linear membrane strain).

Figure 8.5	Evolution with increasing pressure of the normalized longitudinal membrane strain distribution on the top skin surface (normalized by the corresponding far-field linear membrane strain).	226
Figure 8.6	Evolution with increasing pressure of the normalized longitudinal bending strain distribution on the top skin surface (normalized by the corresponding far-field linear membrane strain).	227
Figure 8.7	Evolution with increasing pressure of the hoop total strain distribution on the top skin surface.	228
Figure 8.8	Evolution with increasing pressure of the hoop membrane strain distribution on the top skin surface.	229
Figure 8.9	Evolution with increasing pressure of the hoop bending strain distribution on the top skin surface.	230
Figure 8.10	Evolution with increasing pressure of the normalized hoop total strain distribution on the top skin surface (normalized by the corresponding far-field linear membrane strain).	231
Figure 8.11	Evolution with increasing pressure of the normalized hoop membrane strain distribution on the top skin surface (normalized by the corresponding far-field linear membrane strain).	232
Figure 8.12	Evolution with increasing pressure of the normalized hoop bending strain distribution on the top skin surface (normalized by the corresponding far-field linear membrane strain).	233
Figure 8.13	Contributions of the membrane and bending parts to the <i>type-s4</i> behavior.	236
Figure 8.14	Contributions of the membrane and bending parts to the <i>type-s1</i> behavior.	237
Figure 8.15	Contributions of the membrane and bending parts to the <i>type-s2</i> behavior.	238
Figure 8.16	Contributions of the membrane and bending parts to the <i>type-s3</i> behavior.	240

Figure 8.17	Sensitivity of gage placement on the predicted strain response of gage 1 (the closest hoop gage to the slit tip)	242
Figure 8.18	Sensitivity of gage placement on the predicted strain response of gage 9 (the farthest hoop gage to the slit axis in the midslit region).	244
Figure 8.19	Evolution with increasing pressure of midslit hoop total strain distribution in the hoopwise direction computed on the top skin surface.	245
Figure 8.20	Evolution with increasing pressure of midslit hoop membrane strain distribution in the hoopwise direction.	246
Figure 8.21	Evolution with increasing pressure of midslit hoop bending strain distribution in the hoopwise direction computed on the top skin surface.	247
Figure 8.22	Iso-nonlinear plot with the reduced experimental failure results for metallic and quasi-isotropic cylinders with longitudinal cracks/slits.	258
Figure 8.23	Iso-error plot showing the percentage error of the predicted failure pressures using linear and nonlinear methodologies for the Aluminum 2024 cylinders with thickness of 1.0 mm.	261
Figure 8.24	Membrane stress intensification plot for the simulation of damage growth in a stiffened (0/45) _s cylinder with an initial slit length of 51 mm which fails at an internal pressure of 1.0 MPa.	268
Figure 8.25	Membrane stress intensification plot for the simulation of damage growth in a stiffened (0/45) _s cylinder with an initial slit length of 78 mm which fails at an internal pressure of 0.6 MPa.	269
Figure 8.26	Typical fracture path of an unstiffened cylinder. Note that bifurcation points are located approximately 200 mm from the cylinder ends [36].	271
Figure 8.27	An illustration of flapping induced by damage bifurcation in a pressurized cylinder.	276
Figure 8.27	Hypothesized damage progression in cylinder 5.	281
Figure C.1- C.24	Predicted and experimental strain responses	321- 344

List of Tables

Table 3.1	Baseline Material Properties	57
Table 3.2	Bending Properties for the Cylinder Skins	58
Table 3.3	Slit and Stiffener Spacing Geometry for all <i>Type-2</i> Cylinders	64
Table 3.4	Summary of the Test Matrix for the Experimental Investigation	66
Table 3.5	Stiffener Configurations for the <i>Type-3</i> Cylinders	73
Table 5.1	Effects of Different Crack Increments Δa on the Computed Fracture Parameters of a Center-Cracked Plate	86
Table 5.2	Linear Membrane Stress Intensification Factors for the Three Cylinder Skins Computed Using the Nodal Release Technique	103
Table 5.3	Effects of the Stiffening Bands on the Linear Stress Intensification Factors for the (0/45) _s Cylinder	122
Table 5.4	Effects of the Stiffening Bands on the Linear Stress Intensification Factors for the (45/0) _s Cylinder	123
Table 6.1	Strain Gage Locations for the <i>Type-1</i> (0/45) _s Cylinder	173
Table 6.2	Strain Gage Locations for the <i>Type-1</i> (45/0) _s Cylinder	174
Table 6.3	Strain Gage Locations for the <i>Type-2</i> (0/45) _s Cylinder	175
Table 6.4	Strain gage Locations for the <i>Type-2</i> (45/0) _s Cylinder	176
Table 7.1	Failure Data for All Cylinders	205
Table 8.1	Predicted and Experimental Failure Pressures of Cylinders Tested	250
Table 8.2	Characteristics of Cylinders Tested in Previous Work	251
Table 8.3	Data for Al 2014 Cylinders [23]	253
Table 8.4	Data for Al 2014-T6 cylinders [22]	254

Table 8.5	Data for X-52 C steel cylinders [24]	255
Table 8.6	Data for (0/45)_s AW370-5H/3501-6 Graphite/Epoxy Cylinders [36]	256
Table 8.7	Data for [90/±45/0]_s AS4/3501-6 Graphite/Epoxy Cylinders [26]	257
Table 8.8	Bending Stiffnesses of the <i>Type-3</i> Cylinders Tested	265
Table 8.9	Effects of Different Cylinder Geometries on the Magnitude of the Bending Parameter	279

NOMENCLATURE

a	Half-slit length
a_0	Characteristic length from Whitney-Nuismer Average Stress Criterion
A_{ij}	Terms in axial stiffness matrix from Classical Laminated Plate Theory
B_{ij}	Terms in membrane-bending coupling stiffness matrix from Classical Laminated Plate Theory
C	Empirical Containment Ratio
d_0	Characteristic length from Whitney-Nuismer Point Stress Criterion
D_u	Hoop bending stiffness of the unstiffened region in a cylinder
D_s	Hoop bending stiffness of the stiffened region in a cylinder
D_{ij}	Terms in bending stiffness matrix from Classical Laminated Plate Theory
E	Extensional modulus of isotropic material or quasi-isotropic laminate
E_L	Longitudinal extensional modulus
E_T	Transverse extensional modulus
<i>Error</i>	Percentage difference between the linear and nonlinear stress intensification factors
e	Percentage difference between the cylinder failure pressures predicted via linear and nonlinear methodologies
F	Stress function in the Donnell-Mushtari-Vlasov shell theory
F'	Normalized stress function in the Donnell-Mushtari-Vlasov shell theory
\bar{F}_i^j	Nodal Forces ($i=1$ to 6 , $j=1$ (top) or 2 (bottom)) in STAGS finite element work

G_{LT}	Shear modulus
G_I	Mode-I energy-release-rate
G_{II}	Mode-II energy-release-rate
h	Cylinder skin thickness
H_c	Composite fracture parameter from the Mar-Lin equation
k^{bend}	Bending stress intensification factor
K_I	Mode-I stress intensity factor
K_{II}	Mode-II stress intensity factor
K_{Ic}	Critical stress intensity factor
K^{ext}	Membrane stress intensification factor
K_{linear}^{ext}	Linear membrane stress intensification factor
K^{total}	Total stress intensification factor (taking into account both membrane and bending contributions)
L	Cylinder length
m	Order of stress singularity at fiber/matrix interface which serves as exponent in the Mar-Lin equation
M_{xx}	Bending moment resultant per unit length along the longitudinal direction
M_{yy}	Bending moment resultant per unit length along the hoop direction
M_{xy}	Twisting moment resultant per unit length
N_{xx}	Membrane force resultant per unit length along the longitudinal direction
N_{yy}	Membrane force resultant per unit length along the hoop direction
N_{xy}	Shear force resultant per unit length

p	Cylinder pressure
$p_{failure}$	Cylinder failure pressure
p^{linear}	Failure pressure of a cylinder predicted by linear methodology
p^{NL}	Failure pressure of a cylinder predicted by nonlinear methodology
p_x	Edge load in the x-direction
p_y	Edge load in the y-direction
Q_i	Transverse shear force resultant
R	Cylinder radius
s	Spacing between two hoop stiffeners
sa	Distance of the first hoop gage in the slit tip region to the slit tip
sb	Distance of the second hoop gage in the slit tip region to the slit tip
sc	Distance of the third hoop gage in the slit tip region to the slit tip
sd	Distance of the first longitudinal gage in the slit tip region to the slit tip
se	Distance of the second longitudinal gage in the slit tip region to the slit tip
sf	Distance of the third longitudinal gage in the slit tip region to the slit tip
sg	Distance of the first hoop gage in the midslit region to the slit axis
sh	Distance of the second hoop gage in the midslit region to the slit axis
si	Distance of the third hoop gage in the midslit region to the slit axis
sj	Distance of the first longitudinal gage in the midslit region to the slit axis

sk	Distance of the second longitudinal gage in the midslit region to the slit axis
sl	Distance of the third longitudinal gage in the midslit region to the slit axis
t_{ply}	Ply thickness
u	Deformation in the x-direction
u_0	Reference deformation in the x-direction
v	Deformation in the y-direction
v_0	Reference deformation in the y-direction
w	Out-of-plane deformation of a cylinder
w_0	Reference out-of-plane deformation of a cylinder
w'	Normalized out-of-plane deformation of a cylinder
W_i	Component of the work done on a nodal degree of freedom basis
x, y, z	Cartesian coordinate system
x	Longitudinal direction
y	Hoop direction
x', y', z'	Normalized Cartesian coordinate system
α	Nondimensional factor to take into account the bending stress intensification contribution in the total stress intensification factor
Δa	Crack or slit increment used in the Nodal Release Technique
ϵ_{xx}	Total longitudinal strain
ϵ_{xx}^0	Reference surface extensional strain in the longitudinal direction
ϵ_{yy}	Total hoop strain
ϵ_{yy}^0	Reference surface extensional strain in the hoop direction
γ_{xy}	Total shear strain

γ_{xy}^0	Reference surface in-plane shear strain
η	Loading parameter
κ_{xx}	Reference surface curvature in the longitudinal direction
κ_{yy}	Reference surface curvature in the hoop direction
κ_{xy}	Reference surface twist curvature
λ	Geometrical (Folias) parameter
ν	Poisson's ratio of isotropic or quasi-isotropic material
ν_{LT}	Major Poisson's ratio
σ_0	Unnotched laminate strength
σ^f	Fracture stress
σ_{plate}^f	Fracture stress in flat plate
σ_{hoop}^f	Fracture stress in cylinder (hoop direction)
Σ	Distance from cylinder end to the edge of the stiffener
Ψ	Ligament width between the slit tip and the edge of stiffening band

Chapter 1

Introduction

Thin-walled cylindrical shell configurations are structures of interest to engineers. Aircraft fuselages, gas and oil tanks, and rocket motor casings are examples of structures of this general shape found in many engineering applications. The typical loads on these structures are due to internal or external pressure, axial, bending, and torsional loads. The design requirements depend on the specific usage of the structure. For example, for an airplane to be certified for airworthiness in this country, the aircraft manufacturer must show the Federal Aviation Administration (FAA) that such airplane has satisfied the appropriate safety regulations. Particular safety regulations dealing with structural integrity are based on the damage tolerant design philosophy introduced by the U.S. Air Force in the mid 1970s [1, 2]. This approach replaces the safe-life philosophy. More on the early development of the damage tolerant design philosophy can be found in the article written by Lincoln [3].

The damage tolerant design requirements proposed by the Air Force [4] stipulate that damage is assumed to exist in each element of a new structure in a conservative fashion (i.e. located in the most highly-stressed region and oriented in the most severe loading direction). The structure must successfully contain the growth of the initial assumed damage for a specified period of service while maintaining a minimum level of residual static strength. Damage tolerance can therefore generally be defined as the ability of a material or structure to "perform", given particular requirements, with

damage present. Inspection and nondestructive evaluation play important roles in preventing structural failure. To properly apply this design philosophy, realistic damage states that may be present for a specific material or structure need to be defined. Since sharp cracks (part-through or through-thickness) are realistic damage states at the macroscopic level in metallic materials, Linear and Nonlinear Fracture Mechanics have been used to predict or correlate the strength of damaged structures and have become important design tools used to satisfy the damage tolerant requirements for metallic structures.

Part of the damage tolerant design philosophy is the concept of damage arrest which can be defined as the ability of a material or structure to arrest propagating damage before such damage causes catastrophic failure. To arrest a propagating crack, multiple load paths and redundant structures including crack stoppers are usually utilized. The purposes of using crack arrestors are to reduce the stress intensity factor and stress fields near the crack, alter the crack propagation path, and induce other "structural deformation" modes which can reduce the crack propagation driving force. Many structural components in aerospace and marine applications are designed with crack arrest members with these ideas in mind [5-7] .

All the previously mentioned work deals with structures made of metallic materials where the use of fracture mechanics as a design tool has helped designers satisfy the damage tolerant requirements. A completely different approach needs to be taken to satisfy the requirements of damage tolerance for structures made of advanced composite materials. The reason is that damage states in composites and metals are totally different. Damage in composites is more complex and heterogeneous, consisting of many different modes of failure such as fiber fracture, matrix cracking, delamination, matrix

plasticity, and fiber-matrix debonding [8]. Furthermore, damage growth in composites is typically not self-similar and the possibility of interaction between the modes of failure exists.

In the aircraft arena, composite materials have replaced metallic materials in many secondary transport aircraft components such as flaps and ailerons. The trend is to use more of this material for load-bearing structures in transport airplanes. The newly-designed Boeing 777 has a large empennage section made of composites [9, 10]. Yet, there is still hesitation to design primary aircraft structures such as wings and fuselages using this material due to a lack of understanding of their basic damage and failure mechanisms. To address these concerns, NASA has introduced the Advanced Composite Technology (ACT) program with a final objective of increasing the use of composites in primary aircraft structures such as aircraft fuselages [5].

Aircraft fuselage is probably the most complex structural component in an airplane [6]. The main structure can be modeled as a stiffened, thin-walled cylindrical shell of radius-to-thickness ratio on the order of 1000. The structure is loaded by internal pressure up to approximately 55 kPa (8.0 psi) at cruise condition as well as bending from flight loads. All fuselage sections are therefore subjected to tensile loads in the hoop direction due to internal cabin pressurization. In addition to that, the top part of a fuselage, called the crown section, is also subjected to tensile loads in the longitudinal direction, the sides of a fuselage are subjected to shear loads, and the bottom part of a fuselage, called the keel, is subjected to compression loads in the longitudinal direction due to bending induced by normal flight loads. Therefore, different parts of a fuselage are subjected to different primary loading conditions.

In order to provide an additional stiffness against bending and instability induced by bending and to maintain the circular shape of a

fuselage, stiffening elements in the circumferential direction, called the frames, and in the longitudinal directions, called the longerons, are attached periodically to the fuselage skin. For a medium-range transport airplane such as the Boeing 737, the typical spacings between two adjacent frames and longerons are 500 mm (20 inches) and 250 mm (10 inches), respectively [6]. Tear straps or crack arrestors of roughly the same thickness as the skin are usually placed under the frames, halfway between two adjacent frames, and under the longerons to arrest a propagating crack.

These tear straps are intended to arrest a propagating crack which can be induced by an accident scenario such as if one of the turbine blades in an aircraft engine penetrates the fuselage skin and introduces through-thickness damage while the fuselage is pressurized [11]. For this accident scenario, the more realistic case is for the crack to be oriented in the hoop direction. However, since the hoop stress in a cylinder is typically greater than the axial stress (by slightly less than a factor of 2 in a real fuselage due to the presence of the stiffening members [12]), the worst case scenario is for the through-crack to be oriented in the longitudinal direction. The maximum crack size considered in design usually depends on the spacing between two adjacent crack arrest members. That implies that an axial crack as long as 500 mm (20 inches) has to be considered in design.

The problem of a cylindrical shell with an axial crack has therefore received a lot of attention analytically [13-21] and experimentally [22-24] since the 1960s. Methodologies to predict failure of a cylindrical shell containing an axial slit or crack have been developed for both metallic and quasi-isotropic cylinders [15, 16, 25, 26]. With the availability of more computer power, recent research has even addressed the "higher order" effects such as effects of geometric nonlinearity and "non-shell-shalowness"

on the failure of some specific pressure vessels [27-33]. The work, however, only looks at specific cylindrical configuration and has not addressed the general fundamental issues of damage that are applicable to any cylindrical shells. Furthermore, little has been done in the area of damage arrest in pressurized composite cylinders, although some purely experimental work in this area can be found in [26, 34-37].

Building on the findings from previous study, the present work addresses the fundamental mechanisms involved in the damage tolerance and damage arrest of pressurized composite cylinders. Thus, the primary objective of the present investigation is to understand the operative mechanisms and related "scaling" effects involved with the issues of damage tolerance and arrest of composite cylinders.

The overall thesis work is organized in the following sections as follows. In Chapter 2, relevant work on the damage tolerance and damage arrest in pressurized cylindrical shells is reviewed. The problem definition, objectives, analytical and numerical goals, and test plan for the present study are presented in Chapter 3. The analytical and numerical methods undertaken to study the effects of nonlinearity on the response and failure of unstiffened and stiffened cylinders are presented in Chapter 4. Chapter 5 contains the results of the analyses. Experimental procedures for manufacturing, instrumenting, test preparation, and testing are discussed in Chapter 6. The results of the present experimental work are presented in Chapter 7, followed by discussion of the results and their implications in Chapter 8. In Chapter 9, the conclusions and contributions of the present investigation are summarized and recommendations are made for future work. Several appendices contain detailed analytical derivations and some numerical and experimental results.

Chapter 2

Previous Work

In the following section, relevant work in the areas of damage tolerance and damage arrest of pressurized, thin-walled cylindrical shells is reviewed and presented. Several needs are identified as the motivation for the present work.

2.1 Damage Tolerance of Pressurized Cylinders

Much analytical work has been done in the area of damage tolerance of pressurized, thin-walled cylindrical shells [13-18, 20, 21, 38]. The damage state studied has generally been a through-thickness crack oriented in the longitudinal or circumferential direction. This allows the use of the symmetry of the geometry and thus simplifies the solution technique. Only the review of the analytical work done in cylindrical shells with a longitudinal crack is presented here due to its relevance to the damage tolerance aspect of the current work.

These early solutions take into account the structural deformation of a cracked shell under pressure. The response of a cracked shell is shown to be fundamentally different from that of a cracked flat plate loaded under a similar loading condition (loaded uniaxially perpendicular to the slit). Unlike the flat-plate case, there exists coupling between bending and membrane actions in shell structures even when the material is isotropic [39]. This structural coupling induces localized bending and out-of-plane deformation in

the vicinity of the crack as illustrated in Figure 2.1. This out-of-plane response in a cylinder is further amplified by the existence of internal pressure. The cracked region is therefore said to "bulge" outward [13] due to a combination of membrane-bending coupling, which is a characteristic of any shell structure, and internal pressure. Bulging causes the stress intensity in a cracked shell to be higher than that in a cracked plate.

The first analytical solution to this problem was accomplished by Folias [13] in the mid 1960s. This analytical solution is based on the linear, shallow-shell equations and is valid only for isotropic materials. The method of coupled-integral equations was utilized. The combined effects of internal pressure and geometric-coupling were taken into account in the solution. The membrane stress intensification factor, which represents an increase in the local extensional stress at the slit tip in a shell structure, was obtained by taking the ratio of the extensional stress intensity of a cracked shell to that of a cracked plate of the same crack geometry. This so-called curvature correction was shown to depend only on *one* nondimensional parameter λ :

$$\lambda = \frac{a}{\sqrt{Rh}} \sqrt{12(1-\nu^2)} \quad (2.1)$$

where a is the crack half-length, R is the cylinder radius, h is the cylinder thickness, and ν is the Poisson's ratio.

In the original solution by Folias [13], the kernel of the integral equations used to construct the solution was obtained from asymptotic analysis and converged only for very small values of λ ($\lambda \ll 1$). Therefore, the validity of this original solution is also limited to this range of values of λ . Others [18, 19] solved the same problem using slightly different approaches by using the kernels in the coupled-integral equations which are

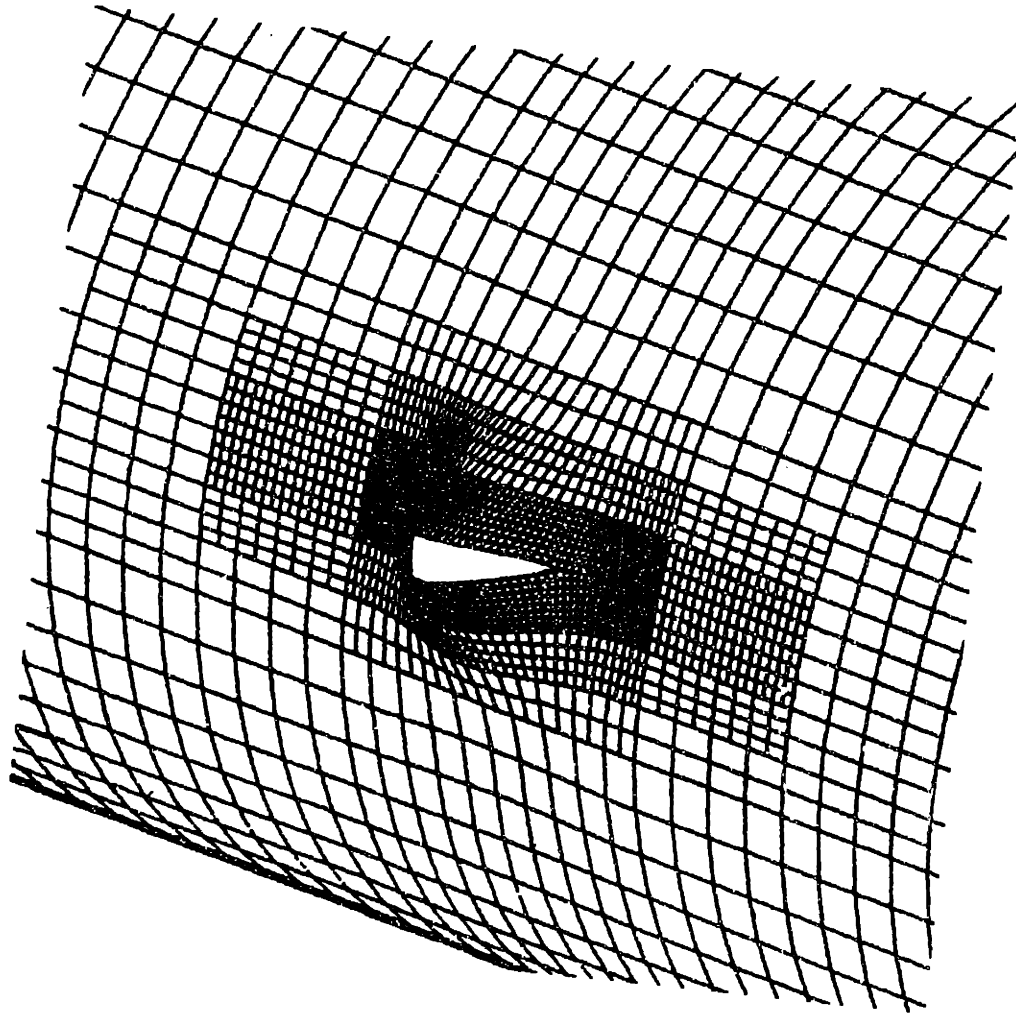


Figure 2.1 Illustration of bulging of the crack face in an axially-cracked cylinders (the out-of-plane deformations are magnified 20 X).

valid for values of λ up to 8, thereby increasing the range of validity of the original solution.

The following simple formula, which is valid for values of λ less than 8, was proposed by Folias [15] to fit the numerical solution of Erdogan and Kibler [18] :

$$K^{em} = (1 + 0.317 \lambda^2)^{0.5} \quad (2.2)$$

where K^{em} is the membrane stress intensification factor and λ is the geometrical parameter defined by equation (2.1). Comparison between the Folias formula shown in equation (2.2) with the Erdogan and Kibler numerical solution [18] is shown in Figure 2.2. The formula fits the data well within approximately 6%.

In the analytical solutions discussed, the only stress intensification considered is the one that is uniform through-the-thickness or the so-called membrane (extensional) stress intensification factor K^{em} . The linearly varying through-the-thickness, or the bending stress intensification factor, was assumed small and neglected. This bending factor cannot simply be combined with the membrane factor when the classical plate or shell theory is used to construct the solution. This is due to the limitation of the classical plate or shell theory in satisfying the physical conditions at the free boundary. In the classical plate or shell theory, the twisting moment and the transverse shear force are combined into the so-called "effective transverse shear force" which is known as the Kirchoff transverse shear force. Thus only four, rather than five, complete boundary conditions are satisfied in the classical theory. This inadequacy in the classical solution causes the angular distributions of the membrane and bending stresses ahead of the crack tip to

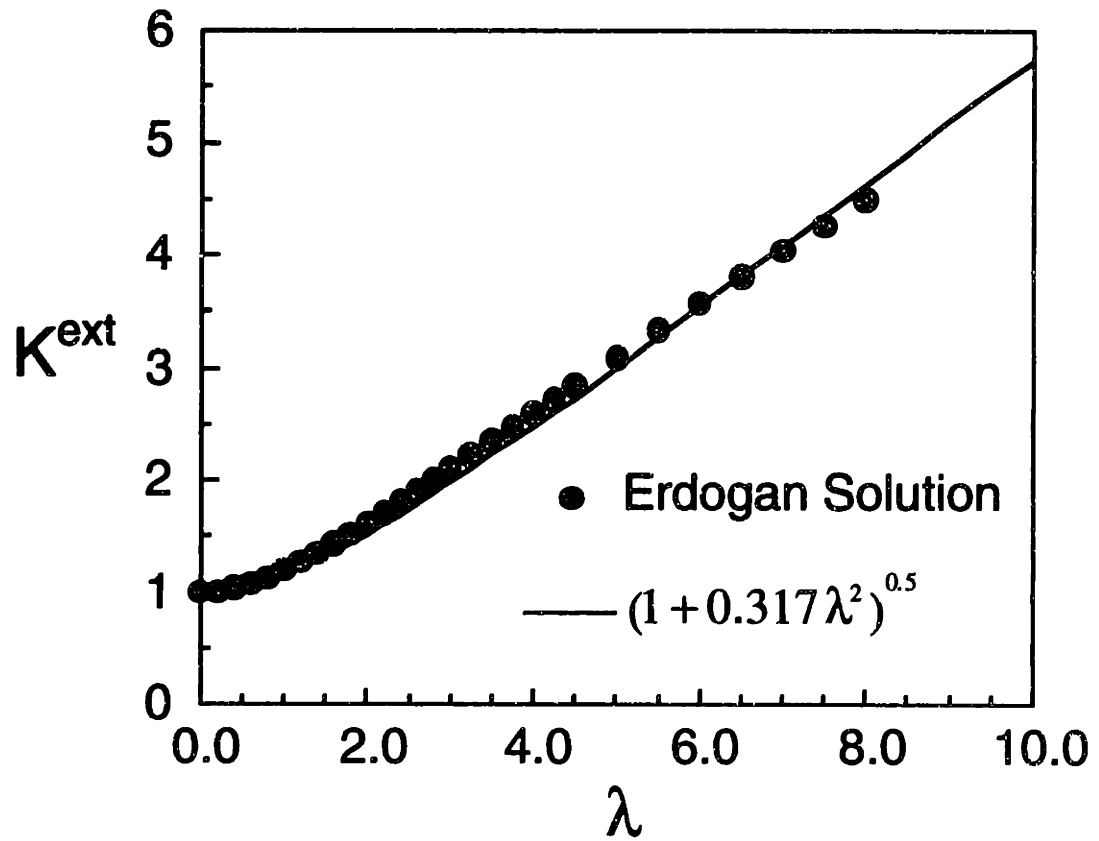


Figure 2.2 Comparison between the Folias formula and the numerical solution of Erdogan and Kibler [18] for the membrane stress intensification.

be different. When a higher order shell theory which includes transverse shear deformation is used to analyze this problem, the angular distributions of the membrane and bending stresses are identical, hence the two stress intensifications can simply be added in this case [21].

To take this bending factor into account in the full analytical solution using the classical plate or shell theory, an "interaction" relation which depends on the magnitudes of the membrane and bending stress intensification factors needs to be utilized. There are several proposed interaction relations that are derived for isotropic, metallic cylinders [19, 38, 40-43]. The generic form of the interaction relation is [38]:

$$K^{total} = K^{ex} \left[1 + \frac{\alpha}{3} \left(\frac{k^{bend}}{K^{ex}} \right)^2 \right]^{0.5} \quad (2.3)$$

where α is a constant whose magnitude is less than one and depends on the Poisson's ratio of the material, and K^{total} and k^{bend} are the total and bending stress intensification factors, respectively. Using the finite element method, Ansell compared the absolute values of the bending and the membrane contributions and found that the magnitudes of the total stress intensification factors computed using equation (2.3) differ by less than 1.0% from the results when the bending factor is neglected for cylinders with the radius-to-thickness ratios ranging from 5 to 2000 [27]. Therefore, this recent analytical and numerical work has shown that the contribution of the bending stress intensification factor in any metallic cylinder can be neglected for all practical purposes.

Besides the analytically-derived stress intensification solutions by Folias and others discussed previously [13-18, 20, 21, 38], there are also other expressions that were derived empirically. The most common empirical

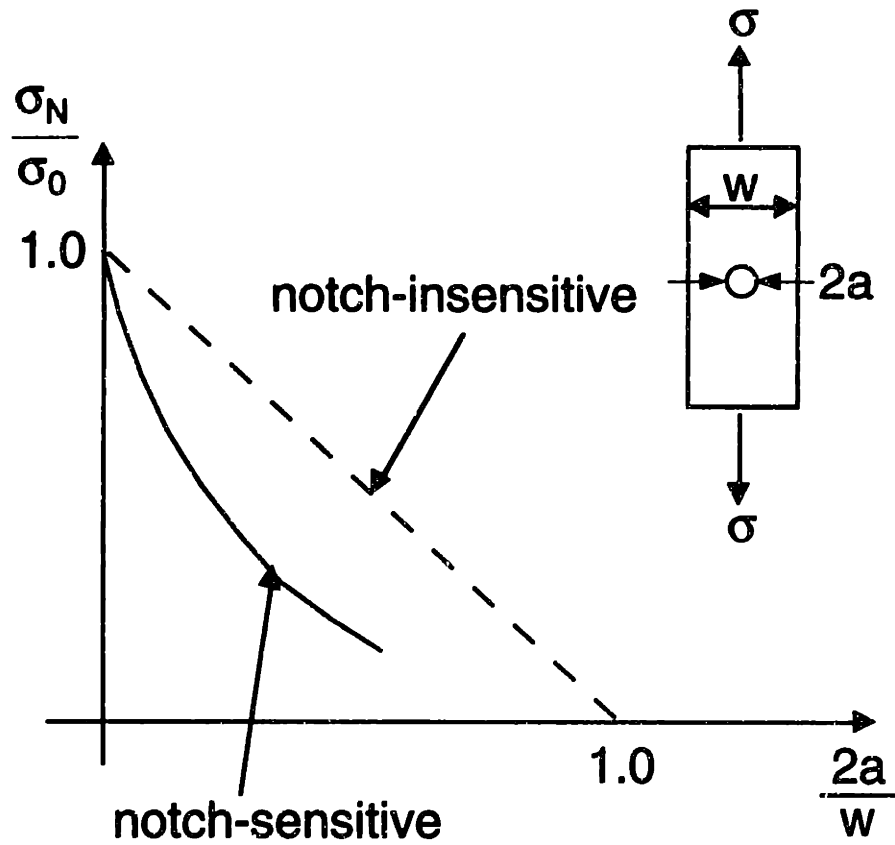
relation for the stress intensification factor was the one proposed by Anderson and Sullivan [23]:

$$K^{cs} = 1 + 5 \left(\frac{a}{R} \right) \quad (2.4)$$

This expression was obtained by comparing the experimental results from the cylinders and the flat plates and is strictly valid only in the limited range of shell geometry ($R/h \approx 100$) and material studied (aluminum). Others modified the expression given in equation (2.4) using one or more fitting parameters to extend its applicability to other cylinder geometries and materials [44, 45]. As these empirical expressions are not based on sound mechanics background, their validity is limited and they are not widely used in practice.

Using the analytically-derived membrane stress intensification factor shown in equation (2.2), a failure prediction methodology for a pressurized cylinder based on the in-plane fracture criterion can be developed. This kind of failure prediction methodology is very appealing, especially in the preliminary design stage, since testing shell-type structures is more difficult and expensive than testing flat coupons. Methodologies have been developed for metallic materials by modifying the Linear Elastic Fracture Mechanics criterion [15, 16] as well as for quasi-isotropic composite materials by modifying composite fracture correlations [25, 26, 46].

These in-plane composite fracture correlations were proposed based on observations that laminated composites are notch-sensitive in the presence of holes and slits [47]. Metallic materials are typically notch-sensitive only in the presence of cracks. Notch-sensitive behavior is illustrated in Figure 2.3. Various fracture correlations have been proposed to explain the notch-sensitivity of composites. An extensive review article on the notch-sensitivity of laminated composites is provided in reference [47]. Since these



σ_N = Notched strength

σ_0 = Unnotched strength

Figure 2.3 Illustration of notch-sensitive and notch-insensitive behavior.

correlations are of importance in constructing the methodology to predict failure of pressurized composite cylinders, two of the commonly used correlations, the Whitney-Nuismer and the Mar-Lin models, are discussed next.

Whitney and Nuismer developed two stress-based fracture criteria for tensile coupons containing holes and slits [48]. The two criteria proposed are: the point-stress criterion and the average stress criterion. In the point stress criterion, it was postulated that laminate failure occurs when the stress over a characteristic distance, d_o , away from the stress concentration is equal to or greater than the unnotched laminate strength σ_o . In the average stress criterion, it was postulated that failure of a laminate occurs when the average stress over a distance, a_o , from the stress concentration is equal to or greater than the unnotched laminate strength σ_o . Therefore, to use the Whitney-Nuismer model, two parameters need to be determined experimentally: the unnotched laminate strength σ_o and the characteristic distance d_o or the averaging dimension a_o . Those parameters have been shown to be dependent on the stacking sequence. Furthermore, since the Whitney-Nuismer correlation is a stress-based criterion, an accurate stress distribution ahead of a discontinuity is also needed. The results depend upon this stress distribution and thus the Whitney-Nuismer correlation is *flaw-shape dependent*.

Another commonly used correlation for laminated composites with through-thickness flaws is the one proposed by Mar and Lin [49]. The Mar-Lin correlation takes into account the bimaterial nature of composites at the micromechanics (fiber-matrix) level and is shown as:

$$\sigma_f = H_c(2a)^{-m} \quad (2.5)$$

where H_c is the experimentally-determined composite fracture parameter [50], $2a$ is the flaw size, and m is the order of the singularity of a crack terminating at a bimaterial (crack/matrix) interface whose magnitude depends on the Young's moduli and Poisson's ratios of the fiber and matrix. The value of m has been computed to be approximately 0.28 for a typical graphite/epoxy bimaterial [50, 51].

By fixing the value of m , the Mar-Lin correlation becomes a one-parameter fit and the only empirical parameter needed is the composite fracture parameter, H_c , which has also been shown to be laminate-dependent. Further work has shown that the Mar-Lin correlation was able to correlate the fracture stress very well for composites that failed in-plane (not due to delamination) [50]. It has also been shown that it is the size of the flaw and not its shape that is important in composites [52, 53].

Using these two in-plane fracture correlations (Whitney-Nuismer and Mar-Lin), there are two kinds of notched cylinder failure prediction methodologies that have been developed. The first one is based on the Mar-Lin correlation [25, 26, 34-37, 46, 54-58]. The other one is based on the Whitney-Nuismer correlation [46, 59-61]. They both require data on uniaxially-loaded coupons (plates) with notches in order to predict the failure (damage tolerance) of pressurized shells. The two general configurations involved are shown in Figure 2.4. To use the Whitney-Nuismer correlation, an accurate stress distribution ahead of a discontinuity is needed. This was accomplished using a numerical technique such as the finite difference technique [46, 59-61]. The Mar-Lin correlation, on the other hand, does not require the stress distribution ahead of the discontinuity and is, therefore, more attractive to use in this case. In this chapter, only the derivation of the cylinder fracture methodology based on the Mar-Lin correlation is presented.

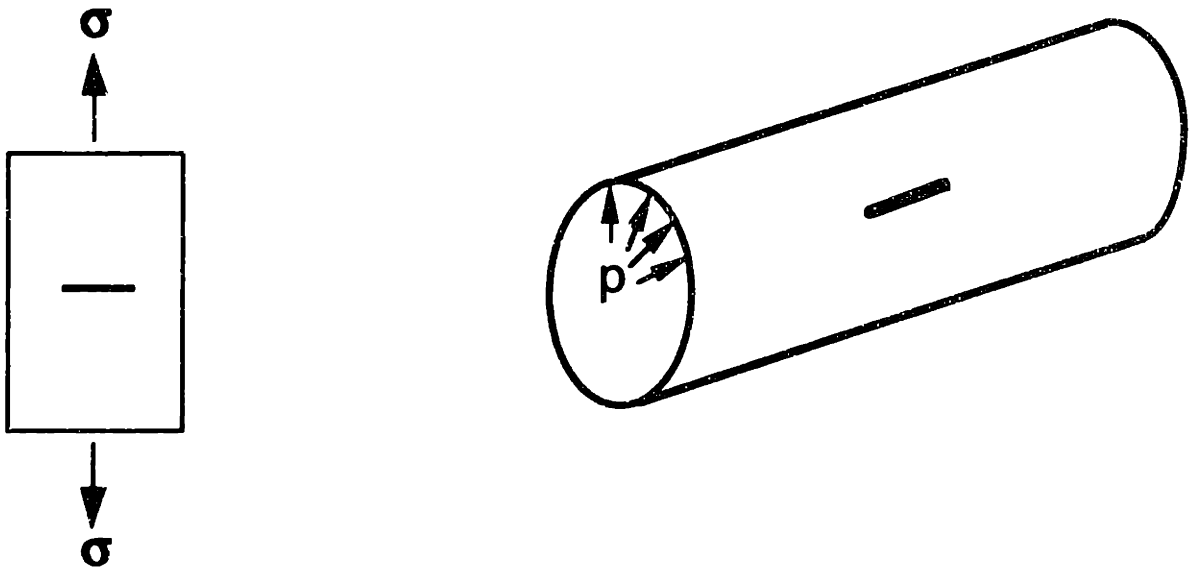


Figure 2.4 Two general configurations involved in the development of the failure prediction methodology: (left) flat coupon and (right) pressurized cylindrical shell.

There are two major assumptions in deriving the failure prediction methodology based on the Mar-Lin correlation. The first assumption is that the longitudinal stress in a cylinder plays no role in the cylinder failure process. This has been shown to be the case for flat coupons where no reduction in fracture stress was observed when the notch was oriented along the direction of the load [52]. The second assumption is that the cylinders have the same failure modes as the plates (i.e. coupons) from which the value of the composite fracture parameter H_c is determined. Unless this second condition is satisfied, different failure mechanisms are operative and thus the composite fracture parameter, H_c , determined from coupon tests may not be applicable in the failure of the cylinders.

The difference in the fracture stress between a pressurized cylinder and a uniaxially-loaded coupon is the stress intensification at the slit tip in the cylinder. Thus, the fracture stress relation between an axially-slitted cylindrical shell and a notched coupon can be written as [25, 26, 36]:

$$\frac{\sigma_{hoop}^f}{\sigma_{plate}^f} = \frac{1}{K^{ext}} \quad (2.6)$$

where σ_{hoop}^f is the hoop fracture stress in a cylinder, σ_{plate}^f is the fracture stress in a flat plate, and K^{ext} is the Folias formula given by equation (2.2). The fracture stress in a flat coupon can be related to the flaw size, $2a$, using the Mar-Lin equation shown in equation (2.5). By substituting equations (2.4) and (2.5) into equation (2.6), the cylinder fracture stress can be written as:

$$\sigma_{hoop}^f = H_c (2a)^{-m} \left[1 + \frac{0.317a^2 (12(1 - \nu_{12}^2))^{0.5}}{R h} \right]^{-0.5} \quad (2.7)$$

The hoop stress is directly related to the pressure via:

$$\sigma_{hoop}^f = \frac{pR}{h} \quad (2.8)$$

Using equation (2.8) in equation (2.7), the internal pressure at failure can be expressed as:

$$p_{failure} = \frac{h}{R} H_c (2a)^{-m} \left[1 + \frac{0.317a^2 (12(1-\nu_{12}^2))^{0.5}}{R h} \right]^{-0.5} \quad (2.9)$$

This modified Mar-Lin correlation has been successfully applied to predict failure of quasi-isotropic fabric [25, 36, 55], sandwich [58], and tape [26, 37, 57] graphite/epoxy composite cylinders. In all of the cases studied, the agreement between the prediction and the experimental results for the quasi-isotropic case was remarkably good.

The methodology presented in equation (2.9) has also been used to predict the failure of structurally-anisotropic cylinders loaded biaxially [26] and uniaxially (in the hoop direction only) [56]. The same curvature correction factor, which is strictly valid only for isotropic cylinders, was utilized in the structurally-anisotropic case. The isotropic assumption is clearly violated in these cylinders as the stiffness in the longitudinal direction is different from that in the transverse (circumferential) direction. To be consistent, a solution of the membrane stress intensification factors for the orthotropic case is therefore needed. As expected, the agreement between the predictions and the experimental failure data in the structurally-anisotropic cylinders is not as good as the quasi-isotropic case. The experimental data were higher than the predicted values in all cases studied [26]. It was shown that cylinders with the smallest slit size ($2a=12.7$ nm) even failed at higher stresses than those in the flat coupon case. It was hypothesized that the

axial loading contributes to the formation of stress-mitigating subcritical damage near the slits, particularly for cylinders with the smallest slit size [56]. This subcritical damage (such as fiber splitting in the 0° (hoop) direction) was believed to contribute to the failure process of such cylinders.

To experimentally study the contribution of the axial stress on the subcritical damage formation, an experimental apparatus that allows the cylinder to be loaded in the hoop direction only was designed. Using the apparatus, the failure pressures of the cylinders were consistently lower than those loaded biaxially. However, these failure data still fell above the predicted values from the methodology. The structural coupling in the form of bending-twisting coupling and the orthotropic nature of the material that are present in this type of cylinder may contribute to the membrane stress intensification factors and to the observed disagreement. Therefore, the expression for the membrane stress intensification factor that can take the orthotropic nature and the structural coupling of the cylinders may be needed for better predictive capability in such cylinders.

Despite some success in the linear failure prediction in the quasi-isotropic case, there are some limitations in the analytical solution by Folias. In addition to the assumption of isotropy, the validity of linear shallow-shell equations was assumed in deriving the membrane stress intensification factors. Further analyses have shown, however, that the maximum "bulging" displacement can be on the order of the shell thickness [27]. This implies that the response of a cylindrical shell with axial crack is nonlinear to some degree. Ansell [27] was the first to include the nonlinear effects in the analyses of axially-cracked cylindrical shells whose geometries resembled a SAAB 340 airplane. The cylinders were analyzed using the ABAQUS finite element code. Ansell's analyses showed that the magnitude of the stress

intensification factors decreases as the loading increases due to stiffening effects. These stiffening effects are due to geometric nonlinearity, making it harder for a crack to open. A reduction in the crack opening displacement leads to a reduction in the energy release rate and the stress intensification factor. These nonlinear effects can, therefore, cause a flawed structure to fail at a higher pressure than that predicted using the Folias solution. Other investigators used different finite element programs [28-32] and semi-empirical parameters [33] to show the same effects in other cylindrical geometries. Some experiments were also performed to verify the analysis results in metallic cylinders [27, 33].

Despite such progress in this area, the nonlinear effects are shown only for specific cylindrical configurations resembling real aircraft fuselages with radius-to-thickness ratios on the order of 1000. It is, therefore, difficult to draw general conclusions on the general effects. No results that are generally applicable for any cylinders have been presented in the literature. Furthermore, the apparent success of the linear theory prediction in the case of laboratory-scaled cylinders with radius-to-thickness ratios on the order of 100 may wrongly imply that the nonlinear effects are actually insignificant. This contradiction necessitates a more general approach to study this problem.

2.2 Damage Arrest in Pressurized Cylinders

Before embarking on a discussion of arrest issues in pressurized cylinders, the general concept of damage arrest is first presented. This general discussion covers both metallic and composite materials.

In many engineering structures made of metallic materials, crack arrest members such as tear straps and stiffening bands are used to arrest a propagating crack [6, 62-64]. These crack stoppers locally alter the stress and strain fields in the stiffened region, constrain further opening of the crack boundary, and finally reduce the stress intensity at the crack tip. Furthermore, crack stoppers can also induce other structural deformation which further reduces the crack propagation driving force. One of the known structural responses induced by tear straps is "flapping" of the skin [11] in a fuselage structure which causes depressurization and leads to a reduction in the crack driving energy and, thereby, crack arrest.

Most of the work done in the area of damage arrest of composite structures to date has been experimental in nature [7, 55, 65, 66]. Early work looked at arrest issues in flat plates [65, 66] and in pressurized cylindrical shells [55]. The damage state considered was a through-thickness slit. There are basically two approaches that were proposed to arrest such damage in composite structures. The first one is to use "buffer" strips which are layers of different materials used to replace the base materials at certain locations. These strips usually have lower stiffness but higher "toughness" than the base materials. However, the introduction of buffer strips in the base laminates can reduce the overall strength of the structures. This arrest concept was explored experimentally [65, 66] and the success of this approach was shown to depend strongly on the initial flaw size as arrest was not accomplished for plates with a small initial flaw size. This damage arrest scheme can also induce other damage modes as significant delamination was observed in the failed specimens.

The second approach to arrest a propagating damage in composites is to use stiffening strips [7, 35, 55]. As in the case of buffer strips, stiffening

strips can also be made of different materials. In this scheme, the base materials are generally unaffected. The stiffening strips can be introduced on the top or bottom surface or even interleaved within the base material. This is similar to the use of crack arrest members in metallic structures where crack arrestors in the form of stiffening bands are typically bolted or bonded to the base structures. The effects of stiffening bands on the fracture path in the flat plate and pressurized cylindrical shell configurations were experimentally studied in the more recent work [35]. The damage was again simulated as a through-thickness slit. The stiffening bands were shown to be ineffective in the flat plate case as damage redirection or turning was not observed in the specimens tested due to the presence of other damage modes such as delamination of the base plate and debonding of the stiffener layers. This is different from what was observed in the pressurized cylindrical shell case where the stiffening bands can induce a change in the damage propagation path from the axial to the hoop directions. Some early experimental work on pressurized composite cylinders supported this finding as well [55].

It was shown that the ability of the circumferential stiffeners to turn the damage propagation from the axial to the hoop directions in a pressurized composite cylinder depends on the number of layers in the stiffening bands. This is in contrast to the results in the flat plate case where no damage redirection was observed due to the existence of other types of damage. A quantitative assessment of the stiffener effectiveness in redirecting the damage in the pressurized composite cylinders in terms of the so-called containment parameter C was proposed [26]:

$$C = \frac{D_s}{D_u} \left(\frac{2a}{R} \right) \quad (2.10)$$

where D_s and D_u are the bending stiffness of the stiffened and unstiffened regions, respectively. The value of the containment ratio increases with likelihood of turning or containing damage which originates at the slit tip between the set of stiffeners. This assessment was based on physical reasoning and experimental observations. As damage approaches the circumferential stiffening bands, bending occurs. Thicker stiffening bands, which have higher bending stiffness than thinner ones, were shown to be more effective experimentally in redirecting damage as an increase of the bending stiffness has more significant effects than that of axial stiffness. Thus, the ratio of the bending stiffnesses of the stiffened to unstiffened regions is important. Furthermore, as the cylinder radius approaches infinity (flat coupon case), stiffening bands were shown to be ineffective in redirecting damage [34, 35]. Therefore, the proposed containment ratio should be inversely proportional to the cylinder radius. The driving energy is represented by the slit size ($2a$). Smaller slit sizes result in a higher failure pressure or higher driving energy (see equation (2.9)) which makes arrest more difficult to accomplish. Therefore the containment parameter should be proportional to the slit size $2a$. The proposed containment ratio was able to rank the anisotropic cylinders, for each laminate considered, according to the amount of damage extending through the stiffeners. In cases when the hoop stiffeners are effective in inducing damage bifurcation and thus turning damage from the longitudinal to the circumferential direction, damage continues its propagation hoopwise during rupture [25, 26, 34, 36, 37].

In summary, most of the work done in the area of damage arrest in pressurized composite cylinders is experimental. Although damage redirection can be induced by the hoop stiffening bands, complete damage arrest was not accomplished as damage continued its propagation in the hoop

direction after bifurcation. There is a therefore a need to further experimentally explore the possibility of completely arresting damage.

The mechanisms of the two structural responses discussed previously, bulging (damage tolerance aspect) and flapping (damage arrest aspect), are related and must be addressed in the design of an all-composite fuselage. Bulging is a dominant response for fracture initiation and for the case where the propagating damage is still oriented in the longitudinal direction. Flapping, on the other hand, is an important structural response in the later stage of damage propagation after the crack has changed its propagation path from the longitudinal to the circumferential direction. As discussed previously, these two relevant mechanisms (bulging and flapping) have not been studied in a general way. The available analytical and experimental work to date only addresses the damage issues for specific cylindrical configurations. Thus, more work which addresses the issues of damage tolerance and arrest in any cylindrical shell is needed to understand these two structural responses and related "scaling" effects.

Chapter 3

Approach

To utilize composites in the design of an aircraft fuselage, the issues of damage (resistance, tolerance, and arrest) and their mechanisms need to be addressed and understood. As noted in Chapter 1, "damage tolerance" can be defined as the ability of a material or a structure to "perform" given particular requirements with damage present, and "damage arrest" can be defined as the ability of a material or structure to arrest propagating damage before such damage causes catastrophic failure. The approach taken in this work to look further into these issues is presented herein.

3.1 Problem Definition

In addressing the damage tolerance and damage arrest concepts, the following three key items need to be first defined within the context of the work: damage, structure, and performance requirement(s). Damage in the present work is simulated as a through-thickness longitudinal slit; the structure is a thin-walled cylindrical shell; and the performance requirement is to sustain pressure loading. Through-thickness damage is a well-defined damage state and is thus used in the present work to identify the important and operative mechanisms in the damage tolerance and arrest in pressurized composite cylinders.

Basic methodology to predict the failure initiation pressure of composite and metallic cylindrical shells containing a longitudinal, through-

thickness damage has been established based on the earlier analytical solutions [15, 25, 26]. As discussed previously in Chapter 2, one of the limitations of the earlier analytical solutions is that they did not take into account the existence of large deformation induced by bulging when such a cylinder is loaded. Thus, geometric nonlinearity is one of the structural mechanisms relevant to the damage tolerance aspect of pressurized composite cylinders containing a longitudinal slit. Despite the abundant analytical and experimental work done in this area to date, particularly in some large cylinders resembling actual fuselages with radius-to-thickness ratios (R/h) on the order of 1000, the basic understanding of the mechanism is still very limited in scope as the available results are presented only for specific cylindrical configurations. Furthermore, the apparent success in the failure prediction methodology based on the linear solution in laboratory-scaled specimens ($R/h \cong 100$) may wrongly suggest that nonlinearity is unimportant for all cylinders. This contradiction is due to a lack of understanding of the general mechanisms and therefore necessitates a more general assessment.

Once fracture is initiated and damage propagation begins, such damage can induce a catastrophic or complete structural failure. Thus, arresting such damage before final failure is crucial in maintaining the structural integrity. In a real aircraft fuselage, one of the key mechanisms of damage arrest is the so-called "flapping mechanism" which involves bending and tearing of the fuselage skin. Flapping occurs when a longitudinal crack has turned or bifurcated, allowing the pressurizing gas to quickly leave the fuselage and, therefore, decreasing the crack propagation driving force. Thus, the study of flapping and how it pertains to damage arrest is related to the study of tear straps or stiffening bands attached to the fuselage skin as

these stiffening elements can induce the structural responses which lead to flapping.

Unlike the issue of geometric nonlinearity, where some work has been done in the past, little has been done in the area of damage arrest in pressurized composite cylinders. In the limited work that is available, only the effects of stiffening bands oriented in the circumferential direction have been studied experimentally. Neither possible interaction between damage and stiffening bands as damage grows and approaches the stiffeners, nor the use of other reinforcement schemes (i.e. stiffening bands in the longitudinal direction) has been addressed in the previous work. Furthermore, although damage bifurcation could be induced by such stiffening bands, as was observed in those cases, damage typically continued its propagation in the circumferential direction during rupture. The experimental results thus showed that flapping in all of the laboratory-scaled specimens tested did not induce a complete damage arrest. Thus, in order to have a better understanding of the mechanisms of arrest in composite cylinders, it is necessary to address both the basic damage arrest mechanisms as well as the scaling effects which may arise when laboratory-scaled specimens are used to model and study damage arrest in full-scale structures.

3.2 Objectives

The general objective of the present study is to understand the operative mechanisms of damage tolerance and arrest in pressurized composite cylinders. Specifically, the study has two main objectives: one, to understand the effects of geometric nonlinearity on the response and failure of pressurized composite cylinders and thereby to better understand the

operative mechanisms of damage tolerance and, two, to understand the operative mechanisms of damage arrest in pressurized composite cylinders by studying the combined effects of longitudinal and hoop stiffening bands on the bifurcation and resulting flapping response in such structures and the possible interaction between damage and stiffeners as damage grows. Emphasis is placed on a general understanding that can be used to address the possibility of scale effects that may arise when laboratory-scaled specimens are used to model full-scale structures. In the next sections, the overall approach for the analytical and experimental investigations is outlined. The details of the analytical and experimental procedures can be found in Chapters 4 and 6, respectively.

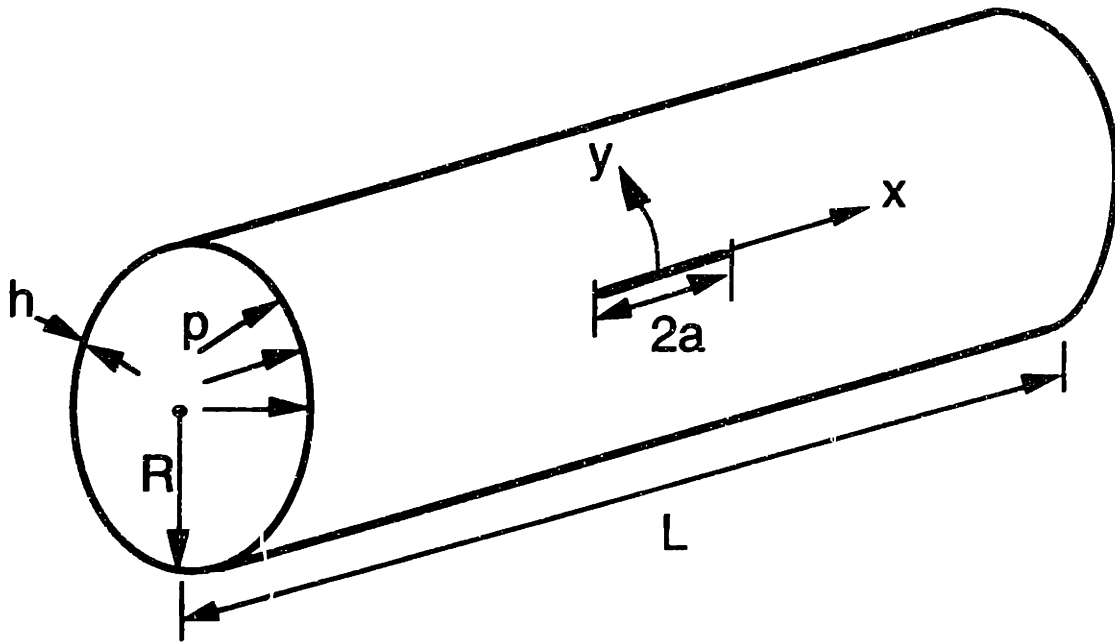
3.3 Overview of Work

The approach taken in the present investigation is to study the mechanisms of damage tolerance and arrest in pressurized composite cylinders using a unified approach consisting of analytical, numerical, and experimental work. To gain an understanding of the issues related to damage tolerance and damage arrest, the analyses look at two different, yet related, problems: one, fracture initiation load (damage tolerance) and, two, flapping (damage arrest) in such cylinders. In the analytical and numerical modelling, different cylinders which resemble configurations of real fuselages and laboratory-scaled specimens were studied to reveal the different mechanisms that may exist at different scales. Experiments on laboratory-scaled specimens were performed to provide results that can help identify key issues in the response and that can also serve as validation of the analytical and numerical findings.

3.3.1 Analytical and Numerical Work

In addressing the damage tolerance aspect, cylindrical shells containing a longitudinal crack were analyzed using the governing equations for a shell structure that undergoes large deformation. At the initial stage, the simple Donnell-Mushtari-Vlasov nonlinear shell equations [39] were used to obtain the governing nondimensional parameters. To make sure that this simpler nonlinear shell theory was able to capture the physics of the problem, the same nondimensional parameters were also derived using a higher order nonlinear shell theory such as the Sanders shell theory [67]. The Sanders theory can be used to model deep shell problems and has therefore been regarded as one of the most accurate, yet complicated, nonlinear shell theories [39].

After these parameters had been obtained from the governing equations, the applicability of such parameters to characterize any cylinder response was verified using the finite element method. Different cylindrical configurations that resemble actual fuselage structures ($R/h \cong 1000$) were analyzed. The generic geometry of the cylinder is depicted in Figure 3.1. The analysis tool utilized was the general purpose STAGS (Structural Analysis of General Shells) finite element code [68]. The stress intensification factors, both linear and nonlinear, were computed numerically using the nodal release technique [69]. These analyses were divided into three phases. The first phase was intended to assess the accuracy of the numerical technique used to compute the stress intensification factor. This was accomplished by comparing the numerically-computed stress intensification factors obtained in the present work with the numerical results available in the literature [18]. After sufficient confidence had been attained in the numerical



NOTE: Not to Scale

Figure 3.1 Illustration of generic geometry of a longitudinally-cracked cylindrical shell under internal pressure.

technique utilized, different cylindrical shells were analyzed in the second stage of the analyses in order to verify the applicability of the nondimensional parameters derived from the governing equations. In the final or third stage, an engineering estimation scheme to estimate the effects of nonlinearity on any cylindrical shell containing a longitudinal crack was formulated and proposed.

To prepare for the experiments performed in order to validate the numerical results in this damage tolerance study, scaled specimens of 305 mm (12 inch) diameter and 760 mm (30 inch) length, the same cylindrical geometry tested in past work in the Technology Laboratory for Advanced Composites (TELAC) at MIT, were also analyzed using the same numerical technique. The cylinders were constructed from HerculesTM graphite/epoxy AW370-5H/3501-6 fabric material with the nominal properties tabulated in Table 3.1. The specimen geometry is shown in Figure 3.2. Three different wall constructions (the two experimental laminates (0/45)_s* and (45/0)_s, and a homogenized isotropic skin) were studied to assess the effects of different bending stiffnesses on the stress intensification and the strain distributions in such cylinders. In the homogenized isotropic case, the Young's modulus is equal to E_L and Poisson's ratio is equal to ν_{LT} as computed from the Classical Laminated Plate Theory for the other two laminate configurations [8]. By comparing the results with the available numerical solutions for the isotropic case [18], the accuracy of the method to compute the stress intensification factors and effects of different bending properties can be assessed. The bending properties of the three wall constructions are tabulated in Table 3.2.

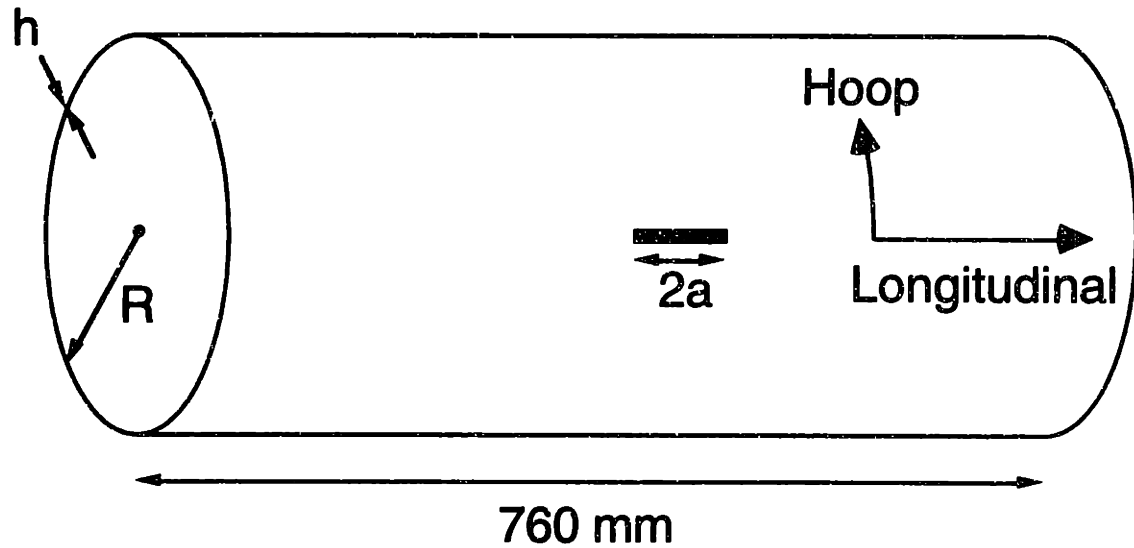
* Laminate notation using parentheses, (), indicates fabric construction.

Table 3.1 Baseline Material Properties

Properties	AW370-5H/3501-6	AS4/3501-6
E_L [GPa]	72.5	142.0
E_T [GPa]	72.5	9.8
ν_{LT}	0.06	0.30
G_{LT} [GPa]	4.4	6.0
t_{ply} [mm]	0.350	0.134

Table 3.2 Bending Properties for the Cylinder Skins

Bending Stiffness [GPa mm³]	(0/45)_B	(45/0)_B	Homogenized Isotropic
D₁₁	15.80	10.68	13.21
D₂₂	15.80	10.68	13.21
D₁₂	1.84	6.95	4.36
D₁₆	0.0	0.0	0.0
D₂₆	0.0	0.0	0.0
D₆₆	1.87	6.98	4.43



$R = 152 \text{ mm}$
 $h = 1.4 \text{ mm}$
 $2a = 5.1 \text{ mm}, 78 \text{ mm}, \text{ and } 104 \text{ mm}$

NOTE: Not to Scale

Figure 3.2 Geometry of a longitudinally-cracked, unstiffened, laboratory-scaled cylinder investigated in the present work.

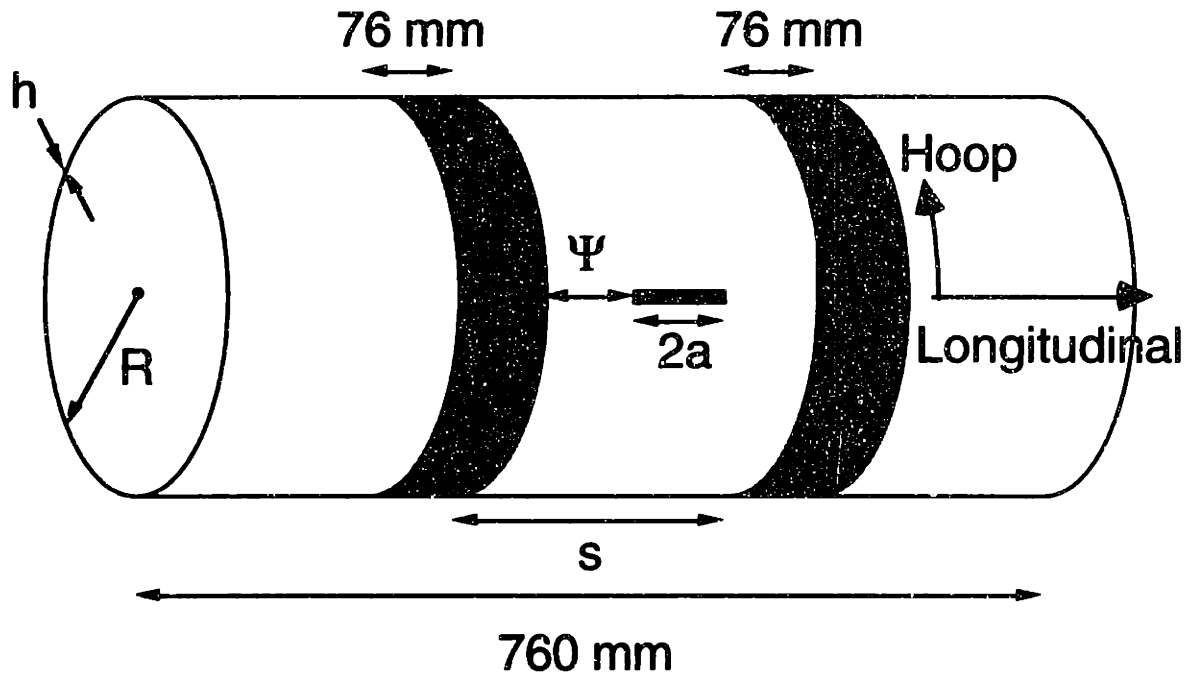
Longitudinal slits of length 51 mm, 78 mm, and 104 mm, which correspond to the values of the geometrical parameter λ of 3.2, 4.8, and 6.4, respectively, were considered in the analyses. In an actual fuselage structure, the "extreme" situation typically considered in design (i.e. one-bay crack) can correspond to a value of λ in the vicinity of 12, depending on the specific geometry. If the same value of λ had been chosen in the present experimental work involving laboratory-scaled specimens, the hoop stress in such cylinders would have been unrealistically low to model the real situation in an actual fuselage. Thus, slightly smaller values of λ were considered in the present work. The three slit sizes chosen were also considered to model the somewhat self-similar damage propagation observed experimentally in these fabric cylinders.

The metrics of interest from these analyses are the nonlinear stress intensification factors and the nonlinear strain distributions. From the computed stress intensification factors, the nonlinear effects on the failure of such cylinders can be assessed. The numerical results can also be used to guide further experimental efforts in order to verify the numerical results experimentally by finding regions on the cylinder surface where significant differences exist between the linear and nonlinear solutions as predicted from the analyses. These were designated as the "regions of interest" to be investigated using strain gages in the experimental portion of this work. Comparison between the numerical and experimental strain responses made in these regions provide means to validate the numerical results in the damage tolerance part of the investigation.

As discussed previously, very little analytical and numerical work has been done in the area of damage arrest of pressurized composite cylinders. The initial damage path in cylinders constructed from this fabric material

system has been shown to be rather self-similar as damage typically propagates in the longitudinal direction before bifurcation takes place near the edge of the stiffening bands [25, 36]. It was hypothesized that such damage propagates perpendicular to the orientation of the maximum tensile strain near the slit tip [36]. The presence of stiffening bands can change the orientation of the maximum tensile strain which induces damage to turn. The interaction between damage and the stiffening bands during the initial damage propagation (as damage approaches the stiffeners) was thus the focus of the present numerical study.

The stiffened geometry considered in this part of the numerical work is depicted in Figure 3.3. The ligament is defined as the region between the slit tip and the edge of the stiffening bands and is characterized by its width ψ . The ligament width ψ was chosen to be 20 mm in order to accommodate two strain gages in the longitudinal direction during the experimental phase of the work. The propagation of damage in such a cylinder can be viewed in two ways: one, keeping the stiffener spacing fixed while the crack length increases and, thus, the ligament length decreases or, two, keeping the ligament width constant while both the crack length and stiffener spacing change accordingly. In the former, the ligament length gets smaller and more shell elements are needed in order to maintain an acceptable element aspect ratio in that region. Otherwise, numerical difficulties can occur which can lead to erroneous results. In the second option, the number of elements and the element aspect ratio can be kept constant as damage propagates. This second option was considered more practical as the first option would require an excessive number of elements to model the entire structure. The second option was thus chosen.



$R = 152\text{ mm}$
 $h = 1.4\text{ mm}$
 $\Psi = 20\text{ mm}$
 $s = 2a + 40\text{ mm}$

NOTE: Not to Scale

Figure 3.3 Geometry of a circumferentially-stiffened cylinder analyzed in the present investigation.

The existence of two length parameters that are independent (crack length and ligament width or crack length and stiffener spacing) during damage propagation allows a nondimensionalization of this problem using any two length parameters described. The two parameters chosen are the ligament width ψ and the half-crack length a . The present numerical work covered different ψ/a ratios ranging from the so-called "non-interacting case" when damage is far from the stiffening bands (large values of ψ/a) to the case when damage approaches and is close to the stiffening bands (small values of ψ/a). The ψ/a ratios investigated in the present numerical work are shown in Table 3.3.

3.3.2 Experimental Work

The experimental portion of the work can also be divided into the damage tolerance and damage arrest aspects. The experiments performed dealing with damage tolerance were intended to complement the numerical work and to serve as a validation of the numerical results. The experiments performed in the damage arrest aspect were intended to complement the numerical work, assess the effects of a combined longitudinal and hoop stiffening bands on the damage propagation in pressurized composite cylinders, and point out key experimental results that need to be addressed further.

As mentioned previously, the HerculesTM graphite/epoxy AW370-5H/3501-6 fabric was chosen as the material for all cylinders in the present study. This material system and the specimen geometry were chosen for two reasons. First, the fracture path for cylinders manufactured using this material system has been shown to be rather self-similar and relatively easy to identify from post-mortem inspection. Since one of the objectives of the

Table 3.3 Slit and Stiffener Spacing Geometry for all Type-2 Cylinders

$2a$ [mm]	ψ/a^b	Stiffener Spacing [mm]
51	0.78	91
78	0.51	118
104	0.38	144
208 ^a	0.19	248
312 ^a	0.13	352
416 ^a	0.096	456

^aonly numerical analyses (no experiments) were performed

^b ψ is 20 mm in all cases

present investigation is to understand the operative mechanisms of damage arrest, a clear fracture path is desirable. The second reason is that previous damage tolerance and damage arrest studies on pressurized composite cylinders in TELAC were performed using this material system and the same cylindrical configuration [26, 36]. This previous work includes: measurement of fracture parameters for flat coupons, comparison between the notched strength prediction with experiments, and determination of the effectiveness of the hoop stiffening elements in inducing damage bifurcation. This fabric material system was therefore chosen so that previous results could be effectively utilized.

The experimental investigation in the present work was focused on three different kinds of cylindrical configurations: one, unstiffened construction designated as the *type-1* cylinder shown in Figure 3.2, two, circumferentially-stiffened construction designated as the *type-2* cylinder shown in Figure 3.3, and, three, construction stiffened in the longitudinal and circumferential directions designated as the *type-3* cylinder as shown in Figure 3.4. Both the *type-1* and *type-2* cylinders were manufactured in 4-ply, quasi-isotropic configurations with $(0/45)_s$ and $(45/0)_s$ stacking sequences. The *type-3* cylinders were manufactured in a 4-ply, quasi-isotropic configuration with a stacking sequence of $(0/45)_s$ only. These cylindrical configurations were chosen to be consistent with previous experimental work [26, 36] and to supplement the analytical and numerical work done on the same configurations. The number of specimens manufactured for each type is shown in Table 3.4.

The experiments using the *type-1* cylinders were used to get the strain responses and not necessarily the failure data which were already available in previous work [26, 36]. Thus, only two *type-1* cylinders, one each with

Table 3.4 Summary of the Test Matrix for the Experimental Investigation

Cylinder Configuration	Stacking Sequence	
	(0/45) _s	(45/0) _s
Type-1	1 ^a	1
Type-2	3	3
Type-3	5	0

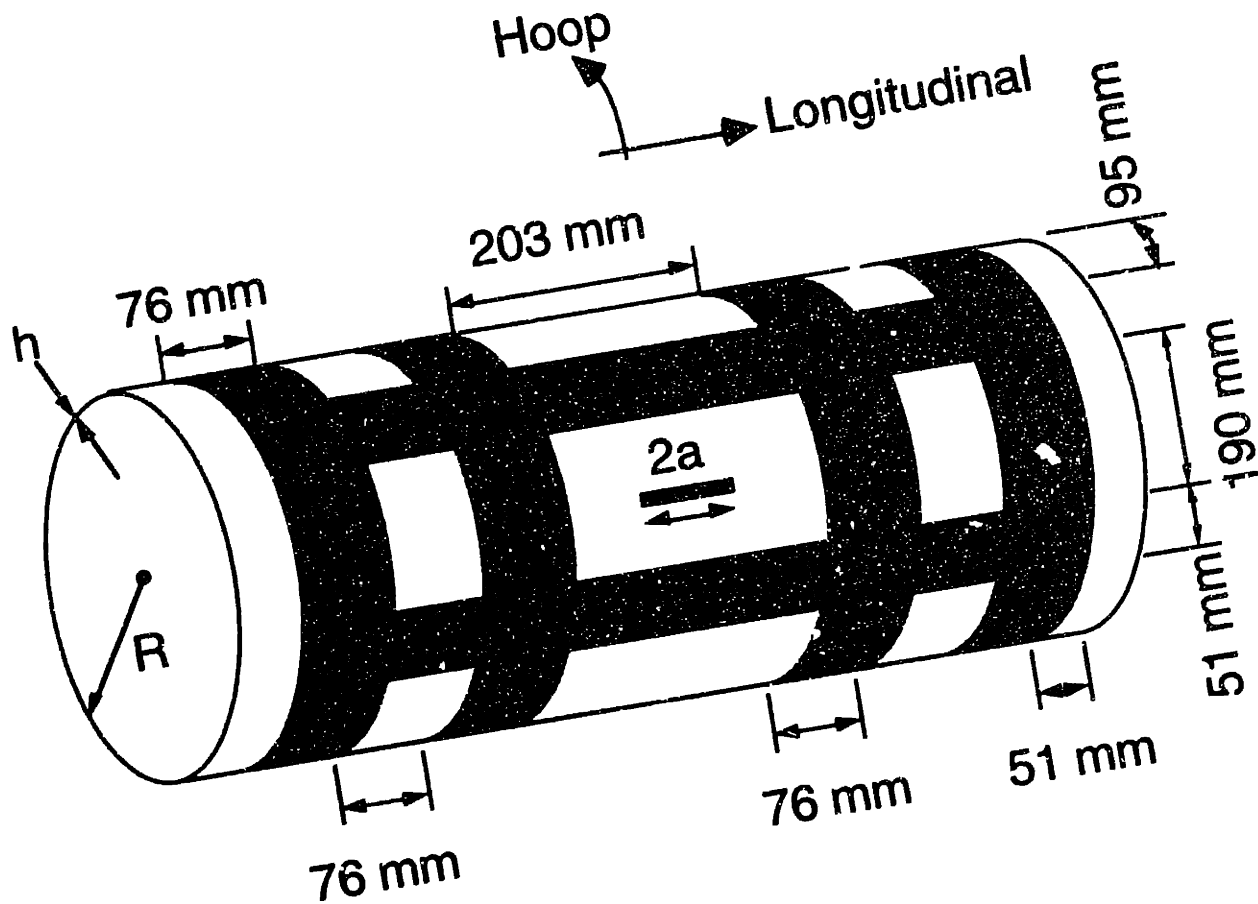
^a indicates number of cylinders

(0/45)_s and (45/0)_s quasi-isotropic configurations, were manufactured. Initially, a 51 mm longitudinal slit was cut into each cylinder. Three tests were performed sequentially at different slit sizes (51 mm, 78 mm, 104 mm) in each of the *type-1* cylinders. The slit sizes were chosen to be consistent with the numerical modelling previously described. Strain gages were bonded in the "regions of interest" determined from the numerical results described in Chapter 5. The cylinders were pressurized quasistatically using nitrogen gas. Since three tests were performed sequentially, it was important that catastrophic failure did not occur during the first two tests (i.e. when the slit sizes were equal to 51 mm and 78 mm). Therefore, the cylinder could be pressurized only up to a predetermined pressure level. This predetermined value should not be too low that no nonlinearity is detected, nor should it be too high that the slit tip regions are significantly damaged. This pressure was determined based on the strain response obtained from the analysis and results from previous work. After the pressure had reached the predetermined value, the pressurization was stopped, the cylinder was depressurized, and the slit was lengthened. The tests were then started again with a longer slit size after new strain gages were placed on the cylinder since the locations of the "regions of interest" had changed for the longer slit size.

Unlike the *type-1* cylinders, the stiffener spacings in the *type-2* cylinders depend on the slit sizes. These cylinders could not be modified and reused after the first round of tests was completed. Therefore, a total of six *type-2* circumferentially-stiffened cylinders with the geometry shown in Figure 3.3 were needed, three each of the (0/45)_s and (45/0)_s layups. The stiffening bands in the *type-2* cylinders were manufactured from four layers of the same fabric material system to be consistent with the *type-B* stiffener

used to construct the *type-3* cylinders as discussed later. The bands were cocured on the outer surface of the cylinder skins. The hoop stiffener spacing depends on the slit size as illustrated in Figure 3.3. The actual spacings are tabulated in Table 3.3 along with the ratio of the ligament width to slit half-size. Note that these cylinders have the same geometry as those which were numerically analyzed. The same slit sizes as those in the *type-1* cylinders (51 mm, 78 mm, and 104 mm) were cut into these *type-2* cylinders to provide consistency for comparative purposes. Strain gages were bonded in the regions determined from the numerical analysis. All cylinders were pressurized quasistatically to failure to collect the strain data. The measured response was compared with the numerical prediction from finite element analyses.

The specimen geometry of the *type-3* cylinders is illustrated in Figure 3.4. Only one slit length, equal to 79 mm, was considered for all cases. There are several reasons for this. First, it was intended not to have an excessively high failure pressure (driving energy) during rupture which would prevent damage bifurcation from taking place. Previous work showed that damage bifurcation did occur for cylinders with this slit length [36]. Second, it was intended that the interaction between the stiffening bands and the stress fields near the initial slit tips be minimal and not affect the fracture initiation pressure. The distance between the two stiffeners was 203 mm, therefore longer initial slit sizes might violate this criterion. Lastly, it was also intended to set the first nondimensional ratio in the proposed containment parameter [26] (the ratio between the slit size and the cylinder radius) constant for all cases studied here so that the effects of bending stiffness could be isolated.



$R = 152 \text{ mm}$
 $h = 1.4 \text{ mm}$
 $2a = 79 \text{ mm}$

NOTE: Not to Scale

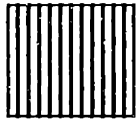
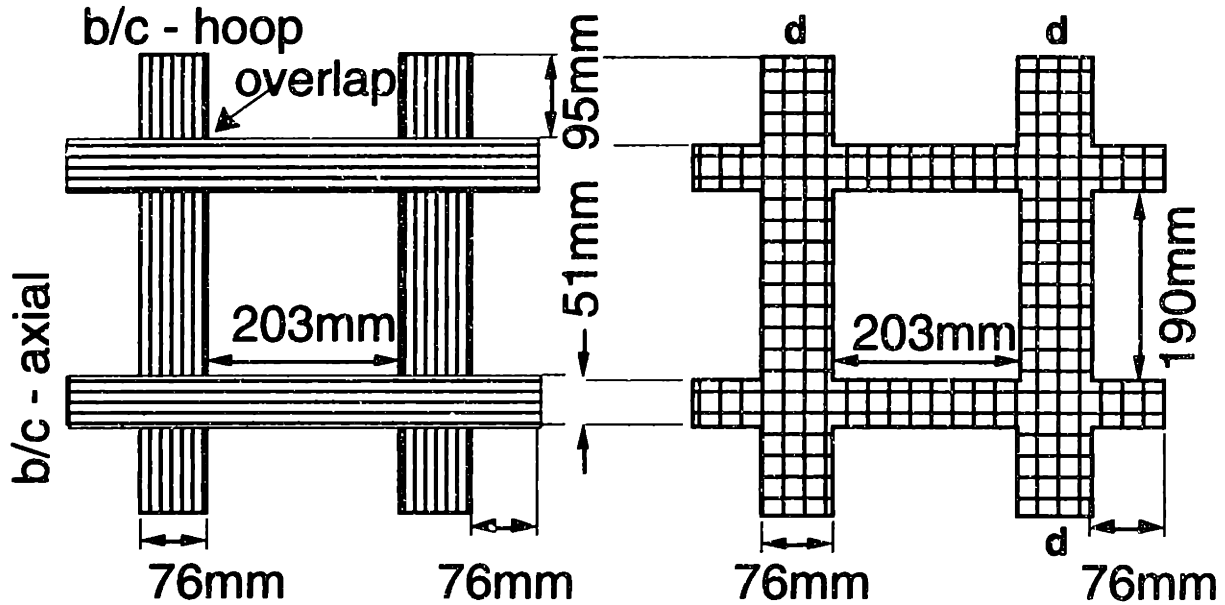
Figure 3.4 Geometry of the cylinder stiffened in the longitudinal and circumferential directions.

Two different stiffener configurations (*type-A* and *type-B* stiffeners) depicted in Figure 3.5 were studied. The *type-A* stiffener consists of alternating continuous and broken stiffeners in the longitudinal and hoop directions. This scheme was chosen in order to eliminate overlaps (additional material) at locations where the two types of stiffeners met. For example, the first layer of the hoop band was continuous but the first layer of the longitudinal band was discontinuous/broken. The scheme was then reversed in the subsequent layer (i.e. in the second layer, the longitudinal band was continuous while the hoop band was not). The stiffeners of this type were manufactured from Hercules AS4/3501-6 graphite/epoxy unidirectional tape material with the fibers running parallel to the reinforcing direction. The nominal properties of the AS4/3501-6 material are tabulated in Table 3.1. This material was chosen to be consistent with previous work [26, 36]. In the *type-A* stiffener, due to the material system used (unidirectional material) and the alternating continuous and broken stiffener layers, matrix cracking in and through the stiffener layers is a possible damage mode. This can lead to subsequent delamination [70, 71]. Thus, matrix-crack paths exist in the *type-A* stiffener configuration.

In contrast, the *type-B* stiffener consists of two pieces of continuous "checkerboard" stiffener configuration with no layers overlapping and no discontinuous layers at the intersection of the main piece. The material for the *type-B* stiffener was chosen to be the same woven fabric as the base material (AW370-5H/3501-6). This stiffener configuration, including the use of fabric material, was chosen to eliminate matrix crack paths, which have been shown to induce other damage modes such as delamination, in the main piece (region of interest for damage arrest). It is also worth noting that since the stiffnesses in the longitudinal and hoop directions for fabric material are

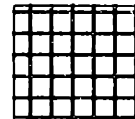
Type A-stiffener

Type B-stiffener



AS4/3501-6

b = broken
c = continuous



AW370-5H/3501-6

NOTE

Two pieces of stiffeners connected at "d" for each cylinder stiffened with type-B stiffeners

Figure 3.5 Illustrations of two different stiffener configurations investigated (half of cylinder configuration shown).

almost identical, the longitudinal and hoop stiffeners have roughly the same stiffness values. The two stiffener geometries are shown in Figure 3.5. The stiffener configurations studied are tabulated in Table 3.5. It is worth noting that these stiffener configurations were chosen sequentially. As discussed later in Chapter 6, the *type-A* configuration did not work due to the presence of matrix-crack paths. Work was then continued using the *type-B* stiffener configuration.

In both stiffener configurations, each cylinder was stiffened with four longitudinal stiffeners. Preliminary study using only three longitudinal stiffeners resulted in a distorted cylinder cross-section after the cure was completed. That particular cylinder almost had a somewhat triangular cross-section, which then caused difficulties to put the cylinder in its endcaps. By using four (rather than three) longitudinal stiffeners and placing additional hoop stiffeners, each made of four layers of the tape material (in the *type-A* cylinder) and of the fabric material (in the *type-B* cylinder), near each cylinder end, this distortion was practically eliminated. In addition, the longitudinal stiffener width of 51 mm was less than the 76 mm width of the hoop stiffeners to reduce the "hardness" of these points. This further aided in maintaining the circular cross-section. This additional hoop stiffeners were located close to the endcap (approximately 51 mm from the endcap) and thus did not influence the damage path. Therefore, this construction, which utilized four longitudinal stiffeners and additional hoop stiffeners near each cylinder end, was utilized in the present work.

All cylinders were pressurized to failure and photographs were taken after the tests to identify the damage path. An assessment of the effectiveness of the combined effects of longitudinal and hoop stiffening bands was then made.

Table 3.5 Stiffener Configurations for the *Type-3* Cylinders

Cylinder	Configuration Type ^a	Number of plies in the hoop direction	Number of plies in the axial direction
1	A	4 (0° tape)	8 (0° tape)
2	B	2 (0° fabric)	2 (0° fabric)
3	B	4 (0° fabric)	4 (0° fabric)
4	B	4 (45° fabric)	4 (45° fabric)
5	B ^b	4 (0° fabric)	8 (0° fabric)

^a see Figure 3.6

^b Four additional 0° fabric layers in the longitudinal direction

Chapter 4

Analytical and Numerical Methods

The analytical and numerical methods used in the present investigation are described in this chapter. The chapter is divided into two main parts: one, derivation of the governing nondimensional parameters and, two, numerical solution technique utilized. Results of the analyses are presented in Chapter 5.

4.1 Derivation of the Nondimensional Parameters

To assess the influence of geometric nonlinearity on the failure of *any* cylindrical shell containing a longitudinal crack, the derivation of "structural scaling" parameters from the governing equations of a shell structure undergoing large deformation is needed. One way to determine the nondimensional or scaling parameters in any engineering problem is to perform nondimensionalization of the governing equations that properly model the physical problem of interest. In the present work, the physical problem that is being modelled is the existence of large out-of-plane displacement, known as *bulging*, near the crack region in a pressurized cylindrical shell. The geometry of the cylindrical shell considered is shown in Figure 3.1. The proper governing equations to model this physical situation are the nonlinear shell equations.

Among the nonlinear shell equations available in the literature [39], the Donnell-Mushtari-Vlasov (DMV) nonlinear shell theory was initially

chosen to derive the parameters due to its simplicity. The nonlinearity assumed in the DMV theory includes large deformation and moderate rotation [39]. The moderate rotation kinematics imply that the maximum rotation that can be handled by such theory should be less than 10° [72]. The kinematics or strain-displacement assumption inherent in the DMV theory is that of shell-shallowness. This shell-shallowness assumption implies that the shell geometry resembles that of a flat plate with small initial curvature. This implies that the ratio of the depth of the cylinder to the cylinder radius is small (much less than 1). The cylinder is assumed to be constructed using isotropic or quasi-isotropic homogenized composite materials. The Sanders nonlinear shell theory [67], which is a higher-order theory and valid for the case of deep shells, was used to derive the same parameters as shown in Appendix A. Numerical solutions using the Donnell and the Sanders theories are expected to be identical for this case since the size of the crack oriented in the longitudinal direction does not influence the shallowness condition. However, when the crack is oriented in the circumferential direction, the size of the crack does influence the shallowness assumption. Therefore, the numerical solutions using the two theories are not expected to agree for this latter case and it would be necessary to use the higher order theories that are valid for deep shells. However, the generality of the approach outlined here is not lost for the present geometry by using this simpler shell theory. Therefore, only the derivation using the DMV theory is presented here for the sake of simplicity.

The DMV governing equations for such cylindrical shells are [39]:

$$\frac{1}{E h} \nabla^4 F = \frac{1}{R} w_{,xx} + w_{,xy}^2 - w_{,xx} w_{,yy} \quad (4.1)$$

$$\frac{E h^3}{12(1-\nu^2)} \nabla^4 w = -\frac{1}{R} F_{,xx} + F_{,x} w_{,yy} + F_{,yy} w_{,xx} - 2 F_{,xy} w_{,xy} + p \quad (4.2)$$

where F is the stress function, w is the out-of-plane displacement, p is the internal pressure, x is the longitudinal coordinate, y is the hoop coordinate, E is the material modulus, and ν is the Poisson's ratio. The "comma notation" (,) indicates a derivative with respect to the parameters which follow the comma. It is convenient to perform nondimensionalization of equations (4.1) and (4.2) via:

$$x' = a x \quad (4.3)$$

$$y' = a y \quad (4.4)$$

$$w' = \frac{\lambda^2 h}{[12(1-\nu^2)]^{1/2}} w \quad (4.5)$$

$$F' = \left(\frac{E h^3}{12(1-\nu^2)} \right) F \quad (4.6)$$

where λ is the same geometrical parameter obtained from the linear solution [13-15, 17-19, 21] shown as:

$$\lambda = \frac{a}{\sqrt{R h}} \sqrt[3]{12(1-\nu^2)} \quad (4.7)$$

In the nondimensionalization process, a is the half-crack length, h is the cylinder thickness, and E and ν are the material parameters. Henceforth, the primed quantities correspond to the physical variables and the unprimed quantities are dimensionless.

By substituting equations (4.3) through (4.6) into equations (4.1) and (4.2) and utilizing equation (4.7), the nondimensional governing equations can be written as:

$$\nabla^4 F - \lambda^4 w_{,xx} = \lambda^4 [w_{,xy}^2 - w_{,xx}w_{,yy}] \quad (4.8)$$

and

$$\nabla^4 w + F_{,xx} = F_{,xx} w_{,yy} + F_{,yy} w_{,xx} - 2F_{,xy} w_{,xy} + \lambda^2 \sqrt{12(1-\nu^2)} \eta \quad (4.9)$$

where η is given as:

$$\eta = \frac{p}{E \left(\frac{h}{R}\right)^2} \quad (4.10)$$

Therefore, unlike the linear theory, where only one parameter, the geometrical parameter λ , is needed to characterize the cylinder response, the nonlinear formulation requires *two* parameters: the geometrical parameter λ and the loading parameter η .

The η -parameter is a measure of the driving force of the nonlinearity and can also be written as

$$\eta = \left(\frac{pR}{h}\right) \frac{1}{E} \frac{1}{\left(\frac{h}{R}\right)} \quad (4.11)$$

where each of the three components represents a part of the physical driving force for nonlinear behavior. This can be reasoned as follows. One, the driving force for nonlinearity is directly proportional to the hoop stress $\left(\frac{pR}{h}\right)$ since the higher the hoop stress, the larger the out-of-plane deformation and thus the more nonlinear the response. Two, this parameter is inversely proportional to the material (homogenized laminate) stiffness (E) since E is a measure of the material (and therefore structural) resistance to deformation. Three, this parameter is also inversely proportional to the shell ratio $\left(\frac{h}{R}\right)$ since, for a particular cylinder with a known radius, the smaller the magnitude of the shell ratio, the smaller the shell wall rigidity resulting in

larger out-of-plane (bulging) deformation and greater nonlinear response. The η -parameter obtained via the equations is therefore consistent with that obtained by considering the physics of the situation.

In summary, the response of any cylindrical shell containing a longitudinal crack has been shown to depend on two nondimensional parameters: the geometrical parameter λ and the loading parameter η . The applicability of the two nondimensional parameters to characterize any cylinder response is verified using the finite element method as described in later sections.

4.2 Numerical Solution

The STAGS finite element code [68] was used to provide the numerical solutions. Both the linear and nonlinear stress intensification factors were computed. As discussed previously, this membrane stress intensification factor, K^m , is the ratio of the stress intensity in a cracked shell to that in a cracked plate of the same crack geometry. There are many numerical schemes that can be used to compute the stress intensity factor of a cracked structure [28, 69, 73, 74]. Some of the more popular techniques are based on path-independent integrals (such as the J-Integral [75]) [73], the crack closure integral [74], and the modified crack closure technique [28, 69]. To compute the stress intensity factors in the present work, the modified crack closure technique [28, 69] was utilized. This is also known as the nodal release technique, and was chosen due to its accuracy, simplicity, and compatibility with the STAGS code. Since the technique is based on an energy argument, as described later, no special finite element is required to

take into account the singular behavior at the crack tip to get accurate results.

In general, energy is the product of forces and displacements. Therefore, the use of this numerical technique requires two separate analyses (runs): one, to compute the nodal forces and, two, to compute the crack face separation distance as functions of the applied loading. This requirement may render this method inefficient for extremely large problems (such as a three-dimensional crack problem). Methods based on the energy-conservation integral (such as the J-integral) [73] may be more efficient for this larger problem. Nevertheless, due to the size of the problem studied in the present work, the nodal release technique is considered efficient for all the cases analyzed in the present work.

The procedure for the computation of the energy-release-rate using the nodal release technique is outlined briefly here. More detailed descriptions can be found elsewhere [28, 69]. Each crack tip in the finite element model is created using two different nodes which are called the master and the slave nodes. These two nodes have the same spatial coordinates and are constrained such that they move the same amount. In the first run, the general nodal forces (three axial forces denoted by subscripts 1, 2, and 3 and three moments denoted by subscripts 4, 5, and 6) at each crack tip needed to ensure compatibility of the two crack tip nodes are computed. In the second run, the crack is lengthened by moving the tip by an increment Δa , which is chosen *a priori*, thus allowing the two original crack tip nodes to have independent degrees of freedom. The separation distances on a nodal degree-of-freedom basis (three translations denoted by subscripts 1, 2, and 3 and three rotations denoted by subscripts 4, 5, and 6) between the two nodes are obtained from this latter analysis. The process is depicted in Figure 4.1. The

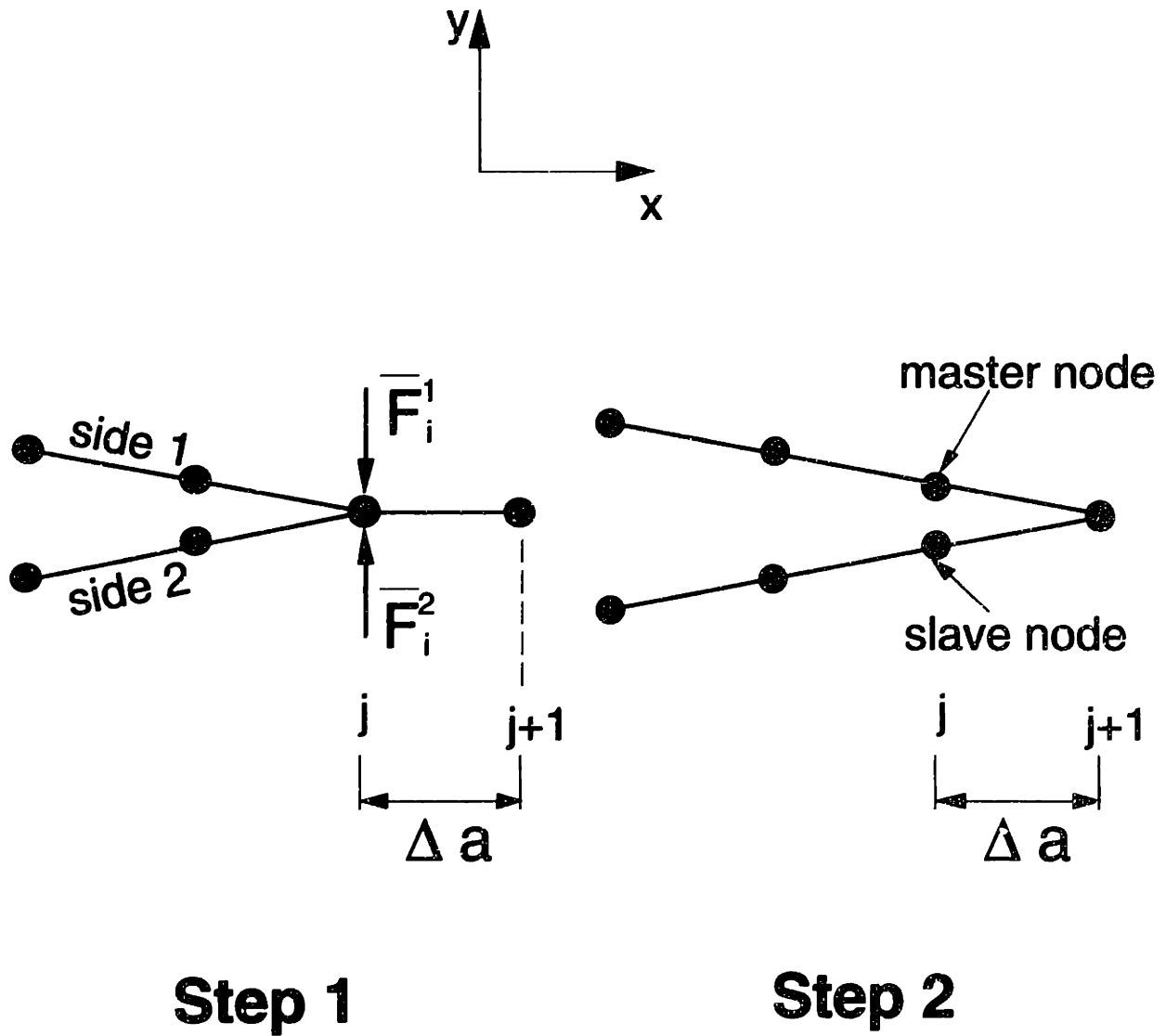


Figure 4.1 Illustration of the finite element mesh topology near a crack tip necessary to use the Nodal Release Technique: crack tip, (left) initially at position (j); (right) is moved to position ($j+1$).

components of the work done on a nodal degree of freedom basis, W_i , at each pressure load are computed by multiplying the corresponding nodal forces, from the first run, and separation distances, from the second run, and dividing the result by surface area generated by the process (twice the product of the shell thickness, h , and crack increment, Δa)

$$W_i = \frac{1}{2h \Delta a} [\bar{F}_i^1 (\bar{u}_i^2 - \bar{u}_i^1)], \quad i = 1, \dots, 6 \quad (4.12)$$

The mode I and mode II energy release rates, G_I and G_{II} , can be computed as [69]

$$G_I = W_2 + W_6 \quad (4.13)$$

$$G_{II} = W_1 \quad (4.14)$$

Once the energy release rates are known, the corresponding stress intensity factors can be calculated using the Irwin's formulae [76]

$$K_I = \sqrt{E G_I} \quad (4.15)$$

$$K_{II} = \sqrt{E G_{II}} \quad (4.16)$$

The mode II contribution in the present problem vanishes due to symmetry in the cylinder geometry and loading condition. As noted, the crack increment, Δa , needs to be chosen *a priori* to use the nodal release technique. This choice depends on the specifics of the problem and is discussed for the present case in Chapter 5.

In the linear case, the linear stress intensification factor is obtained by taking the ratio of the stress intensity factor of a cracked shell obtained numerically with the analytical stress intensity factor of a cracked plate of the same geometry. The stress intensification does not change with magnitude of loading for the linear case, so this calculation can be done at

any loading magnitude and the computed value is applicable for all such cases.

For the nonlinear case, the stress intensification does change with loading as the nodal forces and separation distances needed in equation (4.12) depend on the applied loading. These nodal forces and separation distances are available only at discrete load steps which are typically not evenly spaced. To get a continuous solution, some kind of interpolation of the discrete data is therefore necessary. This kind of interpolation is still needed even if another numerical technique is used to compute the stress intensity factors. The cubic spline method [77] was used to interpolate the discrete nodal forces and separation distances. Once the continuous dependence on the applied loading is known, the nodal release technique is used to obtain the evolution of the energy-release-rate and the stress intensity factor. The nonlinear stress intensification factors are obtained by taking the ratio of the stress intensity of a cracked shell to that of a cracked plate of the same crack geometry at each load step. Once the magnitudes are known, the dependence of the stress intensification factor on the applied loading can be determined.

Chapter 5

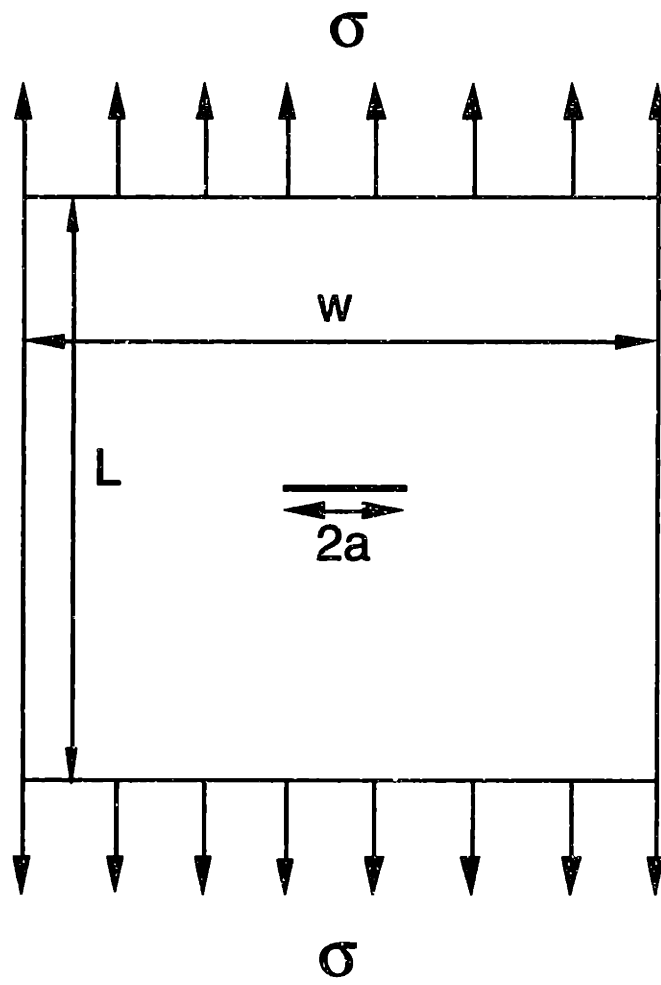
Analytical and Numerical Results

The analytical and numerical results of the present investigation are presented in this chapter. The chapter is divided into four major sections: one, verification of the use of the nodal release technique to compute the membrane stress intensification factors K^m ; two, use of the nondimensional parameters derived in Chapter 4 to characterize different cylinder responses; three, simulation of damage growth in the unstiffened and stiffened cylinders; and four, identification of "regions of interest" for the experimental phase of the work using strain gages.

5.1 Verification of Numerical Solutions

Before the nodal release technique was utilized to compute the stress intensification factors, K^m , in the cylindrical shells considered, the technique was first used to compute the stress intensity factors of two problems that can be solved analytically. These test cases were intended to determine the crack increment, Δa , used in the numerical solutions.

The first problem considered was a large center-cracked panel made of isotropic material loaded perpendicular to the crack plane as shown in Figure 5.1. The Young's modulus of the plate is 100 GPa and its length, width, and thickness are 200 mm, 200 mm, and 1.0 mm, respectively. The plate was loaded by a far-field uniform stress of 100 MPa and had a center crack with a length of 20 mm. The numerical results for the strain energy release rate



$L=200 \text{ mm}, \quad w=200 \text{ mm}$

$2a = 20 \text{ mm}, \quad t = 1.0 \text{ mm}$

$E=100 \text{ GPa}$

Figure 5.1 Geometry of a large center-cracked panel loaded perpendicular to the crack plane.

and stress intensity factors obtained for such panels using the nodal release technique for different values of the crack (slit) increment, Δa , are shown in Table 5.1. For this test case, the exact analytical solutions for the energy release rate, G , and stress intensity factor, K_I , are 3142 J/m^2 and $17.72 \text{ MPa}\sqrt{\text{m}}$, respectively [76]. The error in the computed stress intensity factors is about 0.8% when the crack increment, Δa , is set equal to $0.05a$. Such error is considered acceptable and the Δa value of $0.05a$ was thus chosen.

The second problem considered was that of pressurized cylindrical shells made of metallic (isotropic) material containing a longitudinal, through-thickness crack. This second analysis was considered in order to check the accuracy of the crack increment, Δa , determined previously from the flat plate case and to assess the convergence of the finite element meshes before any nonlinear analyses were started. The linear solutions for the stress intensification factors, K^{ext} , of this problem are available in [18] from the solutions of coupled integral equations. These numerical solutions are available for values of λ less than 8. Twelve cylinders were modelled in this verification process. Each had a radius of 1.52 m, skin thickness of 1.4 mm, and values of λ ranging from 1 to 12, corresponding to crack lengths from 51 mm to 612 mm. The cylinder geometries resemble those of a medium-sized transport airplane. The symmetries in the geometry as well as in the applied loading as depicted in Figure 5.2 allow the modelling of only one-half of each cylinder. The typical finite element mesh of one such cylinder is shown in Figure 5.3. The element used is the four-noded shell element (the so-called 410 element in the STAGS code [68]) and has six degrees of freedom (three translations and three rotations) per node. The mesh gets progressively finer near the slit in order to capture the stress concentration in that region. The nodal release technique with the crack increment Δa equal to $0.05a$ was

Table 5.1 Effects of Different Crack Increments Δa on the Computed Fracture Parameters of a Center-Cracked Plate

$\Delta a/a$	G^a (J/m ²)		K_I^a (MPa \sqrt{m})	
	Computed	% difference from exact	Computed	% difference from exact
0.025	3175	1.0	17.82	0.5
0.050	3195	1.7	17.87	0.8
0.100	3229	2.8	17.97	1.4

^aExact solutions: $G = 3142$ J/m² and $K_I = 17.72$ MPa \sqrt{m}

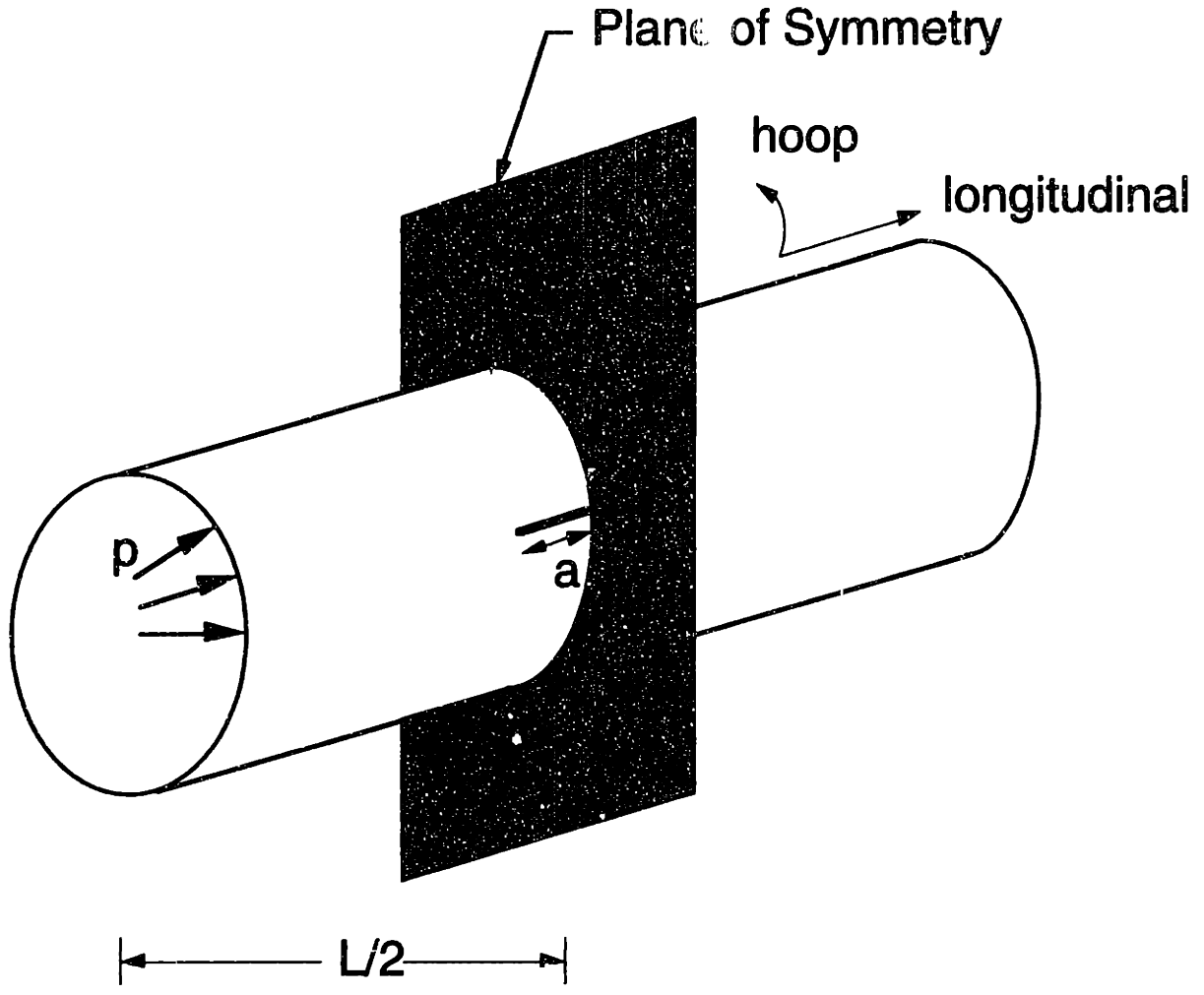


Figure 5.2 Illustration of the symmetry that exists in a cylindrical shell with a longitudinal crack/slit.

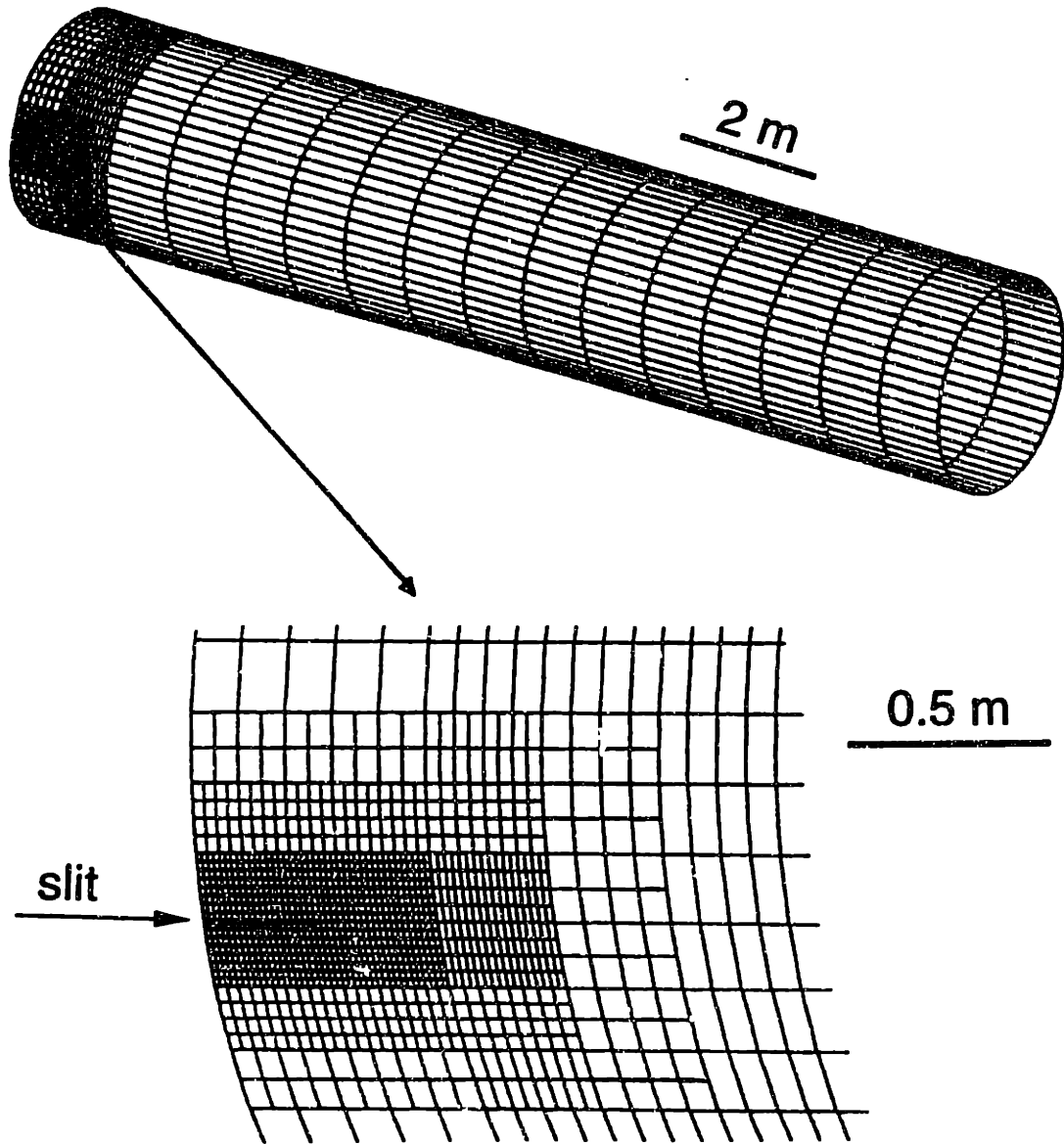


Figure 5.3 Typical finite element mesh for a notched cylinder (the case shown is cylinder with $R=1.52$ m, $h=1.4$ mm, and $2a=0.62$ m): (upper) entire one-half cylinder model, and (lower) blow-up of region near slit tip.

utilized to compute the stress intensification factors. The agreement between the present numerical solution and those in [18] is excellent with differences less than 0.1% as shown in Figure 5.4. Therefore, the crack increment, Δa , used in the technique is justified and the convergence of the finite element mesh is satisfactory. Nonlinear analyses to compute the nonlinear membrane stress intensification factors, K'' , were then started using the same numerical technique and crack (slit) increment Δa .

5.2 Use of Nondimensional Parameters

Different cylindrical configurations with values of λ equal to 3, 6, 9, and 12 were considered in order to evaluate the applicability of the derived nondimensional parameters to characterize the nonlinear response of any cylindrical shell containing a longitudinal crack. Cylinders with the smaller values of λ (3 and 6) correspond to the range of λ investigated experimentally and reported in the literature for isotropic and quasi-isotropic composite cylinders [17, 26, 36], while the larger values of λ (9 and 12) correspond to the "extreme" situation in a narrow-body fuselage structure to model the so-called one-bay crack. This model is sometimes based on an accident scenario of a large turbine blade damaging a fuselage skin while under pressure, as discussed previously. The length of a one-bay crack is typically determined by the spacing between two crack arrest members (approximately 500 mm).

For a specified value of the geometrical parameter λ , different numerical analyses were performed by varying the slit sizes and cylinder thicknesses while keeping the radius constant at either 1.52 or 0.76 m. The smaller cylinder corresponds to the geometry of a smaller, general aviation

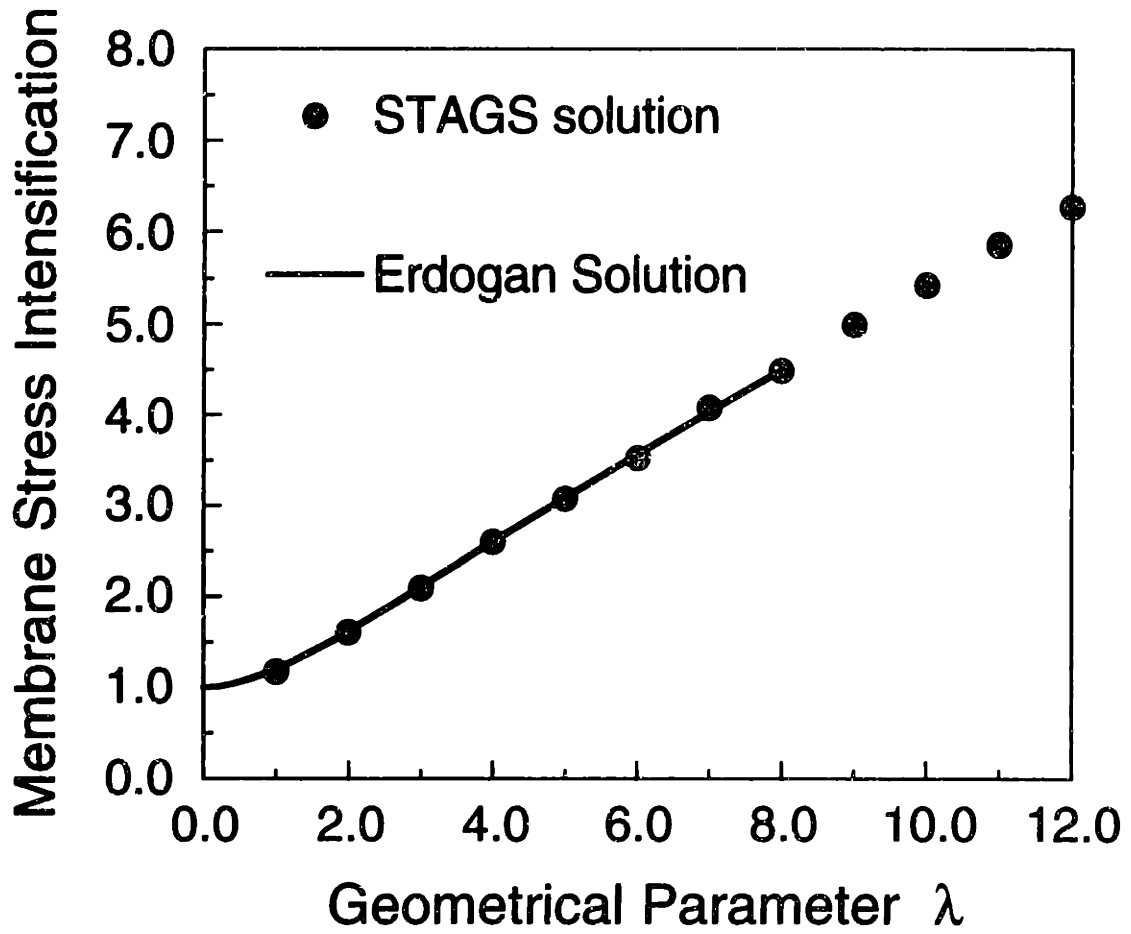


Figure 5.4 Plot of the linear membrane stress intensification versus the geometrical parameter as computed using STAGS code and the Nodal Release Technique and using the Erdogan & Kibler numerical solution.

aircraft, while the larger cylinder corresponds to that of a medium-size transport airplane. The nonlinear membrane stress intensifications of different cylinders for the case of a value of λ of 3 are shown in Figure 5.5. The nonlinear membrane stress intensification factors, K^{ext} , are shown to be strong functions of pressure and specific geometry. The linear K^{ext} , on the other hand, depends solely on λ and is, therefore, independent of the applied pressure. For the cases shown in Figure 5.5, the linear solution for that particular value of λ is equal to 2.098 and corresponds to the nonlinear results when the pressure is equal to zero. An important result is that the magnitude of the nonlinear K^{ext} decreases as the applied pressure increases. Since the response is more nonlinear the greater the deviation of the response from the linear solution, then the nonlinearity increases as the pressure increases. This is because an increase in the driving force (pressure) causes stiffening in the structural response via membrane action contributing to the bending stiffness. This then constrains crack opening and causes a decrease in the energy-release-rate and stress intensity factor. This is consistent with the results from previous numerical work [27-31] where a similar trend was observed for the specific cylinders analyzed.

When the stress intensification factors, K^{ext} , are presented as functions of the loading parameter η , the responses of different cylinders of the same value of λ collapse onto a single curve as illustrated in Figure 5.6. For small values of η (η values less than 0.1 for λ equal to 3), K^{ext} is relatively constant and, therefore, the effects of nonlinearity are not important in that region. As the pressure is increased further (larger values of η), K^{ext} starts to deviate from the linear solution indicating that the nonlinear effects become more important. The same behavior is also observed in cylinders of larger values of λ as illustrated in Figure 5.7. The results can be interpreted

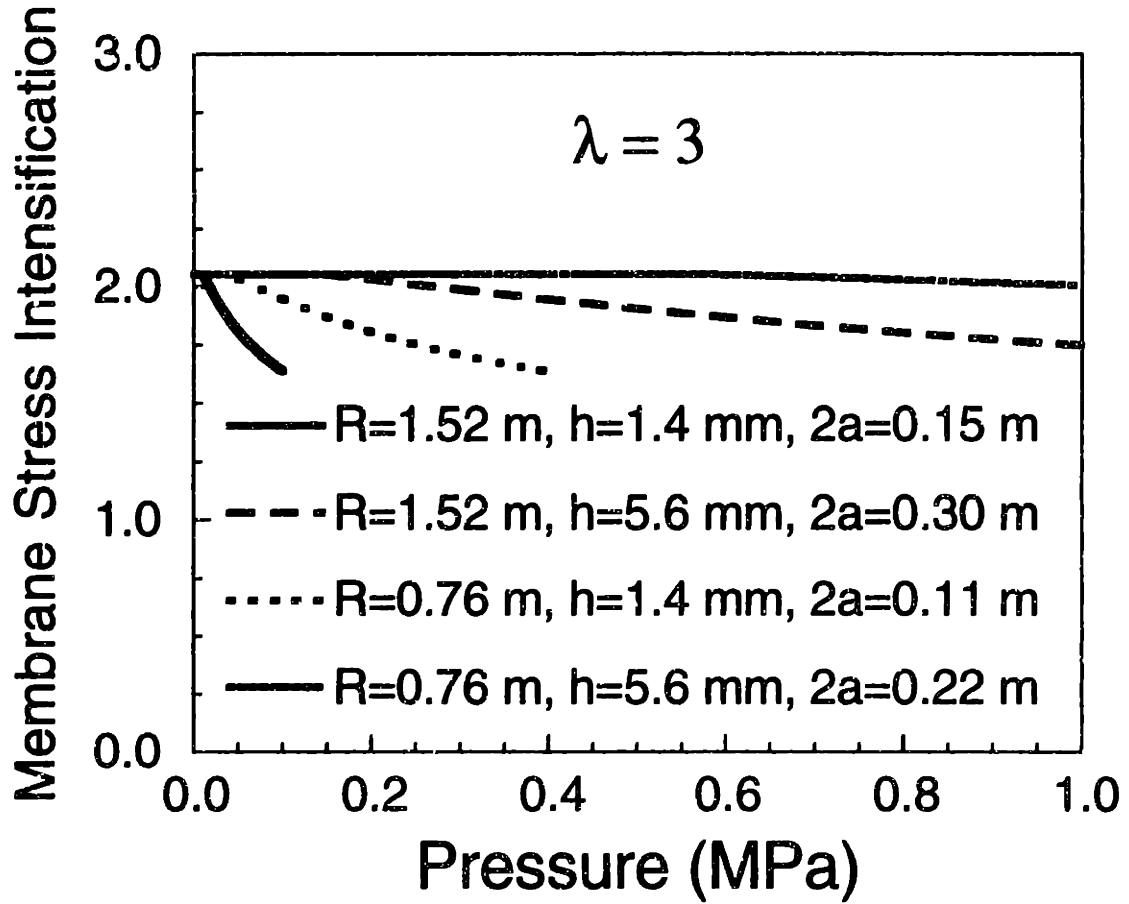


Figure 5.5 Dependence of the membrane stress intensification factor (K^{ex}) on the internal pressure for different cylindrical configurations with the geometrical parameter, λ , equal to 3.

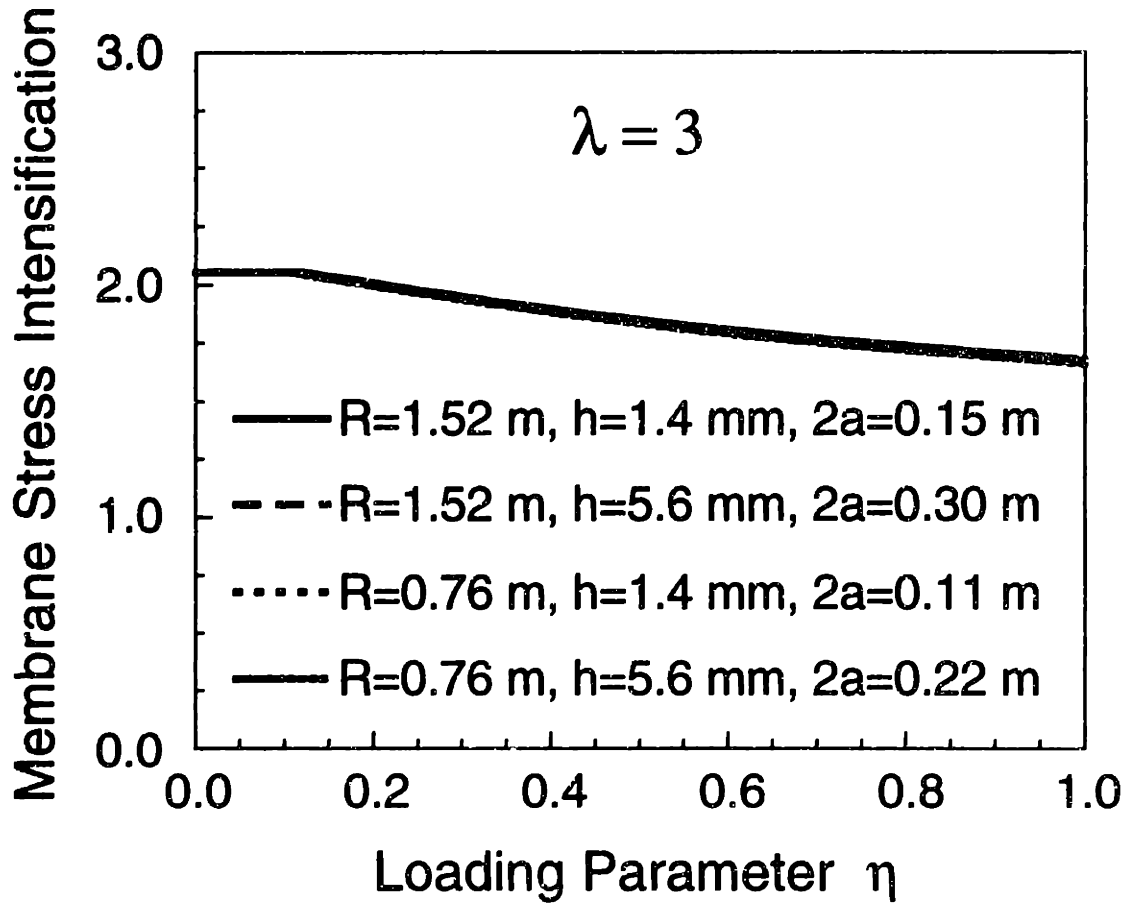


Figure 5.6 Dependence of the membrane stress intensification factor (K^{σ}) on the loading parameter η for different cylindrical configurations with the geometrical parameter, λ , equal to 3.

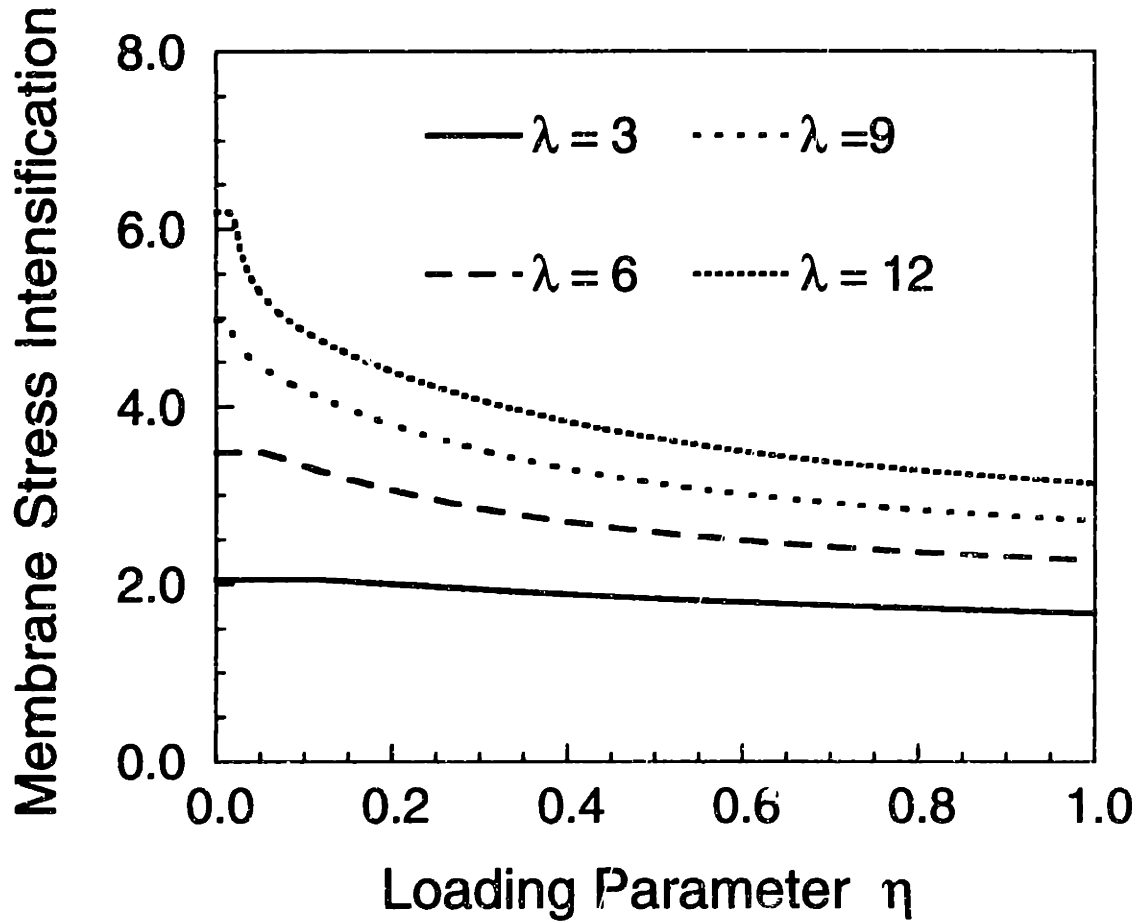


Figure 5.7 Dependence of the membrane stress intensification factor (K'') on the loading parameter η for cylinders with different values of the geometrical parameter λ .

in two ways: one, greater nonlinearity is predicted as damage grows at a constant pressure and, two, greater nonlinearity is also predicted as the loading increases at a constant damage size. Thus, the analyses show the importance of nonlinearity in this type of structure and also confirm the use of the loading parameter, η , to characterize the response of any cylindrical shell with a longitudinal, through-thickness damage.

Based on these numerical results, the nonlinear response of any cylindrical shell with a longitudinal crack has been shown to depend on two nondimensional parameters, λ and η . This is in contrast to the linear case where the solution depends on only the geometrical parameter λ . To be useful in design, these numerical results need to be presented in a ready-to-use format. By using this engineering estimation scheme, the effects of nonlinearity on any cylindrical geometry can be assessed. To accomplish this objective, models of cylinders with different nondimensional crack lengths (λ values ranging from 1 to 12) were analyzed. The cylinder models have the same geometries as those analyzed previously in the verification stage. This estimation scheme is manifested in the form of a "design" chart. Using this chart, the degree of nonlinearity can be estimated once the cylinder geometry, material properties, and crack length are known.

The metric used to characterize the degree of nonlinearity is the percentage error between the linear and nonlinear membrane stress intensification factors K^{ext} . This parameter was chosen because K^{ext} is key in the development of a cylinder failure prediction methodology (see equation (2.9)). The percentage error for each value of λ and η can be computed as

$$Error = \frac{K_{linear}^{ext} - K_{nonlinear}^{ext}}{K_{linear}^{ext}} \times 100. \quad (5.1)$$

These errors were computed for values of λ from 1 to 12. They are depicted in Figure 5.8 where errors ranging from 5 to 40% are shown. Henceforth, Figure 5.8 is called the iso-nonlinear plot. In creating the iso-nonlinear plot, values of λ less than 1 were not considered for the following reason. The magnitude of the linear K^{ext} is relatively small for that particular value of λ (K^{ext} is equal to 1.17 for a value of λ of 1). The magnitude of K^{ext} for an isotropic or orthotropic cylinder cannot be less than 1 since it represents the ratio between the stress intensity of a cracked shell to that of a plate of the same crack geometry. Thus, the maximum percentage error for the case of λ equal to 1 is only around 14%, irrespective of the magnitude of the loading parameter η . The effects of nonlinearity are therefore relatively insignificant for small crack lengths corresponding to values of λ less than 1.

The iso-nonlinear plot can be used as a design chart to assess the degree of nonlinearity in *any* longitudinally-cracked cylinder if all the pertinent parameters (cylinder radius, thickness, crack or slit length, material stiffness, and Poisson's ratio) are known. Knowing those parameters, the geometrical parameter λ can be computed using equation (4.7). The loading parameter η , however, depends on the pressure. If this is the operating pressure, it can be used directly. If this is the failure pressure, it is an unknown that still needs to be determined. Therefore, some kind of fracture/failure criterion or correlation, such as the Mar-Lin composite fracture correlation [49] for quasi-isotropic composite cylinders or Linear Elastic Fracture Mechanics [76] for metallic cylinders, and an iterative solution to be described next are needed.

Since the membrane stress intensification factor, K^{ext} , is a function of pressure, the linear K^{ext} , which is independent of the applied loading, is used along with the particular failure criterion to estimate the failure pressure at

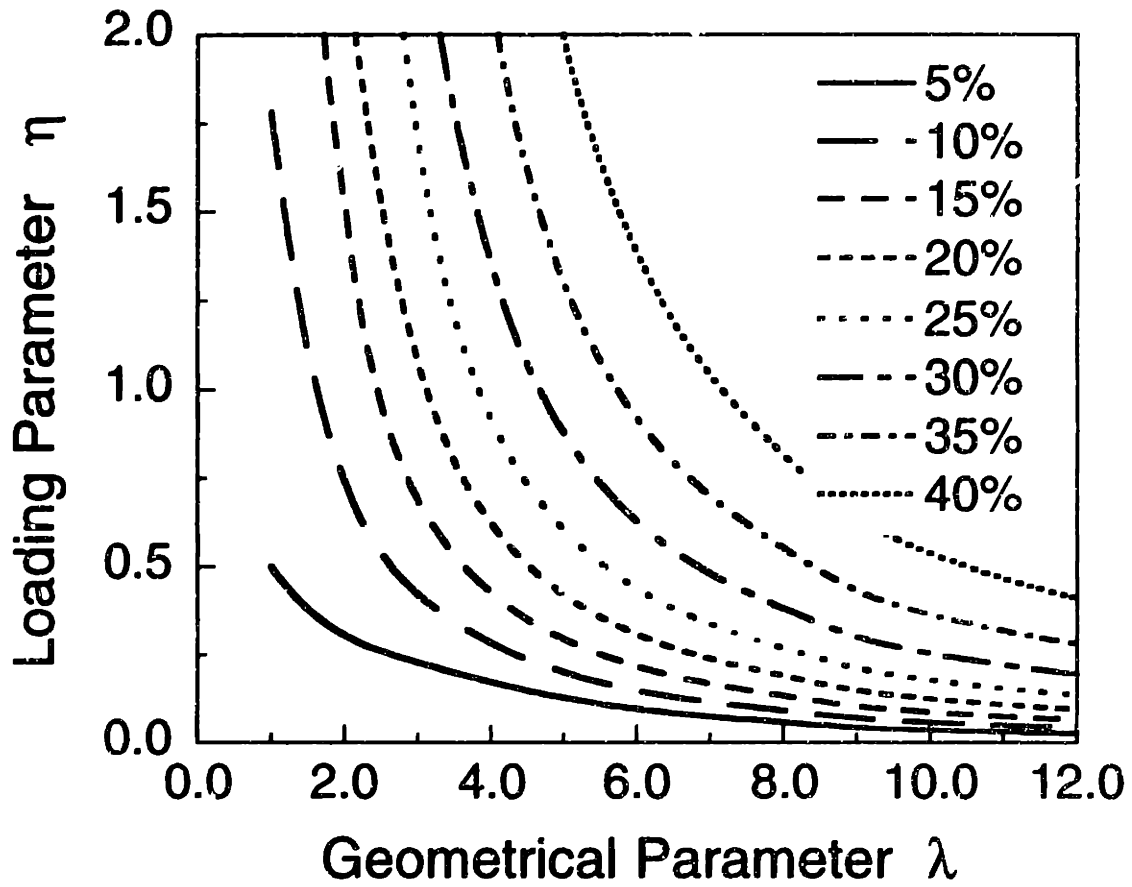


Figure 5.8 Iso-nonlinear plot showing the percentage difference between the linear and nonlinear membrane stress intensification as functions of the two nondimensional parameters.

the first step. Knowing this failure pressure allows the computation of the loading parameter η using equation (4.10). The error between the linear and nonlinear K^{ext} can be estimated from the iso-nonlinear plot (Figure 5.8). Since this error represents the percentage difference between the linear and nonlinear stress intensification solutions, the "updated" (nonlinear) stress intensification factor can be computed using equation (5.1). Using the "updated" stress intensification solution, the "updated" predicted failure pressure can be calculated and the "new" error can be estimated using the iso-nonlinear plot. The whole process is continued until the difference between the "updated" and previous predicted pressure falls within an acceptable tolerance. This can be done for any particular case.

Another way of presenting the analysis results is by plotting the percentage difference between the predicted failure pressures via linear and nonlinear considerations in the so-called *iso-error chart*. The limitation of this presentation is that the chart is *material-* and *laminata-dependent* since it requires the use of a fracture/failure correlation and some material parameter(s). The *iso-error chart* for the AW370-5H/3501-6 cylinder with (0/45)_s stacking sequence is shown in Figure 5.9 where iso-error lines from 10 to 150% are shown. The chart in Figure 5.9 is based on the modified Mar-Lin correlation (equation (2.9)) with the composite fracture parameter, H_c , equal to $698 \text{ MPa mm}^{0.28}$ and the exponent m equal to 0.28 [57]. The steps to create this *iso-error chart* are presented in detail in Appendix B. In the iso-error chart, the percentage differences between the linear and nonlinear failure predictions are plotted as functions of two nondimensional parameters: the geometrical parameter λ and the shell ratio $\frac{R}{h}$. Both parameters are functions of the cylinder geometry only. All possible geometrical configurations for a particular material (given the fracture correlation and

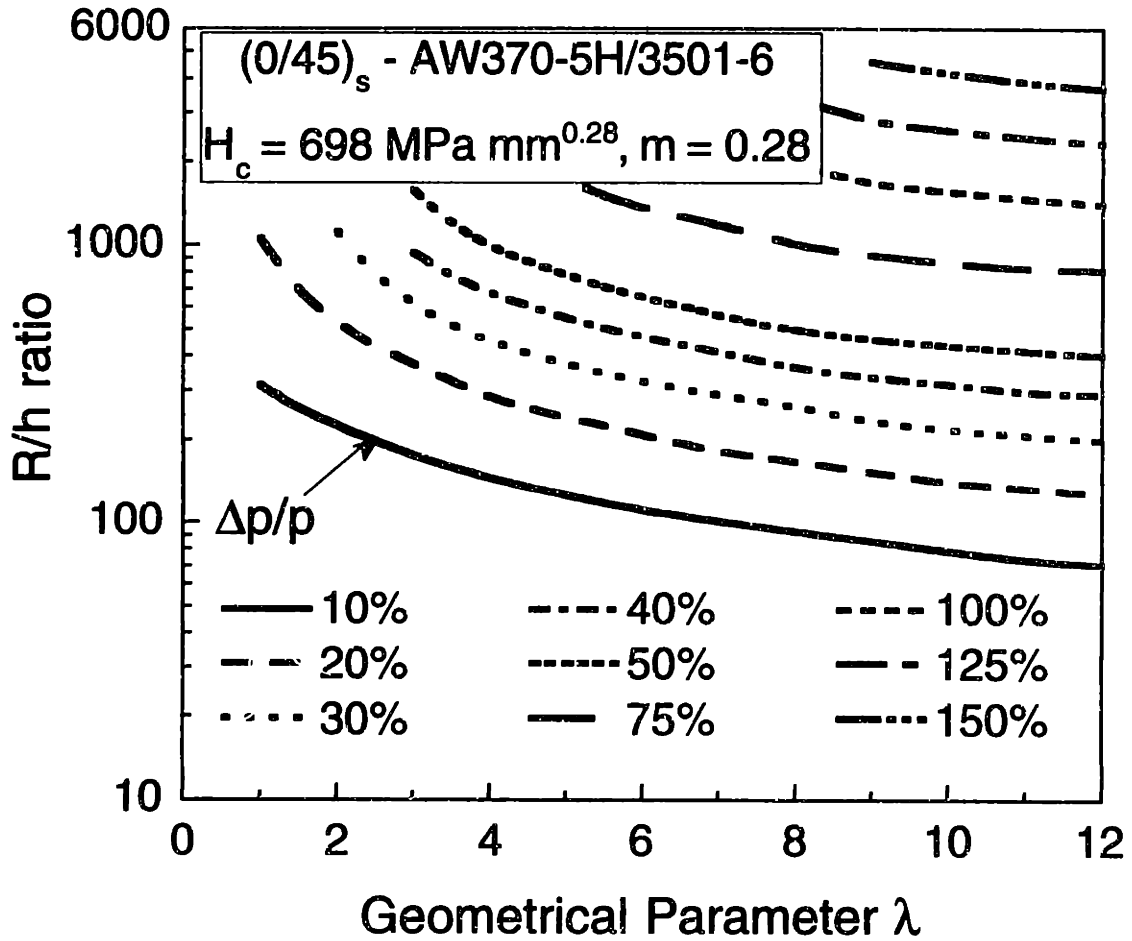


Figure 5.9 Iso-error plot showing the percentage error of the predicted failure pressures using linear and nonlinear methodologies for the (0/45)_s AW370-5H/3501-6 fabric cylinders.

parameters) are captured by these two parameters. Thus, the entire geometric domain is included in this chart for the particular case considered.

The existence of scale effects can be readily seen in the *iso-error chart* shown in Figure 5.9 as the degrees of nonlinearity depend on the shell ratio $\frac{R}{h}$ for cylinders with the same value of λ . Thus, nonlinear effects are directly proportional to the $\frac{R}{h}$ ratio (i.e. the higher this ratio, the larger the nonlinear effects).

5.3 Simulation of Damage Growth

Based on previous experimental observations, damage growth in cylinders manufactured from this fabric material system is relatively self-similar [25, 55] with the initial propagation from longitudinal slits in the longitudinal direction. This initial propagation of damage was numerically simulated in the present work in a quasi-static fashion by changing the slit sizes in sequential models. The results of the analyses are the nonlinear stress intensification factors, K^{exl} , and the strain distributions in both the longitudinal and hoop directions. The strain distributions were used to identify the "regions of interest" where significant differences between the linear and nonlinear solutions are predicted. The strain responses from analyses were later compared with the experimental results obtained using strain gages. Simulations were performed on the unstiffened (*type-1*) and the stiffened (*type-2* and *type-3*) cylinders. In the simulation of damage growth in the *type-3* cylinders, which were stiffened in both the longitudinal and hoop directions, the presence of the longitudinal stiffeners was ignored for two reasons: one, these stiffeners were located far from the slit (approximately

100 mm from the slit axis) and, two, this distance did not change during the initial stage of damage propagation.

5.3.1 Simulation of Damage Growth in the Unstiffened Cylinders

The geometry of the (*type-1*) cylinder is shown in Figure 3.2. The finite element mesh of one such cylinder with a longitudinal slit of 104 mm is shown in Figure 5.10. In order to identify the "regions of interest" on the cylinder surface to guide the experimental phase of the work using strain gages, accurate strain distributions were important. Since the strain gage reading represents an "average" over an actual gage size, the finite element mesh gets progressively finer in the slit region with the size of the smallest element in each model chosen to be smaller than, but on the same order of magnitude as, the gage size of approximately 3 mm. The exact element dimensions are 1.28 mm, 0.98 mm, and 1.30 mm for slit sizes of 51 mm, 78 mm, and 104 mm, corresponding to $1/20$, $1/40$, and $1/40$ of the half-crack length a . To assess the effects of different bending stiffnesses on the nonlinear strain distributions and stress intensification factor K^{ext} , three different cylinder skins were considered: $(0/45)_s$, $(45/0)_s$, and homogeneous isotropic.

The effects of different bending properties on the linear stress intensification factors, K^{ext} , are shown in Table 5.2 by considering similar skin configurations with the same in-plane properties. In all cases, the stress intensification factors increase with slit size (and thus λ). The effects of different bending properties are not significant as the differences among the solutions are typically less than 3%. This suggests that the use of the stress intensification solution based on the isotropic assumption in the previously

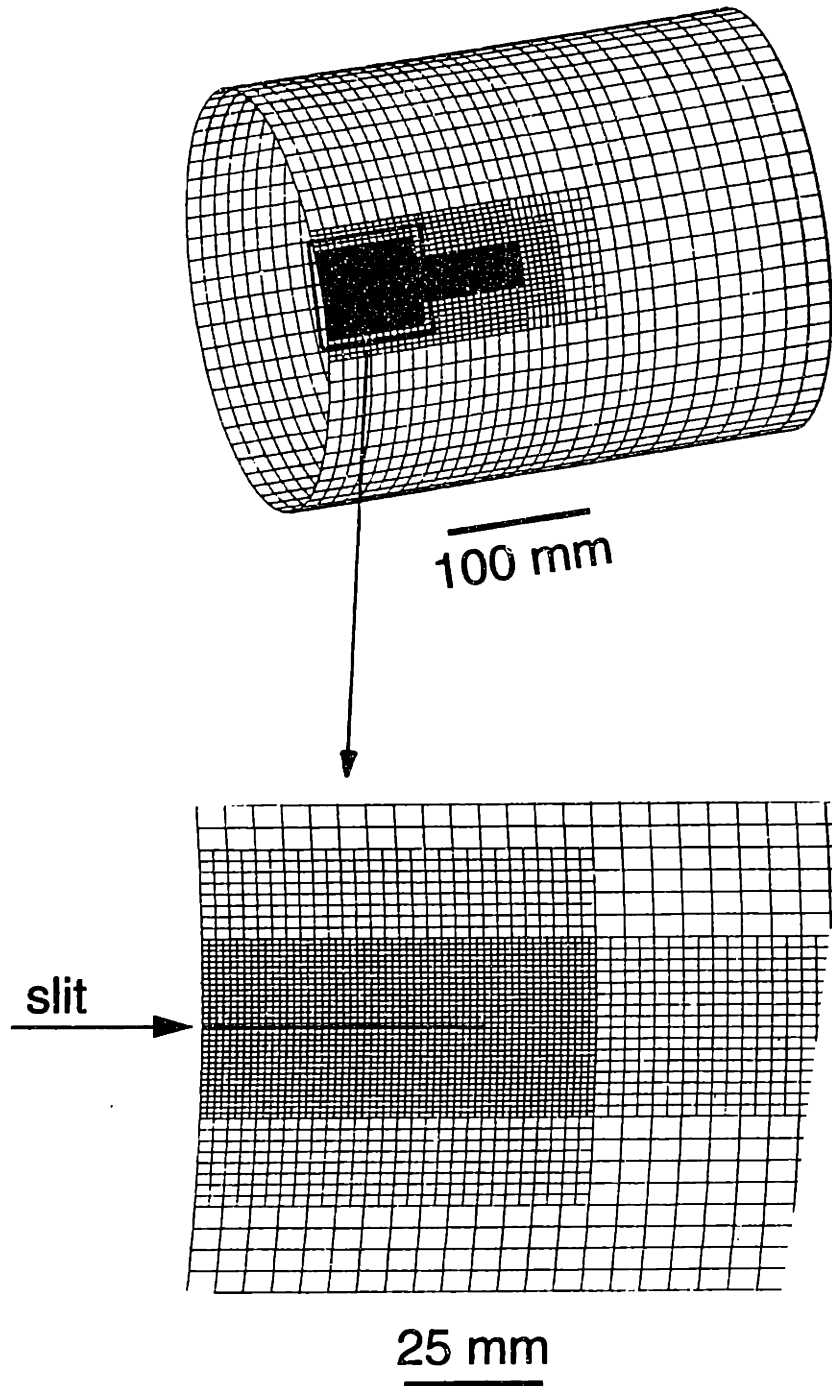


Figure 5.10 Typical finite element mesh for a laboratory-scaled, unstiffened specimen (the case shown is cylinder with $R=152$ mm, $h=1.4$ mm, and $2a=104$ mm): (*upper*) entire one-half cylinder model, and (*lower*) blow-up of region near slit tip.

Table 5.2 Linear Membrane Stress Intensification Factors for the Three Cylinder Skins Computed Using the Nodal Release Technique

Slit Size [mm]	λ	$(0/45)_S$	$(45/0)_S$	Isotropic	Erdogan & Kibler ^a
51	3.16	2.223	2.192	2.201	2.181
78	4.83	3.087	2.967	3.016	3.005
104	6.44	3.895	3.699	3.782	3.773

^aFor the isotropic case from solutions of coupled integral equations.

developed failure prediction methodology [25, 26] for quasi-isotropic composite cylinders, which can have different bending properties, is justified. It is also worth noting that the excellent agreement between the present numerical results for the homogeneous isotropic case with the Erdogan & Kibler numerical solution (less than 0.25% difference) serves as a verification of the numerical accuracy of the nodal release technique utilized.

The effects of bending stiffness, via the same manner, on the nonlinear stress intensification factors, K^{ext} , are shown in Figure 5.11 for cylinders with a longitudinal slit of 104 mm. As noted before, the magnitude of the stress intensification factors for this particular slit size decreases as pressure increases. It is important to note that unlike the linear solutions, which differ slightly depending on the specific wall construction (i.e. bending stiffnesses), the nonlinear solutions for the membrane stress intensification factors, K^{ext} , at higher pressure (greater than 0.3 MPa for this particular slit size) seem unaffected by differences in bending properties. One particular reason is that nonlinearity is induced by the "stiffening" due to the membrane action. The importance of the differences in bending stiffness between these cases thus diminishes, and the membrane contribution, which is the same for the three cases, overcomes these differences as the effects of nonlinearity become more important at higher pressures.

The effects of nonlinearity on the strain distributions in the longitudinal and hoop directions were also investigated. The strains were computed at the centroid of each element on the top surface of the cylinder. Since the hoop strain in a cylindrical shell is related to the out-of-plane displacement as shown in Appendix A, the same nonlinear effects are expected in the out-of-plane deformation of the cylinder in the regions near the slit.

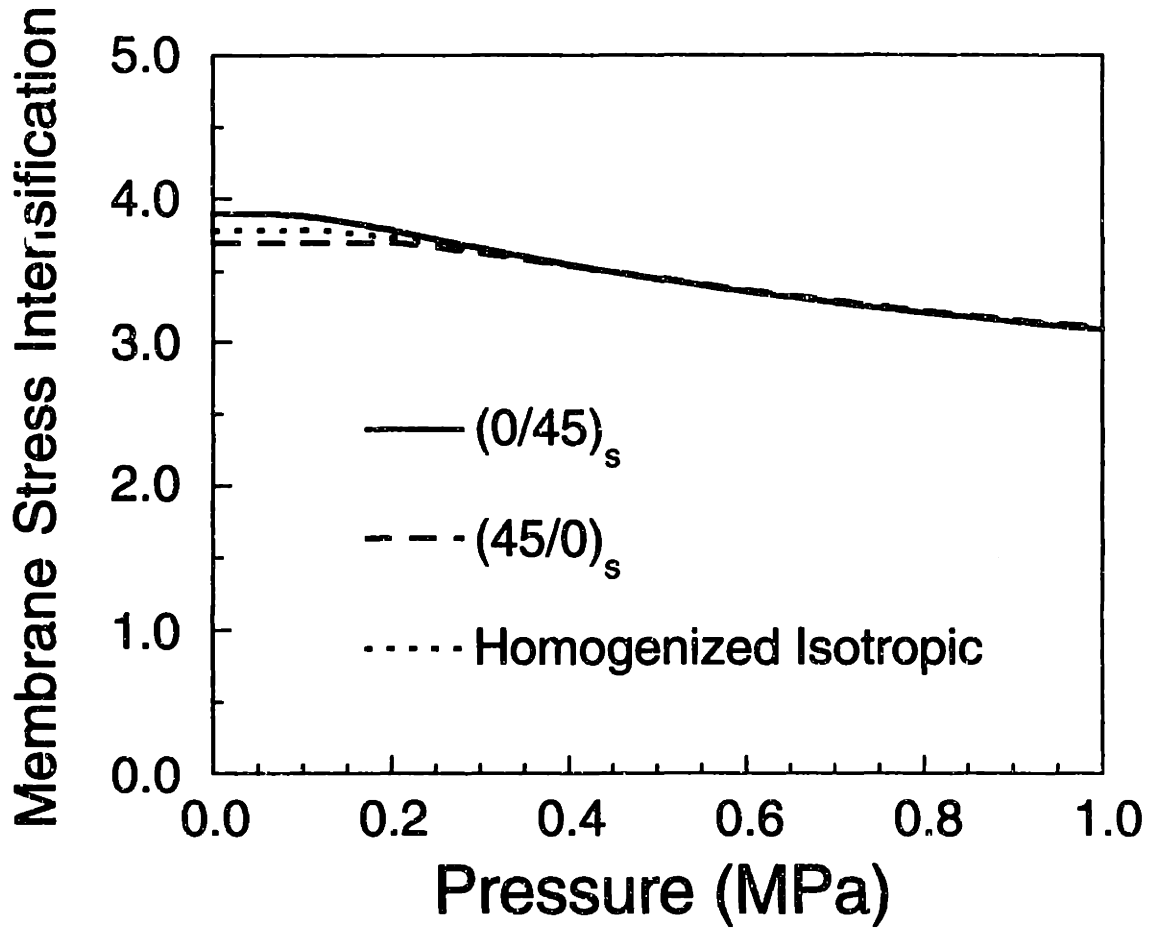


Figure 5.11 Effects of different skin configurations and thus bending properties on the nonlinear membrane stress intensification factors for cylinders with a longitudinal slit length of 104 mm.

The magnitude and shape of the nonlinear strain distributions depend on the applied pressure which needs to be determined *a priori*. In this laboratory-scaled cylinder (radius of 152 mm and thickness of 1.4 mm), the hoop stress at an applied pressure of 1 MPa is approximately 109 MPa. This hoop stress value is typical of that in an actual fuselage (pressure level of 55 kPa at cruise and radius-to-thickness ratio ranging from 1000 to 2000). Thus, a pressure level of 1 MPa was chosen to present the numerical results of nonlinear strain distributions. The strain distributions at the top surface of the (0/45)_s cylinder with a longitudinal slit of 104 mm are shown in Figures 5.12 and 5.13. The strain distributions for the (45/0)_s cylinders are shown in Figures 5.14 and 5.15.

The effects of nonlinearity can be seen clearly in the longitudinal strain distributions shown in Figures 5.12 and 5.14. The longitudinal strains for both stacking sequences are similar. Behind the slit tip (i.e. regions from the center of the slit up to approximately the slit tip), these strains are tensile in the nonlinear case but compressive in the linear case. Furthermore, although both analyses predict that the longitudinal strains are tensile ahead of the slit tip (i.e. $x/a \geq 1$), the shapes of the linear and nonlinear distributions differ significantly there. A large tensile strain occurs in that region due to nonlinear effects. A strain level greater than 7500 microstrain, which decreases gradually as x/a increases, is predicted in the nonlinear case very close to the slit tip. Although the strain level is slightly smaller in the linear case (~ 5000 microstrain), the value decreases abruptly before the value increases again and reaches a maximum at a distance of $1.5 a$ from the center of the slit.

The predicted linear and nonlinear hoop strain distribution are shown in Figures 5.13 and 5.15. Unlike the longitudinal strain distributions, the

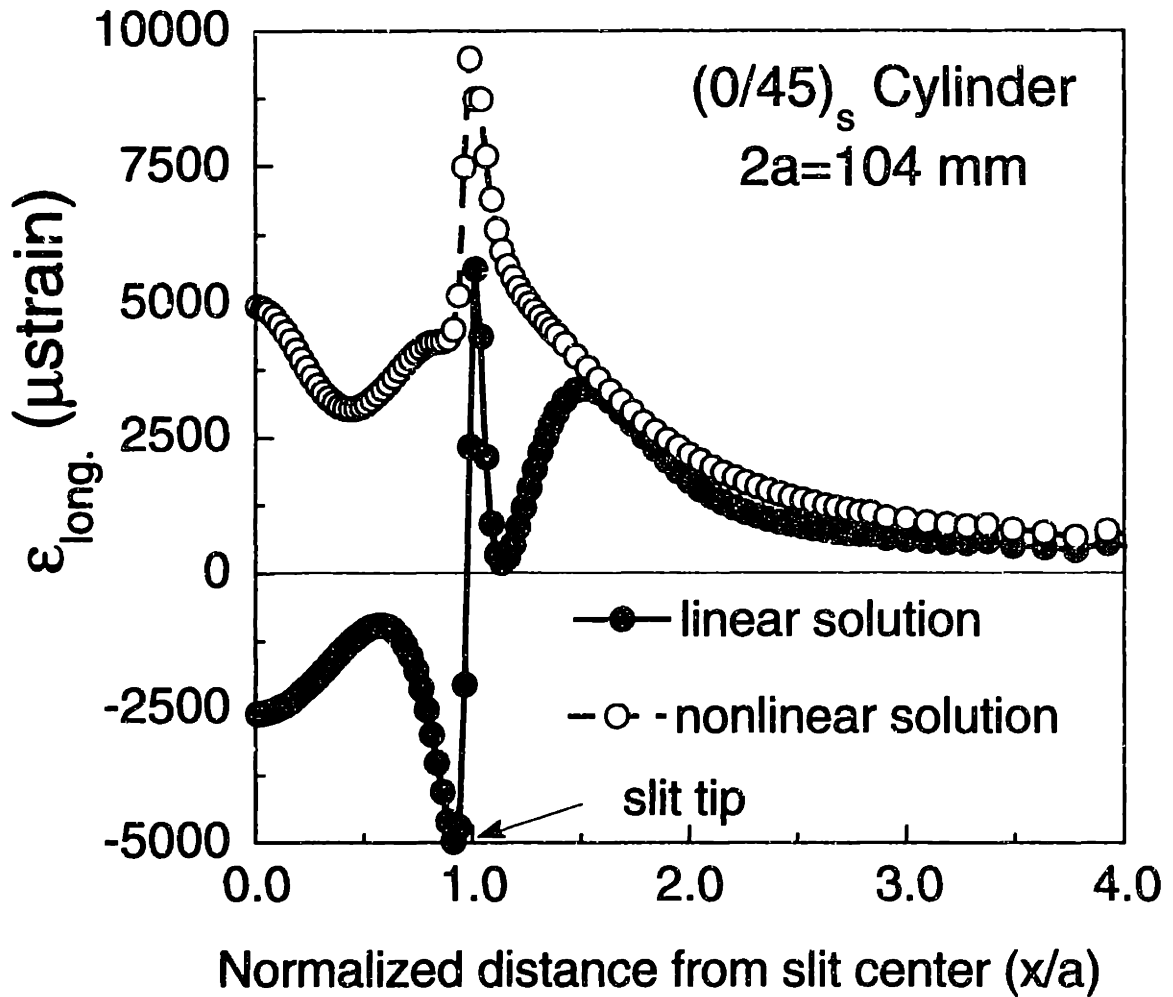


Figure 5.12 Total longitudinal strains on the top surface of the (0/45)_s cylinder with a longitudinal slit length of 104 mm at 1 MPa internal pressure.

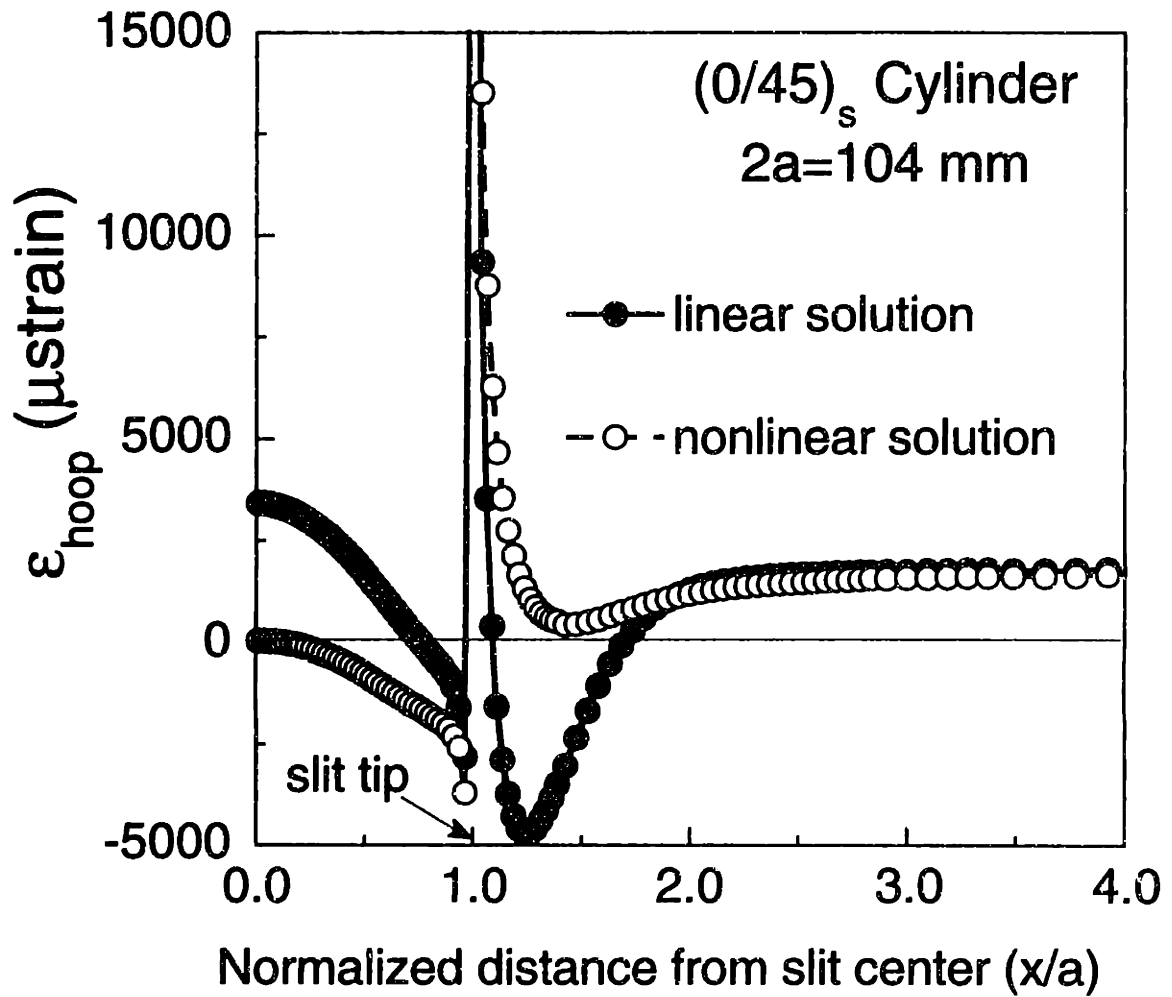


Figure 5.13 Total hoop strains on the top surface of the $(0/45)_s$ cylinder with a longitudinal slit length of 104 mm at 1 MPa internal pressure.

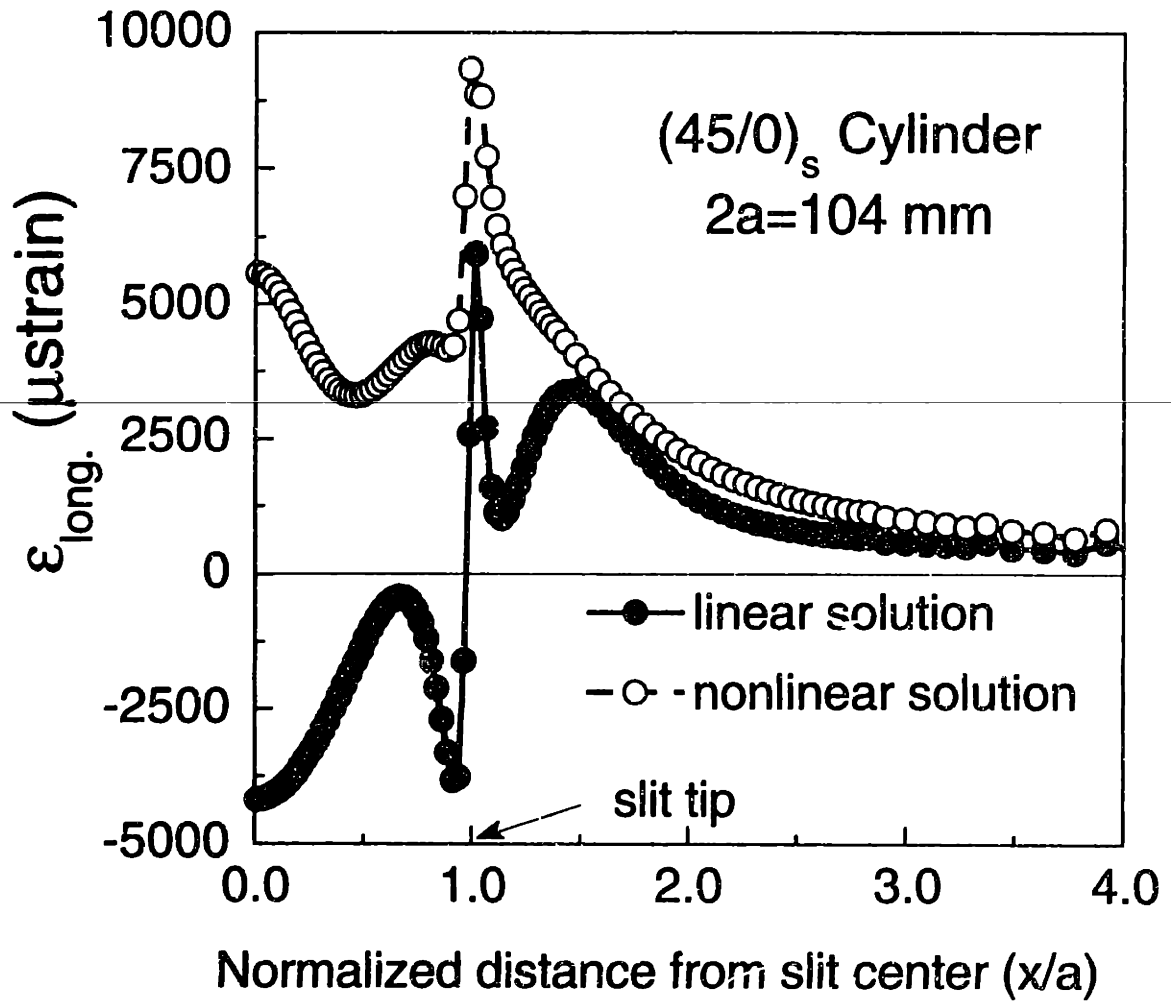


Figure 5.14 Total longitudinal strains on the top surface of the (45/0)_s cylinder with a longitudinal slit length of 104 mm at 1 MPa internal pressure.

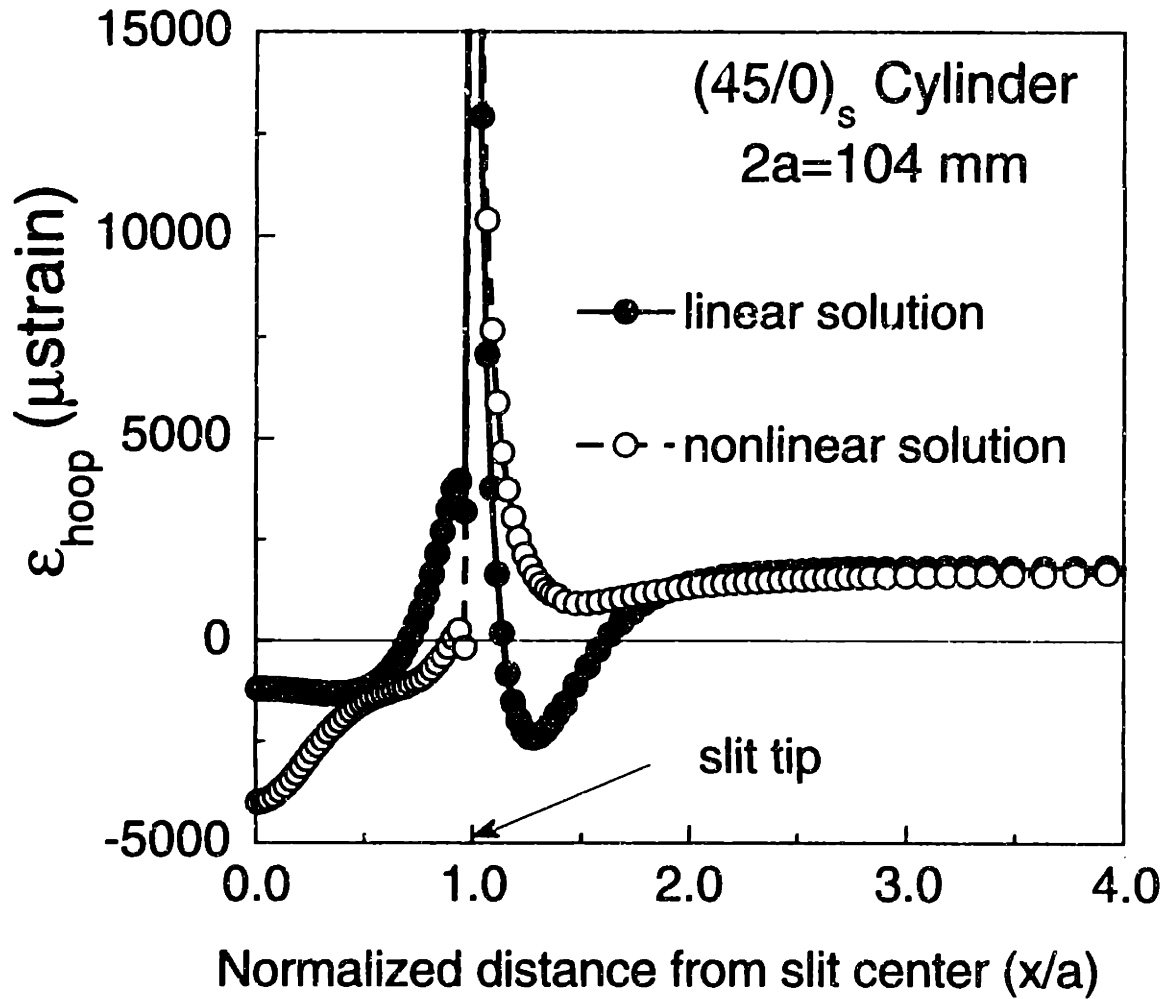


Figure 5.15 Total hoop strains on the top surface of the (45/0)_s cylinder with a longitudinal slit length of 104 mm at 1 MPa internal pressure.

strain distributions in the hoop direction differ for the two stacking sequences in both the linear and nonlinear cases. For example, the strain near the center of the slit is tensile in the $(0/45)_s$ case but compressive in the $(45/0)_s$ case. Ahead of the slit tip, the hoop strain decreases very fast and starts to become compressive at a distance of approximately $0.13 a$ from the slit tip. This is in contrast to what is predicted by the nonlinear solution where the strain remains tensile and the shape of the hoop strain distribution ahead of the slit tip is more shallow than that predicted by the linear solution.

To get a better understanding of the underlying mechanisms behind these predicted strain distributions, the total strains in the $(0/45)_s$ cylinders with a longitudinal slit of 104 mm are decomposed into the membrane (uniform through-the-thickness) and bending (linearly-varying through-the-thickness) parts and are depicted in Figures 5.16 through 5.19. The bending strain on the outer surface of the cylinder is shown. Similar membrane and bending distributions are predicted for the $(45/0)_s$ cylinders. Thus those distributions are not shown here to avoid repetition.

Effects of nonlinearity can be seen in the distribution of the membrane component of the longitudinal strain distribution behind the slit tip ($x/a \leq 1$) where the shape and the magnitude of the two distributions differ significantly. The two solutions become closer as the x/a ratio approaches 1 (i.e. in the region very close to the slit tip). Ahead of the slit tip, the membrane longitudinal strain predicted from the linear solution is initially slightly larger (e.g. on the order of 10%) up to approximately one-quarter slit length from the slit tip where the two solutions cross. Beyond that point, the linear solution is lower than the nonlinear solution (i.e. on the order of 30 - 40%) up to approximately three slit lengths from the slit tip. The effects of nonlinearity diminish at approximately three slit lengths from the slit tip as

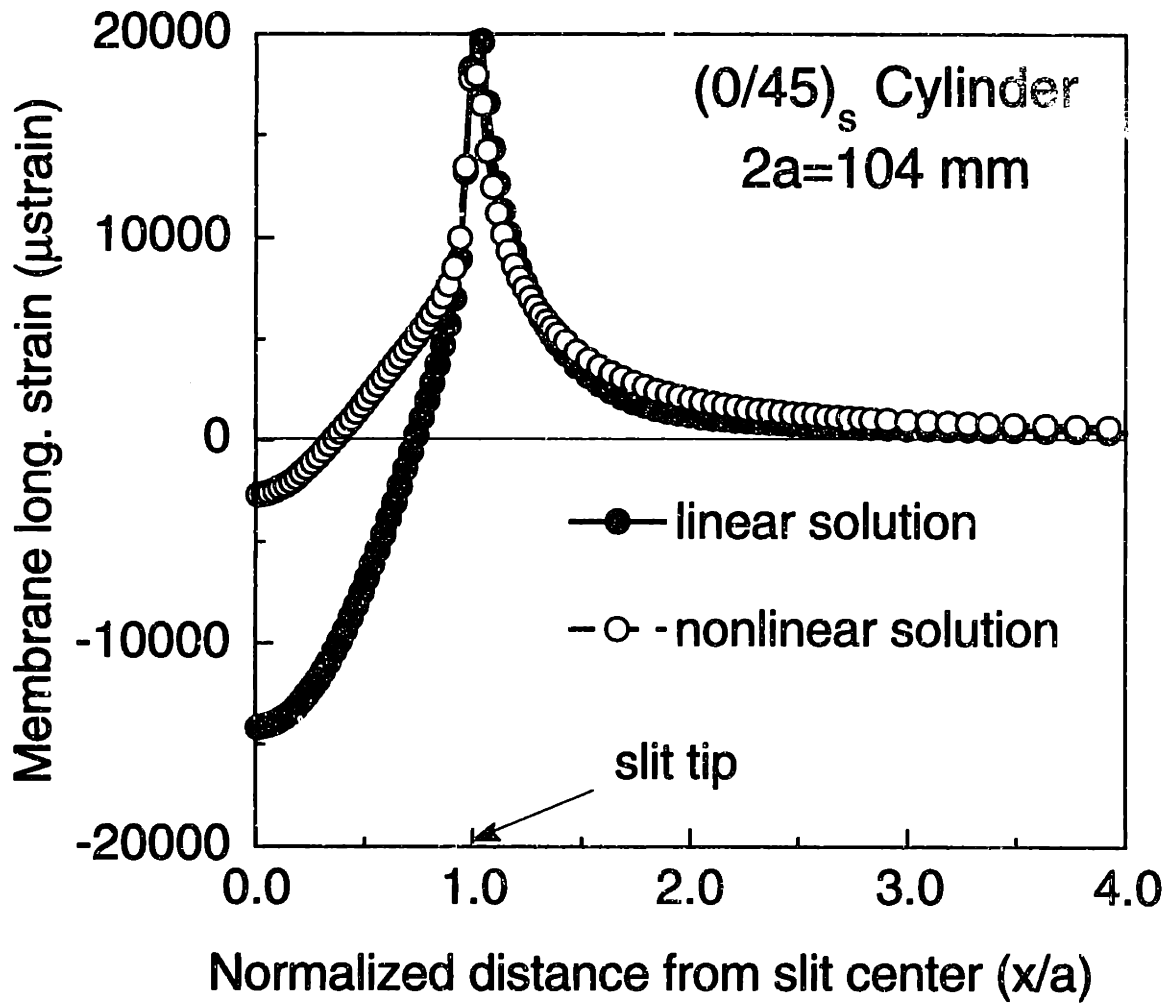


Figure 5.16 Membrane longitudinal strain distributions of a (0/45)_s cylinder with a longitudinal slit length of 104 mm at 1 MPa internal pressure predicted from linear and nonlinear analyses.

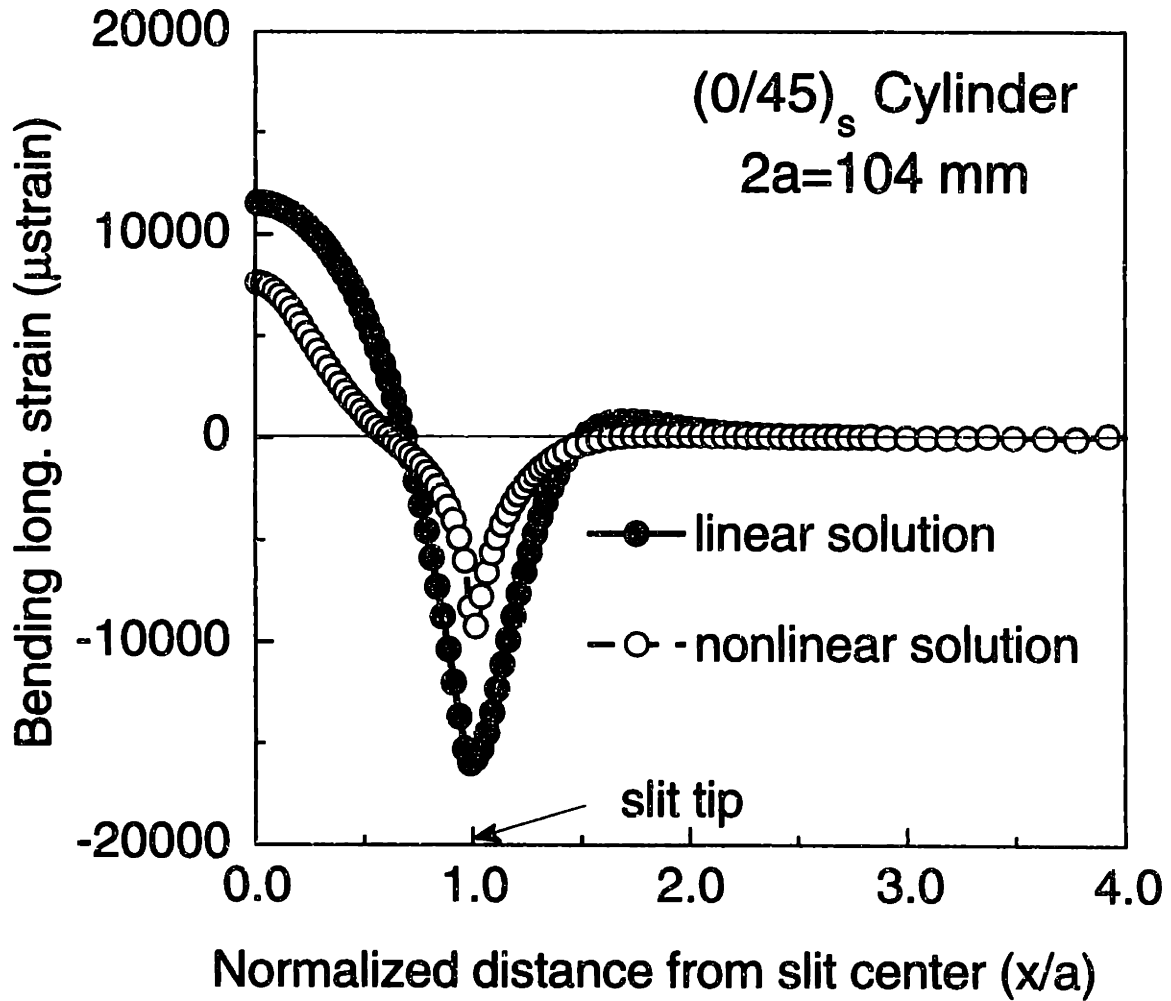


Figure 5.17 Bending longitudinal strain distributions on the top surface of a (0/45)_s cylinder with a longitudinal slit length of 104 mm at 1 MPa internal pressure predicted from linear and nonlinear analyses.

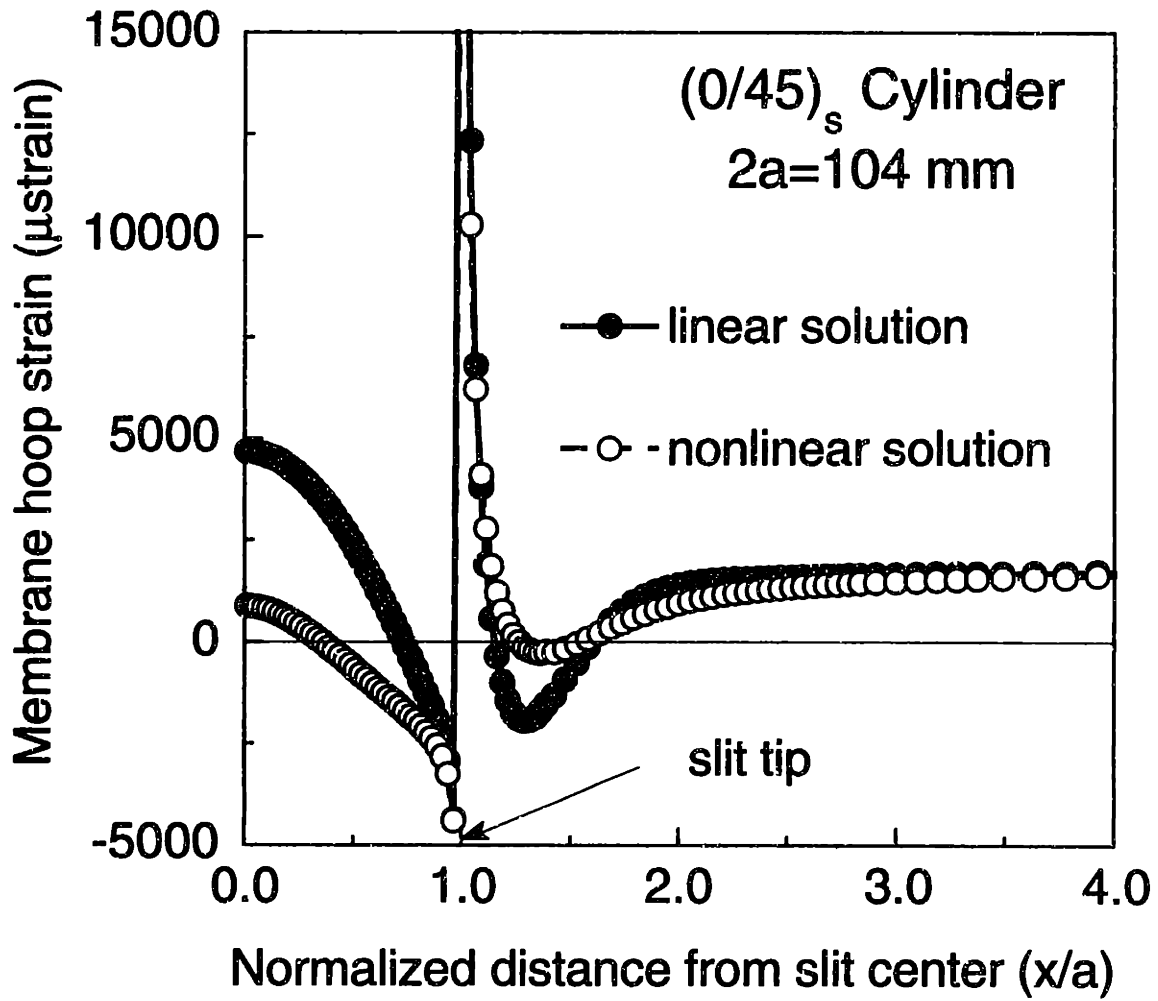


Figure 5.18 Membrane hoop strain distributions of a $(0/45)_s$ cylinder with a longitudinal slit length of 104 mm at 1 MPa internal pressure predicted from linear and nonlinear analyses.

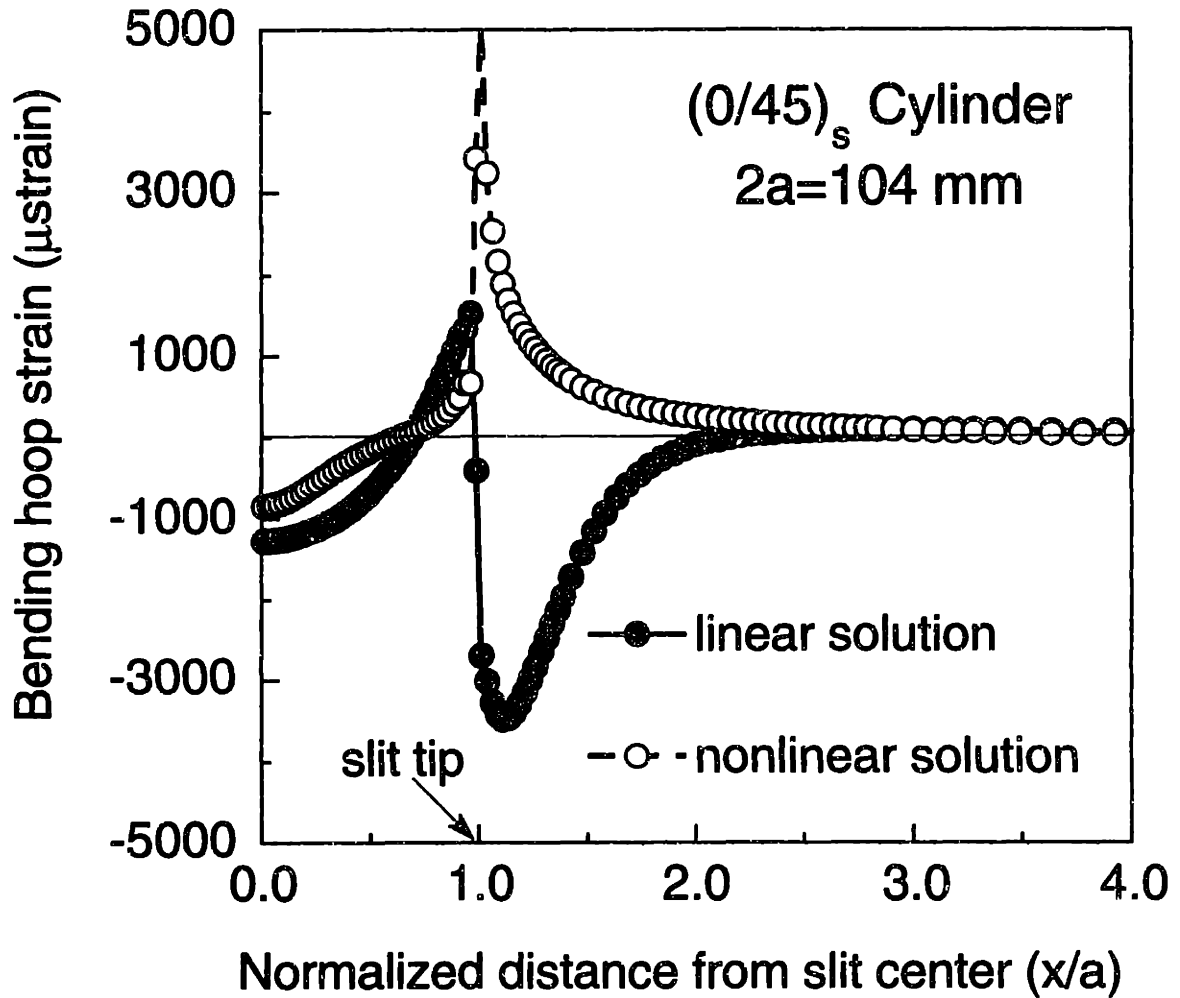


Figure 5.19 Bending hoop strain distributions on the top surface of a (0/45)_s cylinder with a longitudinal slit length of 104 mm at 1 MPa internal pressure predicted from linear and nonlinear analyses.

the two solutions become indistinguishable. Nonlinear effects can also be seen in the bending component of the longitudinal strain distribution. The linear and nonlinear distributions differ in magnitude and, particularly, in shape behind the slit tip ($x/a \leq 1$). Two inflection points, which show transitions from "concave-down" to "concave-up" at an approximate distance of $0.4 a$ from the middle of the slit, and from "concave-down" to "concave-up" at a distance of roughly $0.85 a$ from the middle of the slit, are present only in the nonlinear distribution. The magnitude of the nonlinear bending strain is also consistently lower than that obtained from the linear solution. Furthermore, ahead of the slit tip, the nonlinear solution does not show the presence of an "overshoot", in which the strain value increases to a maximum tensile value before it finally decreases, as exhibited by the linear solution. Both the linear and nonlinear solutions show that the bending contribution is localized and decays within a half-slit distance from the slit tip.

Effects of nonlinearity can also be seen in the membrane and bending strain distributions in the hoop direction. In the membrane distribution, the nonlinear effects can be seen in two regions: one, in the vicinity of the midslit region and, two, ahead of the slit tip. The membrane distribution is actually similar in shape to that of the total distribution. The magnitude, however, differs from the linear solution. In the vicinity of the midslit region, the linear solution is higher than the nonlinear solution. The membrane strains obtained from both solutions decrease monotonically up to a point very close to the slit tip. The states of strain then change from compressive behind the slit tip to tensile ahead of the slit tip. In the regions ahead of the slit tip, the magnitudes of the two solutions decrease monotonically and become compressive. However, the linear solution reaches a lower minimum than the nonlinear solution. These nonlinear effects are even more obvious in the

distribution of the bending strain as depicted in Figure 5.19. Behind the slit tip, there exist two inflection points indicating changes in curvatures from "concave-up" to "concave-down" and vice-versa in the nonlinear bending strain distribution. Note that the shape of the bending distribution from the linear solution remains "concave-up" behind the slit tip. Totally different states of strain (i.e. tensile in the nonlinear solution versus compressive in the linear solution) are predicted ahead of the slit tip. In the linear solution, the bending strain, which is positive (tensile) behind, but very close to, the slit tip, changes and becomes negative (compressive) ahead of the slit tip. One inflection point exists indicating changes in curvatures from "concave-up" to "concave-down" in the bending strain distribution obtained from the linear solution. The nonlinear solution, however, does not predict the existence of "sign-reversal" (i.e. from tensile to compressive) from the region immediately behind to immediately ahead of the slit tip as is predicted by the linear solution. Thus, the two bending strain distributions differ greatly in shape ahead of the slit tip. The linear solution approaches zero from the negative side, while the nonlinear solution does that from the positive side. As previously noted, this indicates significant differences in curvature and thus overall skin deflection in the vicinity of the slit tip.

Based on these strain distributions, two regions on the cylinder surface where nonlinear effects are significant were identified: one, regions near the center of the slit and, two, regions near the slit tip. In these two regions, strain gages were bonded in the experimental phase of the work in order to compare the numerical and experimental results. This is further described in Chapter 6.

5.3.2 Simulation of Damage Growth in Stiffened Construction

It has been experimentally documented that longitudinal damage initially grows in a rather self-similar way in a fabric composite cylinder with a longitudinal slit until damage reaches the edge of the hoop stiffening bands [34, 36, 55]. At that stage, damage bifurcation can take place depending on the specific stiffener configuration. In the present numerical work, the growth of longitudinal damage approaching the stiffening band is simulated using the finite element method. Depending on the specifics of the stiffener geometry, described later, a stiffener attached to a shell structure can be modelled using: one, a beam element (one-dimensional); two, a shell element (two-dimensional); and three, a brick element (three-dimensional).

Stiffener modelling using the beam element assumes that the section properties of the stiffener can be lumped along its centerline, and ignores the width of the stiffener. Thus, this one-dimensional modelling cannot provide detailed descriptions of the stress and strain fields in the vicinity of the stiffener. This kind of stiffener modelling is typically used in the study of buckling and postbuckling of shell structures where only the far-field effects of "stiffening" are of importance. Shell elements are typically used when the stiffening element is "thin" (i.e. roughly the same thickness as the unstiffened part) and is therefore "relatively accurate" in the two-dimensional stress calculations except near or at the junction between the stiffener and the base skin. At that location, the state of stress is more complex and three-dimensional in nature. In order to apply some kind of point-stress or average-stress failure criterion to predict failure in that region, a more accurate (i.e. three-dimensional) stress state is sometimes needed. For this case, three-dimensional (brick) elements are usually used to model the

stiffener. It is important to note that the use of such an element-type can be computationally intensive.

Since the stiffening band used in the present work (four 0-degree fabric layers) has roughly the same thickness as the base cylinder, the stiffener was modelled by using the second option (shell element). This was done inside the STAGS code [68] by changing the wall construction of the stiffened part as depicted in Figure 5.20 just as it is layed up. The bending stiffnesses of the stiffened region were computed with respect to the midplane of the unstiffened cylinder. Both the stress intensification factors and the strain distributions were obtained from the analyses. As in the unstiffened case, the nodal release technique was utilized to compute the stress intensification factors. The finite element mesh of one such cylinder, which is stiffened in the hoop direction, is shown in Figure 5.21.

The linear K^{ext} for the unstiffened and stiffened cases are tabulated in Table 5.3 and 5.4 for the $(0/45)_s$ and $(45/0)_s$ cases, respectively. The ratio between the ligament width and the half-slit length (ψ/a) investigated range from 0.13 to 0.78. The smallest ψ/a ratio corresponds to the situation where the slit tip is close to the edge of the stiffening band. This is to model the situation before the onset of bifurcation [36] (i.e. the so-called "interacting" case). The largest value of the ψ/a ratio corresponds to the case where the slit tip is still far from the stiffeners (i.e. the so-called "non-interacting case"). The deviations of the linear stress intensification factors, K^{ext} , from the unstiffened values are relatively insignificant except for cylinders with the smaller values of ψ/a . For such cylinders, the unstiffened and stiffened linear K^{ext} for the $(0/45)_s$ and $(45/0)_s$ cases differ by 15.1% and 11.6%, respectively. The evolution of the nonlinear stress intensification factor K^{ext} for the $(0/45)_s$ and $(45/0)_s$ cases with the smallest ψ/a ratio are shown in

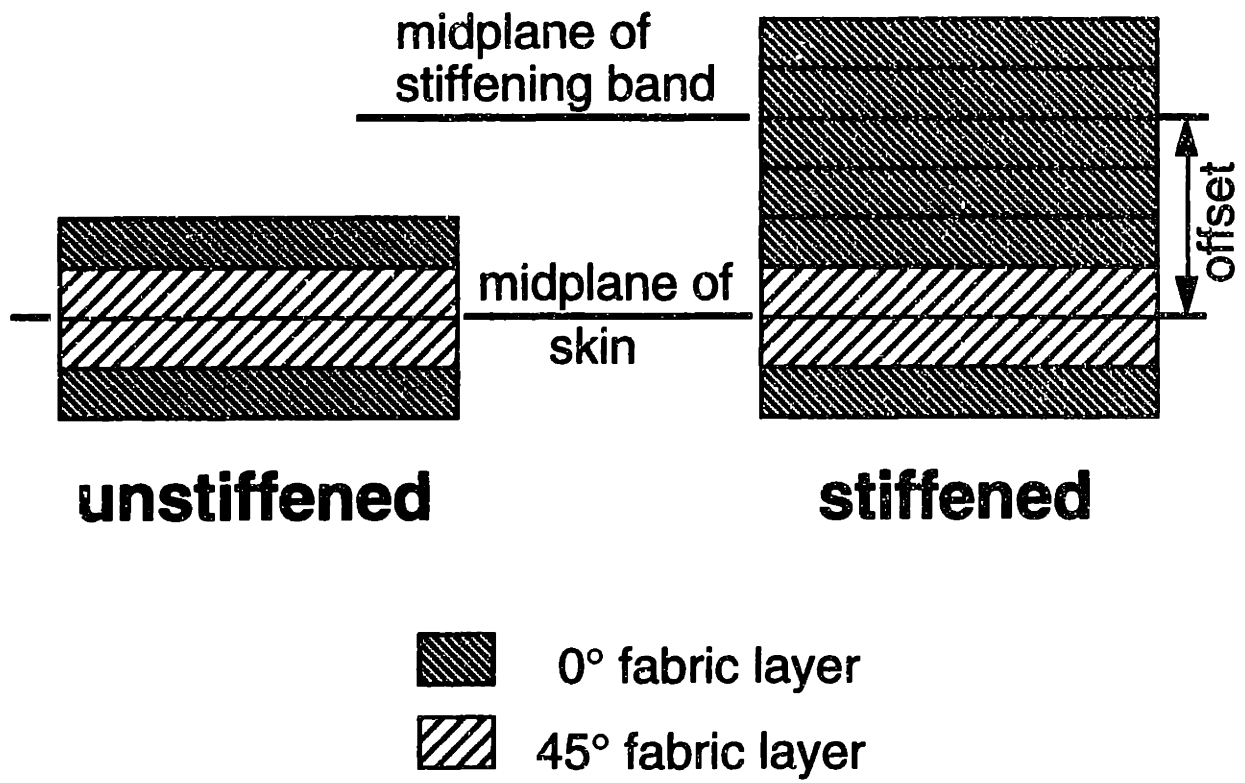


Figure 5.20 Cross-sections of the unstiffened and stiffened regions.

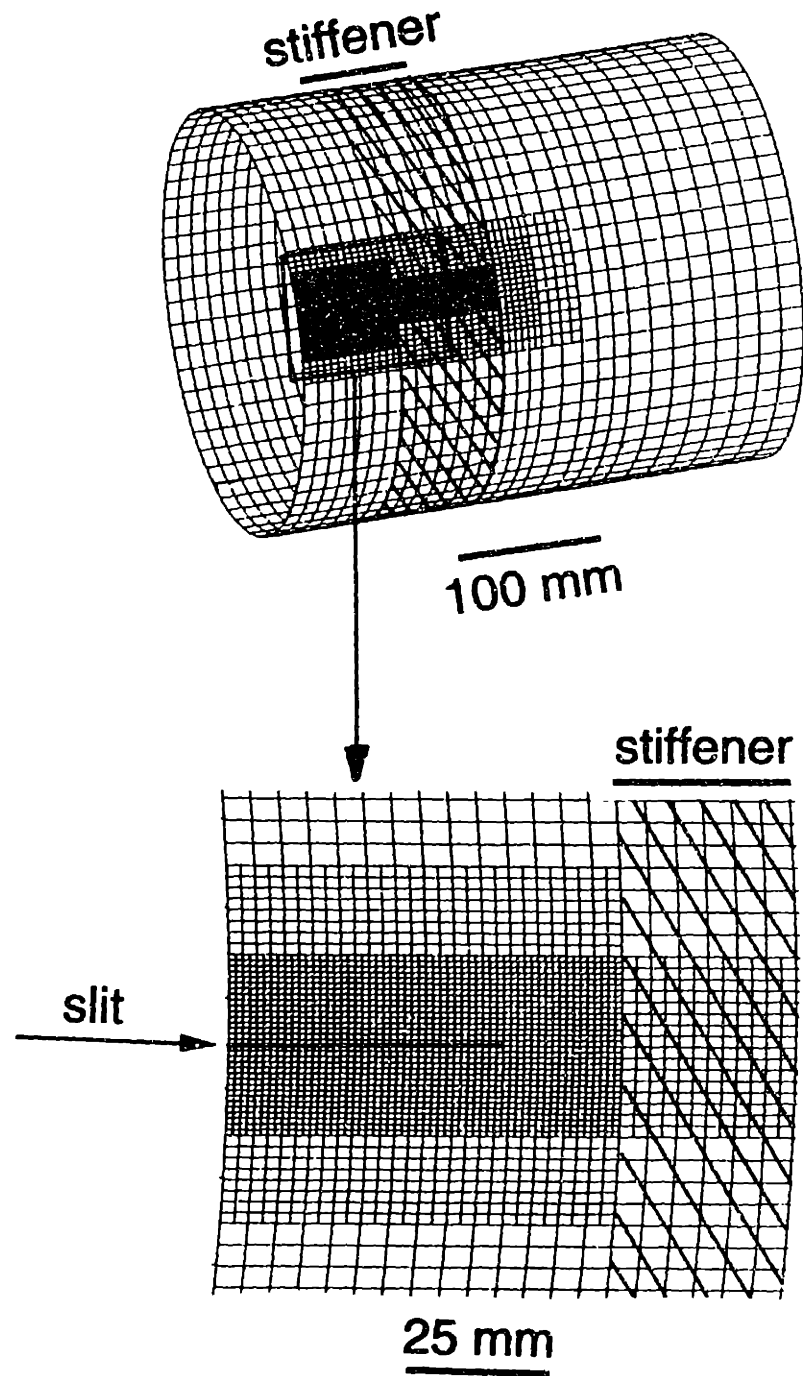


Figure 5.21 Typical finite element mesh for a laboratory-scaled, stiffened specimen (the case shown is cylinder with $R=152$ mm, $h=1.4$ mm, and $2a=104$ mm): (upper) entire one-half cylinder model, and (lower) blow-up of region near slit tip.

Table 5.3 Effects of the Stiffening Bands on the Linear Stress Intensification Factors for the (0/45)_s Cylinder

$2a$ (mm)	$\frac{\psi^b}{a}$	K^{ext} (Unstiffened)	K^{ext} (Stiffened ^a)	Difference
51	0.78	2.223	2.199	1.1%
78	0.51	3.087	3.006	2.6%
104	0.38	3.895	3.735	4.1%
208	0.19	6.638	5.961	10.2%
312	0.13	8.918	7.569	15.1%

^aStiffened with four layers of 0° fabric material

^bLigament width, ψ , is 20 mm in all cases

Table 5.4 Effects of the Stiffening Bands on the Linear Stress Intensification Factors for the (45/0)_s Cylinder

$2a$ (mm)	$\frac{\psi^b}{a}$	K^{ext} (Unstiffened)	K^{ext} (Stiffened ^a)	Difference
51	0.78	2.192	2.182	0.5%
78	0.51	2.967	2.924	1.5%
104	0.38	3.699	3.604	2.6%
208	0.19	6.342	5.881	7.3%
312	0.13	8.696	7.685	11.6%

^aStiffened with four layers of 0° fabric material

^bLigament width, ψ , is 20 mm in all cases

Figure 5.22 where the greater nonlinear effects are again predicted as pressure increases. The effects of different bending properties again diminish as loading increases.

The effects of nonlinearity and stiffening bands on the longitudinal and hoop strain distributions are presented next. As noted previously, these strain distributions are used to identify the "regions of interest" where strain gages are bonded in the experimental phase of the work. In the presentation of the predicted strain distributions, the total and bending strains in the unstiffened regions are computed on the outer surface of the cylinder, while those in the stiffened regions are computed on the outer surface of the stiffener.

The effects of nonlinearity on the strain distributions of the (0/45)_s stiffened cylinders with the smallest value of the ψ/a ratio, which correspond to a longitudinal slit length of 312 mm, are shown in Figures 5.23 and 5.24 for the longitudinal and hoop strains, respectively. For this particular case ($\psi/a = 0.13$), the edge of each stiffening band is very close (approximately 20 mm) to the slit tip. Only the strain distributions in the region between $0.80 a$ and $1.80 a$ from the midslit region are presented here, so that the nonlinear effects near the slit tips and the stiffening bands can be shown more clearly. The hoop stiffener is located between $1.13 a$ and $1.62 a$ from the midslit region. The distributions for the (45/0)_s cylinder are similar and are not shown here for brevity. The distributions are shown at a pressure level of 1 MPa for the same reason as in the unstiffened case.

Significant deviation from the linear solution can be seen in the longitudinal strain distribution in the region behind, but very close to, the slit tip ($x/a \approx 1$). The linear membrane strain distribution has an initial "concave-down" shape which changes to a "concave-up" shape very near the slit tip.

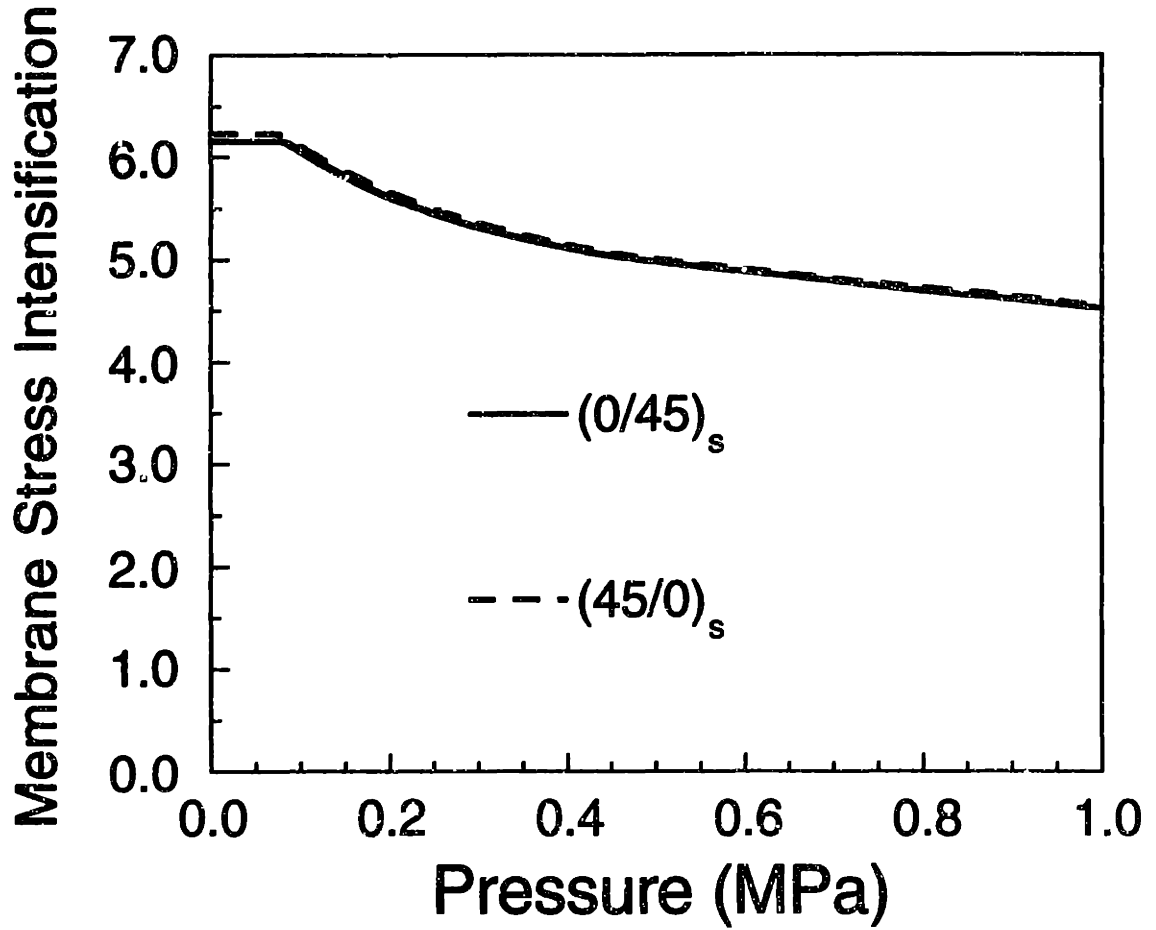


Figure 5.22 The evolution of the nonlinear membrane stress intensification factors for cylinders with a longitudinal slit length of 312 mm corresponding to the ψ/a -ratio of 0.13.

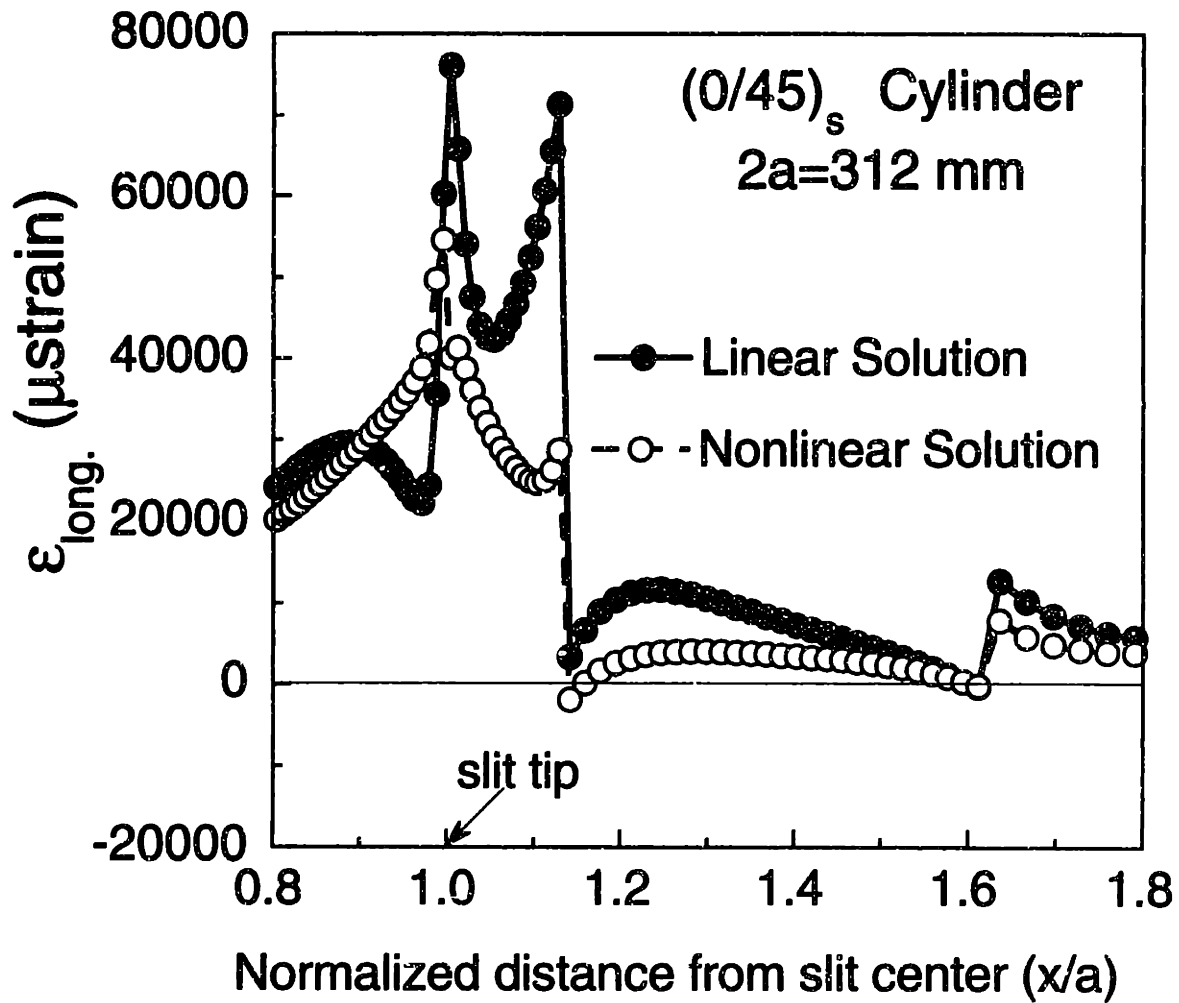


Figure 5.23 Linear and nonlinear total longitudinal strain distributions for the stiffened (0/45)_s cylinders with a longitudinal slit length of 312 mm at 1 MPa internal pressure (total strains are computed on the top surface of the stiffener in the stiffened region and on the top surface of the skin in the unstiffened region).

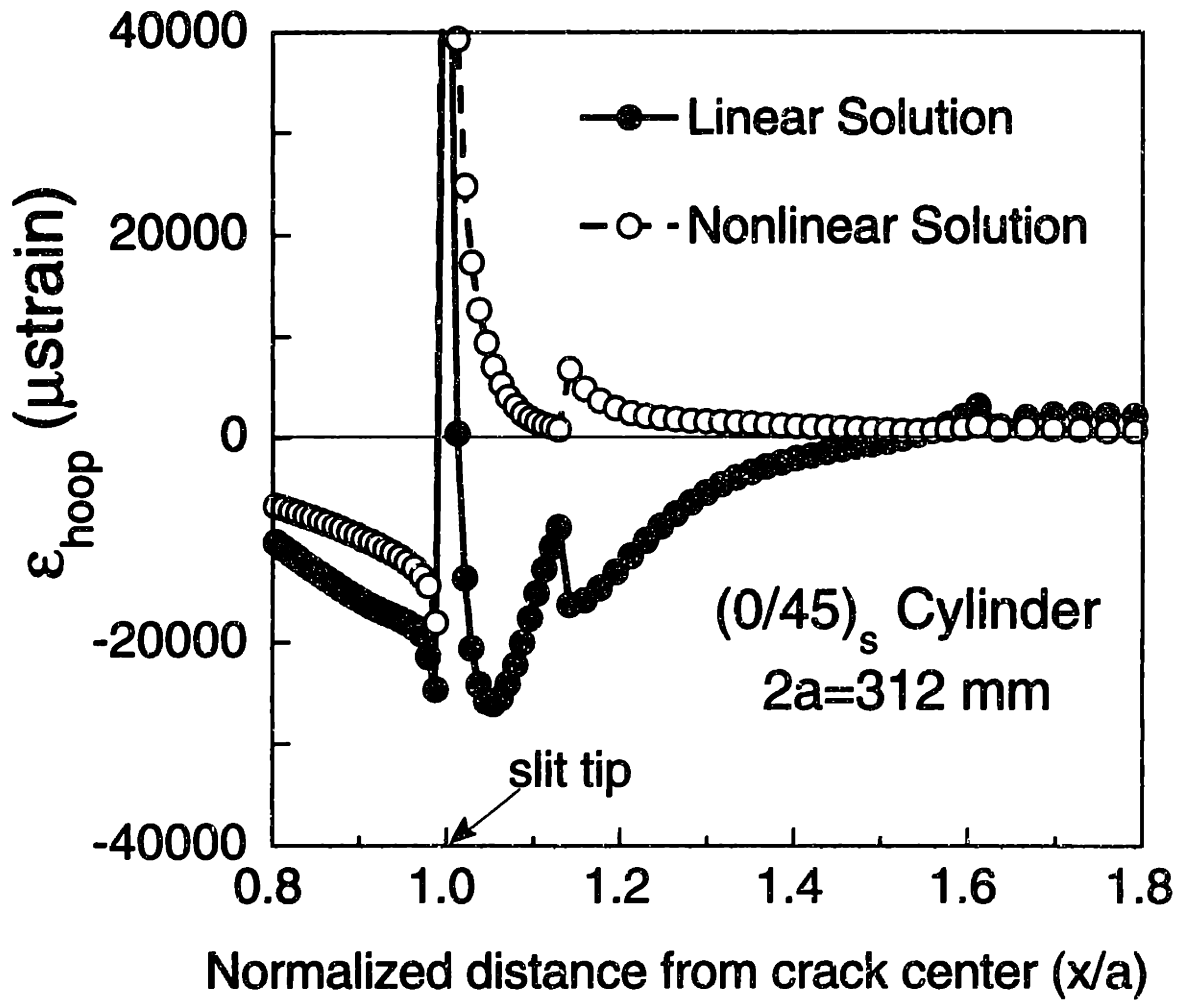


Figure 5.24 Linear and nonlinear total hoop strain distributions for the stiffened (0/45)_s cylinders with a longitudinal slit length of 312 mm at 1 MPa internal pressure (total strains are computed on the top surface of the stiffener in the stiffened region and on the top surface of the skin in the unstiffened region).

The magnitude increases substantially and reaches its global maximum at the slit tip. It then decreases, reaches a local minimum value at a distance of approximately $0.05 a$ from the slit tip, and finally increases again and appears to reach a local maximum value near the edge of the stiffening band at a distance of approximately $0.13 a$ from the slit tip. The nonlinear membrane strain distribution has a totally different shape. The shape of the distribution remains "concave-up" behind the slit tip as its magnitude increases monotonically and reaches a global maximum at the slit tip. The magnitude then decreases, reaching a local minimum at an approximate distance of $0.10 a$ from the slit tip, before again increasing and reaching a local maximum at the edge of the stiffening band at a distance of approximately $0.13 a$ from the slit tip. The magnitude of the nonlinear longitudinal strain is smaller than that of the linear solution in the ligament region, that is between the slit tip and the edge of the hoop stiffener. The existence of strain discontinuities at the two edges of the stiffening band (i.e. at distances of $0.13 a$ and $0.62 a$ from the slit tip) are noted. The reason is that the strains in the stiffened region are computed on the top surface of the stiffening band where the distance from the midplane of the base laminate to the location where the strains are computed is much larger than that in the unstiffened case. Note that the linear and nonlinear membrane strain distributions are "concave-down" in this region. However, the magnitude of the nonlinear strain continues to be smaller than that of the linear strain in that region.

The shapes of the hoop strain distribution predicted from the linear and nonlinear solutions are different in the region behind, but very close to, the slit tip. The linear distribution is initially "concave-up", switches to "concave-down", and reaches its global maximum value at the slit tip. The

nonlinear solution, on the other hand, remains "concave-down" prior to reaching its global maximum value at the slit tip. The nonlinear results are again lower in magnitude than the corresponding linear results. Ahead of the slit tip, the linear solution of the hoop strain decreases monotonically, becomes compressive beyond $0.01 a$ from the slit tip, and reaches a global minimum at a distance of approximately $0.05 a$ from the slit tip. The linear hoop strain then increases and reaches a local maximum value at the edge of the stiffener (i.e. at a distance of approximately $0.13 a$ from the slit tip). The nonlinear solution of the hoop strain also decreases monotonically ahead of the slit tip. However, its value remains tensile and it does not have a global minimum value as exhibited in the linear solution. The existence of strain discontinuities at the two edges of the stiffening band (i.e. at distances of $0.13 a$ and $0.62 a$ from the slit tip) are also noted in the hoop strain distribution for the same reason as the longitudinal case. There are two inflection points predicted in the linear solution where the shape of the distribution changes from "concave-up" to "concave-down" and from "concave-down" to "concave-up". The nonlinear solution does not show the existence of any inflection point in the distribution.

To assess the effects of stiffening bands on the unstiffened and stiffened cylindrical configurations, the total strain distributions in the longitudinal and hoop directions for the unstiffened and stiffened cases are shown in Figures 5.25 and 5.26, respectively. It can be seen that the effects of stiffening bands are localized in the stiffened regions and their surroundings for both the longitudinal and hoop distributions. Strain discontinuities or "jumps" can be seen in the longitudinal and hoop strain distributions in the vicinity of the stiffening band. These "jumps" are caused by the existence of abrupt changes in the membrane and bending stiffnesses

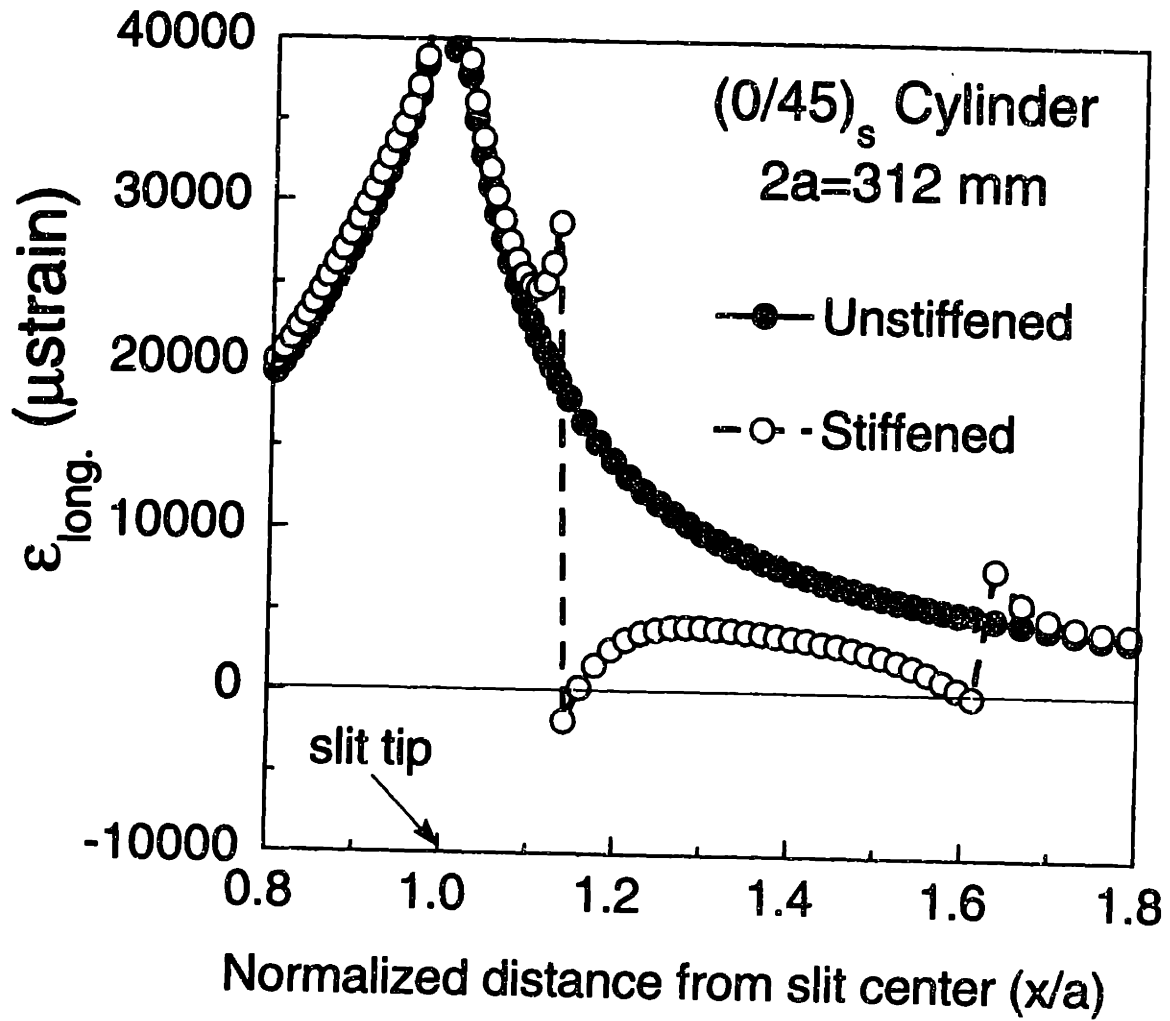


Figure 5.25 Nonlinear total longitudinal strain distributions for the unstiffened and stiffened (0/45)_s cylinders with a longitudinal slit length of 312 mm at 1 MPa internal pressure (total strains are computed on the top surface of the stiffener in the stiffened region and on the top surface of the skin in the unstiffened region).

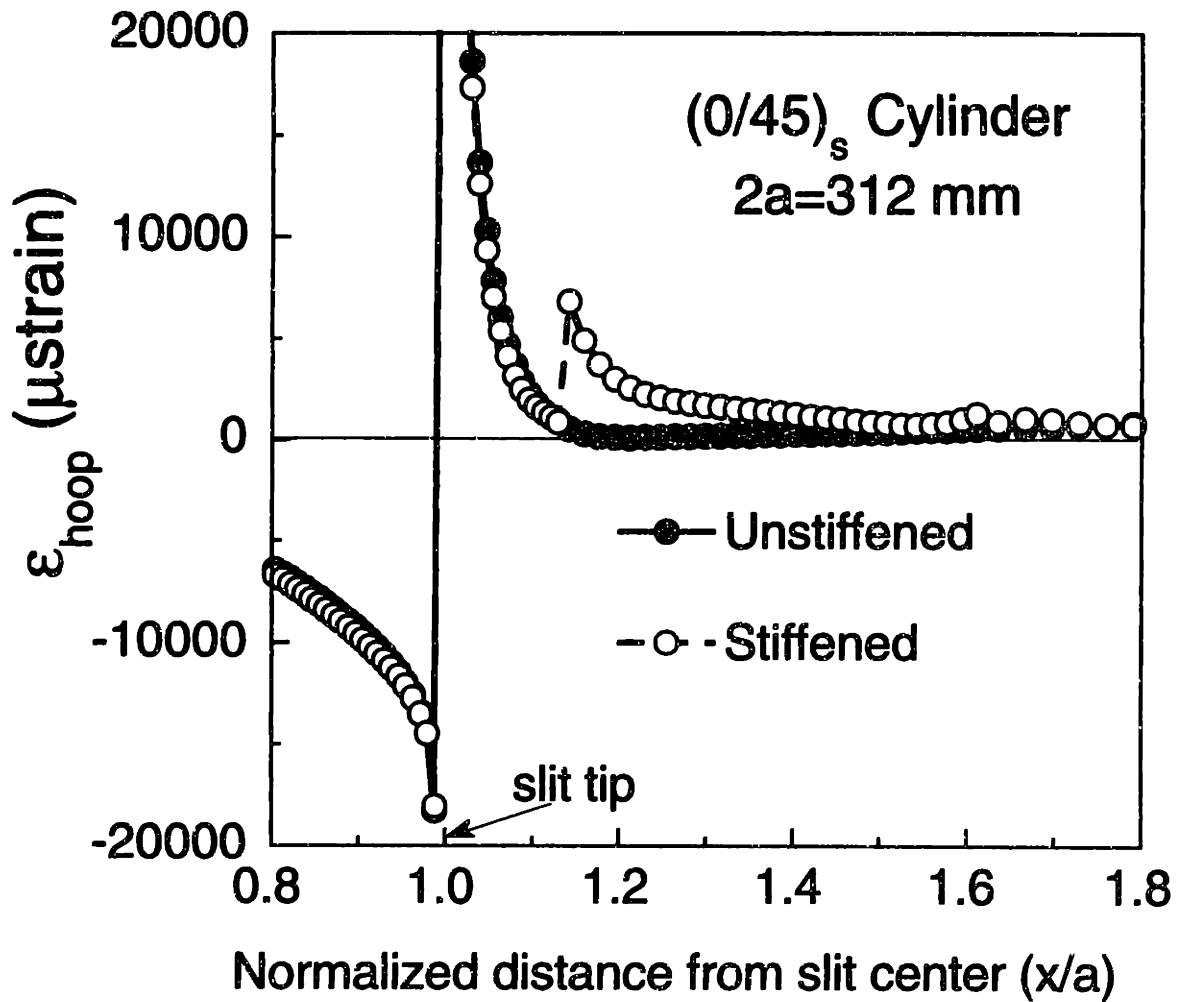


Figure 5.26 Nonlinear total hoop strain distributions for the unstiffened and stiffened $(0/45)_s$ cylinders with a longitudinal slit length of 312 mm at 1 MPa internal pressure (total strains are computed on the top surface of the stiffener in the stiffened region and on the top surface of the skin in the unstiffened region).

of the unstiffened and stiffened regions and vice versa. The longitudinal strain level on the top surface of the stiffened region is smaller than for the unstiffened case. Furthermore, the shape of the longitudinal strain distribution in the stiffened region is "concave-down" as compared to "concave-up" in the unstiffened region. However, the hoop strain level on the top surface of the stiffened region is larger than for the unstiffened case. The shape of the hoop distribution, which is "concave-up", is also different from that of the longitudinal distribution. The strain distributions for the unstiffened and stiffened cases at all other locations are almost identical at distances greater than approximately $0.25 a$ from the edge of the stiffener.

To get a better understanding of the underlying mechanisms behind these predicted nonlinear strain distributions, the total (nonlinear) longitudinal and hoop strains in the stiffened cylinder are decomposed into the membrane (uniform through-the-thickness) and bending (linearly-varying through-the-thickness) parts as depicted in Figures 5.27 and 5.28 for the longitudinal and hoop distributions, respectively. Corresponding membrane and bending distributions for the unstiffened cylinder with a slit length of 312 mm are shown in Figures 5.29 and 5.30. The bending strains in the unstiffened region are computed on the outer surface of the cylinder, while those in the stiffened region are computed on the outer surface of the stiffener.

In the longitudinal strain distribution, the membrane strain behind the slit tip ($x/a \leq 1$) increases and reaches its global maximum at the slit tip. The membrane strain then decreases rapidly ahead of the slit tip and becomes discontinuous at the points on the left and right edges of the hoop stiffening band. This is in contrast to the distribution of the unstiffened case shown in Figure 5.29 where both the membrane and bending distributions

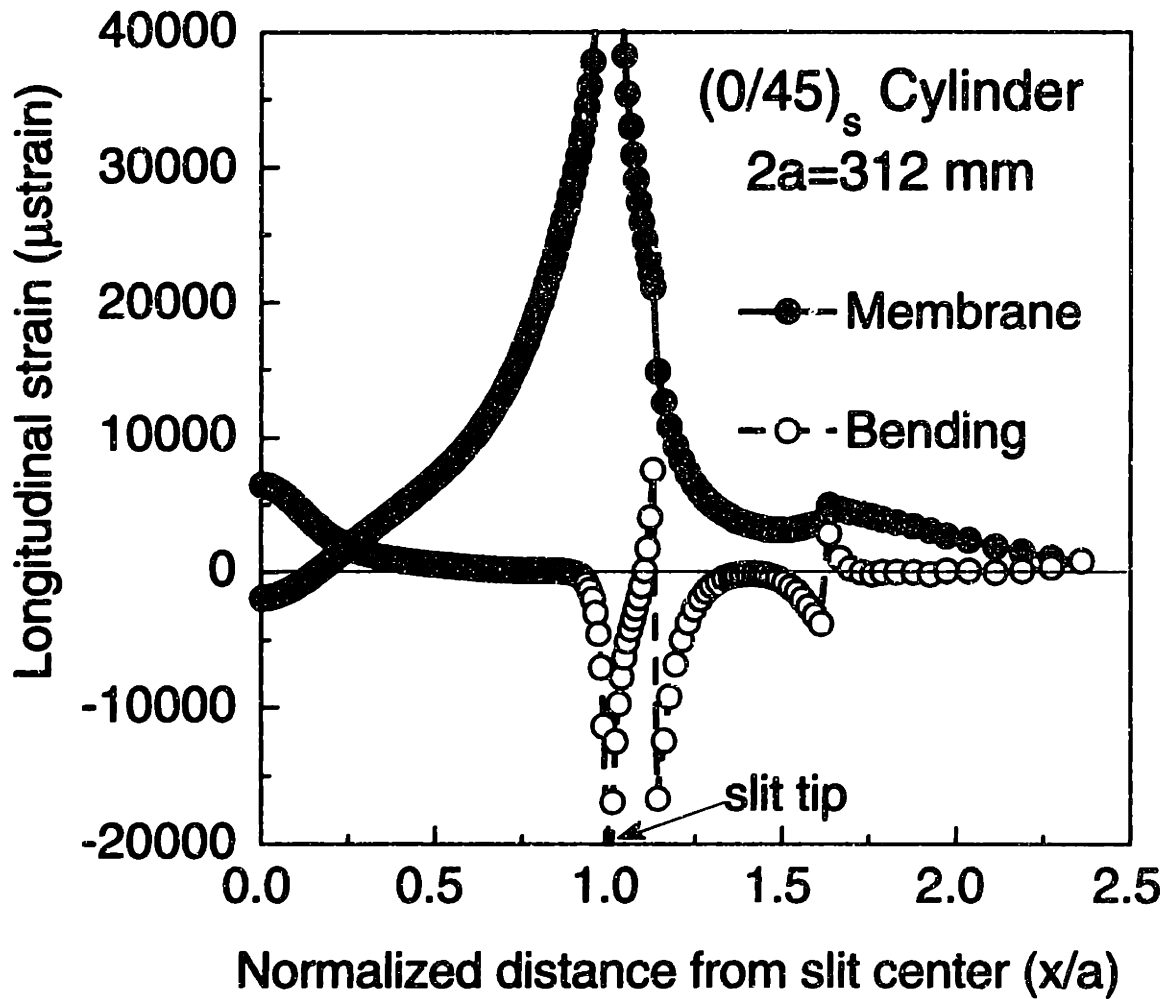


Figure 5.27 Membrane and bending longitudinal strain distributions in a stiffened $(0/45)_s$ cylinder with a longitudinal slit length of 312 mm at 1 MPa internal pressure (bending strains are computed on the top surface of the stiffener in the stiffened region and on the top surface of the skin in the unstiffened region).

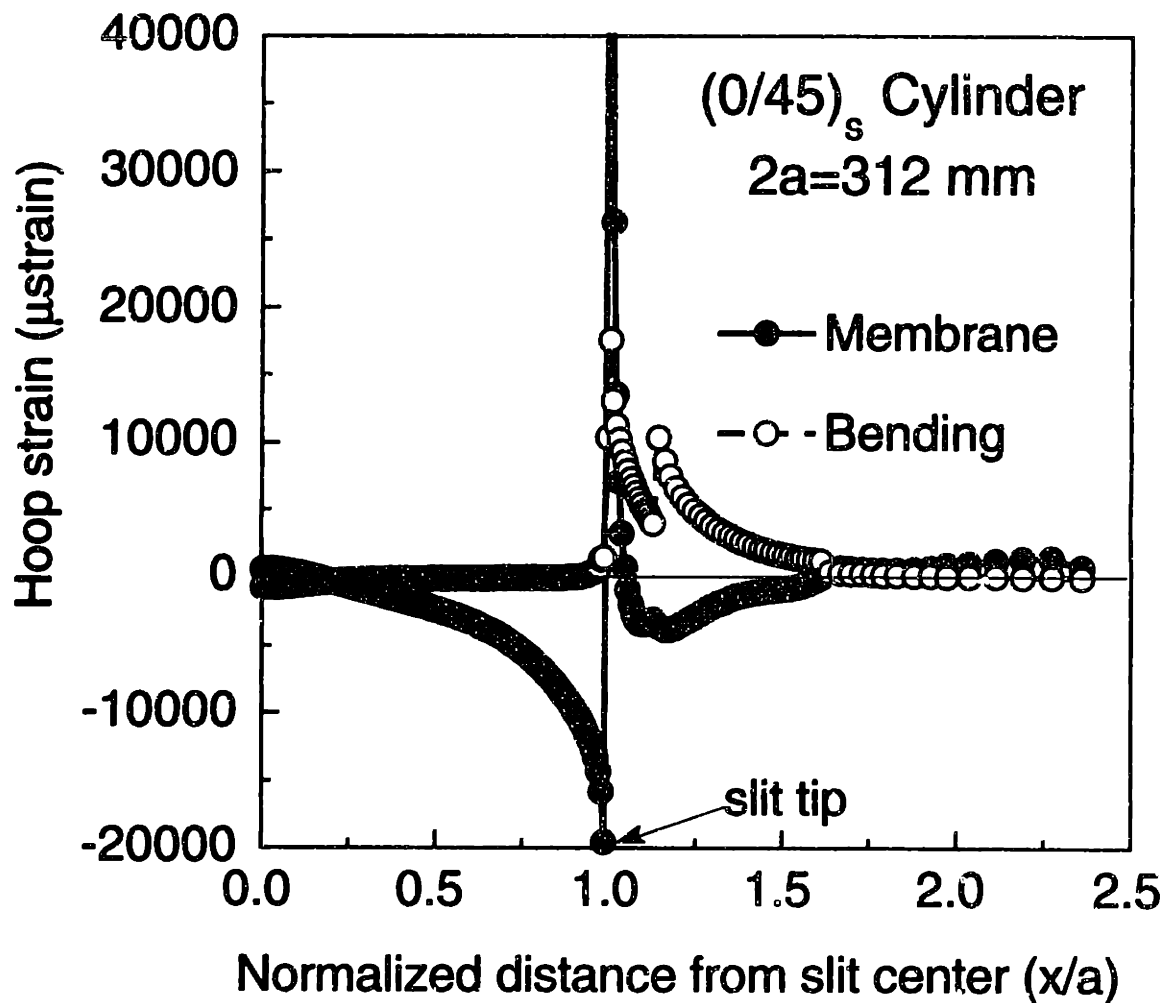


Figure 5.28 Nonlinear membrane and bending hoop strain distributions in a stiffened (0/45)_s cylinder with a longitudinal slit length of 312 mm at 1 MPa internal pressure (bending strains are computed on the top surface of the stiffener in the stiffened region and on the top surface of the skin in the unstiffened region).

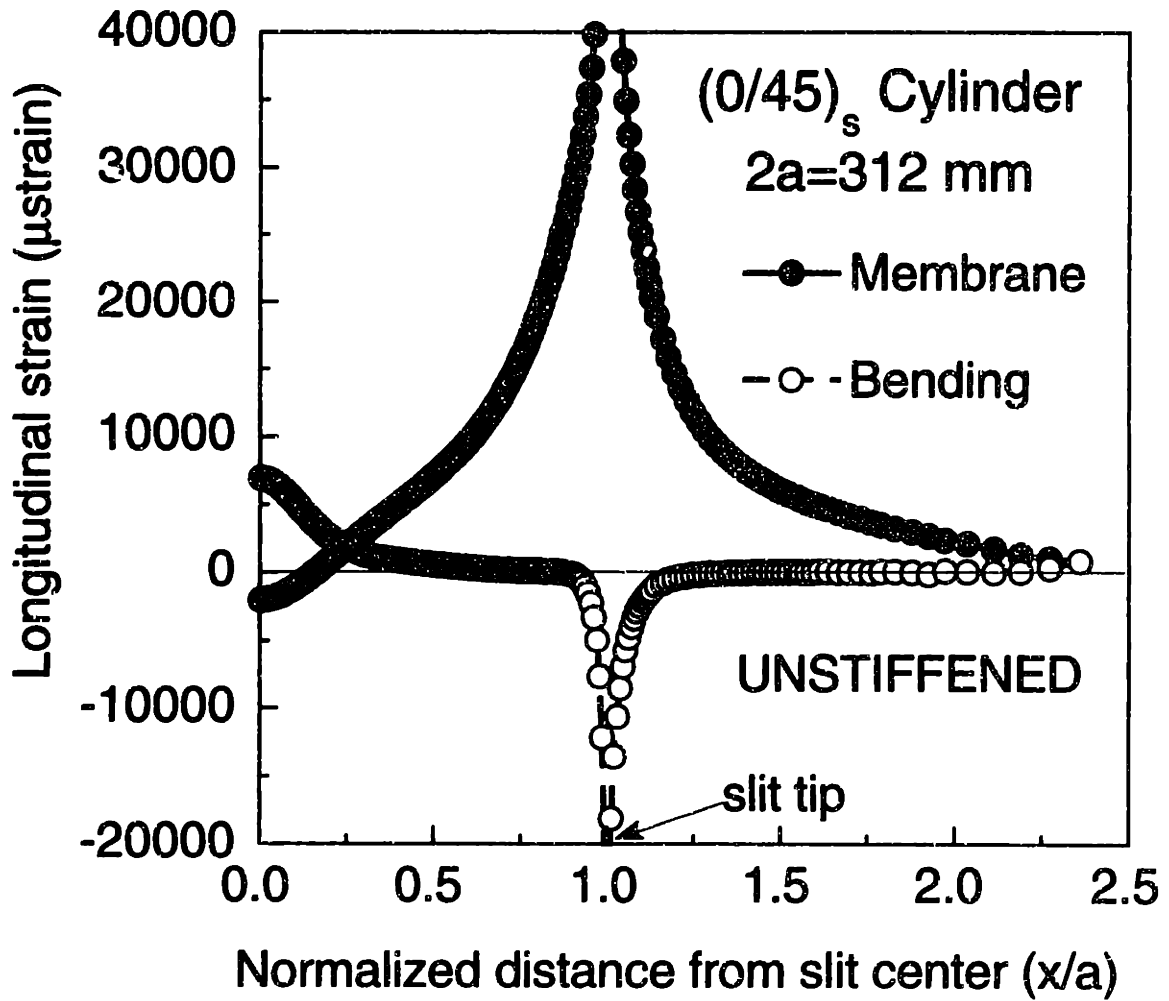


Figure 5.29 Nonlinear membrane and bending (long.) strain distributions in an unstiffened (0/45)_s cylinder with a longitudinal slit length of 312 mm at 1 MPa internal pressure (bending strains are computed on the top surface of the skin).

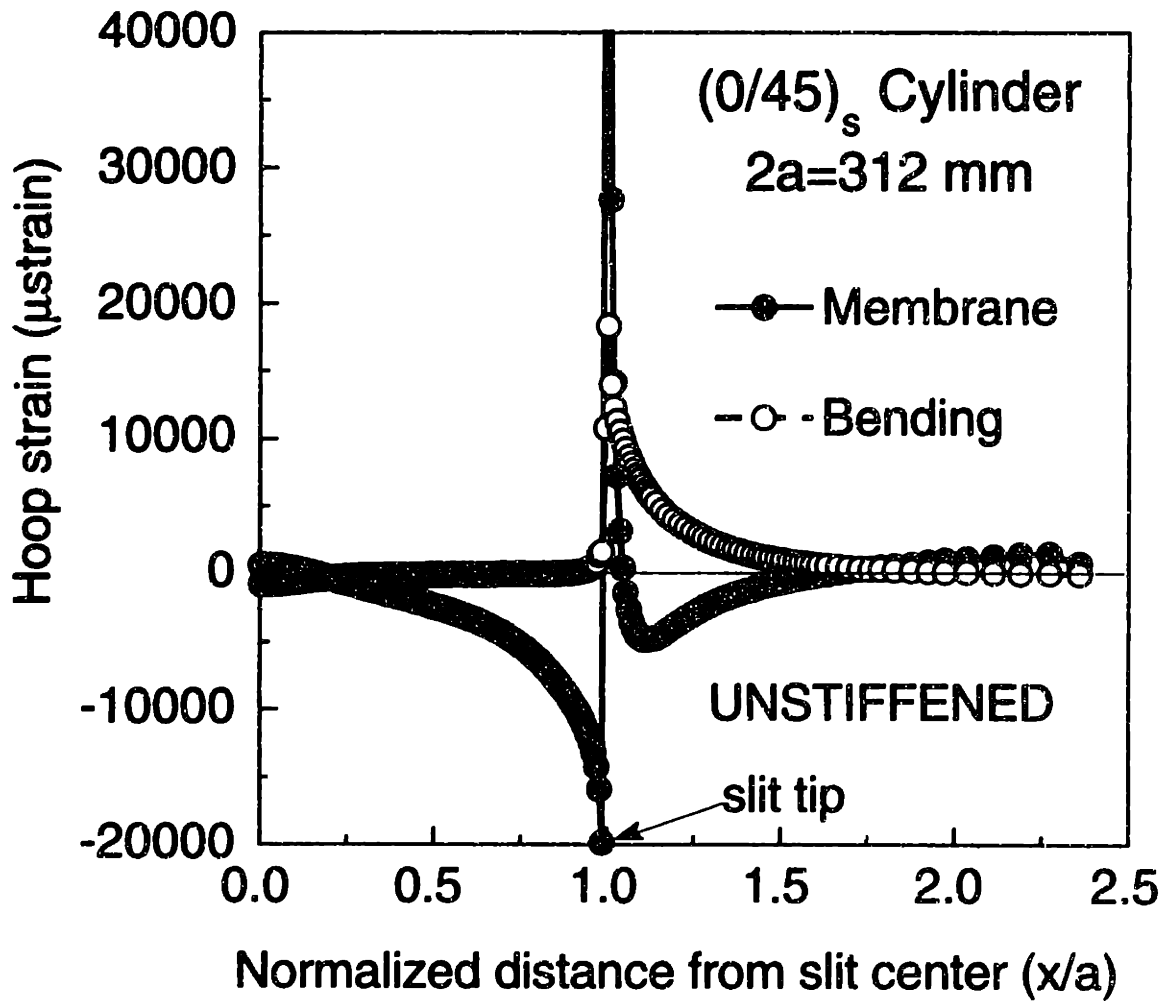


Figure 5.30 Nonlinear membrane and bending (hoop) strain distributions in an unstiffened (0/45)_s cylinder with a longitudinal slit length of 312 mm at 1 MPa internal pressure (bending strains are computed on the top surface of the skin).

are continuous and decrease monotonically from their peak values at the slit tip. The shape of the membrane longitudinal strain distribution in the stiffened region is "concave-up". The bending component in the longitudinal direction is relatively insignificant compared to the membrane part, except in the vicinity of the midslit region, at the slit tip region, and at the left and right edges of the hoop stiffener. The importance of bending on the left and right edges of the stiffening band is manifested in the form of strain discontinuities ("jumps") with these effects quickly dying out away (within $0.25 a$) from these points of bending and membrane stiffness discontinuities. The shape of the bending longitudinal strain distribution is "concave-down" in the stiffened region. By comparing the membrane and bending strain distributions shown in Figure 5.27, it can be concluded that the membrane contribution dominates.

In the hoop strain distribution, the membrane component behind the slit tip ($x/a \leq 1$) decreases gradually and, although it is initially tensile in the vicinity of the midslit region, it becomes compressive beyond a distance of approximately $0.25 a$ from the midslit location. It then changes its sign and becomes tensile ahead of the slit tip. The magnitude of the membrane contribution then decreases rapidly and becomes compressive at a distance of approximately $0.05 a$ from the slit tip. It continues to decrease, reaches a local minimum at approximately $0.10 a$ from the slit tip, and then increases again and reaches a local maximum at the edge of the stiffening band (i.e. at a distance of $0.13 a$ from the slit tip). The magnitude in the stiffened region then decreases, reaches another local minimum at a distance of approximately $0.16 a$ from the slit tip, and increases again. It becomes tensile again at a distance of $0.64 a$ from the slit tip. Note that the membrane contribution is negative (compressive) at the stiffening band

location. The bending part is relatively insignificant behind the slit tip ($x/a \leq 1$). The importance of bending is only in the region close to the slit tip and near the stiffened region where strain discontinuities can again be seen clearly. The shape of the bending hoop strain distribution in the stiffened region is "concave-up". The bending contribution diminishes at a distance of roughly $0.75 a$ from the slit tip. This is in contrast to the distribution of the unstiffened case shown in Figure 5.30 where both the membrane and bending distributions are continuous. The magnitudes of the stiffened and unstiffened cases are practically identical beyond a distance of approximately $0.25 a$ from the edge of the stiffener.

Differences between the linear and nonlinear strain distributions are predicted in two regions: one, the vicinity of the midslit and, two, the ligament area. In those two regions, different states of strains and/or strain gradients for the nonlinear case are predicted from the analyses. However, since the influence of the stiffening bands is confined to the ligament area and is negligible in any other region, the only "region of interest" for the stiffened case is therefore the ligament area which is located between the slit tip and the edge of the stiffening band. Thus, strain gages were bonded in the ligament region in the experimental phase of the work, as described in Chapter 6.

Chapter 6

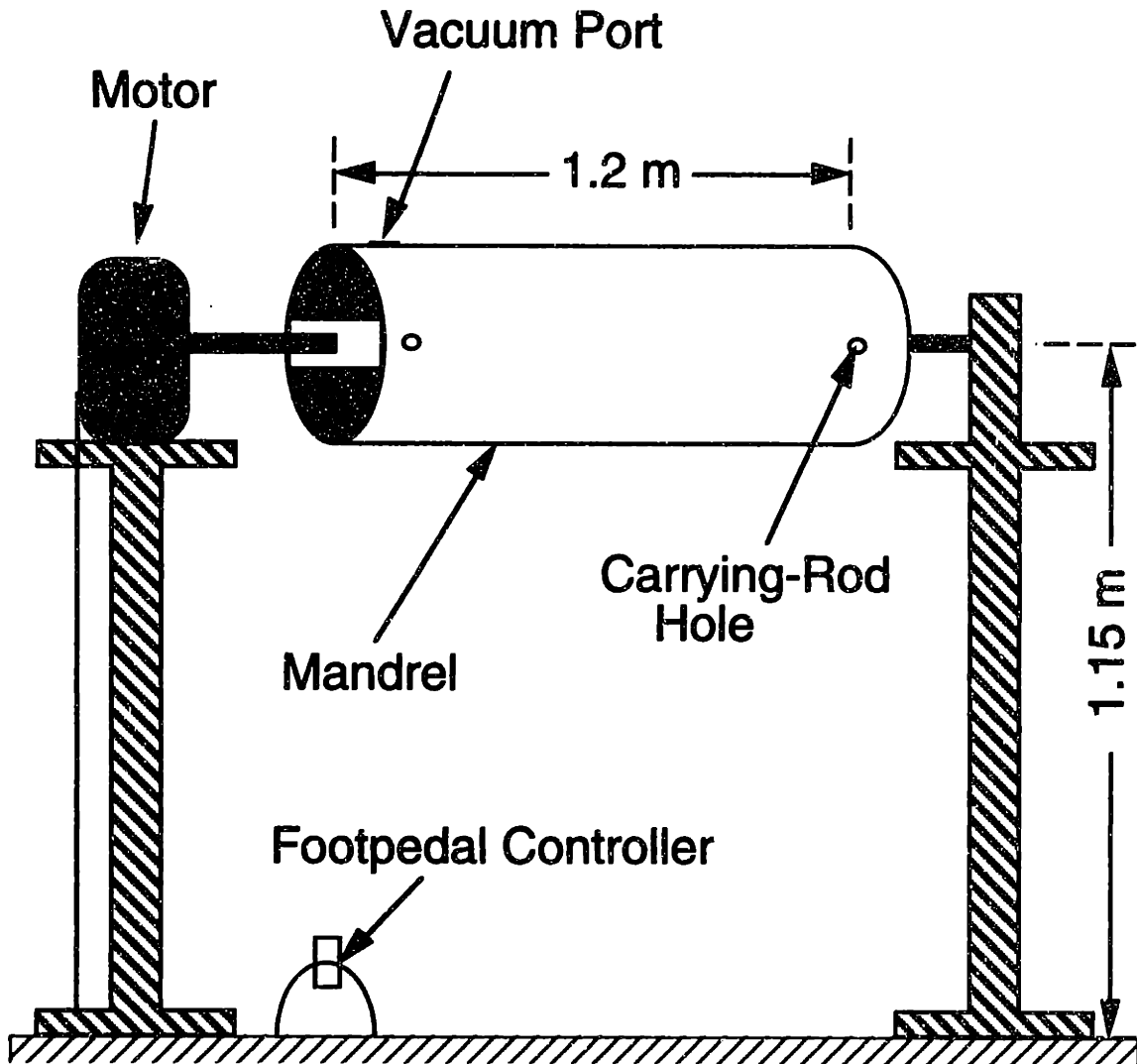
Experimental Procedures

The manufacture, test preparation involving instrumentation, test procedures, and post-test documentation for the unstiffened (*type-1*) and stiffened (*type-2 and type-3*) composite cylinders of the present investigation are described in this chapter.

6.1 Cylinder Manufacture

All cylinders were manufactured according to standard TELAC manufacturing procedures. The graphite/epoxy material system used to manufacture the cylinders was the AW370-5H/3501-6 with a resin content of 43% before cure (a bleed system). The nominal properties are shown in Table 3.1. This satin-weave fabric material was obtained from HerculesTM in a 1.25 meter (49 inch) wide roll and was stored in a freezer at a temperature below -18°C until it was ready to be used.

An aluminum cylinder that has an outside diameter of 305 mm and a wall thickness of 6.4 mm was used as the mandrel for the composite cylinders. The length of the mandrel is 1.2 m. During the layup procedure, the mandrel was mounted on a motorized tubewinder as illustrated in Figure 6.1. A footpedal that is connected to the mandrel was used to rotate the mandrel in counter-clockwise and clockwise directions at an approximate speed of 3 rpm. A vacuum port is located on the mandrel near one end and



NOTE: Not to Scale

Figure 6.1 Illustrations of motorized tubewinder and mandrel.

two holes on the opposite sides of the mandrel at both ends allow rods to be inserted so that the mandrel can be carried and suspended in the autoclave.

Before starting the layup process, the aluminum cylinder was cleaned using methanol to remove dirt and excess epoxy from the previous cure. The mandrel was then sprayed with mold release. A sheet of Guaranteed Non-Porous Teflon (GNPT) was wrapped around the mandrel and secured on the underside with transferable adhesive tape. Care was taken that this GNPT layer was tight and free of wrinkles. The front, back, and ends of the mandrel were designated as shown in Figure 6.2 for reference purposes. The FRONT of the cylinder was designated as the side of the mandrel opposite (approximately 180° hoop angular location) to the vacuum port hole. A through-thickness slit oriented in the longitudinal direction was to be cut in this region and, therefore, it was important to keep any ply seams away from this region. The BACK of the cylinder was designated as the side of the mandrel where the vacuum port was located. The end of the cylinder where the vacuum port was located was designated as the END 1. The other end of the cylinder was designated as the END 2. To determine the circumferential (0° fiber) direction, a wide strip (approximately 150 mm in width) of GNPT, whose sides are straight and parallel, was wrapped tightly around the mandrel and the ends aligned. The 0° fiber direction was then established by wrapping a continuous strip of flash tape around the mandrel with the edge of the flash tape coinciding with that of the GNPT layer. Several small pieces of cork dams were attached to the tape at several locations as illustrated in Figure 6.2 to further guide the placement of plies on the mandrel.

The layup procedure of the base cylinders was the same for the three cylinder types. Before the layup was started, plies of two different angles (0° and 45°) were cut from a 1.25 m wide roll. A slightly different cutting

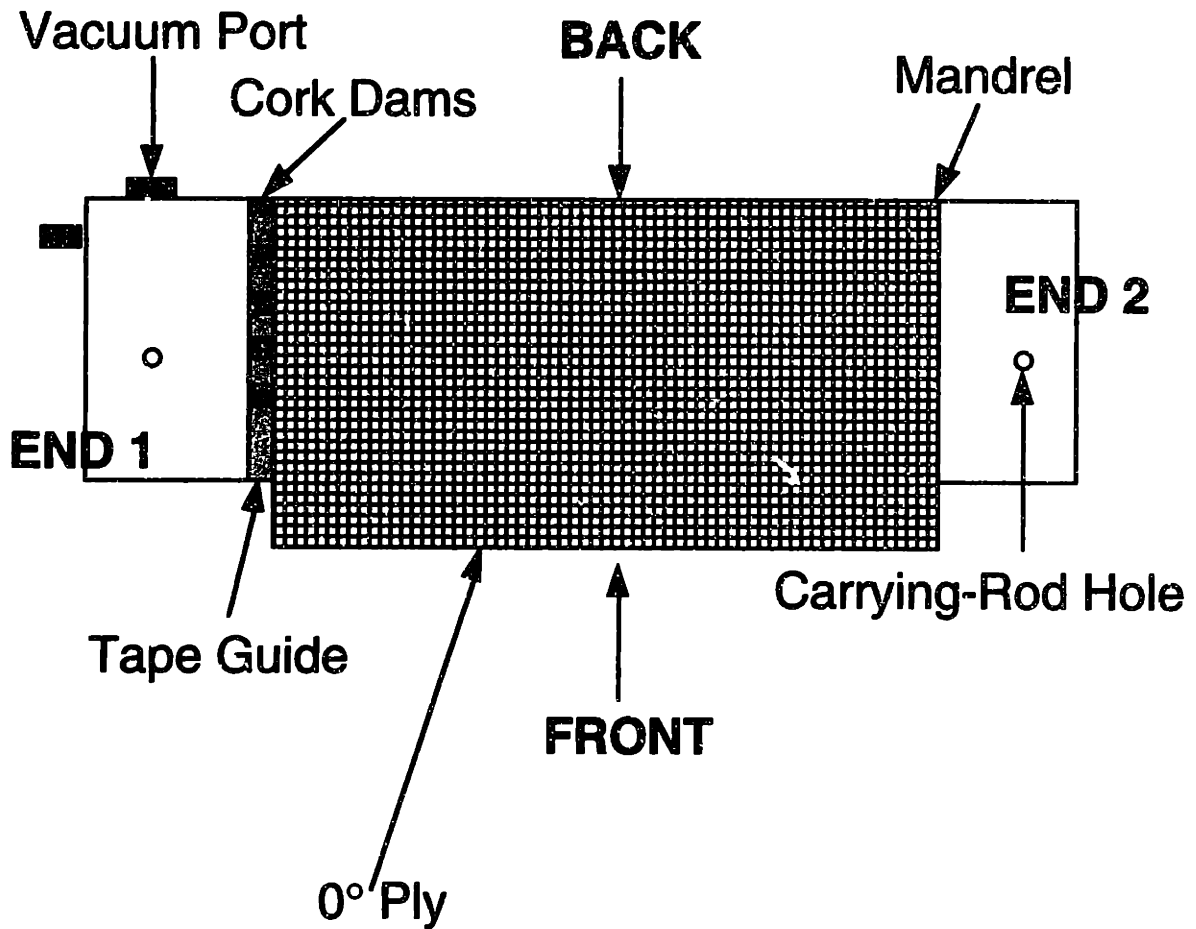


Figure 6.2 Illustration of cylinder layup procedure and terminology.

procedure was used for the angle plies ($\pm 45^\circ$ layers) than that used in [34] in order to make the present layup process easier. In [34], the angle-ply layers of 45° and -45° fiber orientations were cut in one piece with dimensions shown in Figure 6.3 where the seams of a ply overlapped by 12.7 mm. These $+45^\circ$ and -45° plies were cut to balance the layup and to avoid double seam overlaps at the back of the cylinder. Due to the cutting procedure for the angle-ply layers, the previous manufacturing procedure required approximately 5 meters of material from the spool. Some difficulties, in the form of significant ply-warping, were usually encountered in the layup process due to the size of the angle-ply layers. Such ply-warping can distort the angle ply layer and induce some aberration in the fiber direction of an angle ply along the cylinder.

The newly proposed cutting procedure for the $(0/45)_n$ cylinder illustrated in Figure 6.4 was intended to alleviate this warping problem. In this new procedure, the angle plies were laid up by hand using the same procedure used for the 0° plies. The length of each ply, which ranges from 978 mm for the first 0° ply to 983 mm for the last 0° ply, depends on the order of its placement on the aluminum mandrel in order to account for the slight change in the outer cylinder radius as sequential plies are placed. Since all of the plies had the same shape (i.e. rectangular) and overlapped at the back of the cylinder, care had to be taken that the seam overlaps of each ply did not occur at the same location and differed from each other by at least 12.7 mm. This new procedure is more efficient as it only required approximately 4 meters of material from the spool (a reduction of 20% over that needed in the previous work). Good results were obtained using these new cutting and layup procedures.

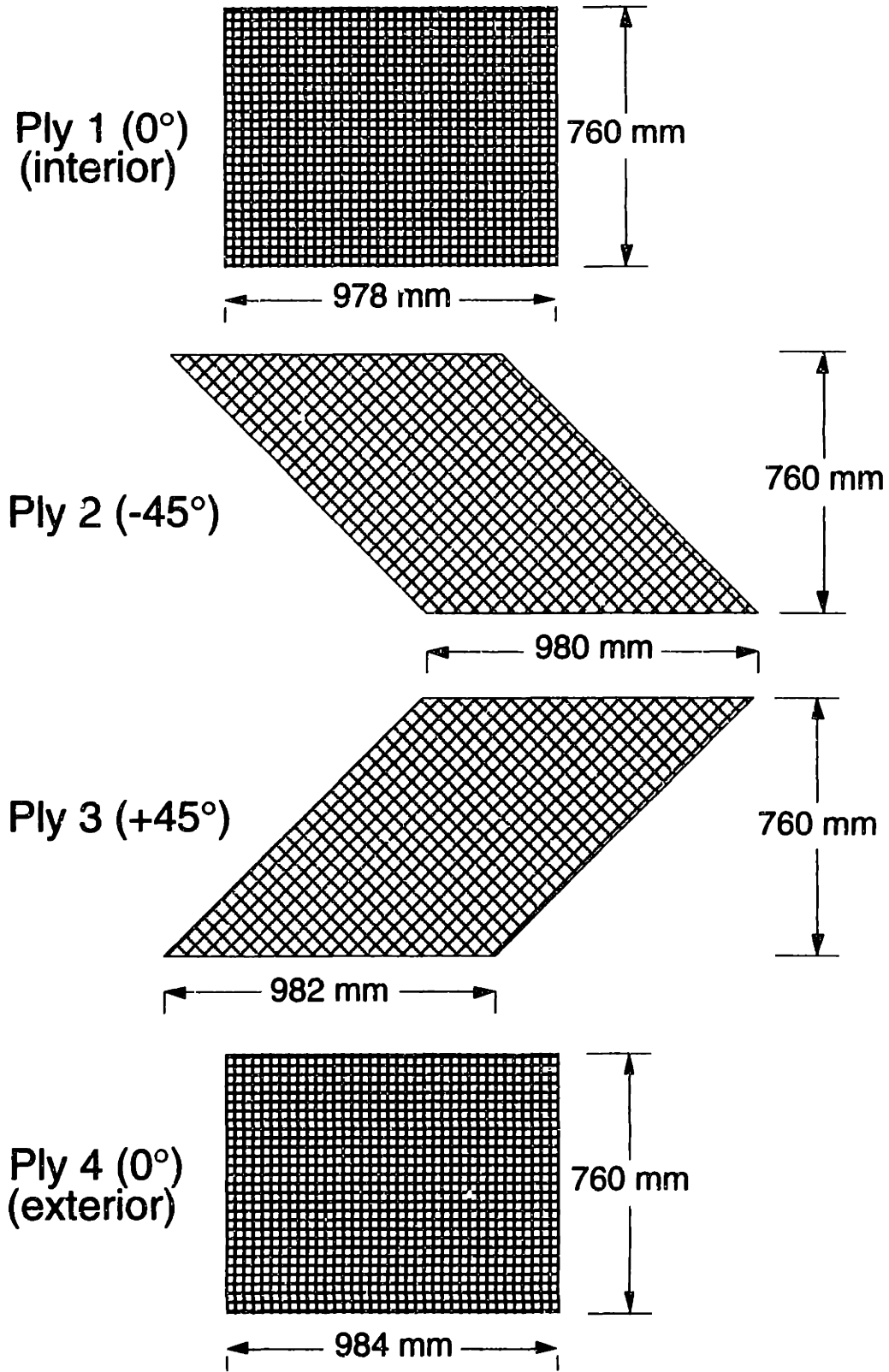


Figure 6.3 Illustrations of the $(0/45)_s$ cylinder ply dimensions and orientations utilized in [34, 37].

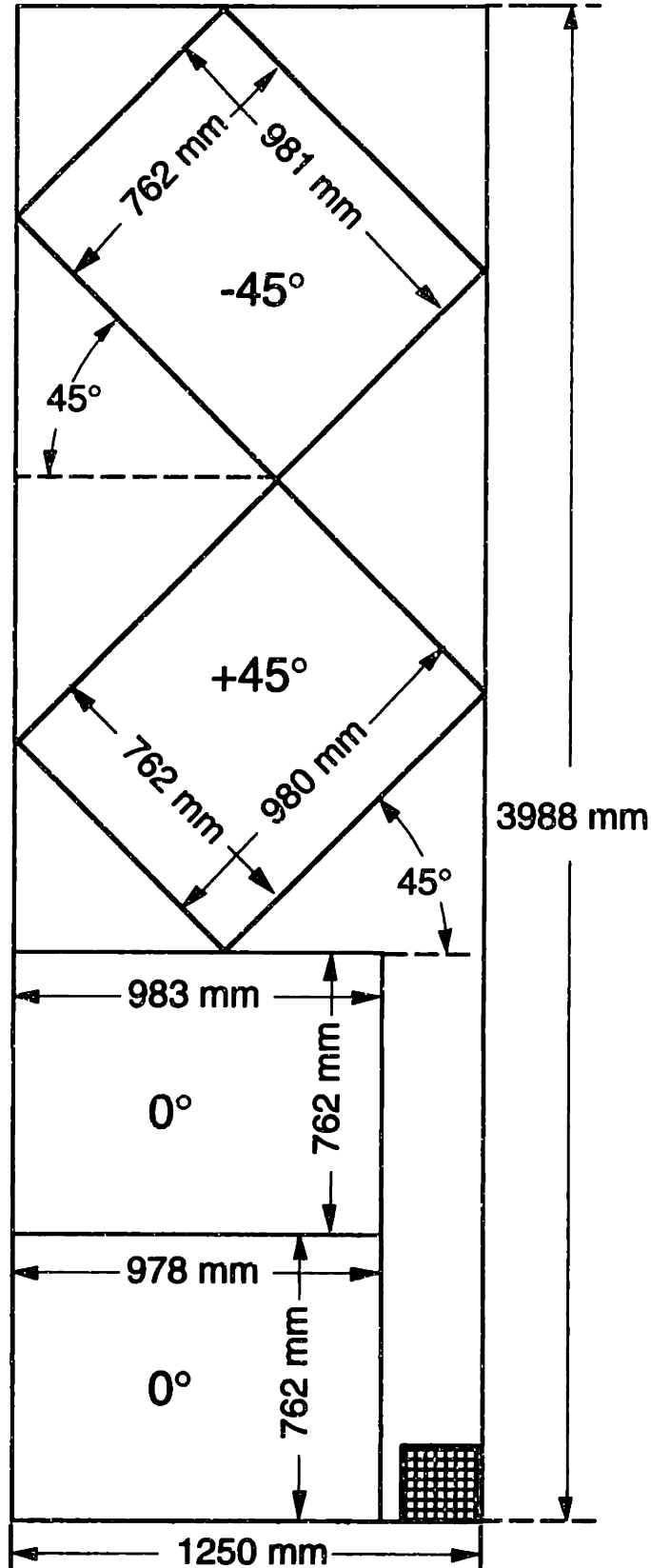


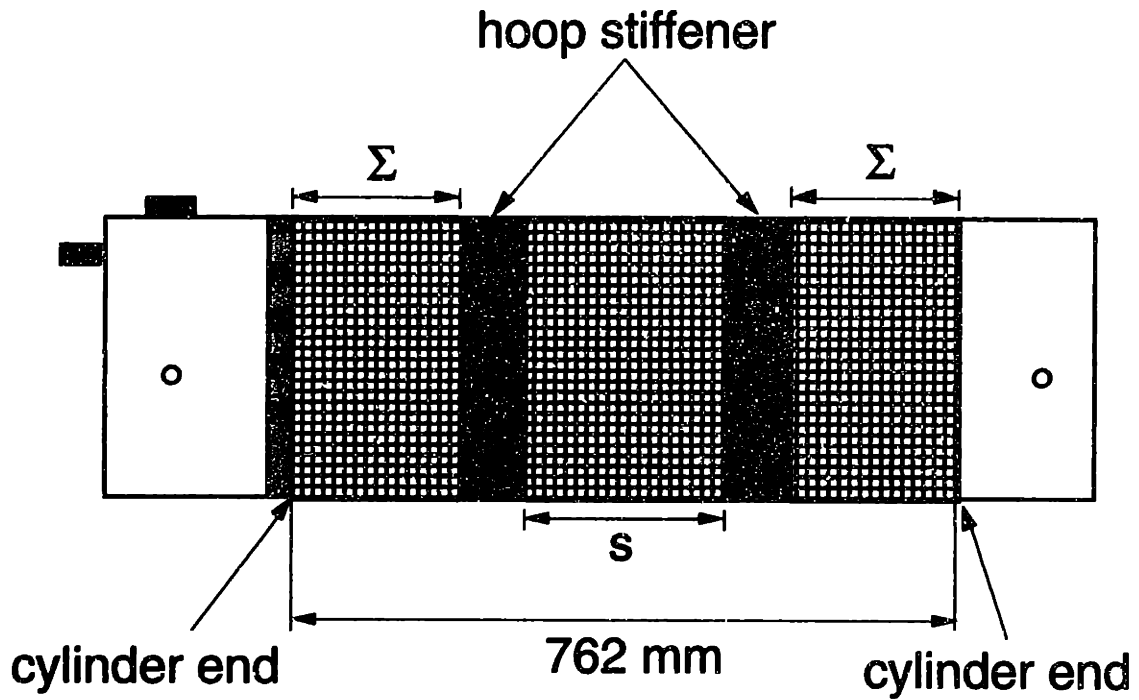
Figure 6.4 Illustration of the (0/45), cylinder ply dimensions and orientations utilized in the present work.

In addition to the base materials, stiffener layers were also cut to manufacture the *type-2* and *type-3* cylinders. In the *type-2* cylinders, only fabric stiffener layers of 0° fiber orientation were cut. The width of the stiffener layers was 76 mm in order to be consistent with the previous work [26, 36]. In the *type-3* cylinders, there were two different stiffener configurations: one, the *type-A* stiffener which was constructed from the unidirectional AS4/3501-6 graphite/epoxy material system and, two, the *type-B* stiffener which was constructed from the fabric AW370-5H/3501-6 graphite/epoxy material system as illustrated in Figure 3.5.

The various composite plies were laid up on the mandrel according to the specific cylinder layup. The first ply was oriented using the 0° fiber guide established previously. Subsequent plies were oriented using the first ply as a guide. Some pressure was applied by hand in order to minimize wrinkles. This process was continued until all of the plies were laid up. This overall process was the same for all three cylinder types. After this stage, the layup procedure for the unstiffened (*type-1*) cylinder was completed. Due to the presence of stiffening bands, additional steps for the stiffened (*type-2* and *type-3*) constructions are needed.

The geometry of the *type-2* cylinder is shown in Figure 3.3. Only the circumferential stiffeners were utilized in this cylinder type. Three different slit sizes were considered for this cylinder type: 51 mm, 78 mm, and 104 mm. The spacings between the hoop stiffeners depended on the slit sizes as shown in Table 3.4. The distance between the two cylinder ends to the edge of the stiffening bands is designated as Σ as depicted in Figure 6.5 and can be determined as

$$\Sigma = 305 - \frac{s}{2} \quad [mm] \quad (6.1)$$



NOTE: Not to Scale

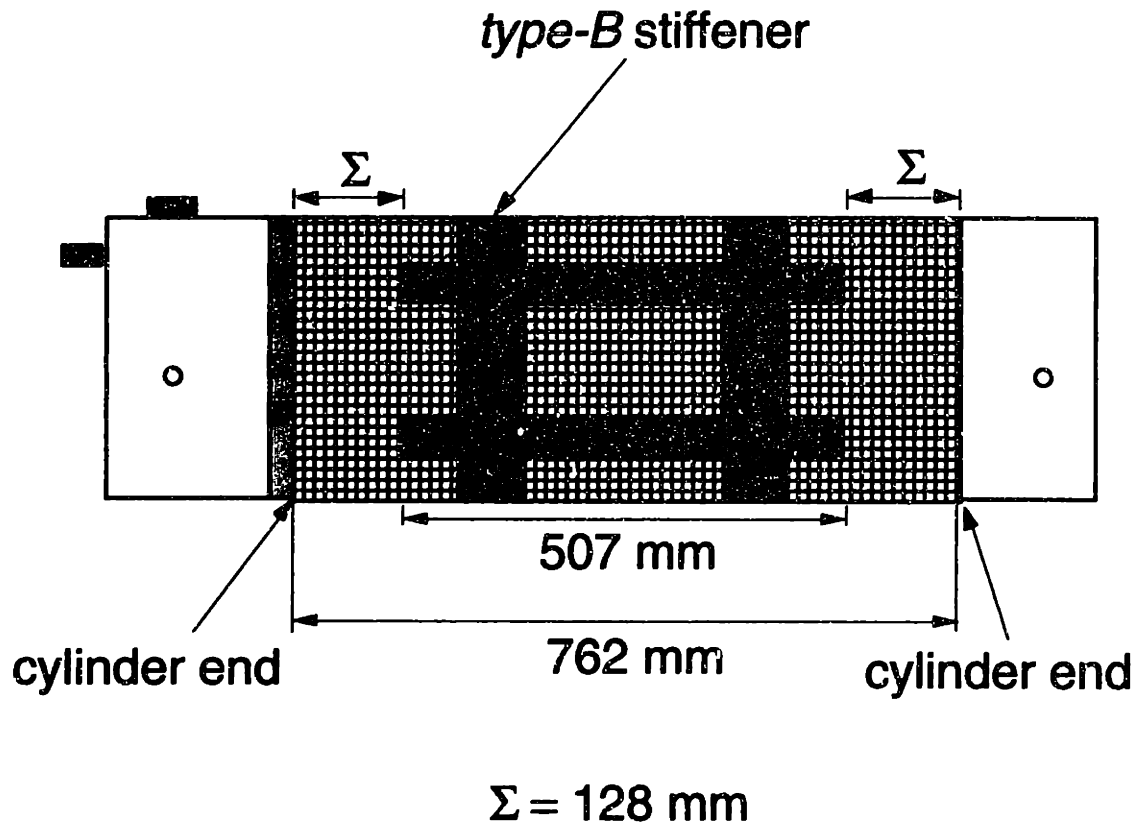
Figure 6.5 Illustration of the alignment and placement of the hoop stiffener on the *type-2* cylinders and *type-3* cylinder with the *type-A* stiffener configuration.

where s is the stiffener spacing which depends on the slit size (see Table 3.4). A wide strip of GNPT, whose sides are straight and parallel, was wrapped tightly around the mandrel so that one of its edges was located at a distance Σ from one of the cylinder ends. The stiffener layers were laid up on the external surface of each cylinder next to this GNPT strip one at a time. Thus, a circumferential stiffener which consisted of four 0° fabric plies was constructed. The same procedure was implemented for the other circumferential stiffener.

The geometry of the *type-3* cylinder is shown in Figure 3.4. Such a cylinder type is stiffened in both the longitudinal and hoop directions. The *type-A* stiffener consists of continuous and broken unidirectional layers in order to avoid overlaps in the regions where the longitudinal and hoop stiffeners meet (see Figure 3.5) and the manufacturing process was thus more involved than for the *type-B* stiffener. The first stiffener layers laid up on the external surface of the cylinder were the continuous stiffeners in the hoop direction, followed by the first layers of the longitudinal stiffeners which were discontinuous. The spacing between the hoop stiffeners was 203 mm for all *type-3* cylinders as discussed in Chapter 3. Thus, using equation (6.1), the distance Σ is approximately 203 mm. The same alignment procedure for the hoop stiffener as the one used in the *type-2* cylinders was used here. Once the first set of hoop stiffeners was laid up, the 90° (longitudinal) direction was determined by using a protractor and another GNPT strip placed in the longitudinal direction. The first longitudinal stiffener layer was laid up next to this longitudinal GNPT strip. Note that there are a total of four longitudinal stiffeners separated from each other by approximately 190 mm. Since the distance between two longitudinal stiffeners is measured in the hoopwise direction, the GNPT hoopwise guide strip, which had been

measured and marked appropriately along its length, was used to establish the hoop direction and this separation distance. The longitudinal direction was established at this location using a protractor and GNPT strip placed in the longitudinal direction. The rest of the longitudinal stiffeners were laid up sequentially and separated by this distance in a similar manner. After all of the longitudinal stiffeners had been laid up, the process was reversed by placing the continuous longitudinal layers and the broken hoop layers at the previously determined locations (i.e. on top of the stiffening bands that had already been laid up on the cylinder). The reversal process was continued until all of the hoop stiffener layers were laid up. Then, four additional continuous layers were added on all four longitudinal stiffeners, resulting in the stiffener configuration that consisted of four 0° layers in the circumferential direction and eight 0° layers in the longitudinal direction.

The stiffener placement of the *type-B* configuration was more straightforward as the longitudinal and hoop stiffeners were constructed in one continuous layer. Two pieces of the *type-B* stiffeners were needed for each cylinder because each piece only covered one-half of the cylinder circumference. Thus, there still exists a discontinuity at the location where the two pieces meet. However, this was not an issue since the longitudinal slit was cut only in the unstiffened region bounded by the continuous *type-B* stiffener pattern. The distance between one of the cylinder ends and the ends of the longitudinal stiffeners is denoted by Σ as depicted in Figure 6.6. This distance was determined using a ruler. The hoopwise orientation was determined using the GNPT strip which was tightly wrapped around the cylinder. The right parts of the first piece of the longitudinal stiffeners in this *type-B* stiffener pattern were aligned such that they were perpendicular to the GNPT strip. The alignment was also checked on the other (left) side



NOTE: Not to Scale

Figure 6.6 Illustration of the alignment and placement of stiffener on the *type-3* cylinder with the *type-B* stiffener configuration.

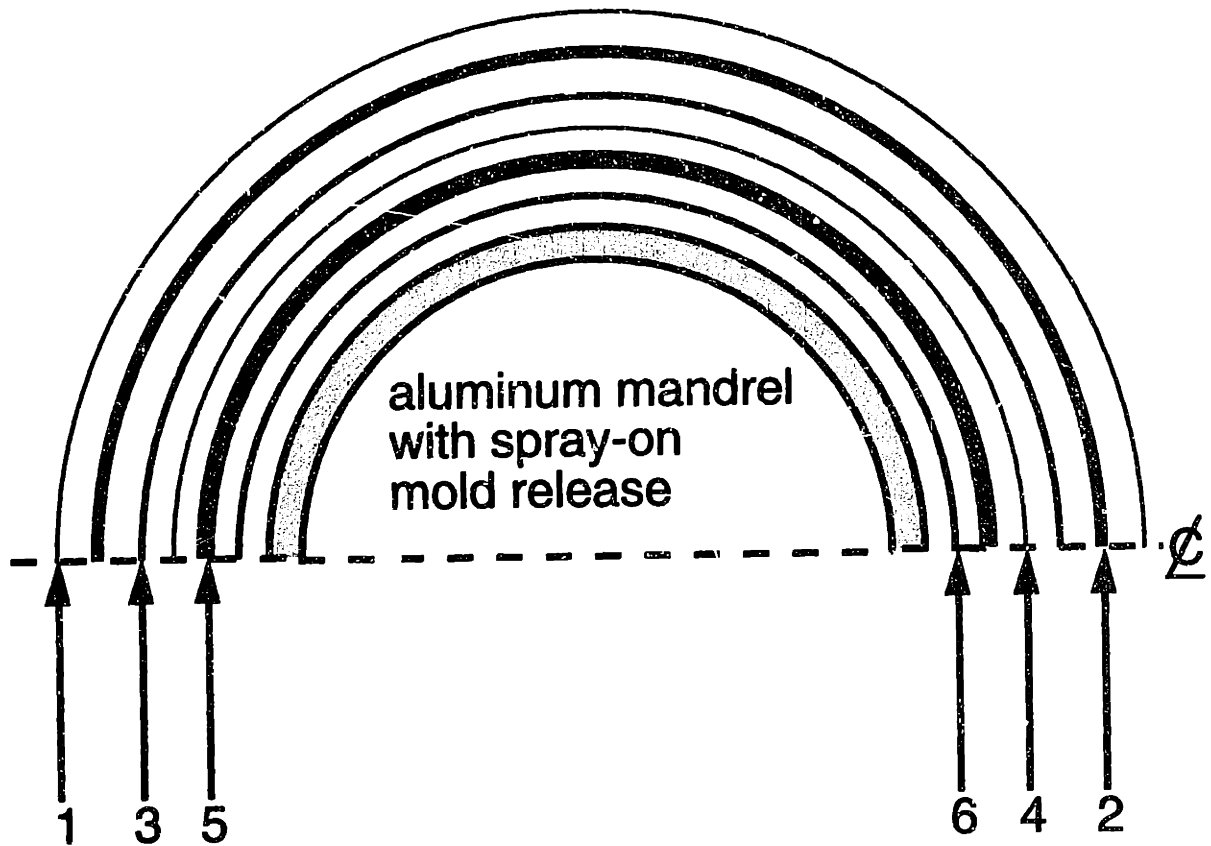
using another GNPT strip. Care was taken that this stiffener was aligned properly. Additional layers were laid up one at a time on top of the stiffening bands that had already been laid up on the cylinder using these as a guide. The same procedure was followed in the alignment and layup of the second piece of the type-B stiffener which was placed adjacent to the first piece.

After all of the stiffener layers were in place, additional 76 mm wide hoop stiffener layers were placed adjacent to the ends of the axial layers approximately 51 mm from the cylinder ends. Preliminary experiments showed that in the presence of axial stiffening bands, there was a tendency for the cylinder cross-section to be distorted after the cure was completed. A distorted cross-section could cause difficulties in placing the cylinder on its endcaps and was avoided by using these additional stiffener layers near the cylinder ends.

The layup process was completed after all of the plies and stiffener layers were in place. The cylinder was then covered with a layer of peel-ply and a sheet of porous teflon. A continuous sheet of bleeder paper was then wrapped around the cylinder to soak up the excess epoxy as a result of the consolidation process during cure. As a "rule of thumb", the bleeder paper should be wrapped at least n times where n is the number of plies in the cylinder. Due to the presence of stiffening bands, more bleeder material was thus needed in the *type-2* and *type-3* cylinders than in the *type-1* cylinders. This sheet was wrapped around the cylinder four times for the *type-1* cylinder, six times for the *type-2* cylinder, and eight times for the *type-3* cylinder. All of the cure materials (peel-ply, porous teflon, and bleeder paper) were wrapped tightly in order to reduce the amount of wrinkles on the cylinder surface after cure. All of the overlaps in those curing materials occurred on the back of the cylinder. A continuous strip of 152 mm wide

fiberglass airbreather was wrapped around the mandrel approximately six times starting at the vacuum port and ending approximately 50 mm from the end of the graphite/epoxy cylinder. This airbreather allowed air and volatiles released during the cure to be removed from the graphite/epoxy. The final step in the cylinder cure assembly was to attach the vacuum bag using vacuum tape. Extreme care was taken to have a tight and wrinkle-free bag. The seam was located on the BACK of the cylinder near the vacuum port. This cylinder curing assembly is shown in Figure 6.7.

The cure cycle for all cylinders is shown in Figure 6.8. Before a cure is started, the vacuum bag test is performed to ensure that there are no leaks in the bag. A full vacuum of 760 mm Hg is pulled and then the vacuum pump shutoff for approximately five minutes. If the gage reading falls by more than 75 mm Hg during this period, the bag is checked meticulously for any holes or damage. Such holes or damage are then repaired using pieces of vacuum tape. The vacuum test is repeated until the bag performance is satisfactory. The cylinder is then put inside the autoclave, the door closed, and the pressure safety lock activated. Full vacuum and 0.59 MPa (85 psi) of external pressure are applied and maintained throughout the entire cure. After the pressure has reached this specified value, the heater is turned on and the temperature is increased to 116°C at a rate of 3°C per minute. The temperature is maintained at 116°C for one hour. After an hour passes, the temperature is ramped up to 177°C at the same rate and maintained at that temperature for about two hours. The cooling process at the same rate (3°C/minute) is started after the two hours has passed. Once the temperature reaches 66° C, the autoclave pressure and vacuum are relieved and the cylinder is removed from the autoclave and cooled to room temperature. All of the external cure materials including vacuum bag,



- 1 = Vacuum Bag
- 2 = Bleeder Paper
- 3 = Porous Teflon
- 4 = Peel-Ply
- 5 = Graphite/Epoxy Prepreg
- 6 = Guaranteed Non-Porous Teflon (GNPT)

Figure 6.7 Curing assembly for graphite/epoxy cylinder.

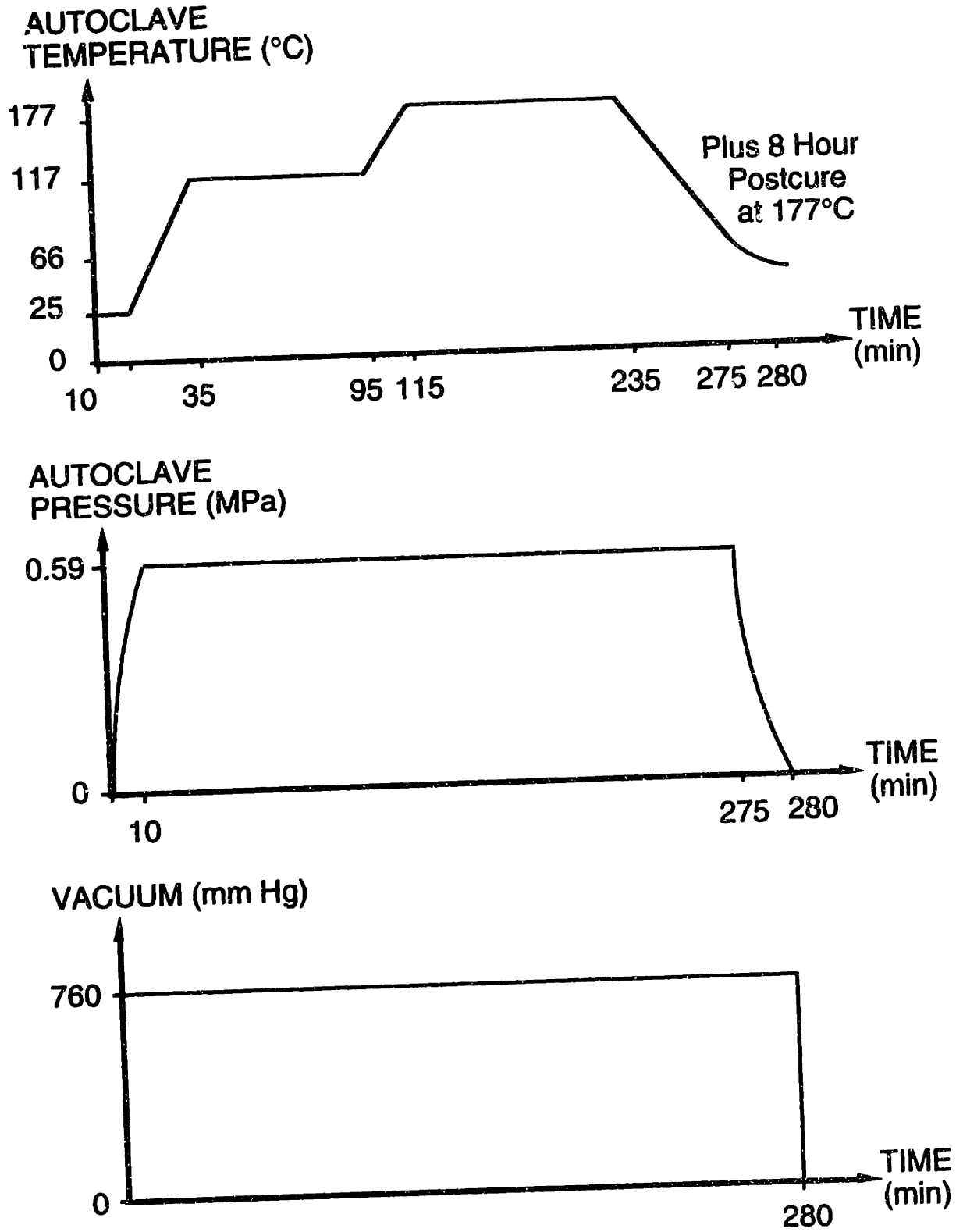


Figure 6.8 Standard cure cycle for the AW370-5H/3501-6 graphite/epoxy cylinders.

bleeder paper, porous teflon, peel-ply, and fiberglass air breather are removed with a metal spatula as they are usually hardened by the excess epoxy. The cylinder is loosened by banging "END 2" of the mandrel on the floor several times and then removed from the mandrel by sliding it off on "END 2". The cylinder is then postcured at 177°C in an oven for eight hours.

Since the ends of the cylinders were typically not smooth, trimming and leveling of the cylinder ends were necessary. To determine the cutting line which was oriented in the circumferential direction, a wide strip of GNPT with straight and parallel edges was wrapped tightly around the circumference of the cylinder and the ends aligned. This line was marked using a white paint pen. A DREMEL™ rotary cutting tool with a 25.4 mm diameter blade with a thickness of 0.64 mm was used to trim the edges of the cylinder ends. During the cutting process, the cutting-tool was held carefully to minimize the need for further filing. After the cutting was completed, the levelness of the cylinder was checked by placing it on a flat surface with the aid of a master square. Filing using a steel file was done cautiously and sparingly, if necessary, to prevent damage to the cylinder ends. Due to this trimming process, the cylinder length decreased slightly (by less than 25 mm).

In order to help identify the damage propagation (fracture) path after the test, square grids of 51 mm by 51 mm were drawn on the surface of the cylinder with a white paint pen. Each square is labeled with a letter and a number. To show this labeling clearly, imagine that the cylinder is cut at an angular hoop location 180° from the slit and then rolled "flat". Using this representation, the labeling process is depicted in Figure 6.9. Columns in the longitudinal direction of the cylinder were designated with the same letter and rows in the circumferential direction were designated with the same

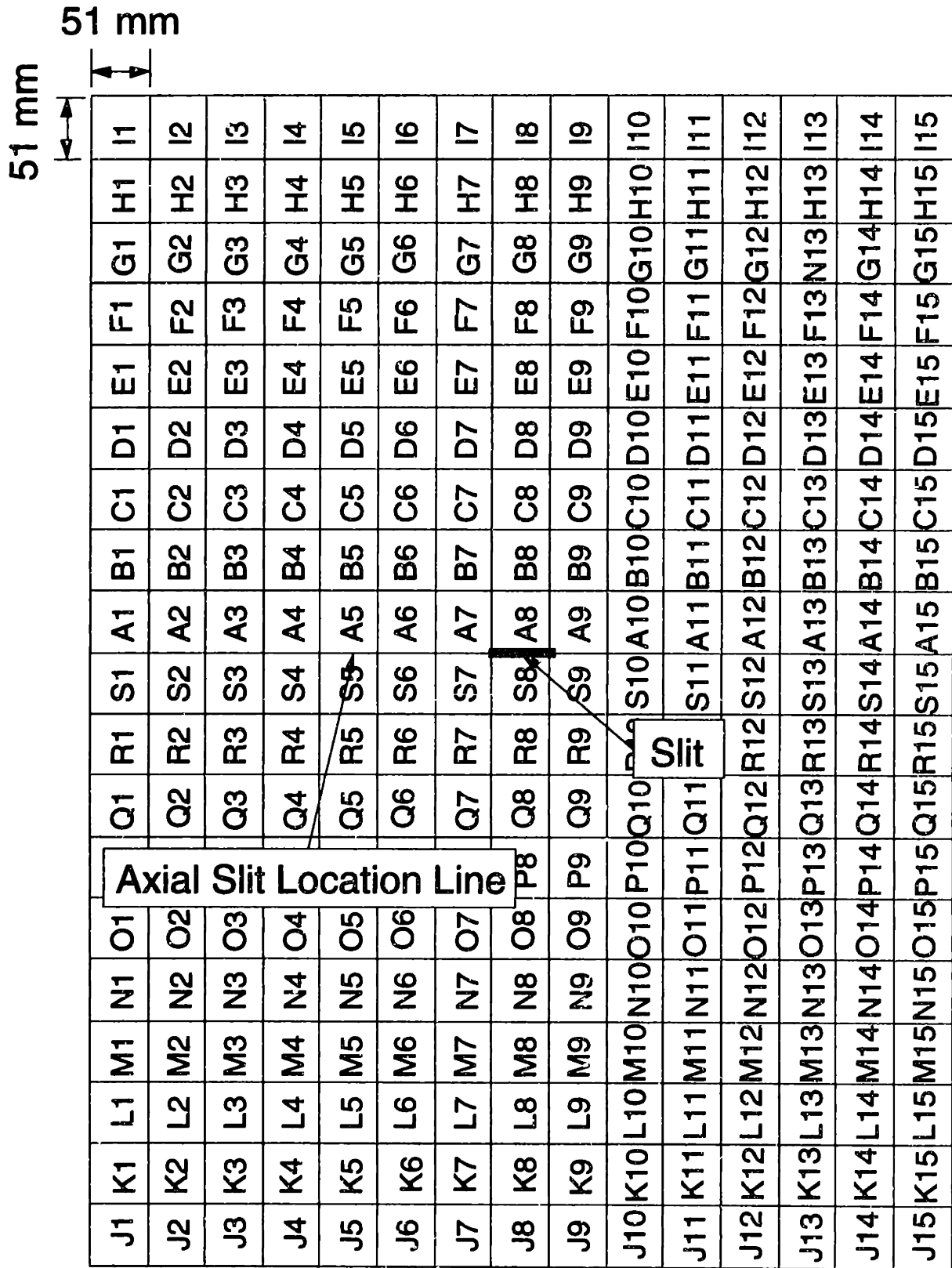


Figure 6.9 Grid on a cylinder for fracture path identification.

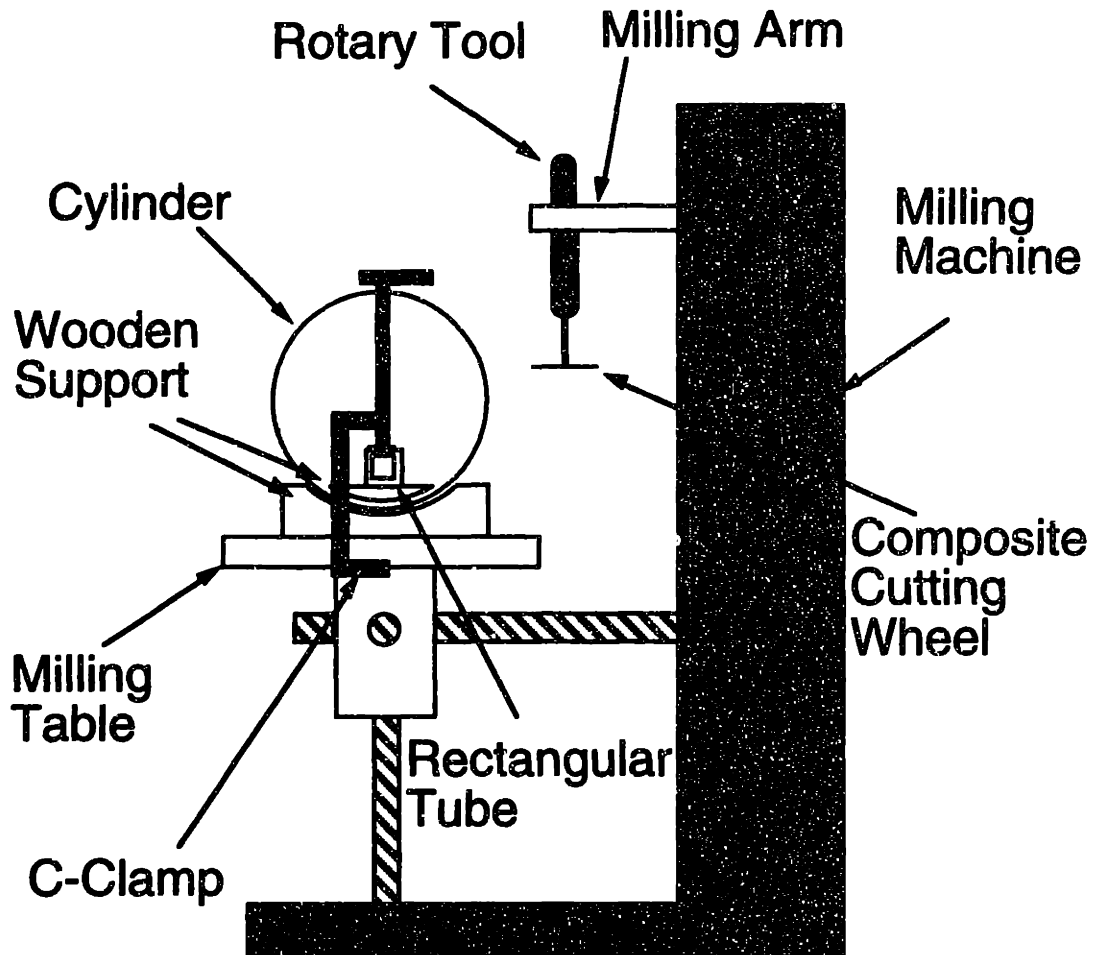
number. The square labeled 'A1' is located at END 1 of the cylinder immediately to the right of the slit location. Numbers increase towards END 2 of the cylinder and letters increase in the counter-clockwise direction when END 1 of the cylinder is up.

Thirty thickness measurements (fifteen measurements along END 1 and fifteen measurements along END 2) were made in the circumferential direction for each cylinder inside the square grid shown in Figure 6.8. Each measurement was made approximately 51 mm from the ends of the cylinder using a micrometer. The average base (unstiffened) thicknesses were 1.36 mm, 1.40 mm, and 1.41 mm with coefficient of variations of 5.3%, 4.0%, and 5.1% for the *type-1*, *type-2*, and *type-3* cylinders, respectively. The nominal thickness of the base cylinder is 1.40 mm. The numerical work performed in the present work was based on the nominal thickness value of 1.40 mm.

6.2 Slit Construction

The longitudinal slit location was on the front of the cylinder (see Figure 6.2). To determine its exact location and orientation, a wide GNPT strip with straight and parallel edges was wrapped tightly around the cylinder in order to establish the circumferential direction. The longitudinal direction was determined by aligning another GNPT strip with straight edges perpendicular to the first strip. Using a metallic ruler, the slit is scribed on the cylinder surface. Pieces of masking tape are placed approximately 1 mm inside of the ends of the marked slit locations to guide the slit cutting process.

Longitudinal slits of lengths between 51 mm and 104 mm were cut into the cylinders using the milling machine set-up depicted in Figure 6.10. The ends of the cylinder are secured in complementary convex and concave



NOTE: Not to Scale

Figure 6.10 Illustration of cylinder slit-cutting setup.

wooden holders on the milling machine table. These holders provide support for the cylinders and prevent cylinder movement during the clamping process which holds the cylinder to the table. The longitudinal slit is located at a hoop angular location approximately 90° from the lowest point of the cylinder on the table. A master square is used to make sure that the distance between the edge of the table and the cylinder is constant along the cylinder length. A rectangular tube with hollow, square cross-section (32 mm by 32 mm by 3.2 mm) with a length of 1.1 m is placed through the center of the cylinder and allowed to rest on the wooden holders. C-clamps are used to clamp the rectangular tube, and thus the cylinder, to the table. The alignment is checked after the clamping process.

A DREMEL™ rotary tool with a 25.4 mm diameter cutting blade with thickness of 0.64 mm spinning at 30,000 rpm is used to cut the slit. The DREMEL™ tool is attached vertically to the milling machine arm after the arm is set perpendicular to the table using a master square. The table is adjusted so that the cutting wheel is in the proper location (i.e. at the same level as the scribed slit). As a final check, the table is moved sideways back and forth to ensure that the blade stays over the scribed line. After all of these preliminary checks are performed, the slit cutting is started at the center of the slit by moving the head of the machine with the attached cutting tool into the cylinder. After the cutting wheel has penetrated the cylinder, the table is moved sideways in both directions to cut the body of the slits. After the cutting is completed, the wheel is withdrawn completely from the cylinder before the DREMEL™ is shut off. This procedure was used to cut the longitudinal slit in part of the *type-1* cylinders (with the 51 mm slit only) and all of the *type-2* and *type-3* cylinders. Since each of the *type-1* cylinders was tested three times with three different slit sizes, a slightly different slit

cutting procedure was implemented in the *type-1* cylinders with 78 mm and 104 mm slit sizes. This was due to the presence of endcaps after the first round of tests with a 51 mm slit was completed.

The presence of endcaps in the *type-1* cylinders after the first test is completed prevented the clamping of the cylinder to secure it to the table. The "new" slit is measured and marked using the same procedure as before. To provide additional friction between the endcaps and the milling machine table and, thus, to prevent the movement of the cylinder during the cutting process, several layers of bleeder paper are placed under the endcaps. The cylinder is secured by hands during the cutting process. The slit cutting is started at the tip of the previous slit by moving the head of the machine with the attached cutting tool into the cylinder. The table is moved sideways in both directions to cut the body of the slits. After the cutting is completed, the wheel is withdrawn completely from the cylinder before the DREMELTM is shut off.

The slits were finished and the slit tips sharpened using jeweler's saws that are sharpened on a grinder. These saws are initially 0.5 mm thick. One pass of the saw across a grinder is made on each side to decrease its thickness. An additional pass is made on each side, with the saw held at an angle, to sharpen the teeth to a point. The post-grinding thicknesses of the saw were not measured. The slit length was measured with the aid of a ruler and a magnifying glass and was within 0.1 mm of the nominal value for all cylinders tested.

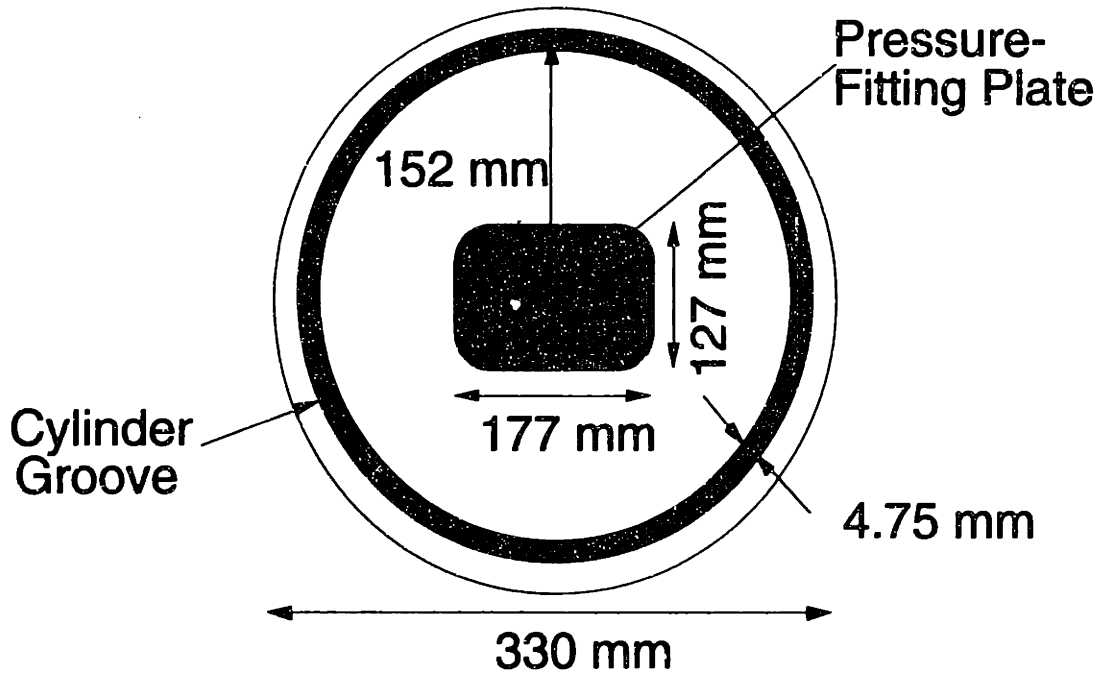
6.3 Specimen Sealing Procedure

All of the cylinders were pressurized to induce a biaxial loading state and, thus, needed to be sealed at both ends. Aluminum endcaps used in this function are depicted in Figure 6.11. Each endcap is 25.4 mm thick and 330 mm in diameter. The ends of the cylinder fit into 13 mm deep and 4.75 mm wide circular grooves located in each endcap. The inside edge of the grooves is located at a radius of 152 mm from the center of the endcap. A pressure fitting is attached to one endcap to allow pressurizing gas to enter.

Before the endcaps from previous tests can be used, they must first be cleaned by heating them in an oven at 260°C for approximately four hours to char the bonding epoxy. This cleaning procedure is very laborious. Hammers, scribes, and spatulas are used to chip the hardened epoxy out of the grooves. The endcaps are returned to the oven occasionally when the surface temperature is cool. Vice grips are used to remove the cylinder remnants from the groove. At the final stage of the cleaning process, scribes, cotton swabs, and methanol are used to clean as much of the cured epoxy as possible from the endcaps.

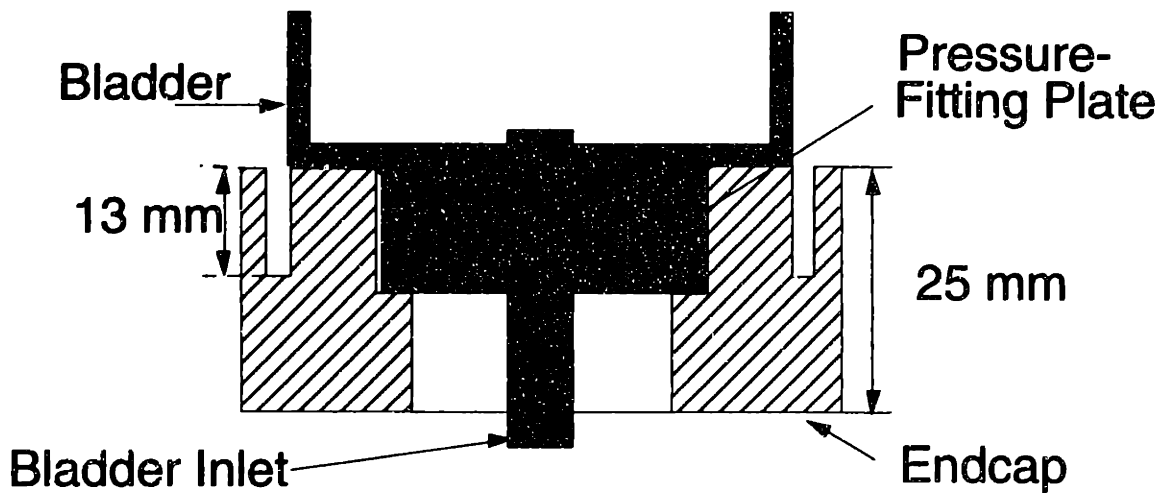
The cylinders are potted into the endcaps sequentially. The endcap, especially the groove where the cylinder ends are inserted, is thoroughly cleaned using methanol to remove any dirt or grit that can interfere with the bonding process. The inside edge of the cylinder is lightly sanded with a 220 grit sandpaper to roughen the surface and, thus, allow the epoxy to adhere. The inside and outside ends of the cylinder are cleaned with cheesecloth to remove any residual dust that remains on the surface. The adhesive used to bond the cylinder to the endcaps is the Skotch-Weld Type 2216 B/A Gray Epoxy manufactured by 3M™. The adhesive is mixed in a plastic container in a ratio of 115 grams of resin to 75 grams of hardener. A tongue depressor

Top View



NOTE: Pressure-Fitting Plate in One Endcap Only

Cross-Sectional View



NOTE: Not to Scale

Figure 6.11 Illustrations of aluminum cylinder endcaps.

is used to stir the mixture well until the color is a uniform gray. The endcap with the hole is bonded to the cylinder first to provide access to the inside of the cylinder during the second bonding process. Before the adhesive is poured into the endcap, the endcap is heated to 80°C for approximately 20 minutes. The adhesive is poured slowly, using the tongue depressor, into the endcap while the endcap is still warm so that the viscosity of the epoxy is lowered and air bubbles can be removed more easily using toothpicks. A layer of epoxy is painted on the inside and outside edges of the cylinder approximately 25 mm from the cylinder ends. The cylinder is then pushed down into the groove on the endcap and toothpicks are used to center the cylinder in the groove. Using tongue depressors, fillets are made at the endcap/cylinder junction on both the inside and outside of the cylinder. After the toothpicks are removed, the cylinder and endcap are heated without pressure in the autoclave for one hour at 90°C. The same procedure is repeated for the other endcap. A photograph of a cylinder with both endcaps bonded is shown in Figure 6.12.

In order to contain the nitrogen gas used to pressurize the cylinders, rubber bladders constructed from 0.8 mm (1/32 inch) thick gum rubber were manufactured. The gum rubber was manufactured by the standard TELAC bladder manufacturing process described in more detail in an internal TELAC document [78]. To construct the bladder, three major pieces, a rectangle, two circular endpieces, and a rectangular reinforcement as shown in Figure 6.13, are cut from the 915 mm wide roll of gum rubber. The dimensions of the rectangular piece are 1041 mm by 800 mm. Each circular endpiece has a diameter of 458 mm and has triangles with a base of approximately 25 mm and a height of 51 mm cut from it to form 16 teeth (with the form of isosceles trapezoids). All pieces were first cleaned

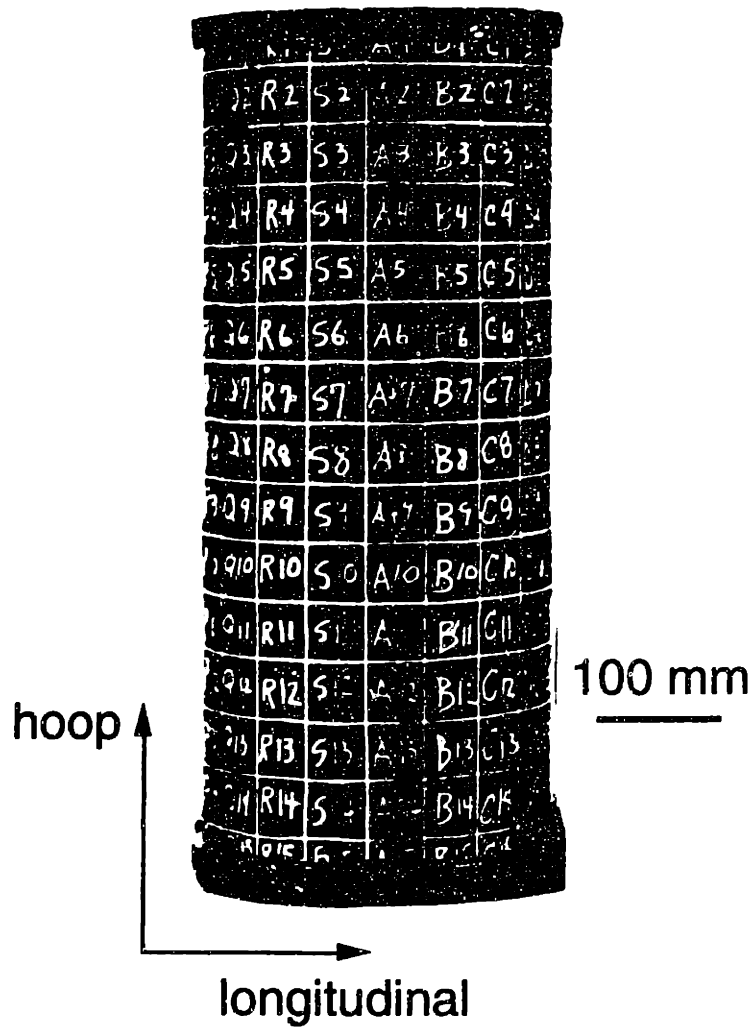


Figure 6.12 Photograph of a cylinder with its endcaps bonded ready for testing.

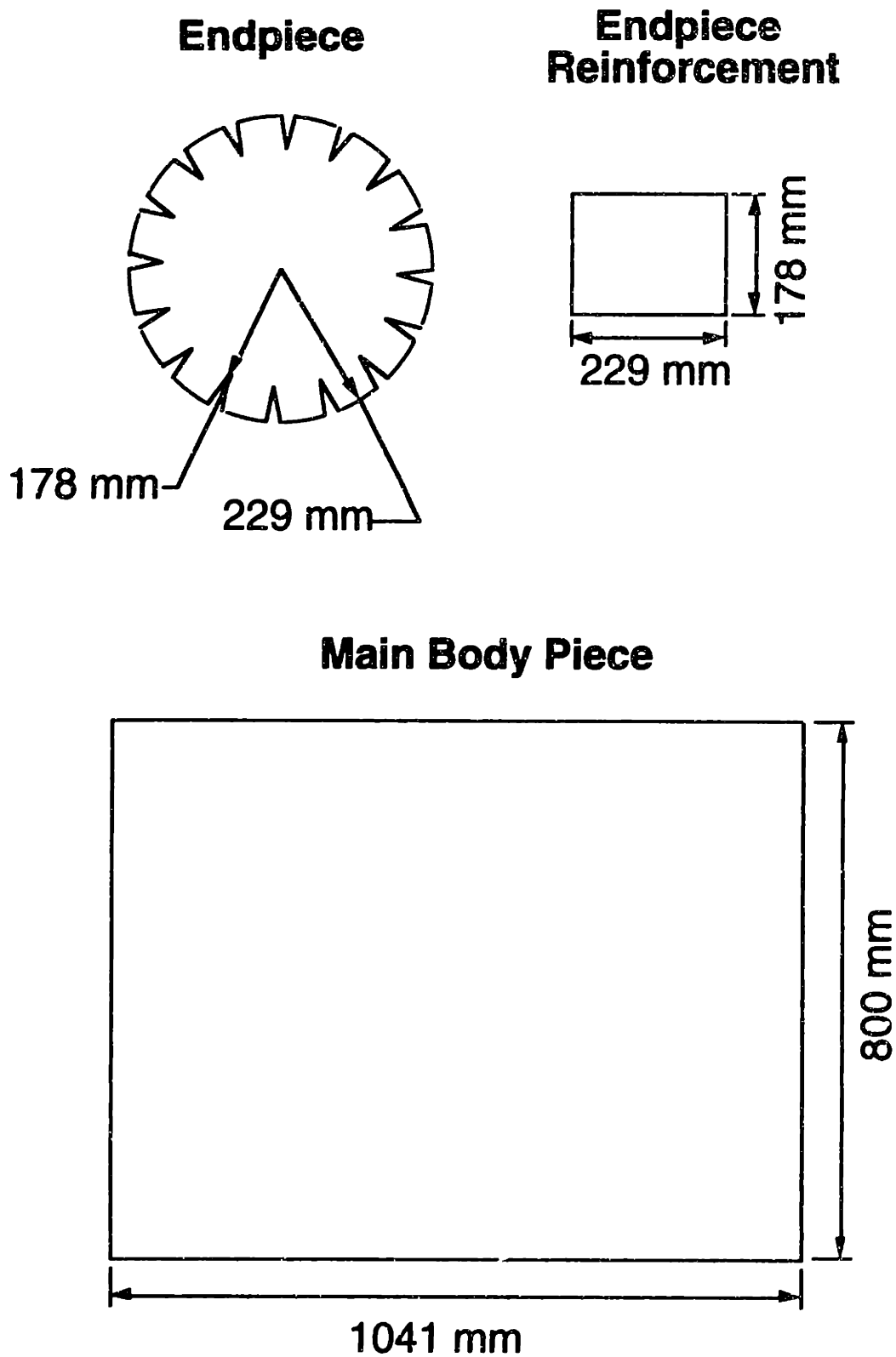


Figure 6.13 Illustrations of rubber pieces for cylinder bladder.

thoroughly using methanol to remove dirt and powder from the rubber surface. Two strips of 13 mm wide vacuum tape, #213-3 made by General Sealants, are placed side by side as close to the end as possible on one of the shorter edges of the rectangular piece. The other shorter edge of the rectangular piece is lapped over the tape by 25.4 mm to form a 1016 mm circumference rubber tube. Two more strips of vacuum tape are placed side-by-side around the outer circumference at both ends of the tube. Care is taken that the first strip of the vacuum tape is located as close as possible to the end. The teeth in the circular endpieces are then connected, one at a time, to the junctions where the two strips of vacuum tape are joined in an alternating fashion. A 25 mm (1 inch) diameter hole is cut in the endpiece that is to be connected to the pressure-fitting aluminum plate. A rectangular rubber piece of dimensions 229 mm by 178 mm is bonded to the aluminum plate using the Neoprene Bonding Cement made by the Greene Rubber Company. This step is taken to ensure that possibility of leaks caused by imperfection due to direct bonding between the aluminum plate and rubber endpiece is minimized as the bladder will now be bonded to this rubber piece. All of the exposed seams in the rubber cylinder are painted with the same bonding agent to prevent leaks.

After the bladder construction had been completed, each bladder was tested by fully inflating it with compressed air. Snoop Liquid Detector™, which generates bubbles when a leak is found, is used to check for possible holes, slits, and incomplete bonding on the bladder. Small pieces of vacuum tape are used to seal the leaks. It is also worth noting that the rubber bladder is constructed slightly larger than the composite cylinder. The bladder rests against the inner surface of the composite cylinder when it is fully inflated during testing and carries no load. Therefore, premature

bladder failure is prevented using this design. Due to their poor load-carrying capabilities, the bladders do not measurably increase the strength of a cylinder under pressure loading. A small rectangular rubber piece was taped using pieces of masking tape of 25 mm (1 inch) in width on its circumference on the inner surface of the cylinder at the slit region to prevent part of the bladder from bulging through the slit. The width of the rubber piece is 76 mm and its length is slightly larger than the slit size (approximately 50 mm larger).

6.4 Instrumentation

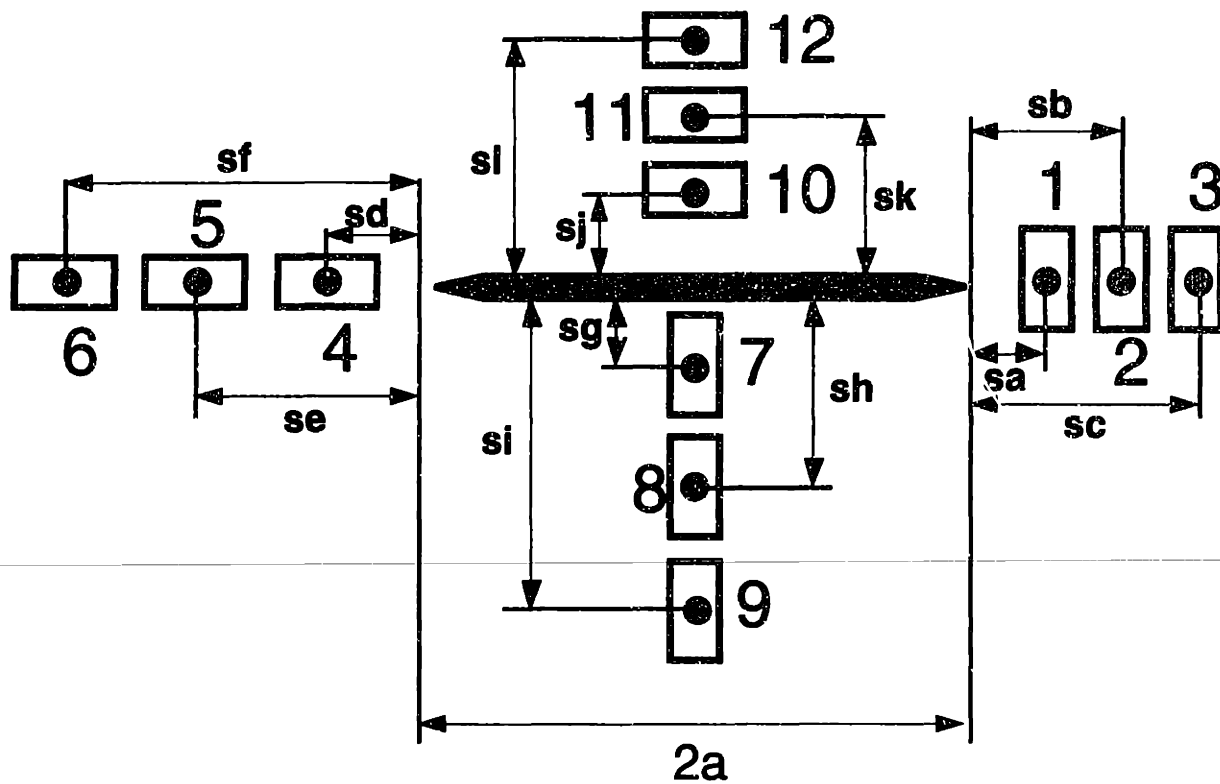
Two types of instrumentation, strain gages and a pressure transducer, were utilized in the present experimental work. The pressure transducer was used to monitor the pressure and thus the pressurization rate, obtain the response during the test, and determine the failure pressure. A pressure transducer made by DyniscoTM (PT 119H-7.5 C) that can measure pressure up to 5.2 MPa (750 psi) was used in the present work. Only the *type-1* (unstiffened) and *type-2* (circumferentially-stiffened) cylinders were instrumented with strain gages in order to provide the data for comparison with the results of the numerical analyses. The *type-3* cylinders with stiffener in both the longitudinal and hoop directions were tested only to study the fracture paths induced by different stiffener configurations. All of the strain gages utilized in the present experimental work were manufactured by the MicromasurementTM Company. The strain gage type used is the EA-06-125AD-120. The length of the active gage element is 3.5 mm and the width is 3.0 mm.

The gage placements were guided by the results from numerical analyses discussed in Chapter 5. For the *type-1* cylinder, two regions were identified as the "regions of interest": one, regions near the slit tips and, two, regions near the middle of the slit. A total of 12 strain gages were bonded in the regions of interest as depicted in Figure 6.14. Six of those gages were bonded near the slit tips (three gages to measure hoopwise strain and three gages to measure strain along the longitudinal direction). The other six gages were placed in the midslit region (three hoop gages and three longitudinal gages). For the *type-2* cylinders, five strain gages (three gages for hoopwise strain and two gages to measure strain along the longitudinal direction) were bonded in the ligament region (i.e. the region between the slit tip and the hoop stiffeners) as illustrated in Figure 6.15. Photographs of the slit region in the *type-1* and *type-2* cylinders are shown in Figures 6.16 and 6.17. The exact locations of the gages, noted as the center of the gages, were measured using a ruler and an eye-piece magnifier and are shown in Tables 6.1 to 6.4.

Standard methodology is followed to apply gages. Gages were applied after the two endcaps had been bonded since the heat applied during the bonding of the endcaps could damage the gages.

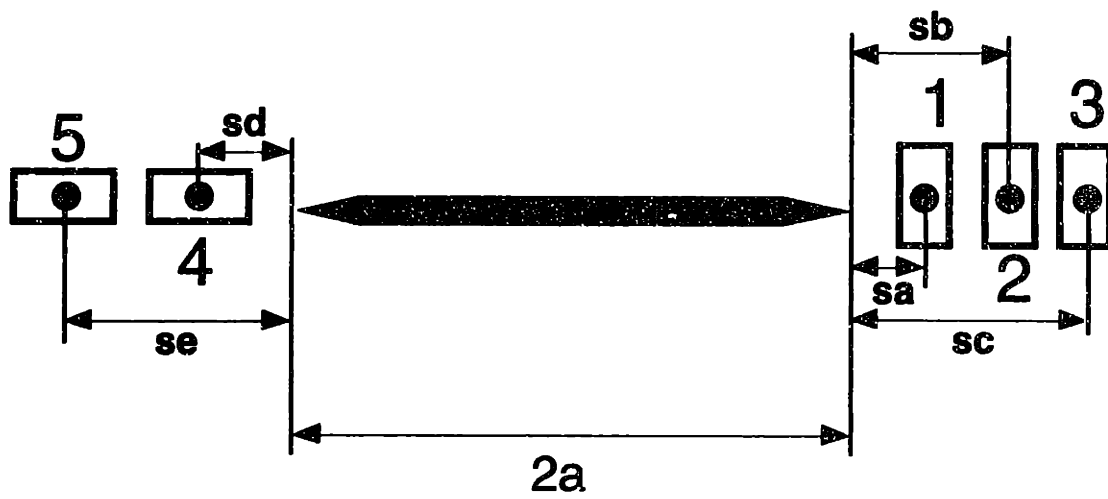
6.5 Testing

All testing was performed in a blast chamber at TELAC. The rubber bladder, complete with the pressure fitting plate, is inserted inside the cylinder. The pressure fitting plate is placed securely on the cutout of one endcap as illustrated in Figure 6.11. The cylinder endcaps rest on an I-beam on the blast chamber floor as illustrated in Figure 6.18. The cylinder is



$2a = 51 \text{ mm}, 78 \text{ mm}, \text{ and } 104 \text{ mm}$

Figure 6.14 Schematic of the strain gage locations in the *type-1* (unstiffened) cylinders.



$2a = 51 \text{ mm}, 78 \text{ mm}, \text{ and } 104 \text{ mm}$

Figure 6.15 Schematic of the strain gage locations in the *type-2* cylinders (circumferentially stiffened).

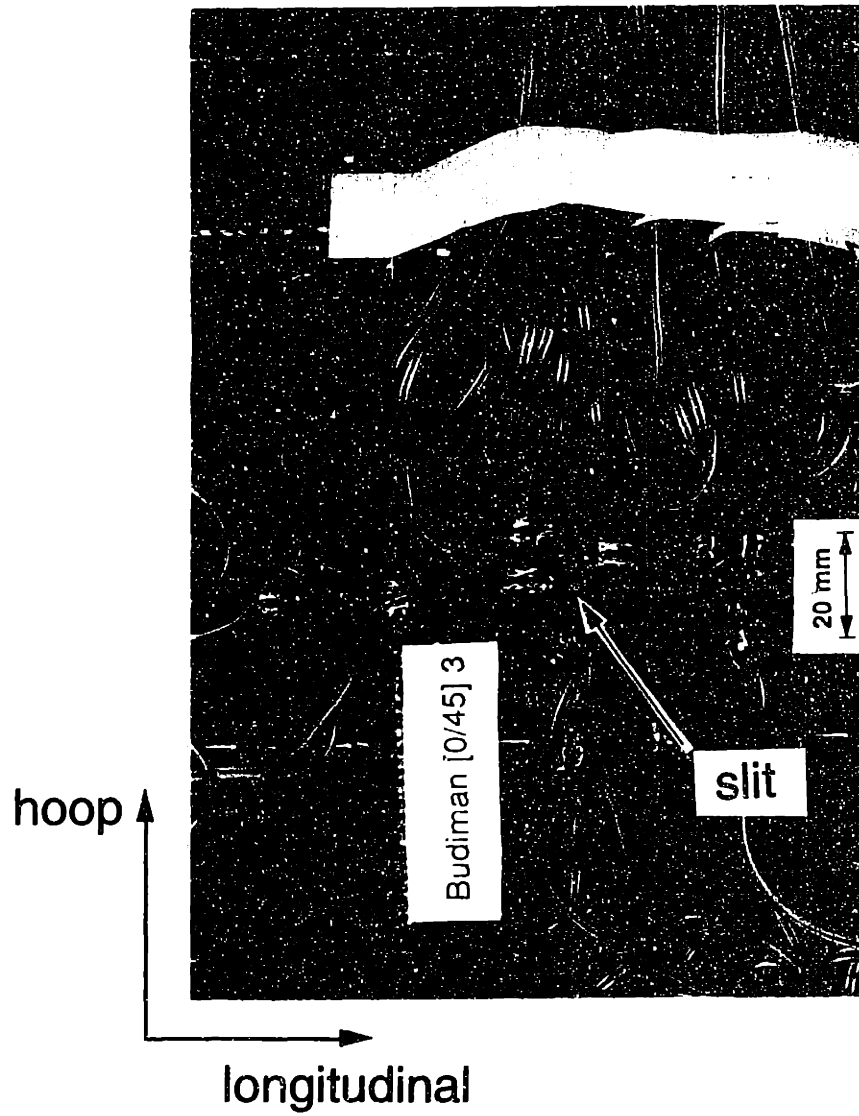


Figure 6.16 Photograph of the gage region in a *type-1* cylinder.

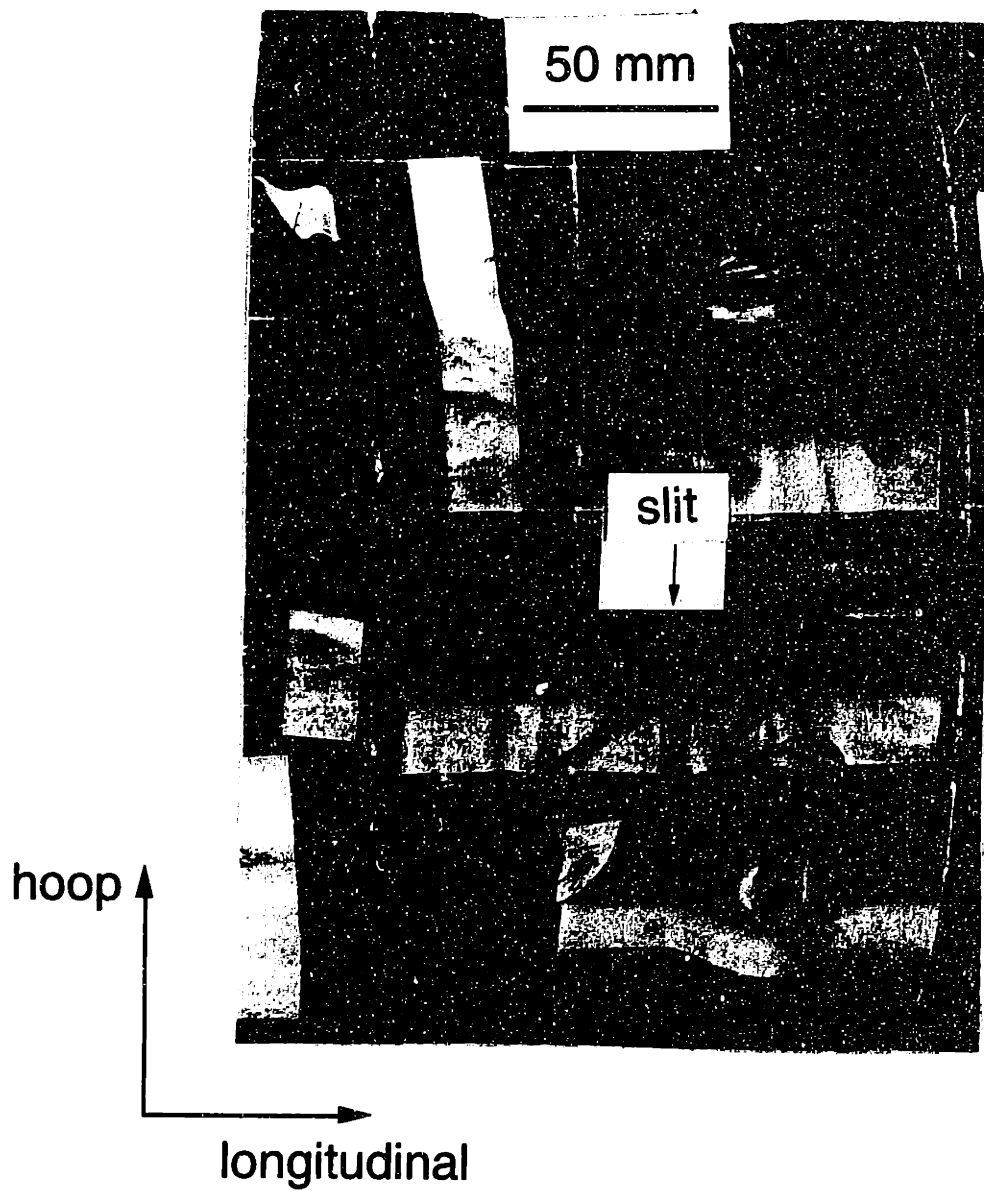


Figure 6.17 Photograph of the gage region in a *type-2* cylinder.

Table 6.1 Strain Gage Locations for the *Type-1* (0/45)_o Cylinder

Parameter	Slit size (2a)		
	51 mm	78 mm	104 mm
sa	28.0	41.5	54.5
sb	33.0	45.5	59.0
sc	37.0	50.0	63.8
sd	28.3	41.8	54.8
se	37.8	53.3	67.3
sf	48.8	64.8	78.3
sg	3.2	3.2	3.2
sh	14.2	14.2	14.2
si	25.2	25.2	25.2
sj	2.9	2.9	2.9
sk	7.9	7.9	7.9
sl	12.4	12.4	12.4

Table 6.2 Strain Gage Locations for the *Type-1* (45/0), Cylinder

Parameter	Slit size (2a)		
	51 mm	78 mm	104 mm
sa	28.0	41.5	54.5
sb	32.5	46.0	59.0
sc	37.0	50.0	63.0
sd	28.3	41.8	54.8
se	38.3	52.8	64.8
sf	48.8	63.3	75.3
sg	3.2	3.2	3.2
sh	13.7	13.7	13.7
si	24.7	24.7	24.7
sj	2.9	2.9	2.9
sk	6.9	6.9	6.9
sl	10.9	10.9	10.9

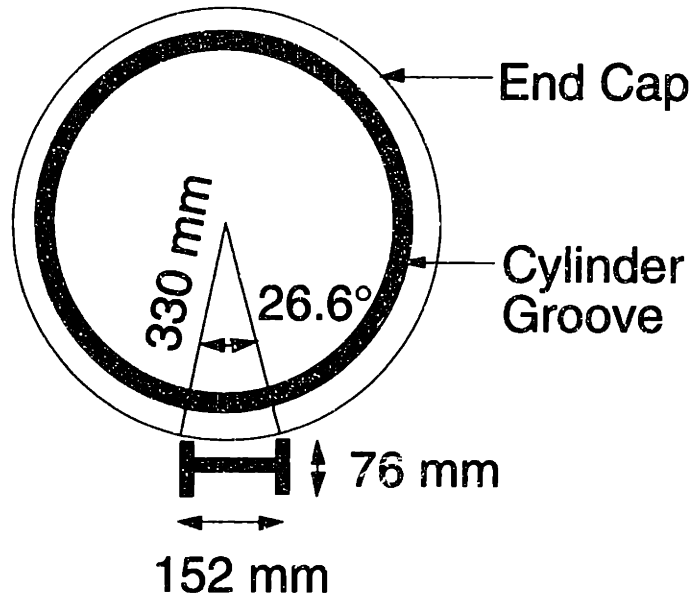
Table 6.3 Strain Gage Locations for the *Type-2 (0/45)*, Cylinder

Parameter	Slit size (2a)		
	51 mm	78 mm	104 mm
sa	27.8	41.0	54.3
sb	32.8	45.5	58.5
sc	38.3	50.5	64.0
sd	28.0	41.8	54.5
se	38.5	52.3	67.3

Table 6.4 Strain Gage Locations for the *Type-2 (45/0)*, Cylinder

Parameter	Slit size (2a)		
	51 mm	78 mm	104 mm
sa	27.8	41.0	54.3
sb	32.3	45.5	59.0
sc	36.5	50.5	64.0
sd	28.3	41.8	54.5
se	38.8	52.3	67.3

Front View



Side View

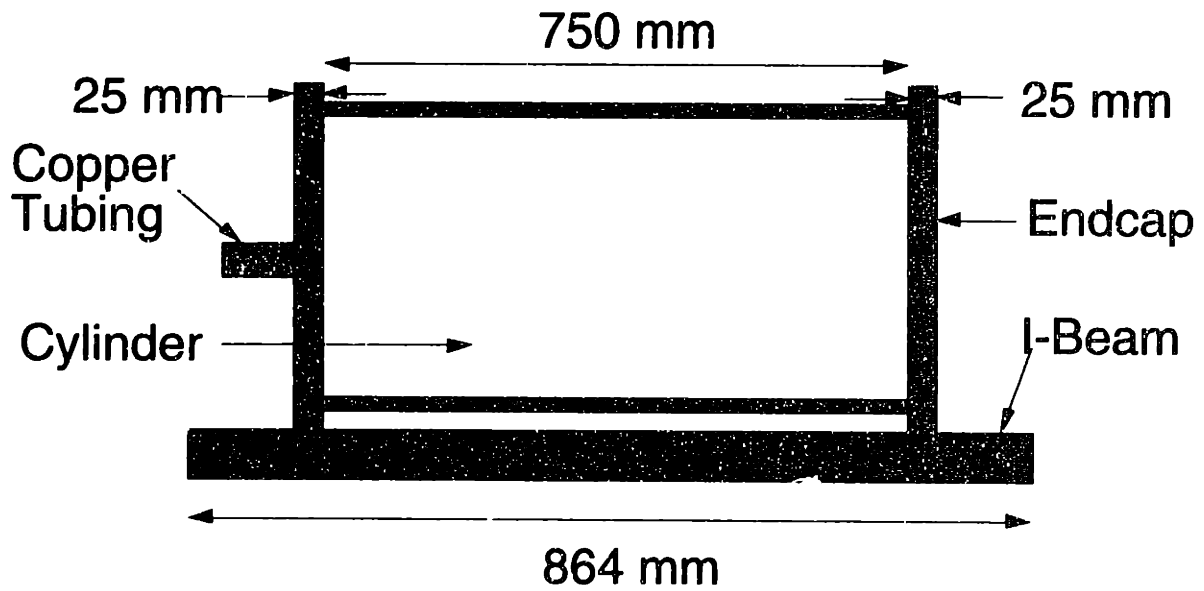


Figure 6.18 Test setup of a cylinder inside the blast chamber.

oriented slit-up so that the majority of its fracture path is not constrained by the I-beam support. Two to three layers of sandbags surround the cylinder on all sides to absorb the shock that might occur during final rupture of the cylinder, protect the instrumentation inside the chamber, and contain the endcaps. Care was taken that the sandbags did not make any contact with the test specimen. A schematic of the test setup is shown in Figure 6.19.

Cylinder pressurization was accomplished using nitrogen gas provided by a bottle located outside the blast chamber. Nine and a half meters of copper tubing and flexible hoses were used to feed the nitrogen through a port hole in the side of the blast chamber to the instrumentation box that contained the pressure transducer, the attachment points for strain gages, and other instrumentation to send the pressure data to an X-Y plotter and a computerized data acquisition system outside the chamber. An additional two meters of 6.5 mm inside-diameter copper tubing was used to feed the nitrogen to the cylinder.

The pressurization was done manually at an approximate rate of 0.40 MPa/minute (1 psi/second). The pressurization rate was monitored via a dial gage and a chart recording of the pressure transducer output. Strain and pressure data were collected at 0.5 second intervals by a Macintosh IIx computer equipped with the Labview™ data acquisition program. The *type-2* and *type-3* cylinders were pressurized to failure. Each of the *type-1* cylinders was tested in three phases, each phase with a different slit length. In the first two phases where the slit lengths were 51 mm and 78 mm, the cylinder was pressurized to approximately 60% of its predicted failure pressure as determined from equation (2.9).

Due to the limitation in the data acquisition hardware, only data from six channels could be taken at once. Thus, each phase of *type-1* cylinder

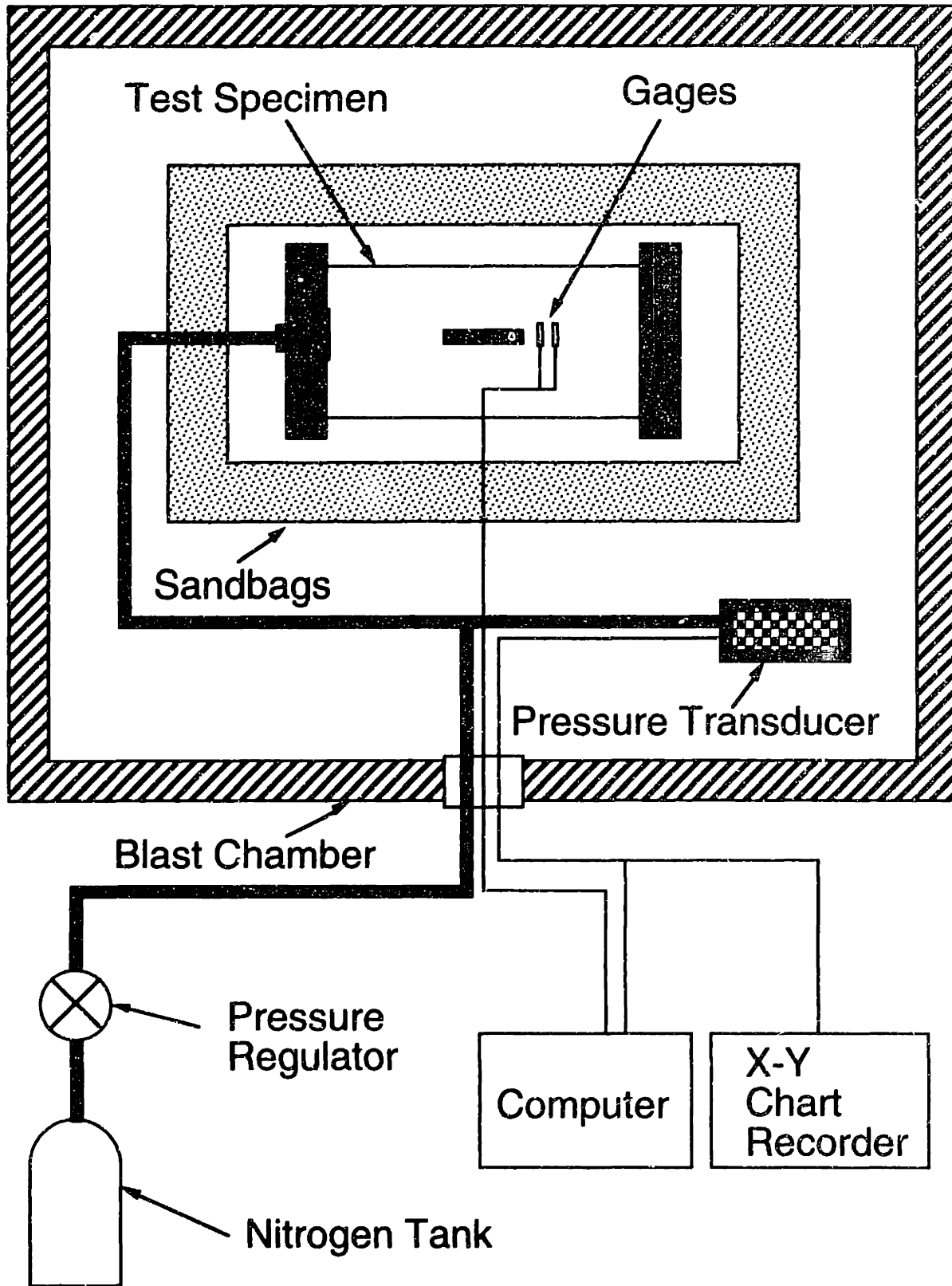


Figure 6.19 Schematic of the blast chamber setup for cylinder testing.

testing consisted of two separate pressurization tests. The first pressurization test was used to obtain the responses of gages 1 through 6 which are located near the slit tips. The second test was used to obtain the responses of gages 7 through 12, which are located in the midslit region. In the third phase of testing, where the slit length is equal to 104 mm, the order of the pressurization was reversed. The strain responses of gages 1 through 6 (near the slit tip) up to the cylinder failure load are considered more important than those of the midslit gages, since they can be used to assess possible damage initiation or growth near the slit tip(s). Thus, the order of pressurization was reversed for the case of slit length of 104 mm. After the cylinder had failed, photographs of the failed specimens were taken and the fracture paths were drawn.

Chapter 7

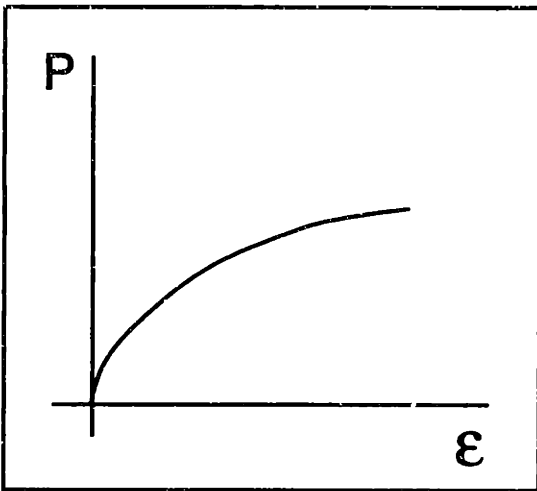
Experimental Results

The experimental results of the present investigation are presented in the three major sections of this chapter. The first section contains comparisons between the experimental and numerical (predicted) strain responses of the *type-1* (unstiffened) and *type-2* (stiffened in the hoop direction) cylinders. The failure data of cylindrical shells with a longitudinal crack are presented in the second section. Finally, the damage paths of the *type-3* cylinders, which are stiffened in both the longitudinal and hoop directions, are presented in the last section.

7.1 Strain Responses

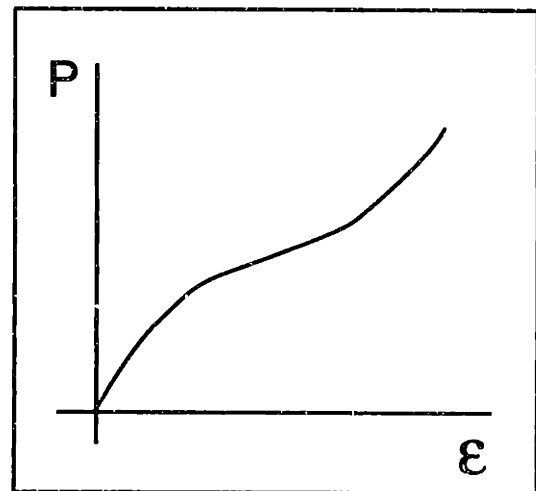
The strain responses at the locations shown in Figures 6.14 and 6.15 for the *type-1* (unstiffened) and *type-2* cylinders (stiffened in the hoop direction), were obtained numerically from finite element analyses and compared with the experimental measurements using strain gages. The numerical strain responses were obtained at a point (i.e. at the centroid of each gage). These are presented along with the measured values. It is important to note that the measured strain values using strain gages involve some kind of "averaging" over the gage area of the active element. The size of the active element of the strain gage used is 3.5 mm in length by 3.0 mm in width. Depending on the specific cylinder analyzed, this "averaging" process

Softening



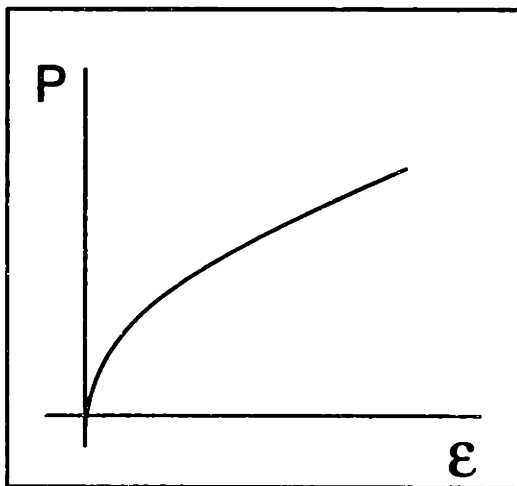
(a) *type-s1* response

Softening-Stiffening



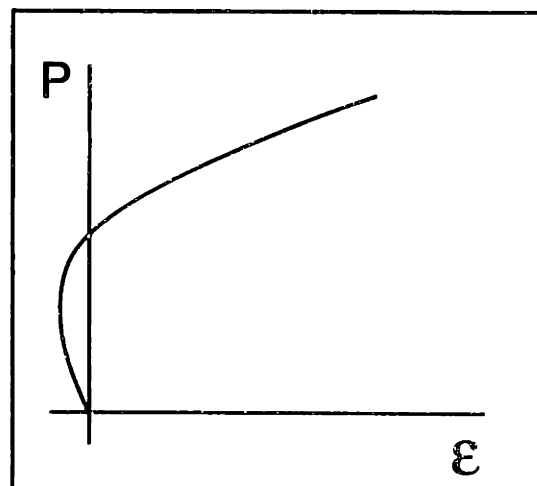
(b) *type-s2* response

Softening-Linear



(c) *type-s3* response

Sign-Reversal



(d) *type-s4* response

Figure 7.1 Characteristic types of strain responses (predicted and measured) in the *type-1* and *type-2* cylinders.

can cover up to a total of nine finite elements (three element lengths/widths in each direction).

There were a total of twelve strain gages in the *type-1* cylinders: six gages located near the slit tips (three gages to measure hoopwise strain and three gages to measure strain along the longitudinal direction) and six additional gages in the vicinity of the midslit region (three hoop gages and three longitudinal gages). The *type-2* cylinders were instrumented with five strain gages in the vicinity of the slit tips (three gages to measure hoopwise strain and two gages to measure strain along the longitudinal direction).

In both the unstiffened and stiffened cases, the gage responses as predicted and measured experimentally can be characterized by four types. These responses are: "softening", designated as the *type-s1* response; a combination of "softening" and "stiffening", designated as the *type-s2* response; "softening" followed by "linear" response, designated as the *type-s3* response; and "sign-reversal", designated as the *type-s4* response. These are depicted in Figures 7.1a through 7.1d.

7.1.1 Unstiffened Case (*Type-1* Cylinder)

Quasi-isotropic composite cylinders with two different stacking sequences ((0/45)_s and (45/0)_s) and three different slit sizes (51 mm, 78 mm, and 104 mm) were considered. The effects of nonlinearity are proportional to the slit size (i.e. the larger the slit size, the more nonlinear the response) as discussed in Chapter 5. The largest nonlinear effects are therefore expected in cylinders with the largest slit size (2a=104 mm). Thus, only the predicted and experimental strain responses for such a cylinder are presented in this chapter. The strain responses for cylinders with smaller slit sizes show

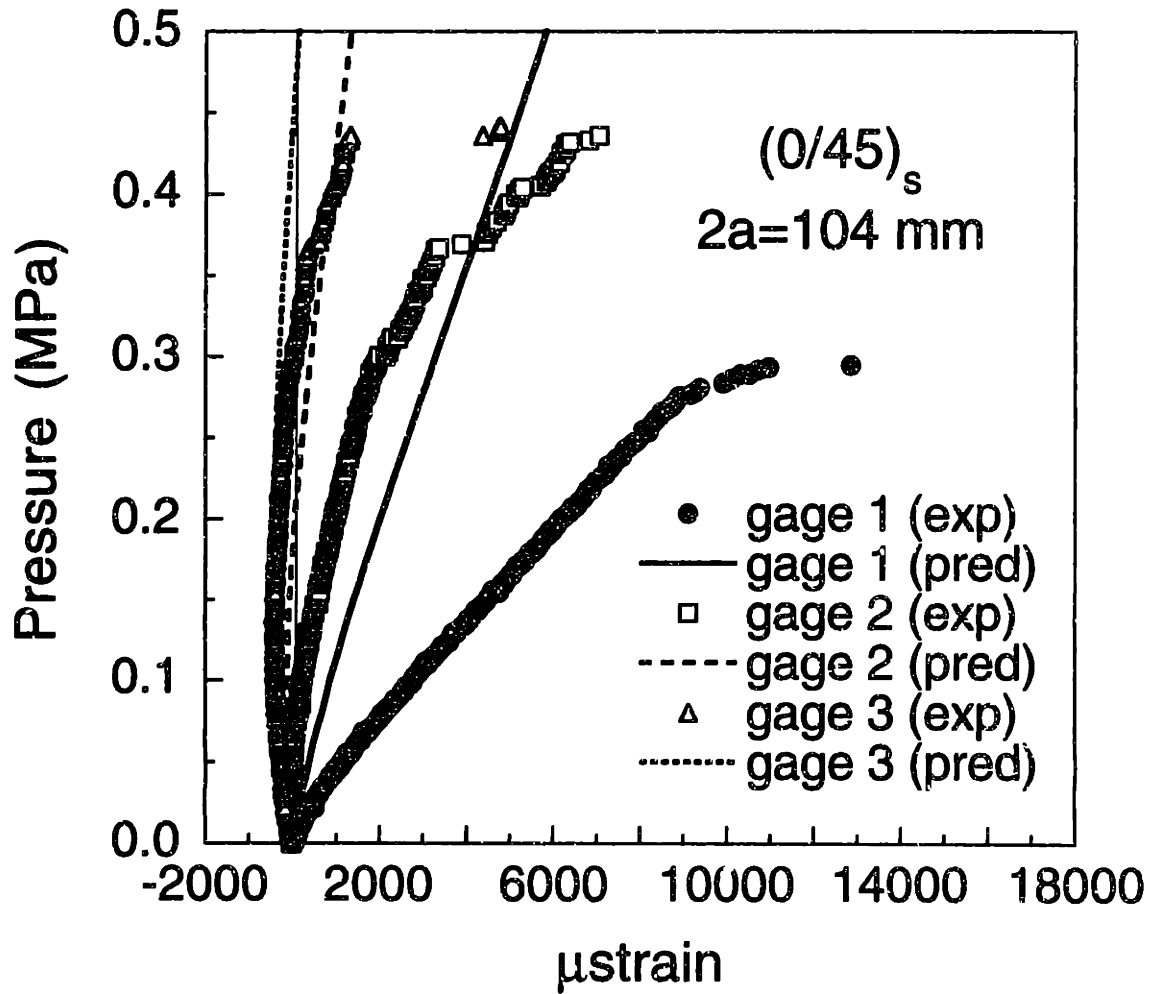


Figure 7.2 Predicted and experimental strain responses for gages 1 to 3 in the unstiffened $(0/45)_s$ cylinder with a longitudinal slit length of 104 mm.

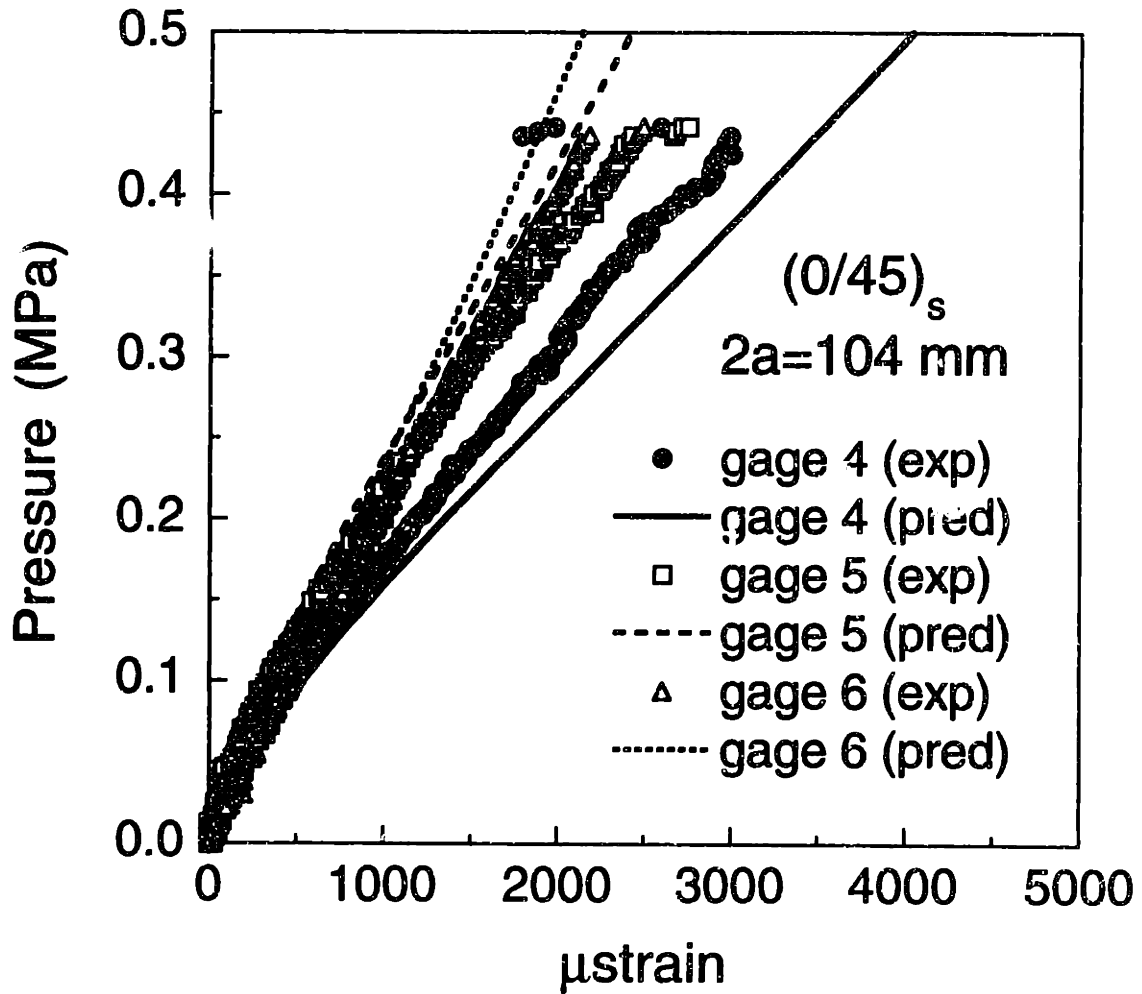


Figure 7.3 Predicted and experimental strain responses for gages 4 to 6 in the unstiffened (0/45)_s cylinder with a longitudinal slit length of 104 mm.

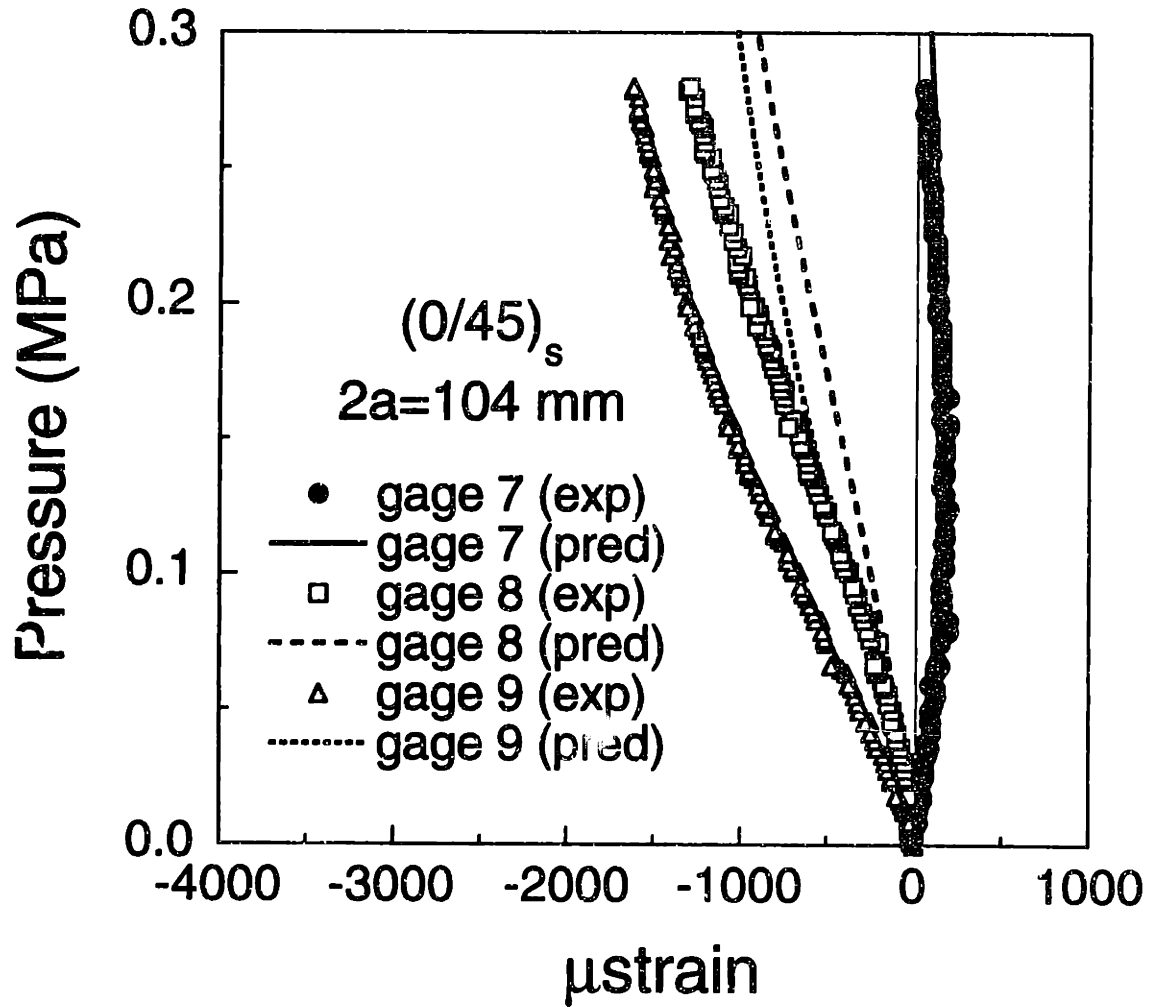


Figure 7.4 Predicted and experimental strain responses for gages 7 to 9 in the unstiffened (0/45)_s cylinder with a longitudinal slit length of 104 mm.

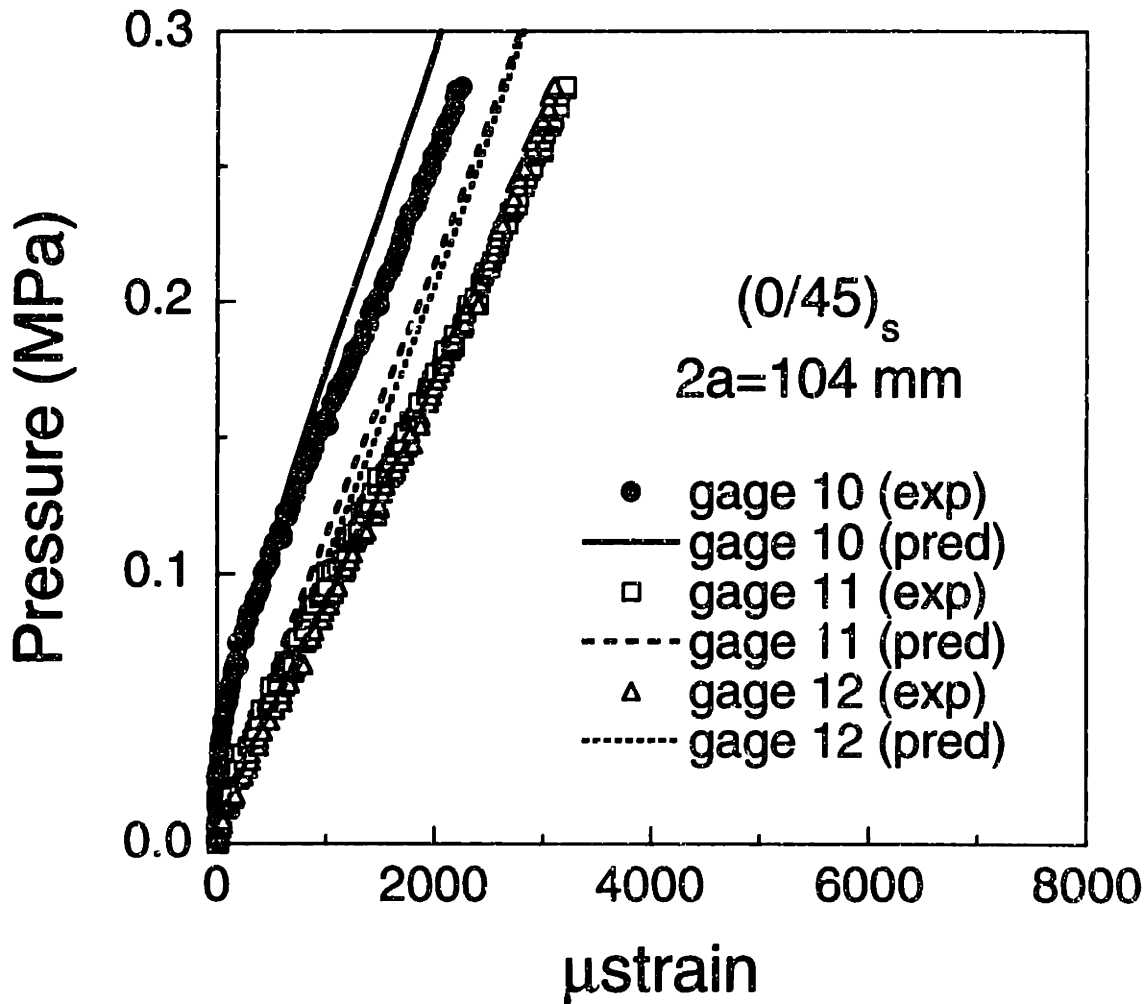


Figure 7.5 Predicted and experimental strain responses for gages 10 to 12 in the unstiffened (0/45)_s cylinder with a longitudinal slit length of 104 mm.

similar trends and are not shown here for brevity. They are shown in Appendix C.

The predicted and measured strain responses for the twelve strain gages in the (0/45)_s cylinder with a longitudinal slit length of 104 mm are shown in Figures 7.2 to 7.5 for gages 1 to 3, 4 to 6, 7 to 9, and 10 to 12, respectively. Damage initiation or growth is indicated in these measured strain responses by the occurrence of strain discontinuities or "jumps". These can especially be seen in the measured responses of the strain gages closest to the slit tips (gages 1 to 6).

Despite the poor absolute agreement observed between the predicted and measured responses for gage 1, where the prediction severely underestimates the measured reading, the analysis correctly predicts the shape of the observed response to be a *type-s3* ("softening" followed by "linear") response. Some explanations for the observed disagreement in the magnitude of the predicted and measured responses, including the sensitivity of measurement to gage placement, are described in Chapter 8. In the response of gage 2, a *type-s4* ("strain-reversal") response is predicted. The predicted strain is compressive at a pressure level less than 0.22 MPa and is tensile at a pressure level greater than 0.22 MPa. The measured response, however, shows a *type-s1* (pure "softening") behavior. Both the predicted and the experimental strain responses of gage 3 show a *type-s4* response ("strain-reversal"). At a pressure less than 0.3 MPa, the state of strain as measured by the gage is negative (compressive). This state of strain changes and becomes positive (tensile) as the pressure increases. The numerical modelling is able to capture the "strain-reversal" phenomenon of gage 3. The maximum negative strain, which indicates the beginning of a "reversal", is predicted to occur at a pressure of 0.18 MPa. This agrees relatively well with

the measured value of approximately 0.14 MPa. However, the pressure level where the transition between the "compressive" to "tensile" states occurs is approximately 0.5 MPa and is much higher than the measured value of 0.3 MPa.

Besides the presence of "softening" and "sign reversal" in the strain responses, strain discontinuities or "jumps", which are induced by damage initiation and growth near the slit tip, can also be seen in the measured responses of gages 1 through 3. The discontinuity in the response of gage 1 seems to have started at an earlier load (i.e. at a pressure of approximately 0.28 MPa). This gage seems to have been damaged beyond the pressure level of 0.3 MPa as noted in Figure 7.2. Strain discontinuities for gages 2 and 3 start to occur at slightly higher pressure levels of 0.3 MPa and 0.35 MPa, respectively. Unlike gage 1, these two gages were not damaged until the pressure level was close to the failure pressure of that particular cylinder at approximately 0.45 MPa.

The numerical and measured strain responses for the longitudinal strain gages near the slit tip (gages 4 through 6) are shown in Figure 7.3. The agreement between the predicted and measured strains are better than the hoop gages. These longitudinal gages exhibit a *type-s3* ("softening" followed by "linear") response. At a low pressure (less than approximately 0.08 MPa), "softening" dominates both the predicted and measured responses of gage 4. This observed "softening" response gradually changes and becomes "linear" at higher pressure. Similar initial "softening" followed by "linear" response is shown in the experimental and predicted responses of gages 5 and 6. The transition points, which indicate a change from "softening" to "linear" responses, take place experimentally at approximately 0.15 MPa and 0.17 MPa for gages 5 and 6, respectively. The transition points for gages 5 and 6

predicted numerically occur at pressure levels of approximately 0.12 MPa and 0.11 MPa, respectively. The crossing between the responses of gages 5 and 6 as measured experimentally occurs at approximately 0.25 MPa. This agrees well with the predicted value of 0.25 MPa.

The predicted and experimental strain responses in the vicinity of the midslit region are shown in Figures 7.4 and 7.5 in the hoop and longitudinal directions, respectively. The strain measurements to obtain the responses of these gages were taken only up to approximately 60% of the predicted failure pressure for reasons described in Chapter 6. Note that the strain levels in both directions (hoop and longitudinal) in this region are relatively small with a maximum value ranging between 2000 and 3000 microstrain. In general, three kinds of strain responses are noted for gages in the midslit region: *type-s1* ("softening"), *type-s2* (combination of "softening" and "stiffening"), and *type-s4* ("sign reversal"). The response of gage 7 (the closest hoop gage to the slit axis) shows a *type-s4* behavior and this is well-captured by the prediction. The strain, as measured by the gage, initially increases with loading, reaches a maximum value, and then decreases monotonically. The maximum positive strain that indicates the beginning of a "reversal" is predicted to occur at a pressure of 0.15 MPa. This agrees well with the measured value of approximately 0.13 MPa. Although the state of strain for that particular gage remains tensile until the pressurization is stopped, the trend is that the strain will become compressive if the loading is continued. A *type-s2* response can be seen in the response of gages 8 and 9. The inflection points, where the curvature of the plot changes, are predicted to occur at 0.22 MPa and 0.12 MPa, respectively. The "inflection" points obtained experimentally cannot be determined accurately due to the presence of "noise" in the data. They can only be estimated by inspecting the plots. The

experimental "inflection points" are estimated to be between 0.18 MPa and 0.20 MPa and between 0.13 MPa and 0.15 MPa for gages 8 and 9, respectively. The agreement between the numerical and experimental results for the "inflection points" are good. No appreciable strain discontinuities or jumps are observed in the measured gage responses in this region. It is worth noting that the prediction is able to capture the shape and trend of the strain response. However, some differences can be seen between the magnitudes of the predicted and measured strains in this region.

The strain responses of the longitudinal gages in the midslit region are also nonlinear and consist of *type-s2* (a combination of "softening" and "stiffening") and *type-s3* ("softening" followed by "linear") responses. The shape of the response of gage 10 (the closest longitudinal gage to the slit axis) shows initial "softening" response at a pressure level less than 0.1 MPa. The numerical analysis predicts that the "transition" point from a "softening" to a linear response occurs at 0.11 MPa and is very close to what is observed experimentally (between 0.11 MPa and 0.12 MPa). The shapes of the responses of the other two longitudinal gages (gages 11 and 12) are similar to each other and show a *type-s2* (combination of "softening" and "stiffening") response. The inflection points are predicted to occur at pressure levels of 0.20 MPa and 0.16 MPa for gages 11 and 12, respectively. The pressure levels where "inflection" occurs experimentally range from 0.16 MPa to 0.18 MPa and 0.14 MPa to 0.16 MPa for gages 11 and 12, respectively.

The predicted and experimental strain responses for the (45/0)_s cylinder with the same slit geometry are shown in Figures 7.6 to 7.9 for gages 1 to 3, 4 to 6, 7 to 9, and 10 to 12, respectively. In general, the shapes of the responses and the trends are similar to those of the (0/45)_s cases. All four

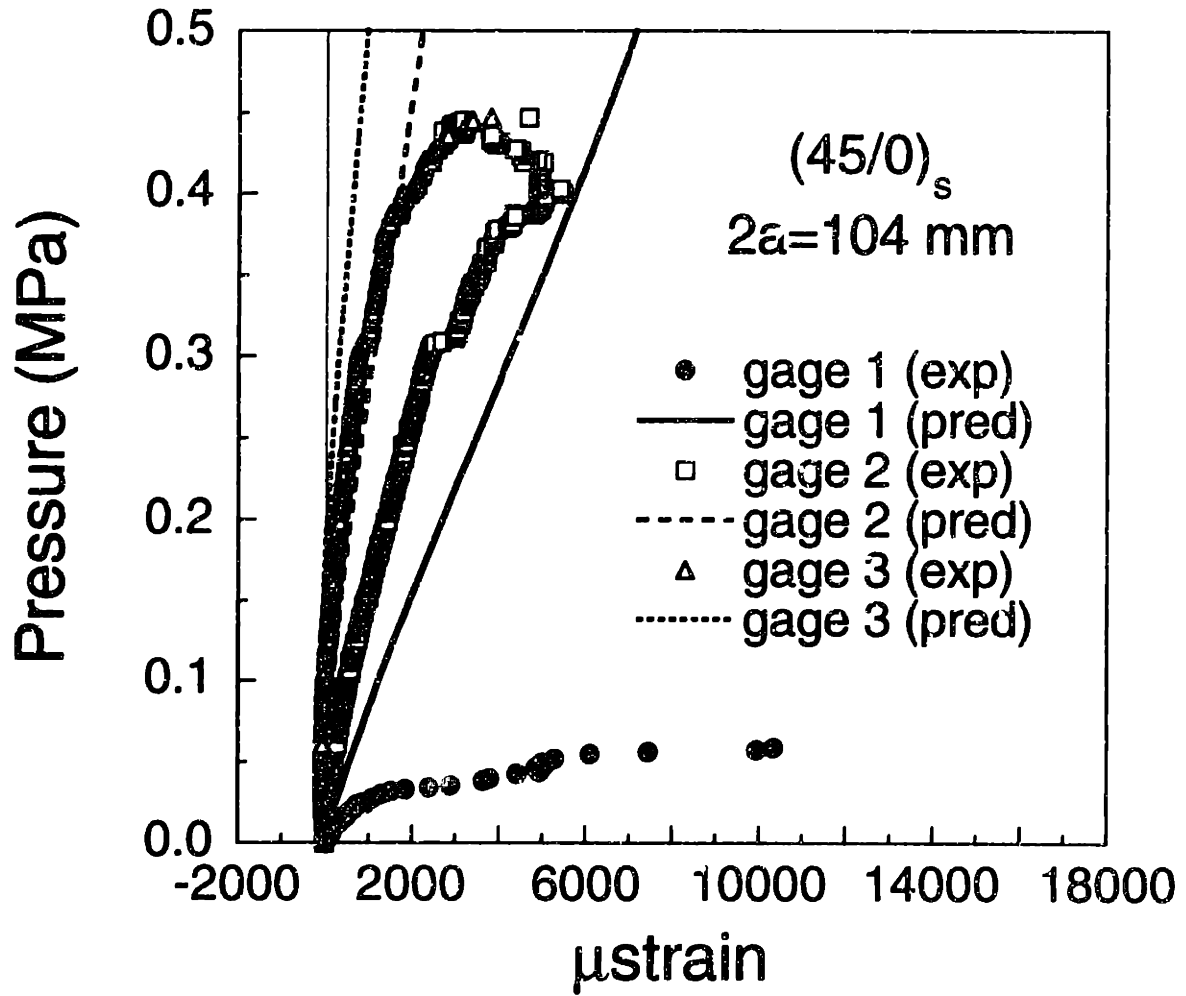


Figure 7.6 Predicted and experimental strain responses for gages 1 to 3 in the unstiffened $(45/0)_s$ cylinder with a longitudinal slit length of 104 mm.

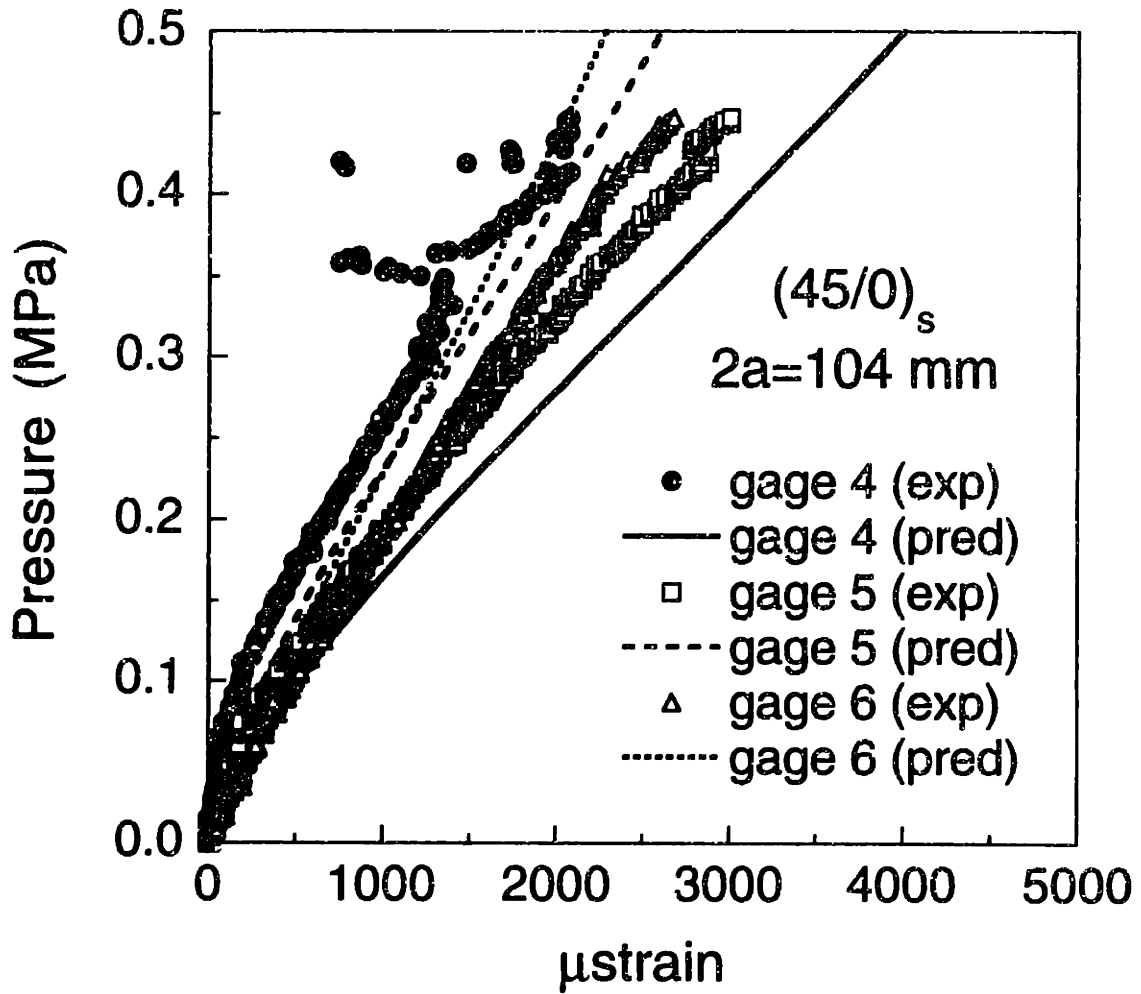


Figure 7.7 Predicted and experimental strain responses for gages 4 to 6 in the unstiffened (45/0)_s cylinder with a longitudinal slit length of 104 mm.

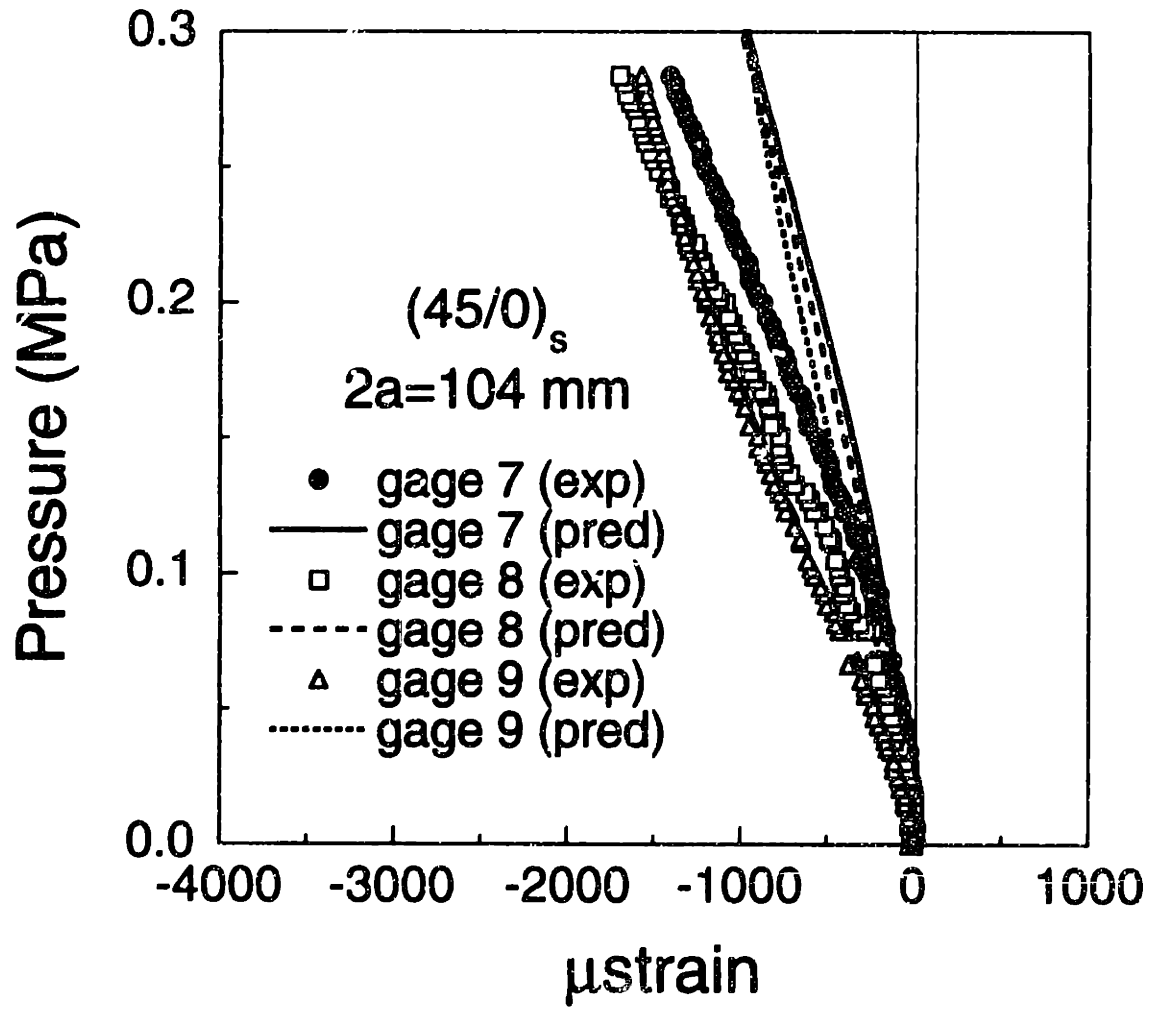


Figure 7.8 Predicted and experimental strain responses for gages 7 to 9 in the unstiffened (45/0)_s cylinder with a longitudinal slit length of 104 mm.

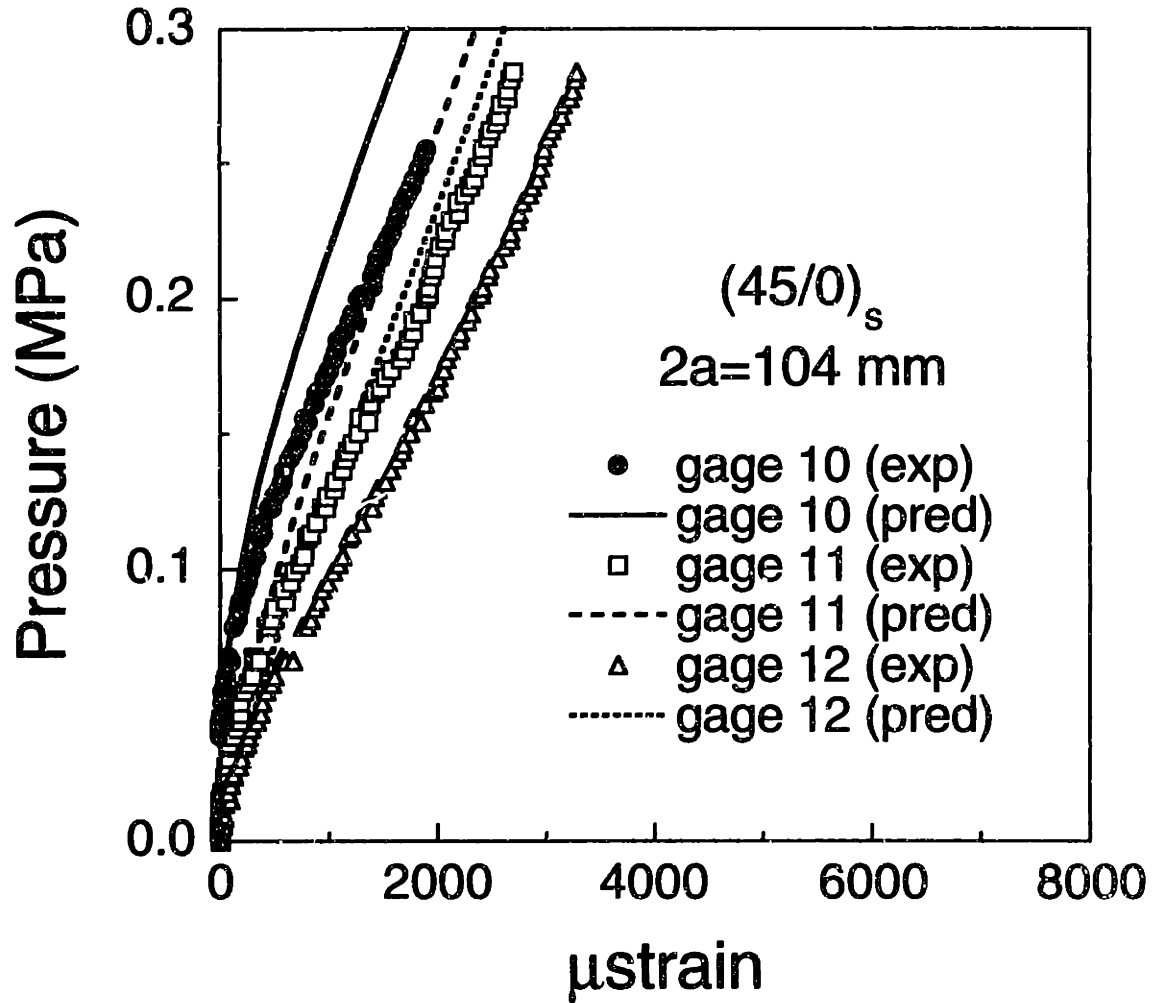


Figure 7.9 Predicted and experimental strain responses for gages 10 to 12 in the unstiffened (45/0)_s cylinder with a longitudinal slit length of 104 mm.

different types of responses discussed previously are observed and predicted. Thus, only major differences from the (0/45)_θ case are discussed here.

One peculiarity can be seen in the strain response of gage 1 where the measured response becomes "erratic" as soon as loading is applied. Strain discontinuities in the readings of gages 2 and 3 are observed at a pressure level of approximately 0.30 MPa. The shapes of the strain responses of gages 4 through 6 are also similar to those discussed previously for the (0/45)_θ case. One notable difference is that the numerical prediction overestimates the measured response of gage 4 (the closest longitudinal gage to the slit tip). Some "erratic" response, which starts at a pressure level of approximately 0.33 MPa, can also be seen in the experimental response of gage 4. The "crossing" between the experimental response of gages 5 and 6 occurs at approximately 0.20 MPa. The agreement with the predicted value of 0.25 MPa is also good.

The predicted and experimental strain responses in the vicinity of the midslit region are shown in Figures 7.8 and 7.9. As in the (0/45)_θ cylinder, the strain levels in both directions (hoop and longitudinal) are relatively small (i.e. the maximum is only between 2000 to 3000 microstrain). The shapes of the strain responses and the trends are similar to the ones discussed previously for the (0/45)_θ cylinder (i.e. *type-s1* ("softening") and *type-s2* (a combination of "softening" and "stiffening")). Unlike the previous case, however, no *type-s4* behavior ("sign reversal") is predicted nor measured in the response of gage 7 (the closest hoop gage to the slit tip). The response of gage 7 in this (45/0)_θ cylinder is of *type-s2* behavior ("softening" followed by "linear" response). Furthermore, the "inflection" points are predicted to occur at 0.28 MPa and 0.18 MPa for gages 8 and 9, respectively. These values are higher than those in the (0/45)_θ case. From the experimental responses, the

"inflection" points are estimated to be between 0.22 MPa and 0.25 MPa and between 0.14 MPa and 0.16 MPa for gages 8 and 9, respectively. These are also higher than the measured values for the (0/45)_s case. Again, the agreement between the prediction and the experimental responses for the locations of the "inflection" points is good. As in the (0/45)_s case, some differences can be seen between the magnitudes of the predicted and measured strains in this region.

The responses of gages 10 through 12 for the (45/0)_s case are again similar to those of the (0/45)_s cylinders. The response of gage 10 also exhibits a *type-s3* (softening followed by linear) behavior. The "transition" between the "softening" and the linear regimes is predicted to occur at a pressure level of approximately 0.17 MPa, while the measured value occurs at a pressure level of approximately 0.12 MPa. As before, the responses of gages 11 and 12 exhibit a *type-s2* (combination of "softening" and "stiffening") behavior. The "inflection" points are predicted to occur at pressure levels of 0.33 MPa and 0.26 MPa for gages 11 and 12, respectively. These values are higher than those in the (0/45)_s case. Although the measured response for gage 11 shows a *type-s2* behavior, the location of the "inflection" point is not very obvious within the range of the pressure level investigated (i.e. between 0.0 MPa and 0.3 MPa) due to the presence of noise in the data. The actual "inflection" point may well occur at a pressure level which is higher than what is seen experimentally. The location of the "transition" point for gage 12 can be estimated from the experimental response to be between 0.16 MPa and 0.18 MPa.

The results presented herein show that the numerical analysis is able to capture the trends and the shapes of the measured strain response. Some differences can be seen between the magnitudes of the predicted and

measured strains in this region. Possible sources of such a disagreement are presented in Chapter 8.

7.1.2 Circumferentially-Stiffened Cylinder (Type-2 Cylinder)

As in the unstiffened case, only the predicted and experimental strain responses for cylinders with the largest slit size ($2a=104$ mm) are presented in this chapter for the same reasons discussed previously. The predicted and measured strain responses for cylinders with smaller slit sizes generally have similar shapes and trends and are presented in Appendix C. As in the unstiffened case, the effects of nonlinearity on the pressure-strain responses are manifested in the four types of responses discussed previously as shown in Figure 7.1.

The predicted and experimental strain responses for the stiffened (0/45)_s cylinder with a longitudinal slit length of 104 mm are shown in Figures 7.10 and 7.11 for gages 1 to 3 and 4 to 5, respectively. As shown in Tables 6.1 to 6.4, the locations for gages 1 to 3 in the stiffened case are approximately the same as those for the unstiffened case. As in the unstiffened case, the numerical prediction underestimates the measured strain response of gage 1. Nevertheless, the analysis correctly predicts a *type-s3* ("softening" followed by "linear") behavior exhibited by gage 1. The response of gage 2 shows a *type-s1* ("softening") behavior. The measured response of gage 3 shows a *type-s4* ("sign reversal") behavior. At a pressure less than 0.3 MPa, the strain is negative (compressive). This state of strain changes and becomes positive (tensile) as pressure increases. The numerical modelling is able to capture this "sign reversal" phenomenon. The maximum negative strain that indicates the beginning of a "reversal" is predicted to occur at a pressure of 0.15 MPa. This agrees relatively well with the

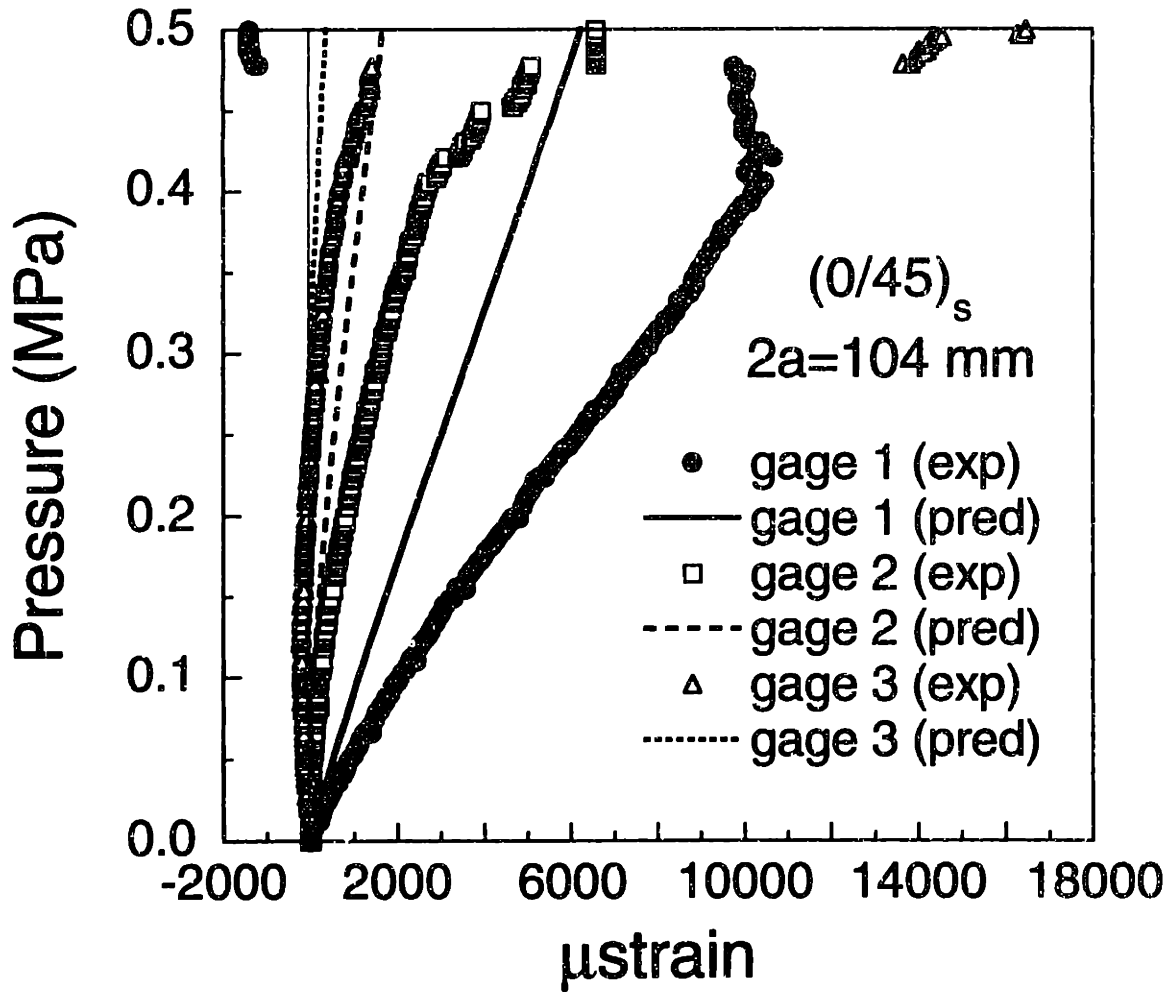


Figure 7.10 Predicted and experimental strain responses for gages 1 to 3 in the stiffened (0/45)_s cylinder with a longitudinal slit length of 104 mm.

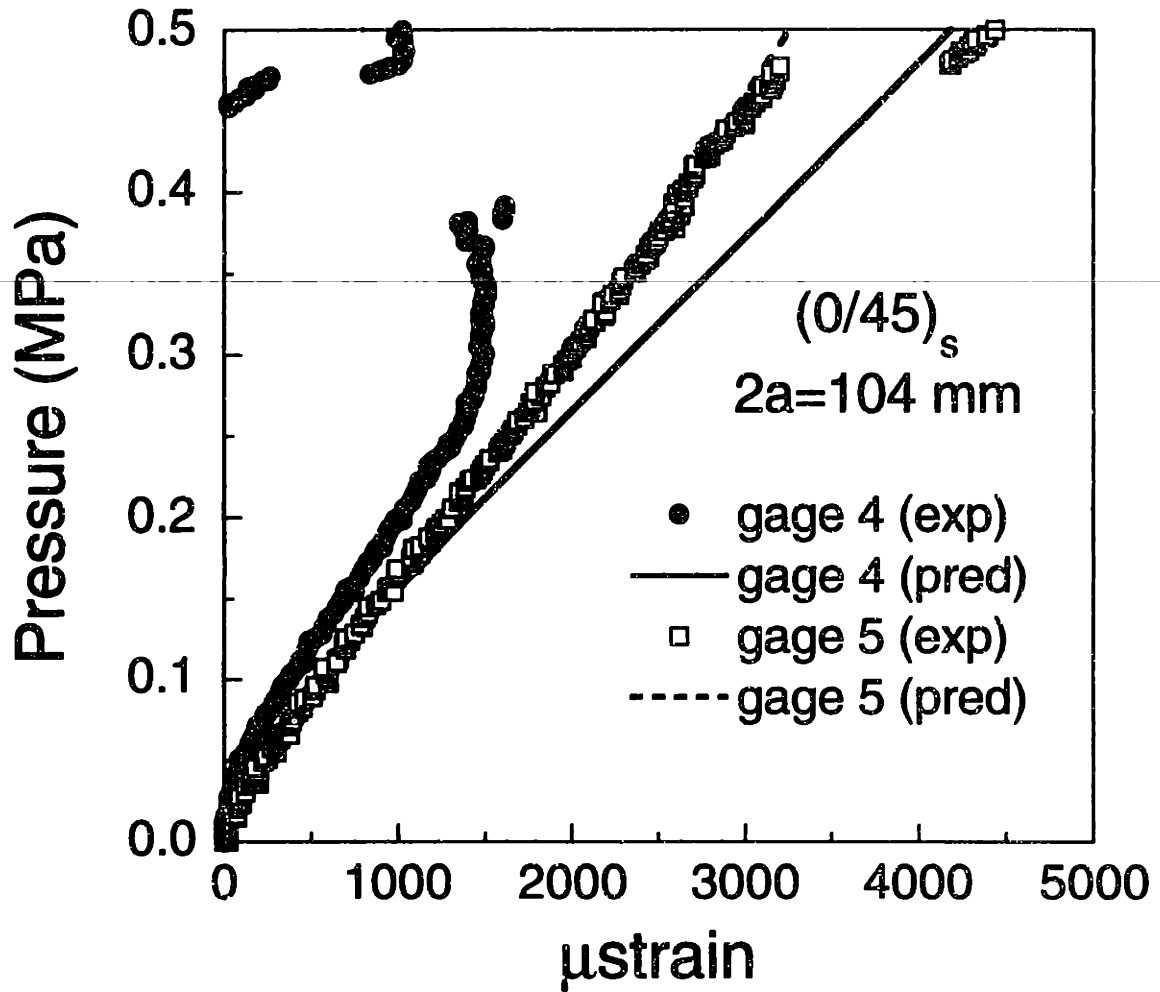


Figure 7.11 Predicted and experimental strain responses for gages 4 and 5 in the stiffened $(0/45)_s$ cylinder with a longitudinal slit length of 104 mm.

measured value of approximately 0.12 MPa. Some strain discontinuities ("jumps"), induced by damage initiation, can also be seen in the measured responses at a pressure level greater than approximately 0.36 MPa.

As noted, the locations for gages 1 to 3 in the stiffened case are approximately the same as those for the unstiffened case. It can be seen that the measured responses of gages 2 and 3 in the stiffened case are close to those of the unstiffened case. The response of gage 1 in the stiffened case, however, is approximately 19% lower in magnitude (i.e. stiffer) than that of the unstiffened case.

The locations of gages 4 and 5 in the stiffened case are also approximately the same as those in the unstiffened case. The readings of the two longitudinal gages in the slit tip region (gage 4 and 5) again show the existence of *type-s1* ("softening") behavior. Gage 4 is placed close to the slit tip, while gage 5 is placed close to the edge of the stiffening band. It is interesting to note that both the predicted and experimental responses of the two gages are almost identical. Damage initiation, in the form of strain discontinuity in the response, can be seen in the reading of gage 4 at a pressure level of slightly less than 0.3 MPa. At the same pressure level, there is no discontinuity shown in the response of gage 4 in the unstiffened case shown in Figure 7.3. The effects of stiffening bands can be seen in the response of gage 5 by comparing strain levels of the unstiffened and stiffened cases where higher strain levels are predicted and measured in the stiffened case.

The predicted and experimental strain responses for the stiffened (45/0)_s cylinder with the same slit geometry are shown in Figures 7.12 and 7.13 for gages 1 to 3 and 4 to 5, respectively. Again, the locations of the gages are approximately the same as those in the unstiffened case. The responses

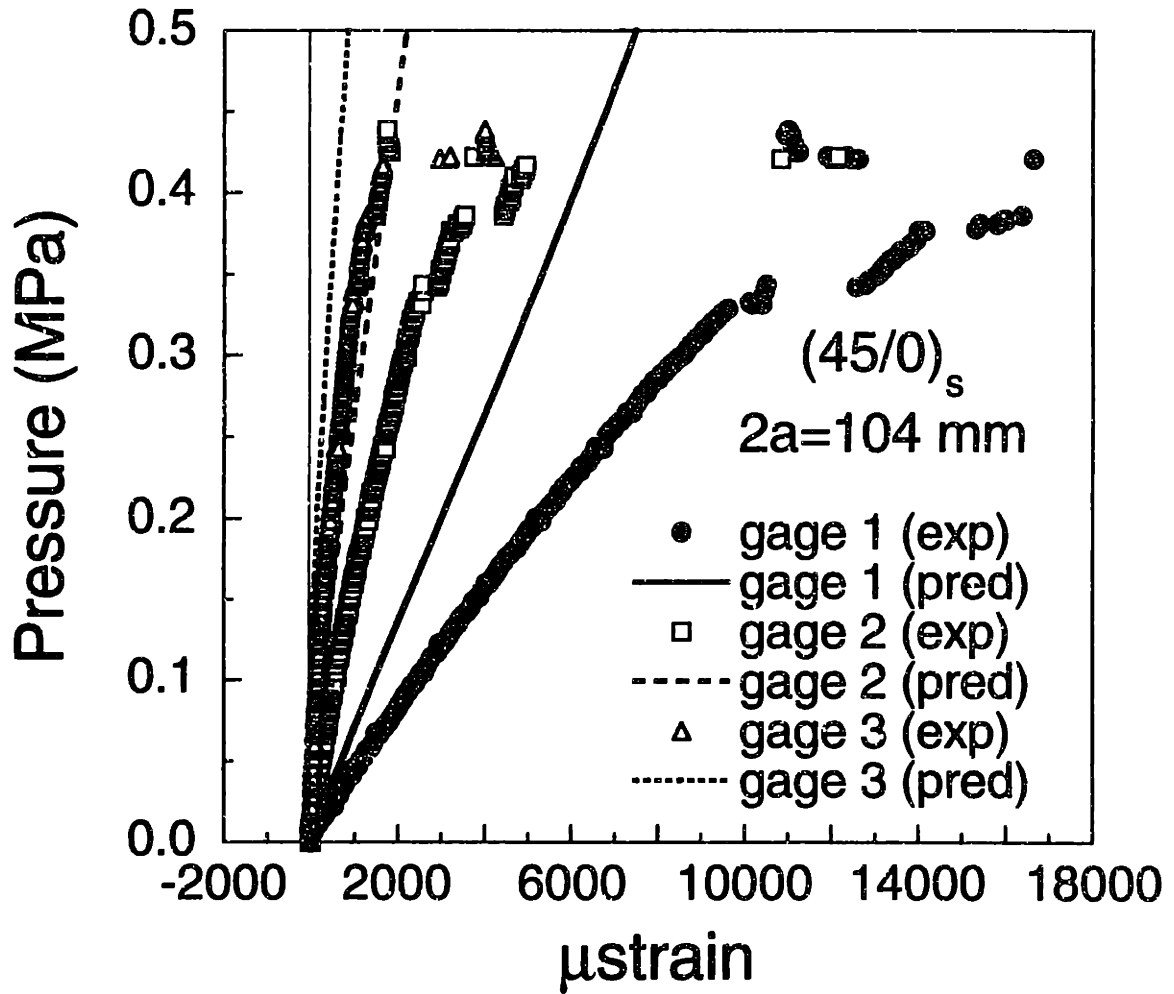


Figure 7.12 Predicted and experimental strain responses for gages 1 to 3 in the stiffened $(45/0)_s$ cylinder with a longitudinal slit length of 104 mm.

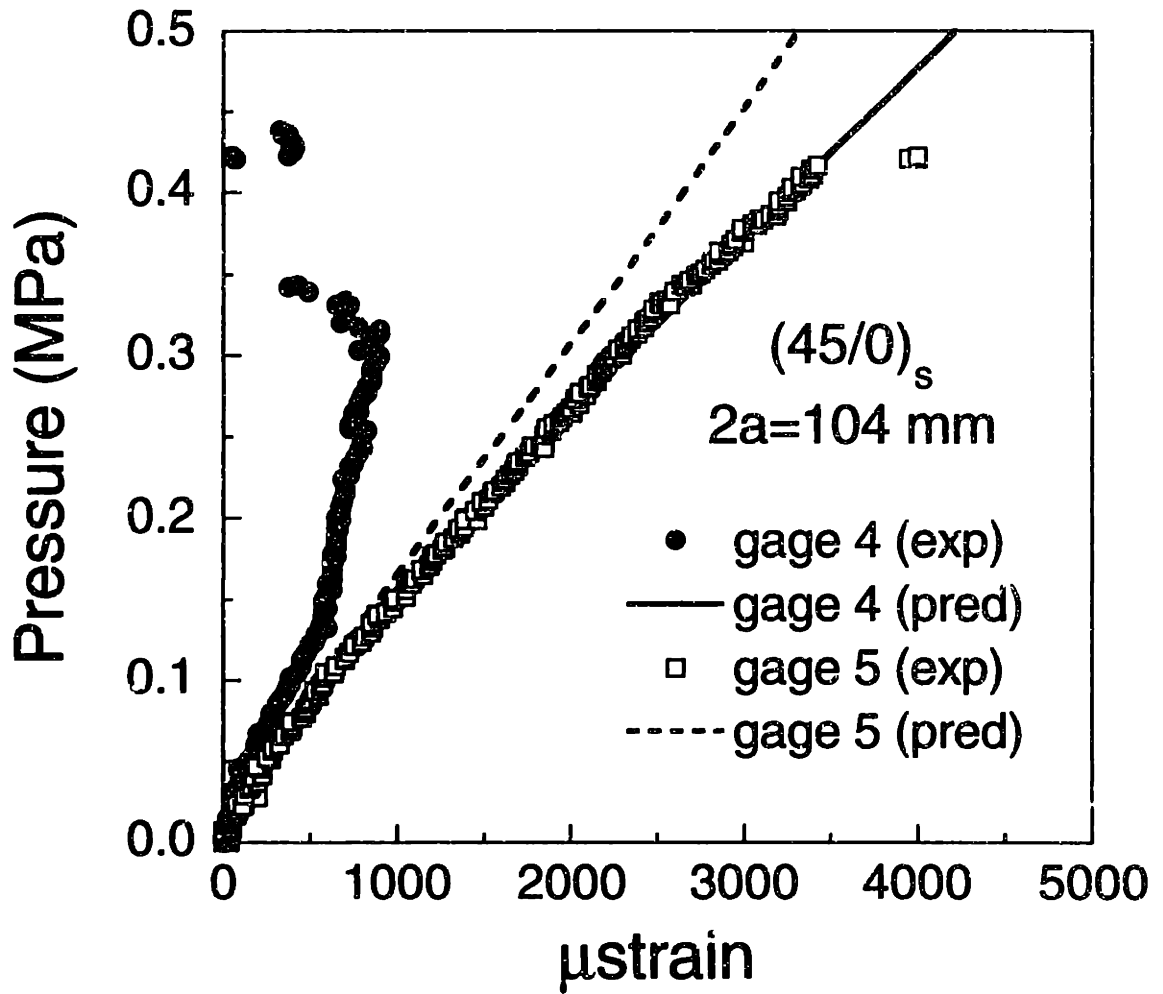


Figure 7.13 Predicted and experimental strain responses for gages 4 and 5 in the stiffened $(45/0)_s$ cylinder with a longitudinal slit length of 104 mm.

and trends for this case are very similar to those of the (0/45)_s cylinder and thus no further discussion is presented here. Damage initiation in this type of cylinder, manifested in strain discontinuities in the readings of the hoop gages, starts at a slightly lower pressure of around 0.33 MPa. Gages 2 and 3 seem to have been damaged at pressure levels greater than 0.33 MPa. When compared with the unstiffened results, the responses of gages 1 and 2 seem unaffected by the presence of stiffening bands. The measured response of gage 4 starts to deviate from the prediction and becomes "erratic" at a lower pressure level (approximately 0.1 MPa) than that of the (0/45)_s case. No strain discontinuity is seen in the response of gage 4 in the unstiffened case. The effects of stiffening bands in the (45/0)_s cylinder can again be seen in the response of gage 5 as higher strain levels are predicted and measured in the stiffened case.

7.2 Failure

The failure pressures of all the cylinders are tabulated in Table 7.1. The predicted failure pressure for each cylinder was also obtained by using the failure prediction methodology in equation (2.9). The composite fracture parameter for the (0/45)_s case as measured experimentally in [57] is $698 \text{ MPa mm}^{0.28}$. The composite fracture parameter for the (45/0)_s case for this material system (AW370-5H/3501-6 graphite/epoxy system) was not measured. However, previous experimental work showed that the magnitude of the fracture parameter of (45/0)_s coupons for a slightly different material system [79] is roughly the same as that of the (0/45)_s case. Thus, the same fracture parameter is used for the (0/45)_s case. The prediction uses the

Table 7.1 Failure Data for all Cylinders

Cylinder Designation	Stacking Sequence	Slit Size [mm]	Failure Pressure [kPa]		
			Exp. ^a	Pred.	Difference
<i>Type-1</i>	(0/45) _s	104	441	454	-2.9%
	(45/0) _s	104	435	454	-4.2%
<i>Type-2</i>	(0/45) _s	51	904	1023	-11.6%
	(0/45) _s	78	499	639	-21.9%
	(0/45) _s	104	505	454	+11.2%
	(45/0) _s	51	810	1023	-20.8%
	(45/0) _s	78	608	639	-4.9%
	(45/0) _s	104	440	454	-3.1%
<i>Type-3</i>	(0/45) _s	79	579	630	-8.1%
	(0/45) _s	79	566	630	-10.1%
	(0/45) _s	79	551	630	-12.5%
	(0/45) _s	79	612	630	-2.9%
	(0/45) _s	79	607	630	-3.7%

^aCOV for slit length of 51 mm is 7.3%; COV for slit length of 78 mm is 7.0%;
COV for slit length of 104 mm is 7.8%.

average measured thickness of 1.38 mm with a coefficient of variation of 5.3%.

The agreement between the predicted and experimental failure pressures is generally good with the coefficients of variations equal to 7.3%, 7.0%, and 7.8% for cylinders with slit length of 51 mm, 78 mm, and 104 mm, respectively. The presence of stiffening bands in the *type-2* and *type-3* cylinders does not affect the failure pressure. All cylinders fail within a reasonable experimental scatter.

7.3 Damage Path of the *Type-3* Cylinders

To present the fracture paths of the *type-3* cylinders clearly, a cylinder is "imaginarily" cut along its longitudinal axis at an angular hoop location 180° from the slit and then rolled "flat". This process is depicted in Figure 7.14. The slit is shown at the center of the drawing and the fracture paths of the five cylinders tested are shown using this scheme.

The fracture path of cylinder 1 is shown in Figure 7.15. Damage initially propagated from each slit tip in the longitudinal direction and then bifurcated and turned 90° near the edge of the hoop stiffeners. For cylinder 1, the two bifurcation points are each approximately 15 mm from the edge of the hoop stiffening bands. It is important to note that the "triangular" region, which is formed by the bifurcated damage and bounded by the fibers in the 45° ply, does not contain the top 0° ply. After bifurcation, damage that had split into four distinct paths continued to propagate in the hoop direction, inducing other damage modes (stiffener debonds) near the junction between the longitudinal and hoop stiffeners and delamination in the unstiffened regions. Some damage turning was also observed in the vicinity of this

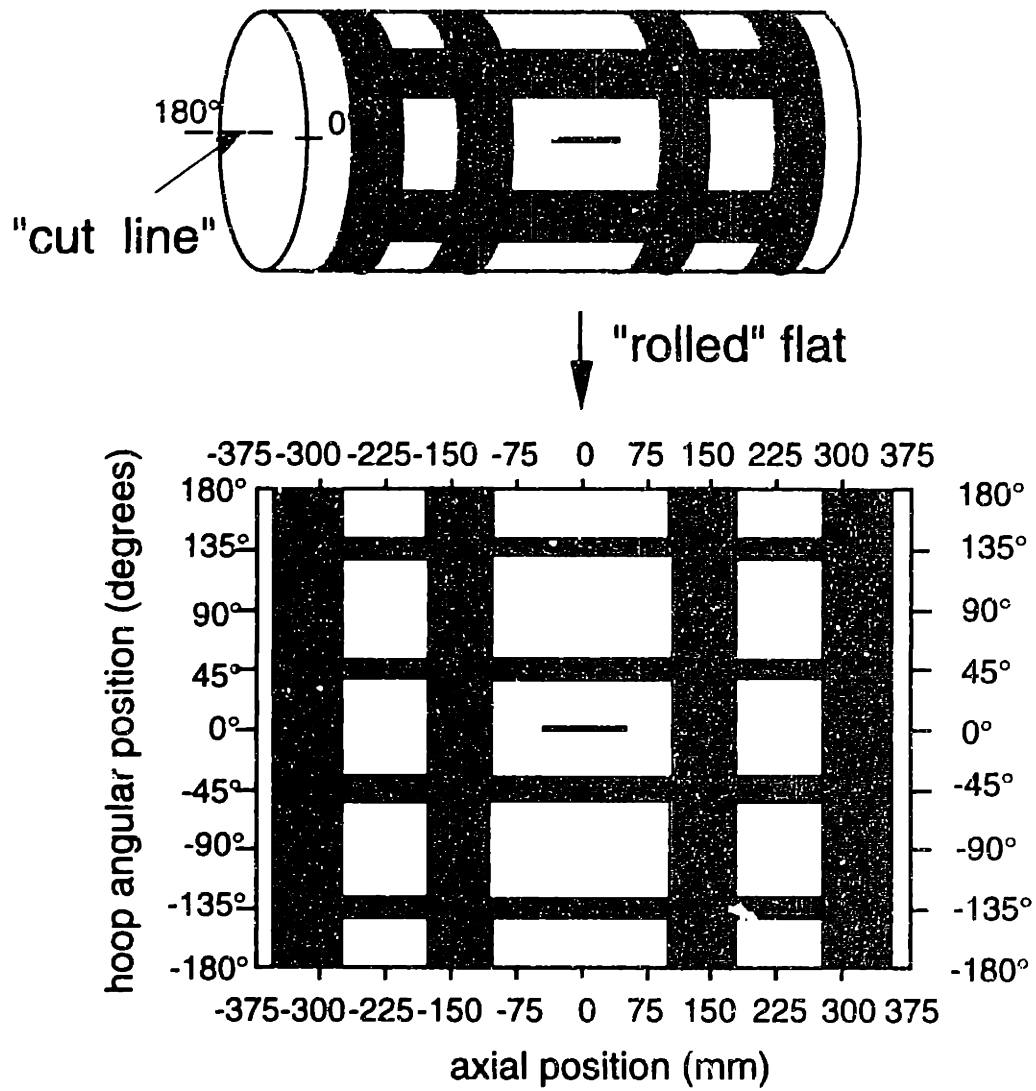


Figure 7.14 Illustration of the presentation of the damage path in the *type-3* cylinder.

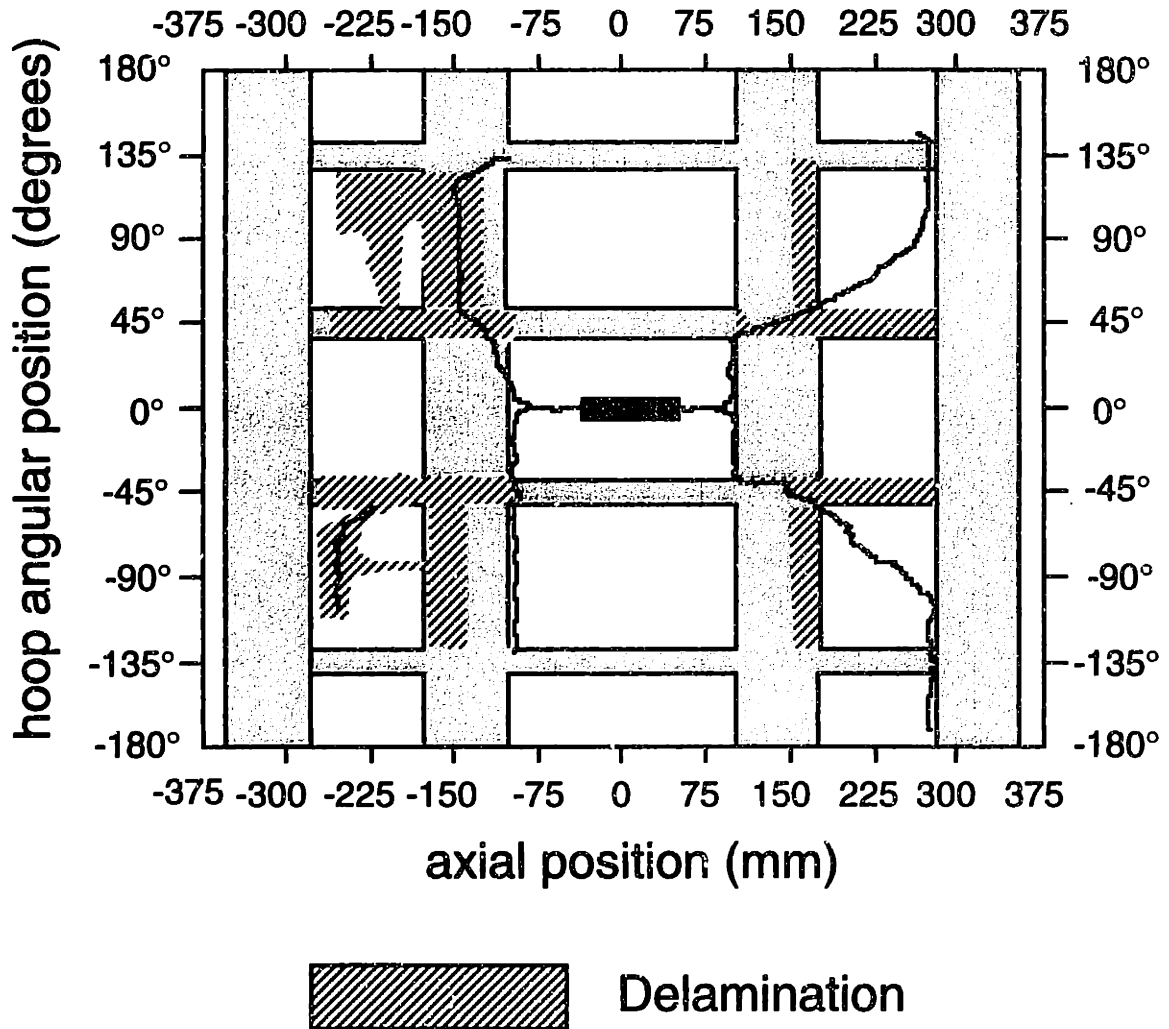


Figure 7.15 Fracture path of cylinder 1 stiffened with four layers of 0° tape (hoop) and 8 layers of 0° tape (longitudinal).

junction. Damage was finally arrested by the next set of longitudinal stiffeners at an angular location approximately 135° from the slit.

The fracture path of cylinder 2 is shown in Figure 7.16. Damage also initially propagated in the longitudinal direction. However, as damage continued to propagate, the presence of the hoop stiffener did not have a discernible effect as no bifurcation from a longitudinal to a hoopwise propagation is observed in this cylinder. Damage propagation continued in the longitudinal direction until it branched into two parts at an approximate angle between 40 and 50 degrees from the longitudinal axis of the cylinder within the first set of hoop stiffeners. To indicate the details at the bifurcation points, a photograph of the damage path of this cylinder is shown in Figure 7.17. In the photograph, the two bifurcation points are indicated by arrows. It is important to note that, unlike the previous case, the "triangular" region formed by the bifurcated damage in this cylinder contains all of the plies. A close-up photograph of this "triangular" region is shown in Figure 7.18. The bifurcated damage maintained this angular direction and then completely turned 90° at the second set of hoop stiffeners placed near the endcaps. As discussed previously, these additional hoop stiffeners were intended to maintain the cross-section of the cylinder after cure and were located close (approximately 50 mm) to the endcaps. These additional hoop stiffeners were not provided to induce damage bifurcation. The overall fracture path in this cylinder is relatively clean with little delamination observed and is very similar to that of an unstiffened cylinder [25]. Thus, for this particular case, the first set of hoop stiffeners is not effective in inducing damage bifurcation.

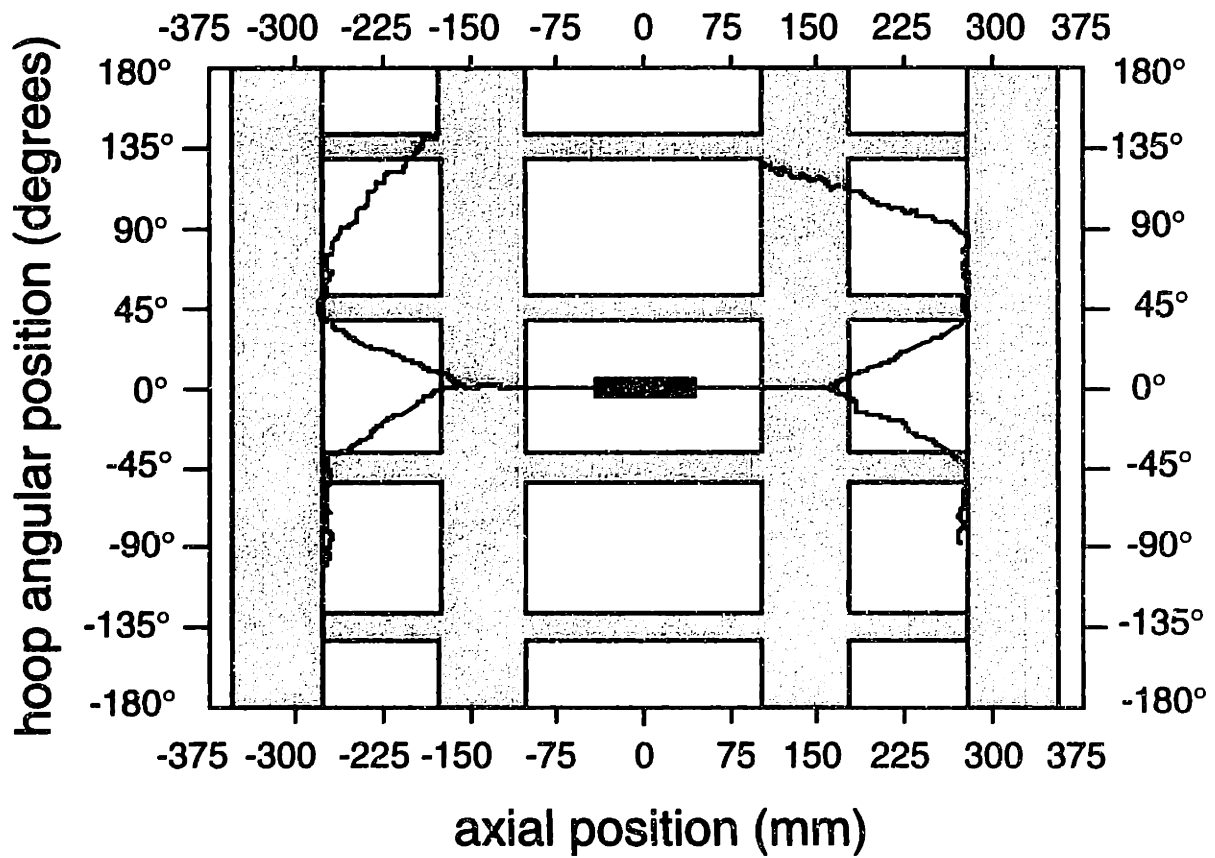


Figure 7.16 Fracture path of cylinder 2 stiffened with two layers of continuous (*type-B*) 0° fabric layers.

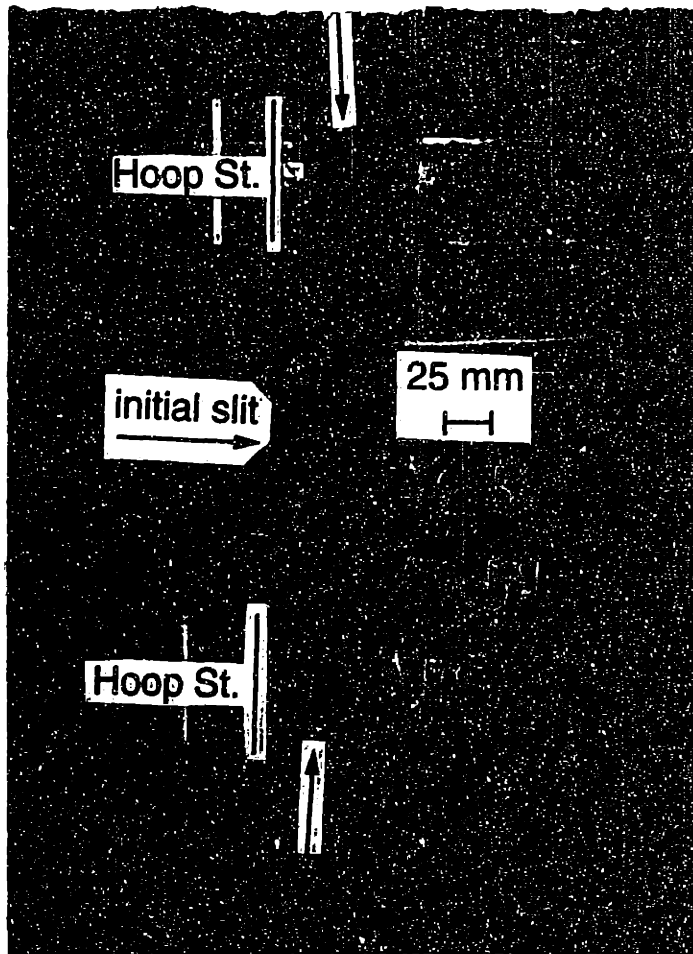


Figure 7.17 Photograph showing damage bifurcation ($\sim 40^\circ - 50^\circ$ turn) within the hoop stiffener (arrows indicate the locations of bifurcation points) in cylinder 2.



Figure 7.18 Close-up photograph of the "triangular" region near the bifurcation point in cylinder 2.

In cylinder 3, which is stiffened with four layers of 0° continuous fabric layers, damage, which initially propagated in the longitudinal direction, was turned near the edge of the hoop stiffeners as shown in Figure 7.19. To indicate the details at the bifurcation points, a photograph of the damage path of this cylinder is shown in Figure 7.20. The bifurcation points are again indicated by arrows. The two bifurcation points are each approximately 15 mm from the edge of the hoop stiffening bands. A close-up photograph of this "triangular" region is shown in Figure 7.21. The nature of the "triangular" region, including the angle between the branched damage, is similar to that of cylinder 1 in which the top 0° ply is missing. After bifurcation, damage continued its propagation in the hoop direction, fracturing and delaminating one set of the longitudinal stiffening bands during its progression. Some debonding of the hoop stiffener from the base cylinder far from the slit region was also observed. Cylinder 4, which is stiffened with four continuous layers of 45° fabric layers, had a similar fracture path as shown in Figure 7.22. However, the bifurcation points in this cylinder are located closer to the edge of the hoop stiffeners (approximately 10 mm). Furthermore, the "triangular" region contains only the bottom two plies (0° and 45° plies), although the angle of the branched damage again coincided with the 45° fibers. Fracture of the longitudinal stiffeners was also observed while damage propagated across the region. As in cylinder 1, damage arrest occurred at the next set of longitudinal stiffeners for both cylinders 3 and 4.

A slightly different fracture behavior was observed when more reinforcement in the longitudinal direction was provided in cylinder 5 as shown in Figure 7.23. This cylinder is stiffened with four layers of continuous 0° fabric and was reinforced with four additional 0° fabric layers

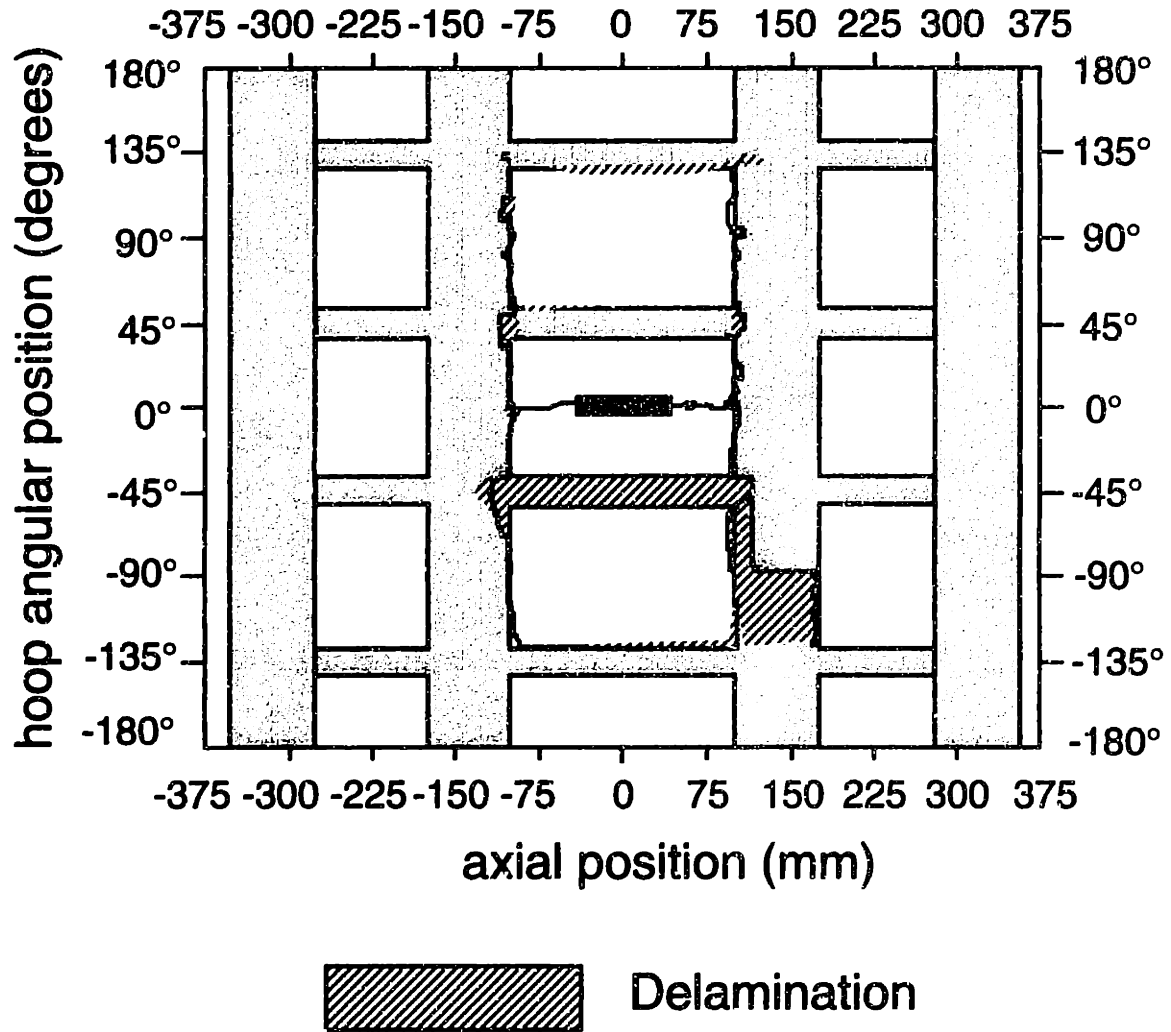


Figure 7.19 Fracture path of cylinder 3 stiffened with four layers of continuous (*type-B*) 0° fabric layers.

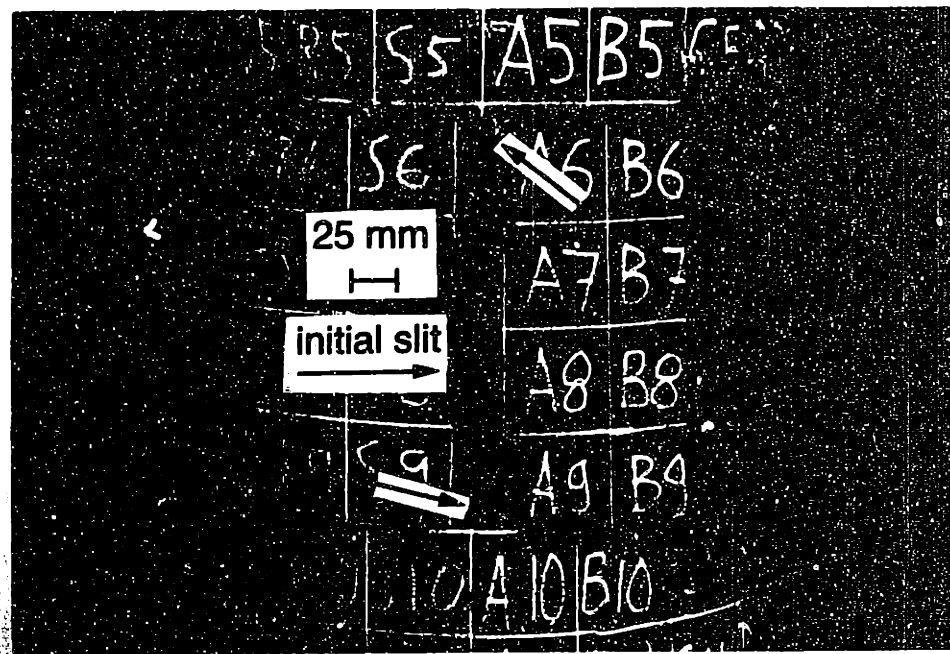


Figure 7.20 Photograph showing damage bifurcation ($\sim 90^\circ$ turn) at the edge of hoop stiffener (arrows indicate the locations of bifurcation points) in cylinder 3.

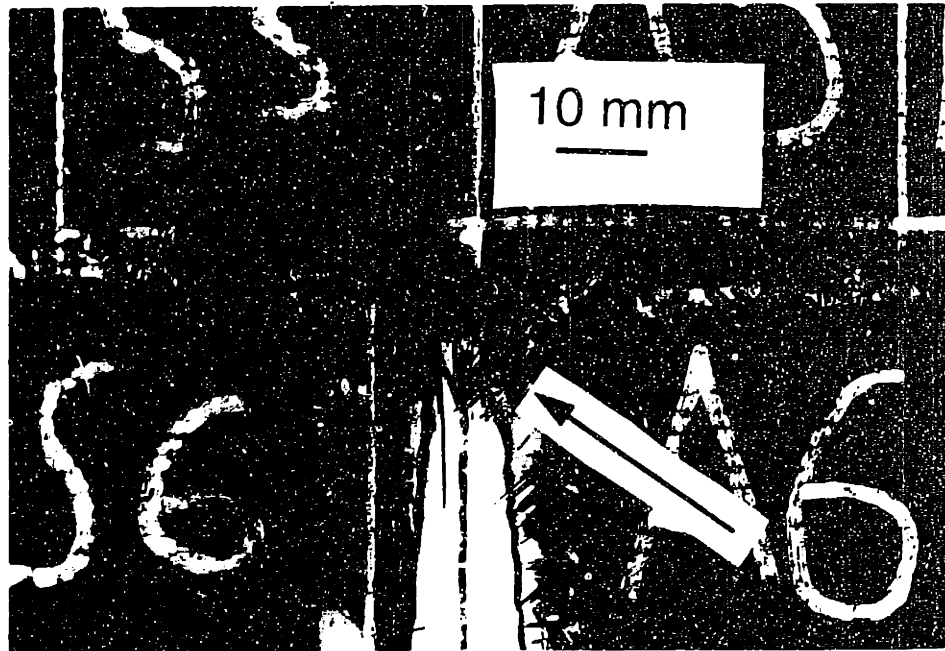


Figure 7.21 Close-up photograph of the "triangular" region near the bifurcation point in cylinder 3.

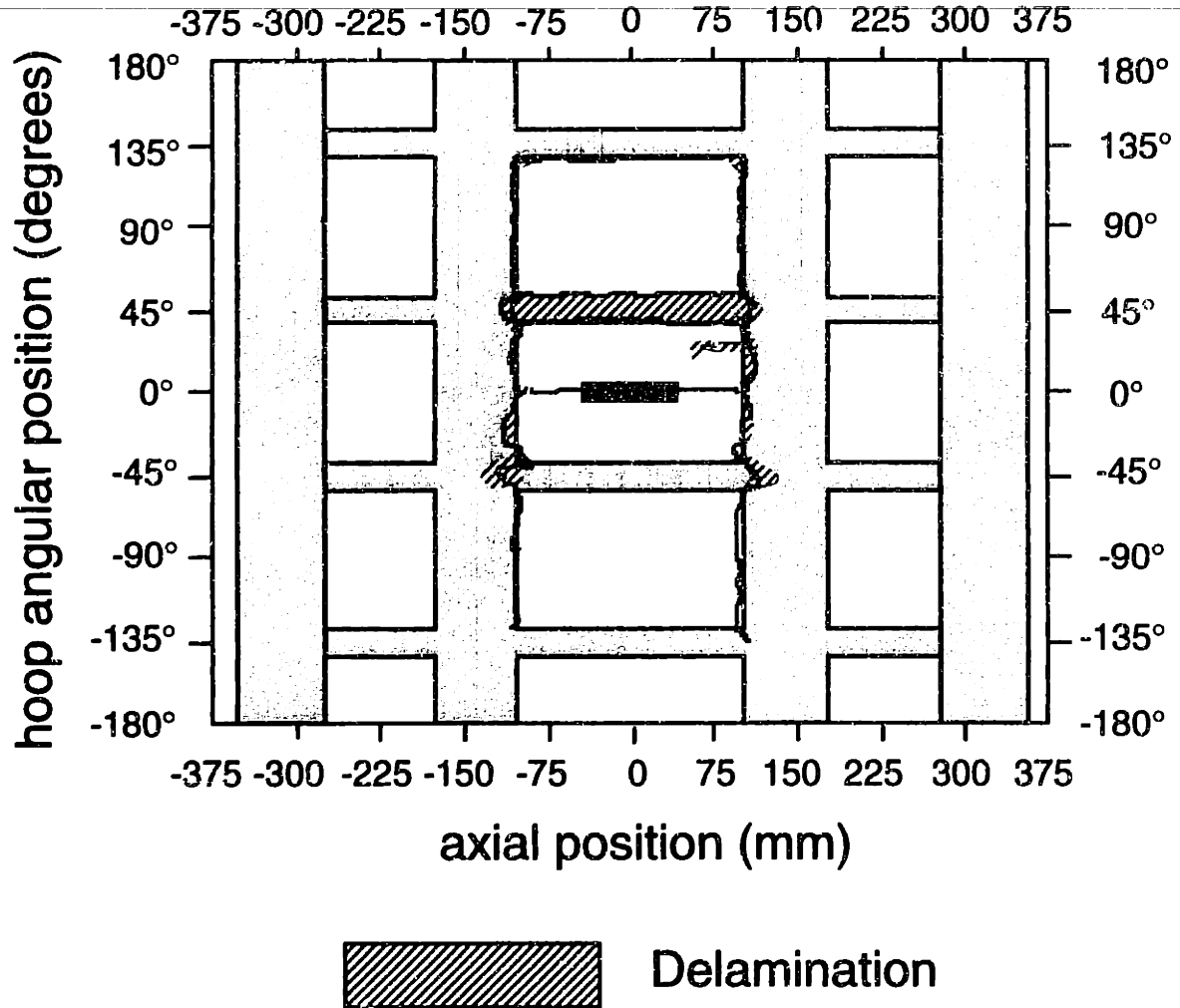


Figure 7.22 Fracture path of cylinder 4 stiffened with four layers of continuous (*type-B*) 45° fabric layers.

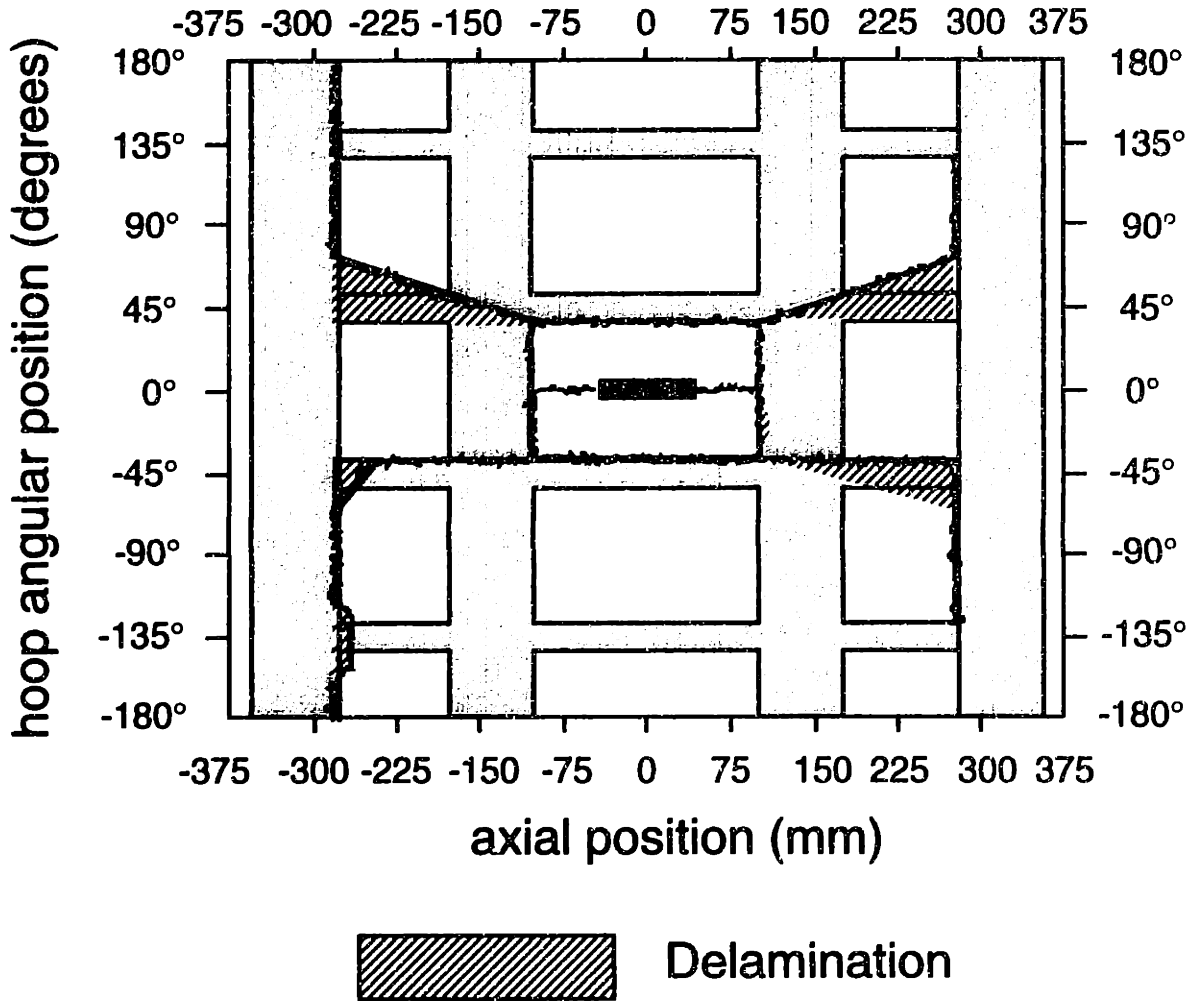


Figure 7.23 Fracture path of cylinder 5 stiffened with four layers of continuous (*type-B*) 0° fabric layers and four additional continuous 0° fabric layers in the longitudinal direction.

in the longitudinal direction. As in cylinders 3 and 4, damage was successfully turned by the hoop stiffeners. The two bifurcation points are each approximately 15 mm from the edge of the hoop stiffening bands, and the nature of the "triangular" region is again similar to that of cylinder 1. Damage then continued its propagation in the hoop direction, reaching the edge of the first set of longitudinal stiffeners where damage redirection to longitudinal propagation was observed. However, some of the bifurcated damage turned and continued to propagate at an angle of approximately 40° from the longitudinal axis of the cylinder, inducing stiffener debonds, fracturing the hoop stiffeners, and delaminating the base cylinder at the $45^\circ/0^\circ$ interface (between the top two plies) in the regions near the location where the two types of stiffener meet. Damage was finally arrested on one side of the second set of longitudinal stiffeners.

In the cylinders where damage bifurcation occurs (cylinders 1, 3, 4, and 5), damage cannot be arrested in the region bounded by the first set of longitudinal stiffeners. In all cases, damage continues its propagation and is not arrested until it reaches the next set of longitudinal stiffeners.

Chapter 8

Discussion

Important findings from the present investigation are discussed in this chapter with the numerical results from Chapter 5 and the experimental results from Chapter 7 used to motivate and provide evidence for discussion. Discussions of the predicted and experimental strain responses are presented in section 8.1. The effects of nonlinearity on the failure of cylindrical shells with longitudinal cracks or slits are discussed in section 8.2. Numerical results on growth simulation in a stiffened case and implications of the results of the damage arrest experiments are discussed in section 8.3. Finally, section 8.4 contains some final notes on the overall issues related to damage tolerance and arrest in fuselage structures.

8.1 Strain Response

The results from the analysis shown in Chapter 5 correctly predict the four basic trends of the measured pressure-strain responses presented in Chapter 7. The response characteristics are: "softening", designated as *type-s1* response; a combination of "softening" and "stiffening", designated as *type-s2* response; "softening" followed by "linear" response, designated as *type-s3* response; and "sign-reversal", designated as *type-s4* response. These are depicted in Figures 7.1a through 7.1d.

To understand the underlying mechanisms of such strain responses, the evolutions of the longitudinal and hoop strain distributions of the (0/45)_s

cylinder with a slit length of 104 mm along the slit axis are obtained from the numerical analysis results. For these distributions, the total and bending strains are computed on the top skin surface. Both the absolute and normalized (with respect to the membrane values in the far-field region at the corresponding pressure levels) strain distributions (membrane, bending, and total) are obtained. As presented in Chapter 5, the nonlinear effects are localized near the slit region. In the far-field region, both the linear and nonlinear solutions are identical. Thus, the far-field strain values provide a consistent normalization factor for both the linear and nonlinear solutions.

The evolution of the longitudinal strain distribution is presented in Figures 8.1, 8.2, and 8.3 for the absolute total, membrane, and bending components, respectively. The evolution of the normalized longitudinal strain distribution is shown in Figures 8.4, 8.5, and 8.6 for the total, membrane, and bending cases, respectively. Similarly, the evolution of the hoop strain distribution is presented in Figures 8.7 to 8.12.

In these evolutions, progression from linear (exhibited by the distribution at the lowest pressure of 0.01 MPa) to nonlinear responses at higher pressure levels can be seen clearly in the strain distributions. These nonlinear effects are apparent in the regions of interest (i.e. in the vicinity of the slit tip and in the midslit region). The general effect is well-demonstrated in the normalized hoop strain distribution ahead of the slit tip as shown in Figure 8.10. The strain attains a very high value at the slit tip and decreases rapidly. In the linear solution, exhibited by the distribution at the lowest pressure level, the strain continues to decrease, reaches a minimum (compressive) value, and then increases again and finally reaches its far-field value. A "well" in the total hoop strain distribution is formed due to a significant bending gradient in the region near the slit tip. However, as

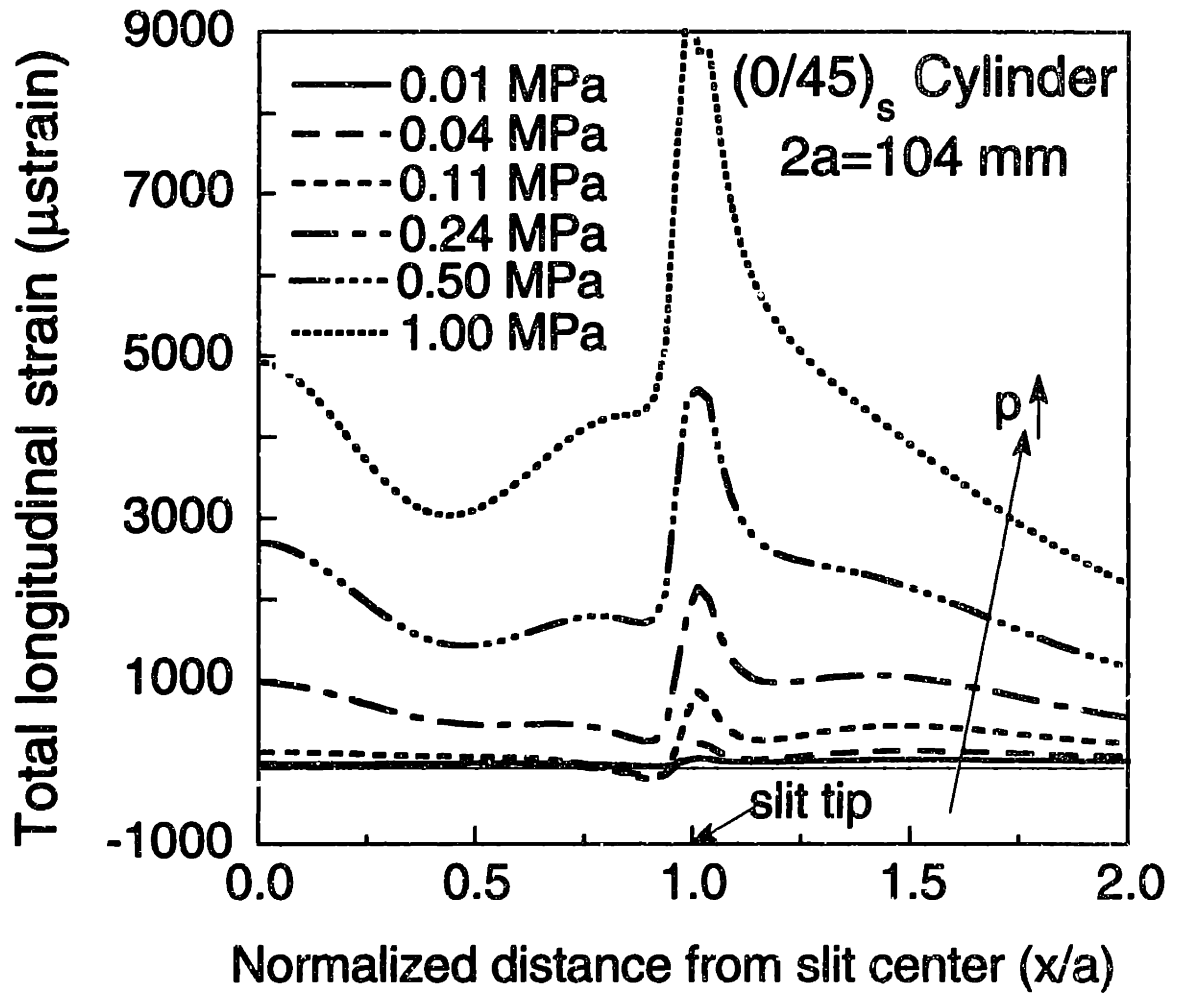


Figure 8.1 Evolution with increasing pressure of the longitudinal total strain distribution on the top skin surface.

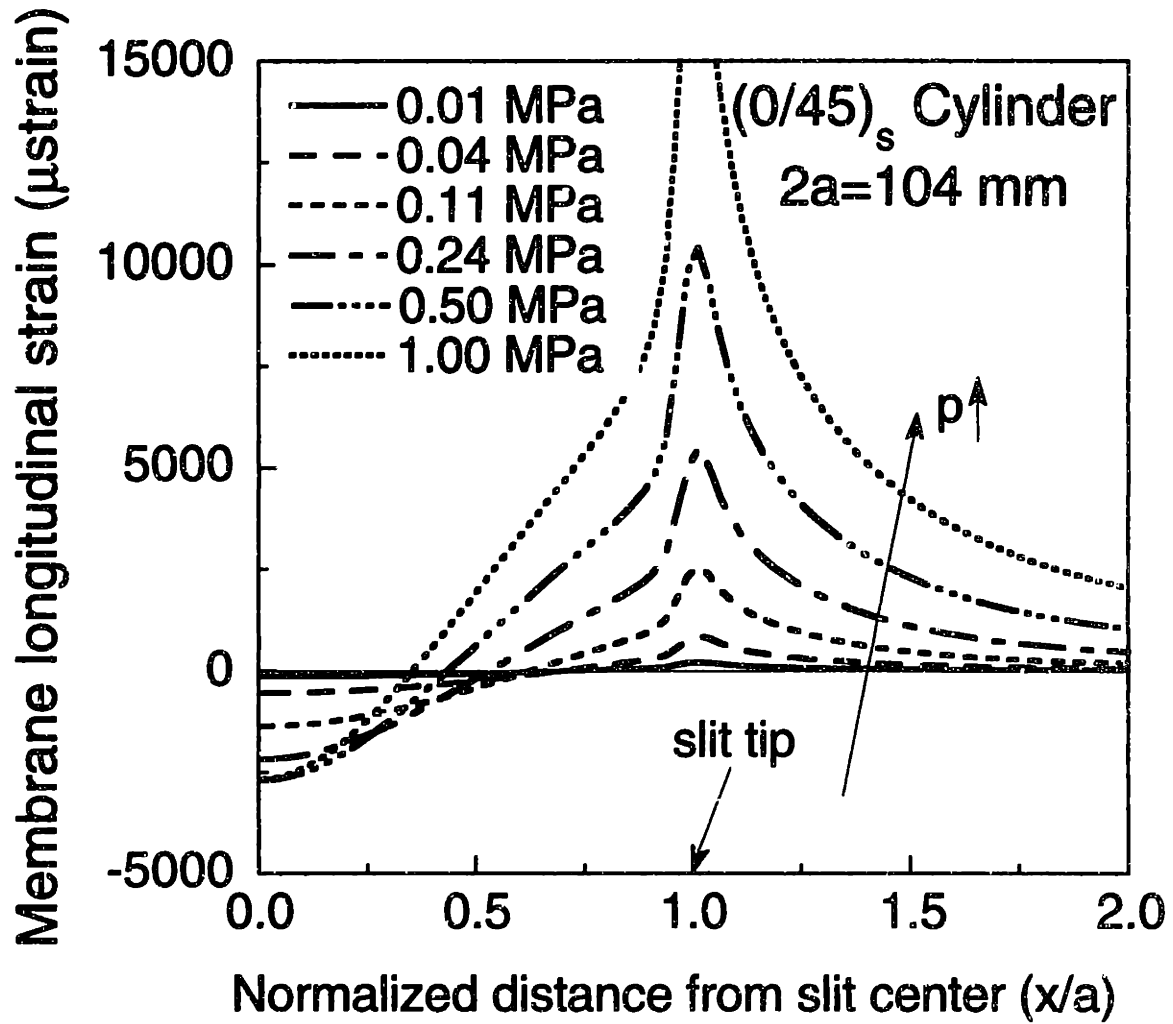


Figure 8.2 Evolution with increasing pressure of the longitudinal membrane strain distribution on the top skin surface.

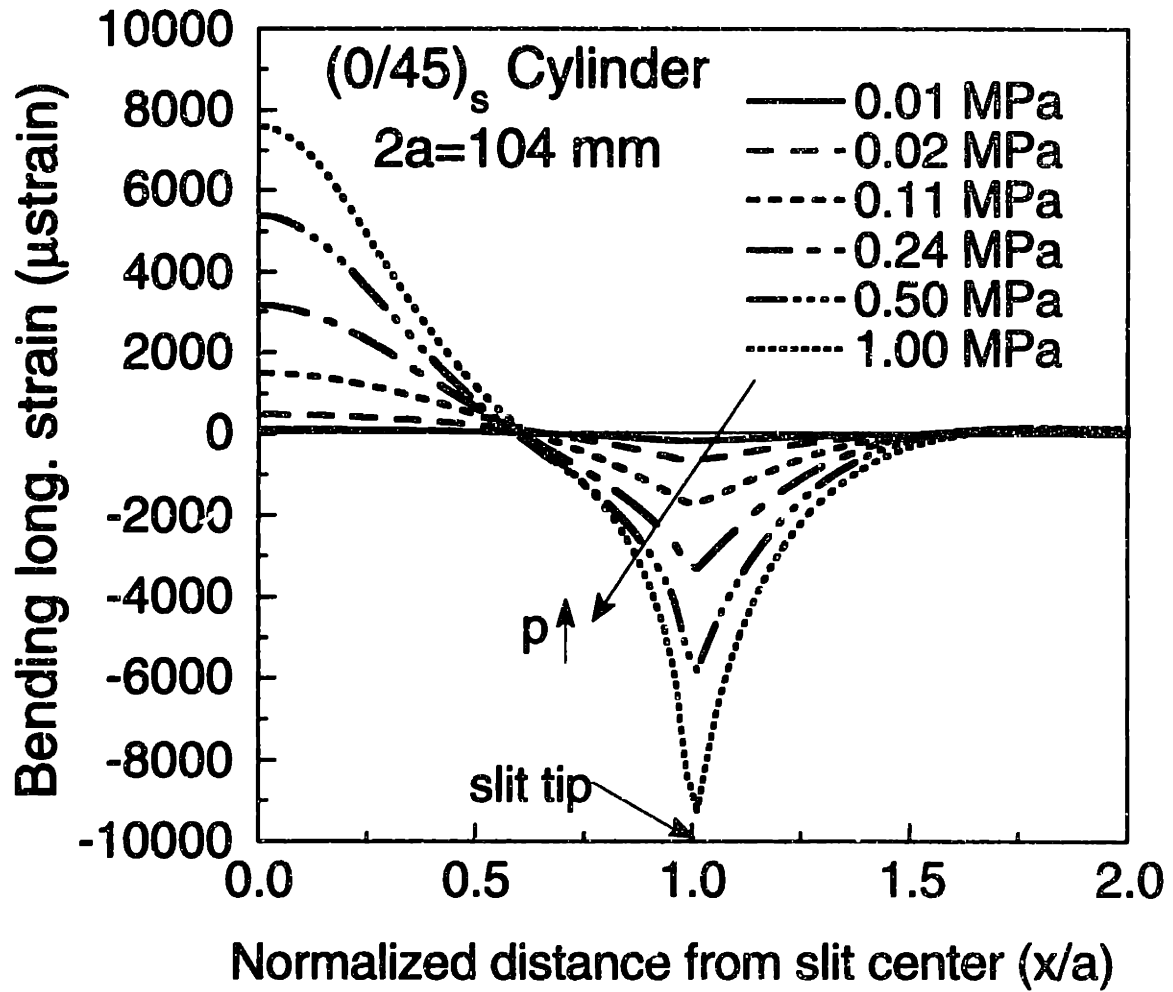


Figure 8.3 Evolution with increasing pressure of the longitudinal bending strain distribution on the top skin surface.

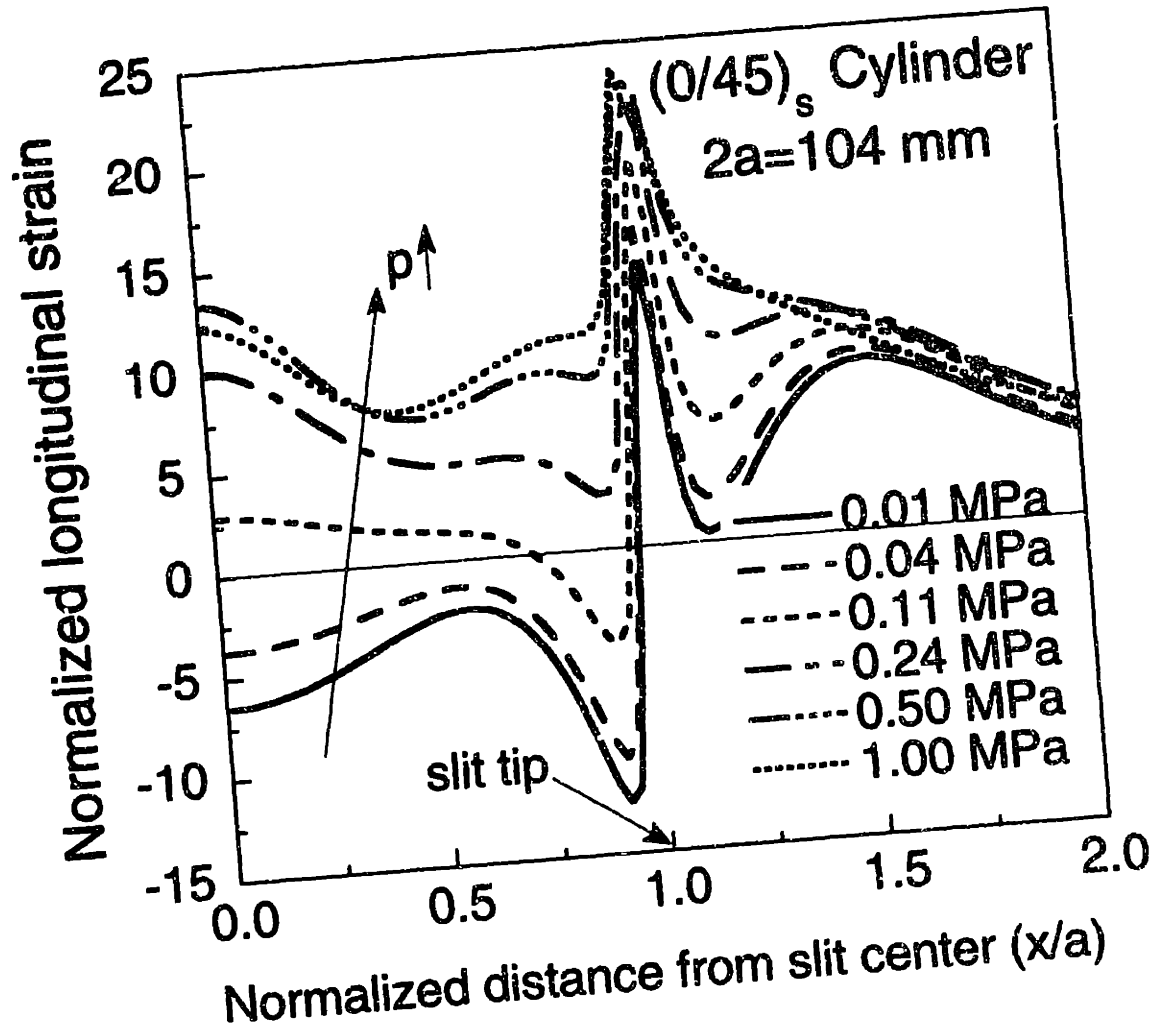


Figure 8.4 Evolution with increasing pressure of the normalized longitudinal total strain distribution on the top skin surface (normalized by the corresponding far-field linear membrane strain).

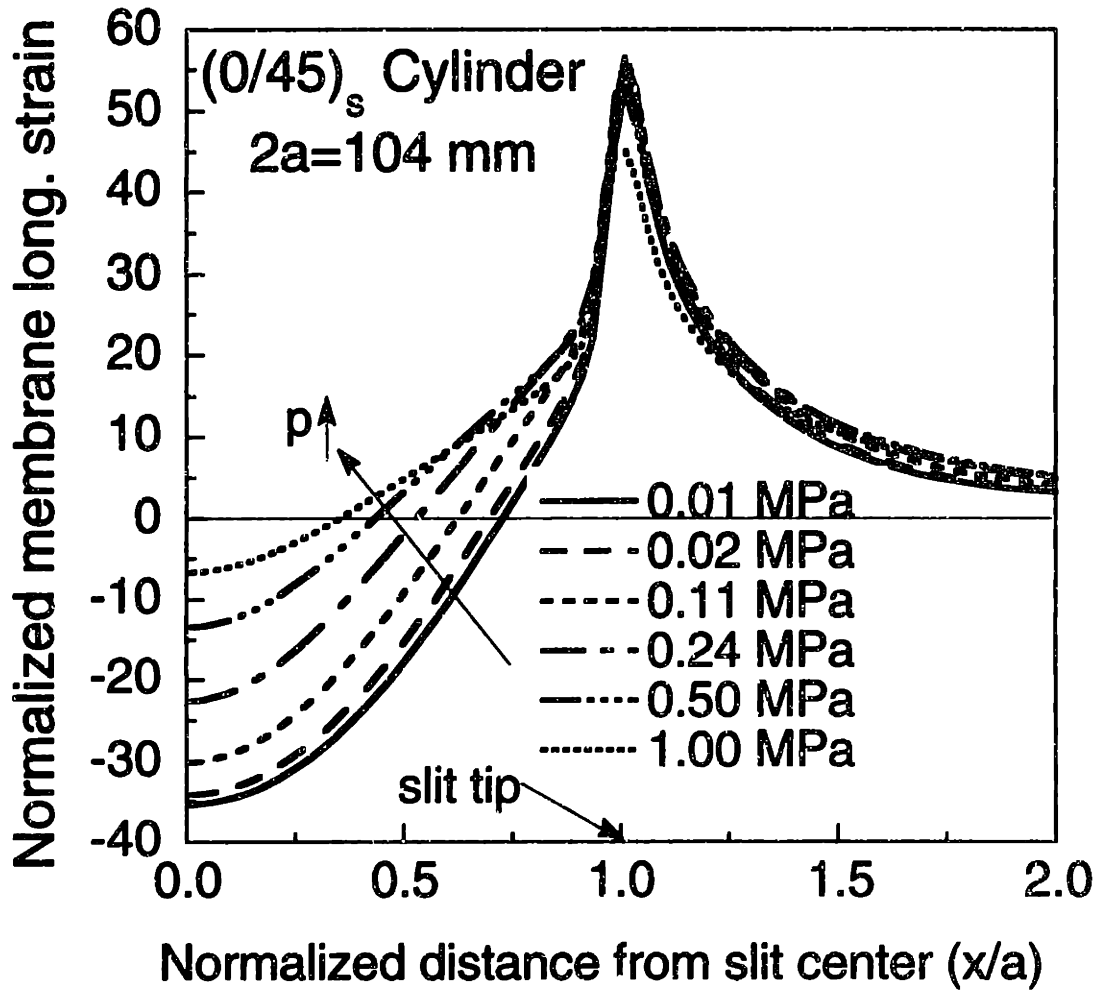


Figure 8.5 Evolution with increasing pressure of the normalized longitudinal membrane strain distribution on the top skin surface (normalized by the corresponding far-field linear membrane strain).

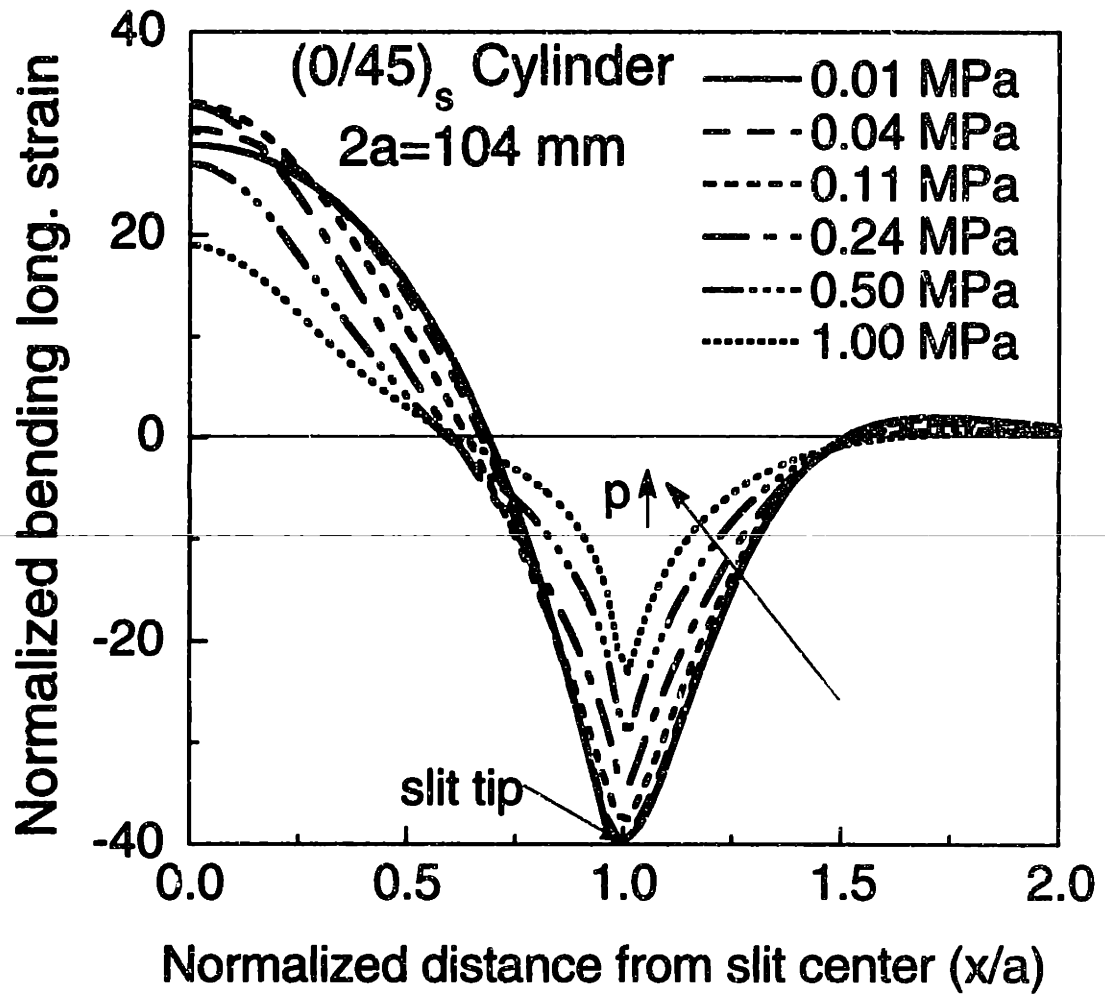


Figure 8.6 Evolution with increasing pressure of the normalized longitudinal bending strain distribution on the top skin surface (normalized by the corresponding far-field linear membrane strain).

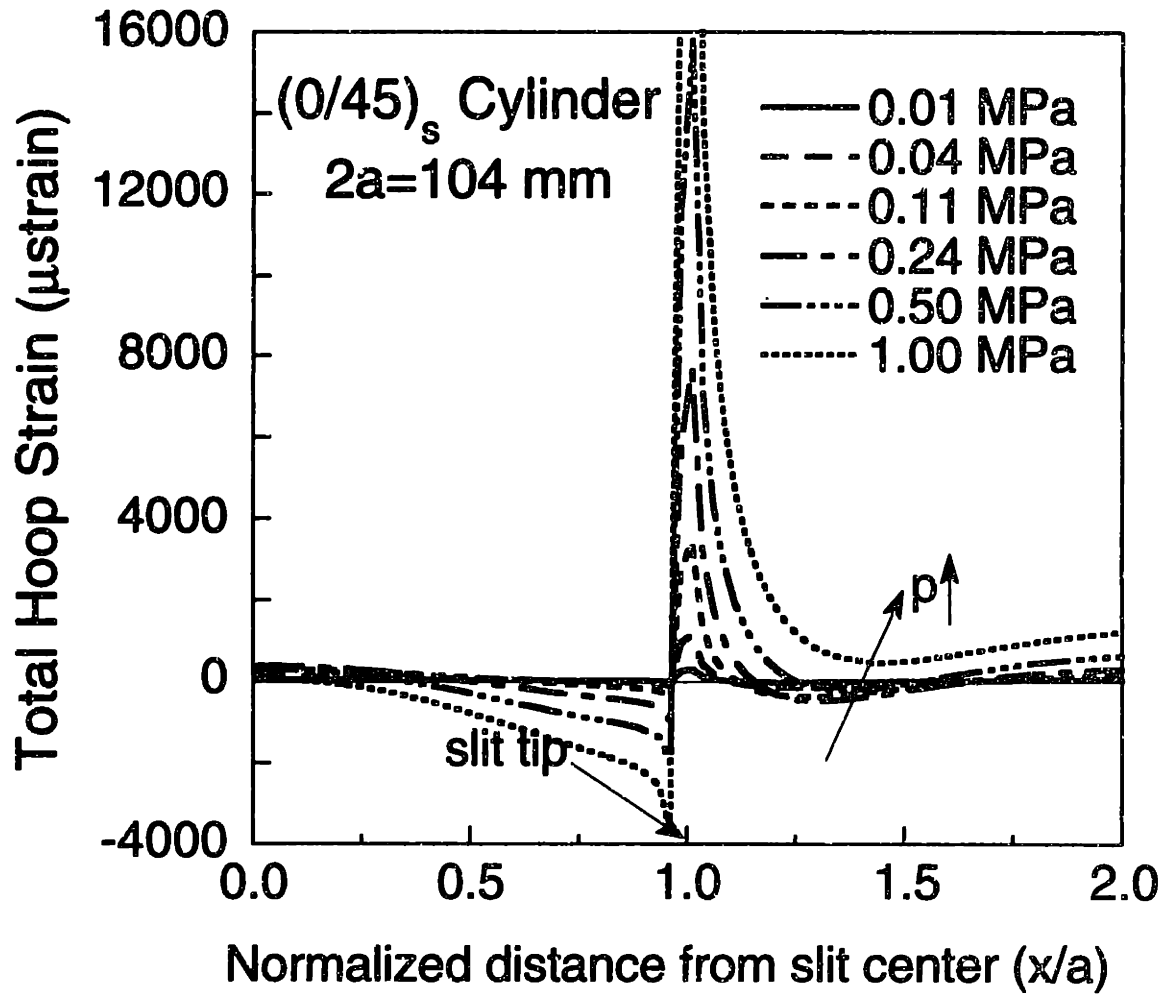


Figure 8.7 Evolution with increasing pressure of the hoop total strain distribution on the top skin surface.

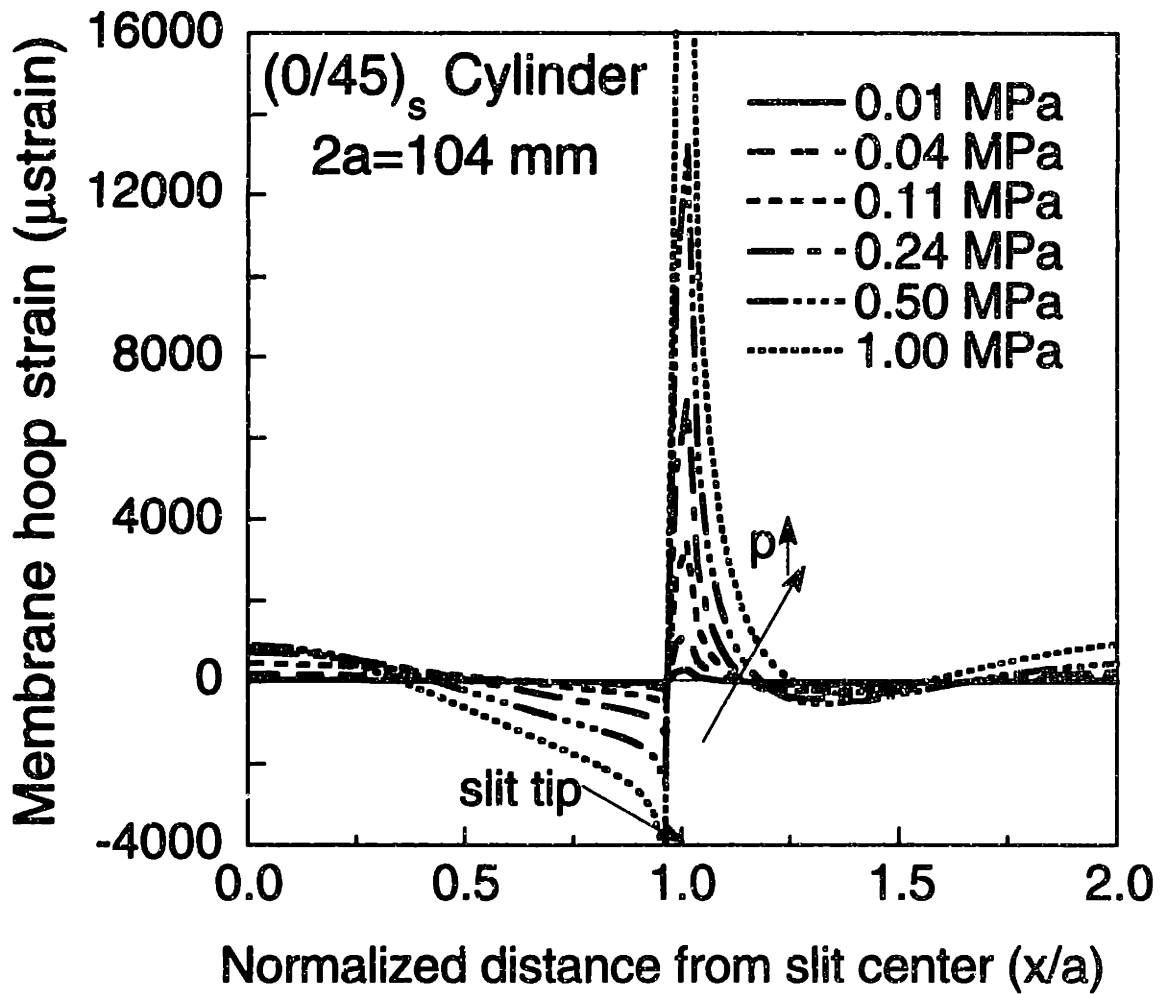


Figure 8.8 Evolution with increasing pressure of the hoop membrane strain distribution on the top skin surface.

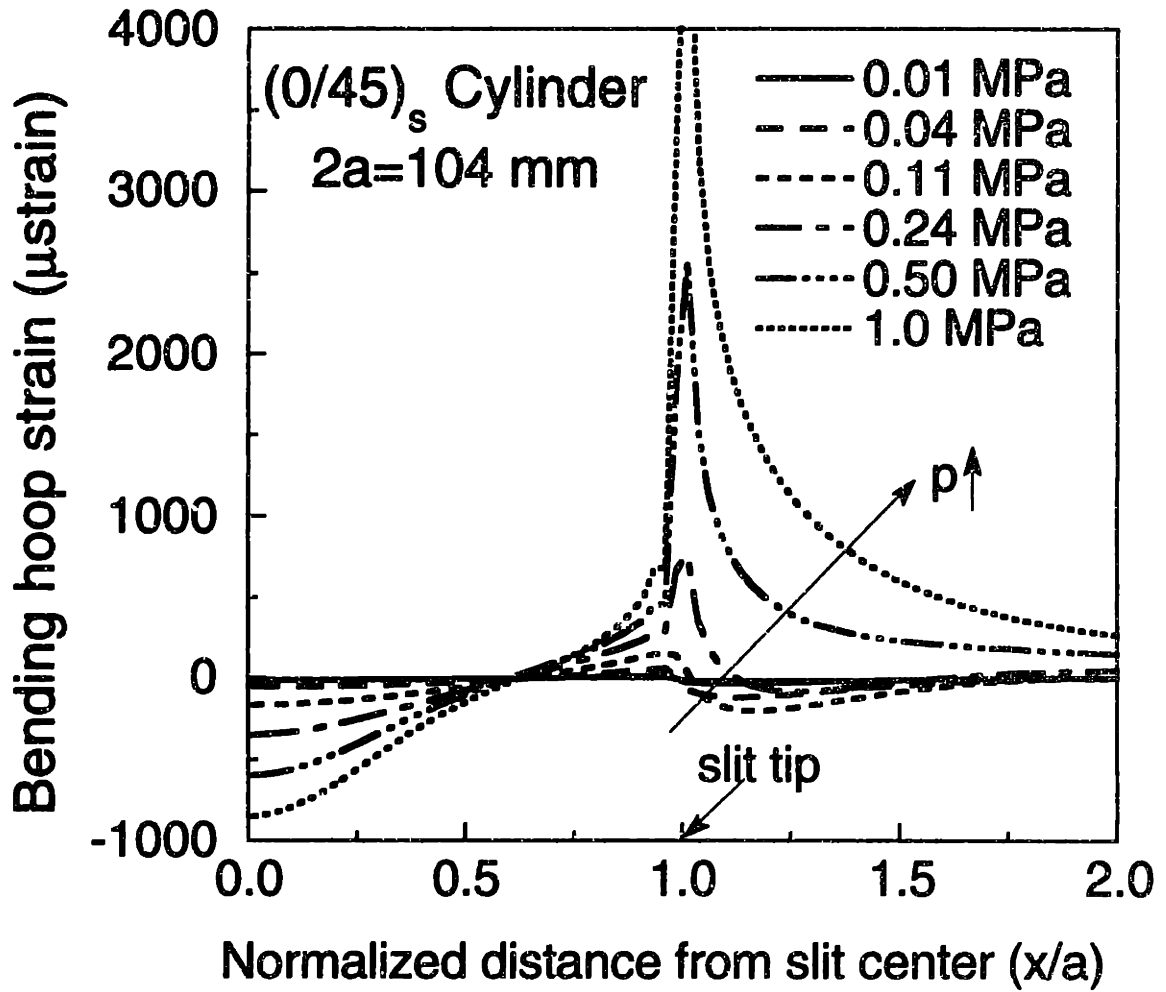


Figure 8.9 Evolution with increasing pressure of the hoop bending strain distribution on the top skin surface.

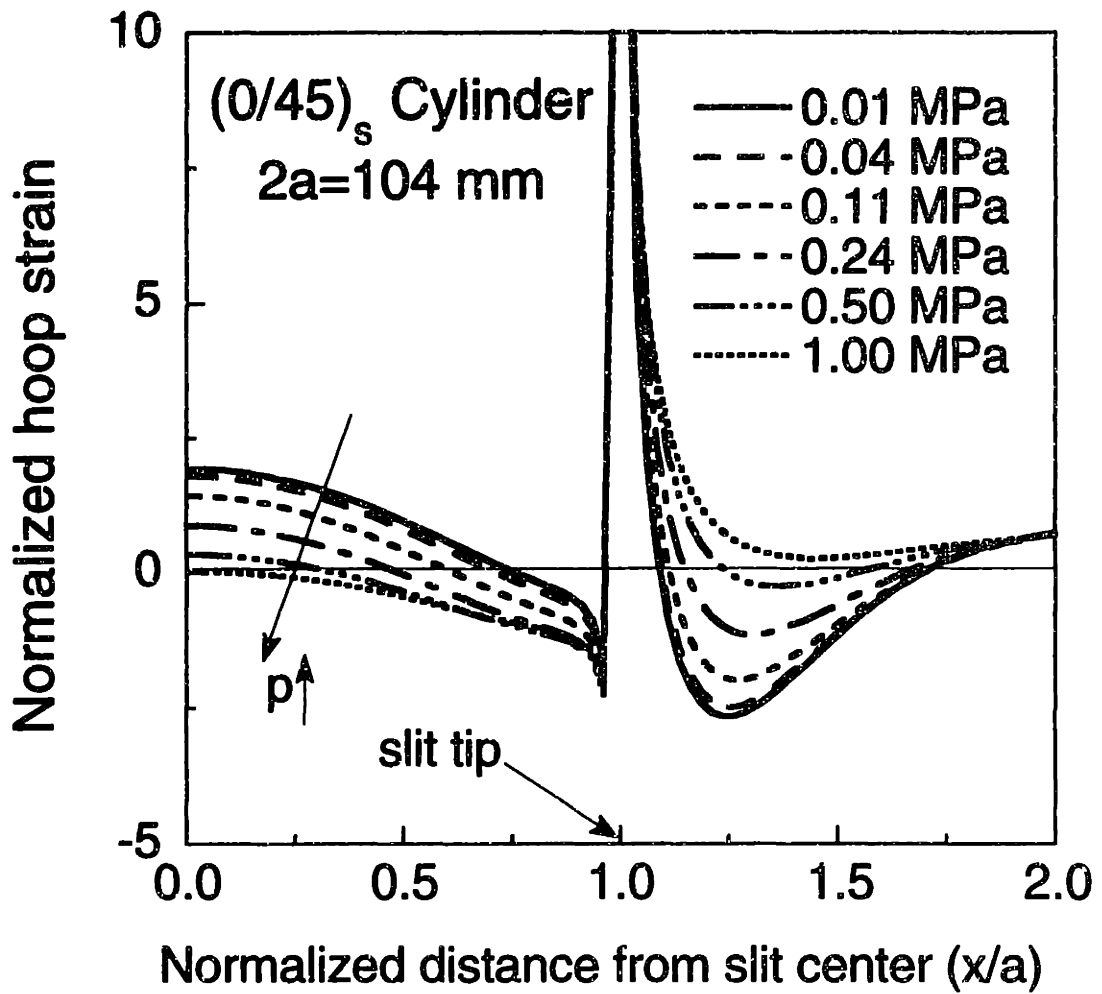


Figure 8.10 Evolution with increasing pressure of the normalized hoop total strain distribution on the top skin surface (normalized by the corresponding far-field linear membrane strain).

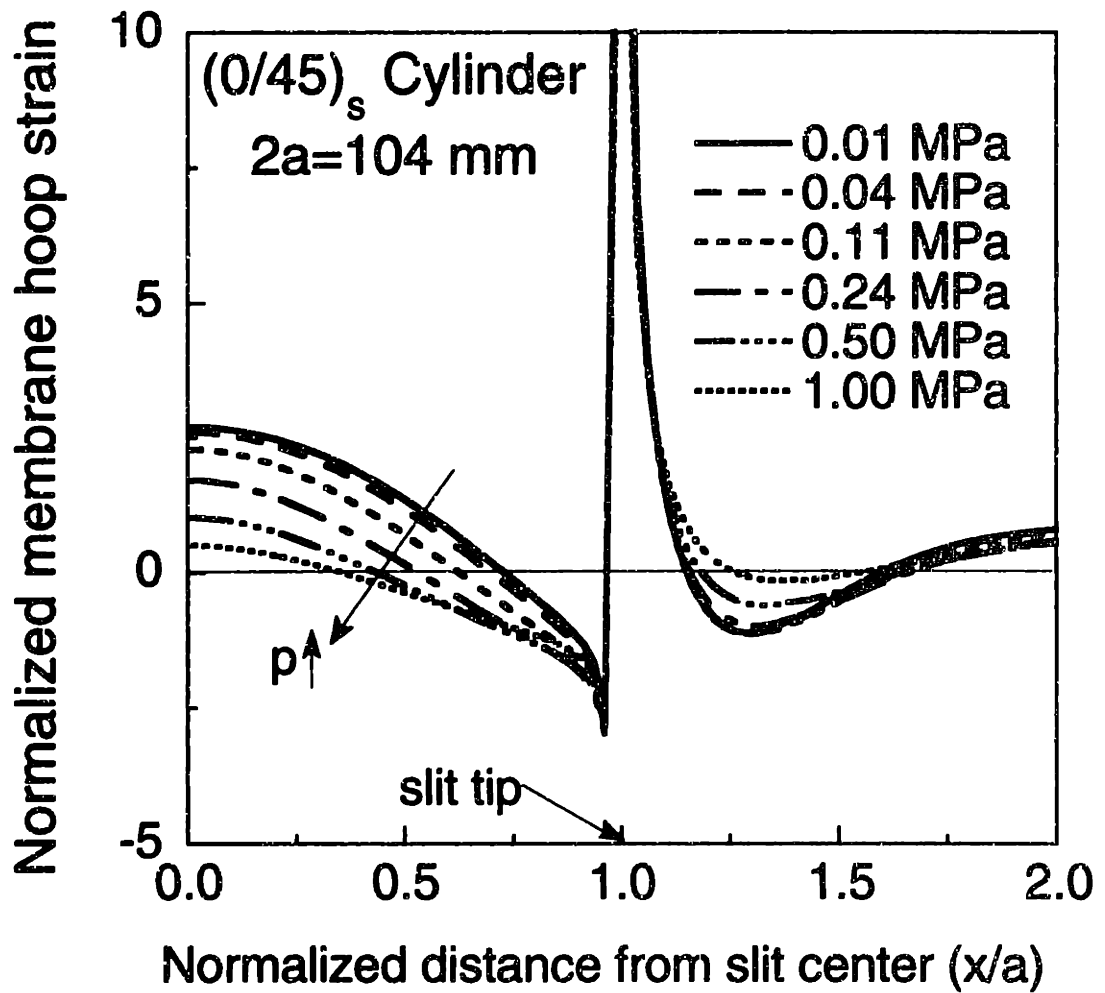


Figure 8.11 Evolution with increasing pressure of the normalized hoop membrane strain distribution on the top skin surface (normalized by the corresponding far-field linear membrane strain).

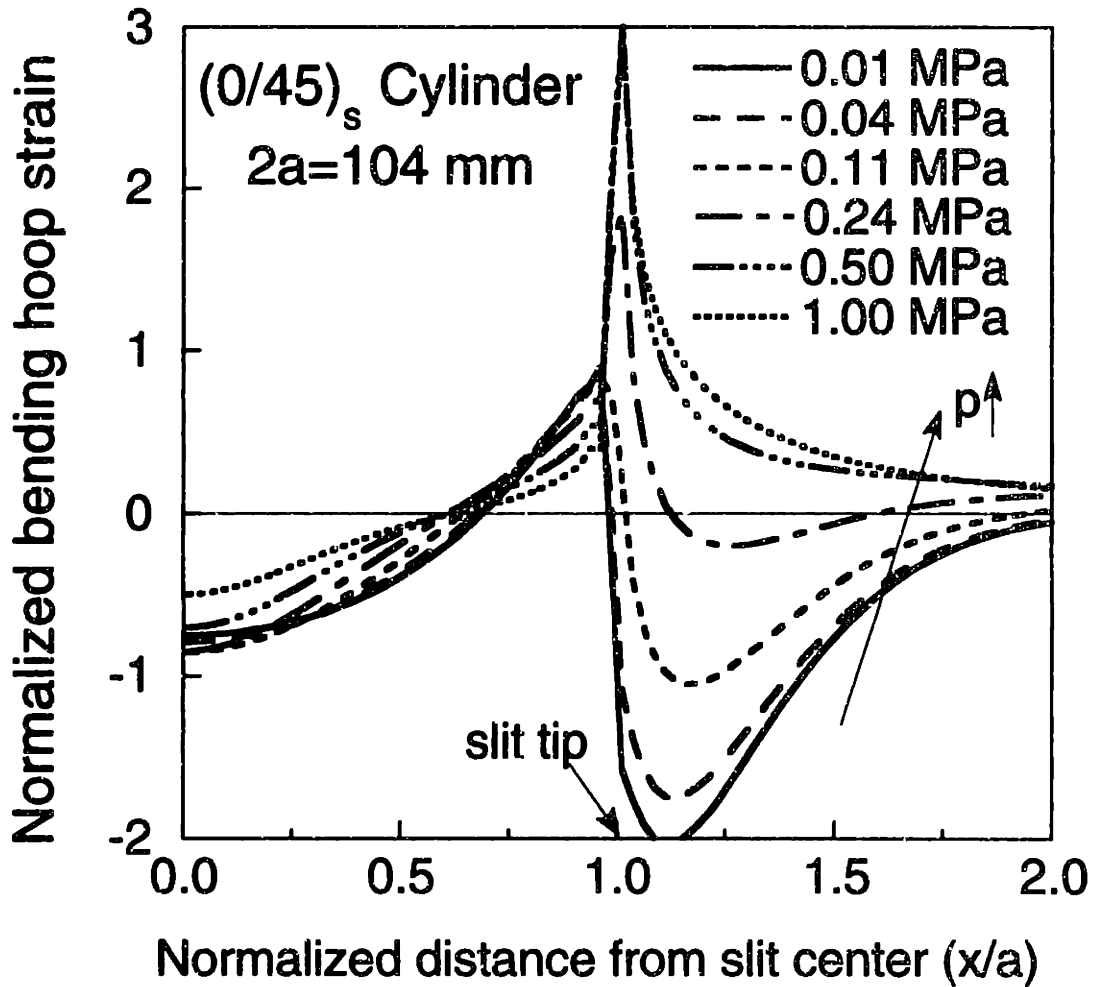


Figure 8.12 Evolution with increasing pressure of the normalized hoop bending strain distribution on the top skin surface (normalized by the corresponding far-field linear membrane strain).

nonlinear effects become more important (i.e. as pressure increases), there exists the so-called membrane stiffening which makes the bending contribution less negative and causes it to become tensile ahead of the slit tip as depicted in Figure 8.12. Thus, any "wells", that is significant strain gradients, in the total strain distribution become more and more shallow as pressure increases due to these membrane-stiffening actions.

The four types of strain responses presented in Chapter 7 are therefore (local) manifestations of the combined effects of nonlinearity on the membrane and bending strain components. Among the four characteristic strain responses, *type-s4* ("strain-reversal") is the one that can be seen most clearly in the strain evolution curves. From Figures 8.1 and 8.7, this "reversal" can be seen in the regions behind ($x/a < 1$) and ahead ($x/a > 1$) of the slit tip for the longitudinal and hoop strain distributions, respectively. In the longitudinal strain distribution, it is noted that the membrane contribution remains compressive in the midslit region for all pressure levels as shown in Figure 8.2. In the same region, the bending part, which is initially very small and tensile at low pressure, remains tensile and increases in magnitude as pressure increases as shown in Figure 8.3. Thus, a "reversal" in the total longitudinal strain in this region is caused primarily by the bending effects that overcome the membrane contribution. A "reversal" in the hoop strain distribution can be seen in two separate regions: one, behind the slit tip between x/a of 0.3 and 0.7 and, two, ahead of the slit tip (between $0.09 a$ and $0.70 a$ from the slit tip) as shown in Figure 8.7. Unlike the longitudinal case, both the membrane and bending hoop strain responses in those two regions described before show "strain-reversal" trends. Note that the bending contribution is more significant than the membrane part in both regions.

A good experimental example of this "strain-reversal" phenomenon can be seen in the strain response of gage 3. This gage is the farthest hoop gage (approximately 12 mm) from the slit tip in the slit tip region. The membrane, bending, and total strain responses of that gage are shown in Figure 8.13. Both the membrane and bending strain responses show "strain-reversal". This is consistent with the numerical results shown previously in Figure 8.7 where "reversal" in both the membrane and bending distributions are noted.

The other types of response (such as "softening", a combination of "softening" and "stiffening", and "softening" followed by "linear" response) are all due to the same nonlinear effects on the overall cylinder deformation. However, the manifestation of nonlinearity on the evolutions of strain distributions for other types of response is not as clearly visible as the "reversal" discussed previously. The nonlinear effects for each type of local response are considered individually next.

The membrane, bending, and total strains for a *type-s1* ("softening") strain response, which is exhibited by the response of gage 1, are shown in Figure 8.14. The membrane strain shows a "stiffening" response which looks "bilinear" with a clear "transition" point. The bending strain computed on the top skin surface shows a "sign-reversal" in which the sign changes from negative (compressive) to positive (tensile) at approximately the same "transition" point as the membrane part. Therefore, the overall "softening" response in the total response is apparently due to a "sign-reversal" in the bending strain response in conjunction to membrane stiffening.

The membrane, bending, and total strains for a *type-s2* (a combination of "softening" and "stiffening") response, which is exhibited by the response of gage 9, are shown in Figure 8.15. In this case, the membrane strain response shows "stiffening". Unlike the *type-s1* case, however, the "stiffening" does not

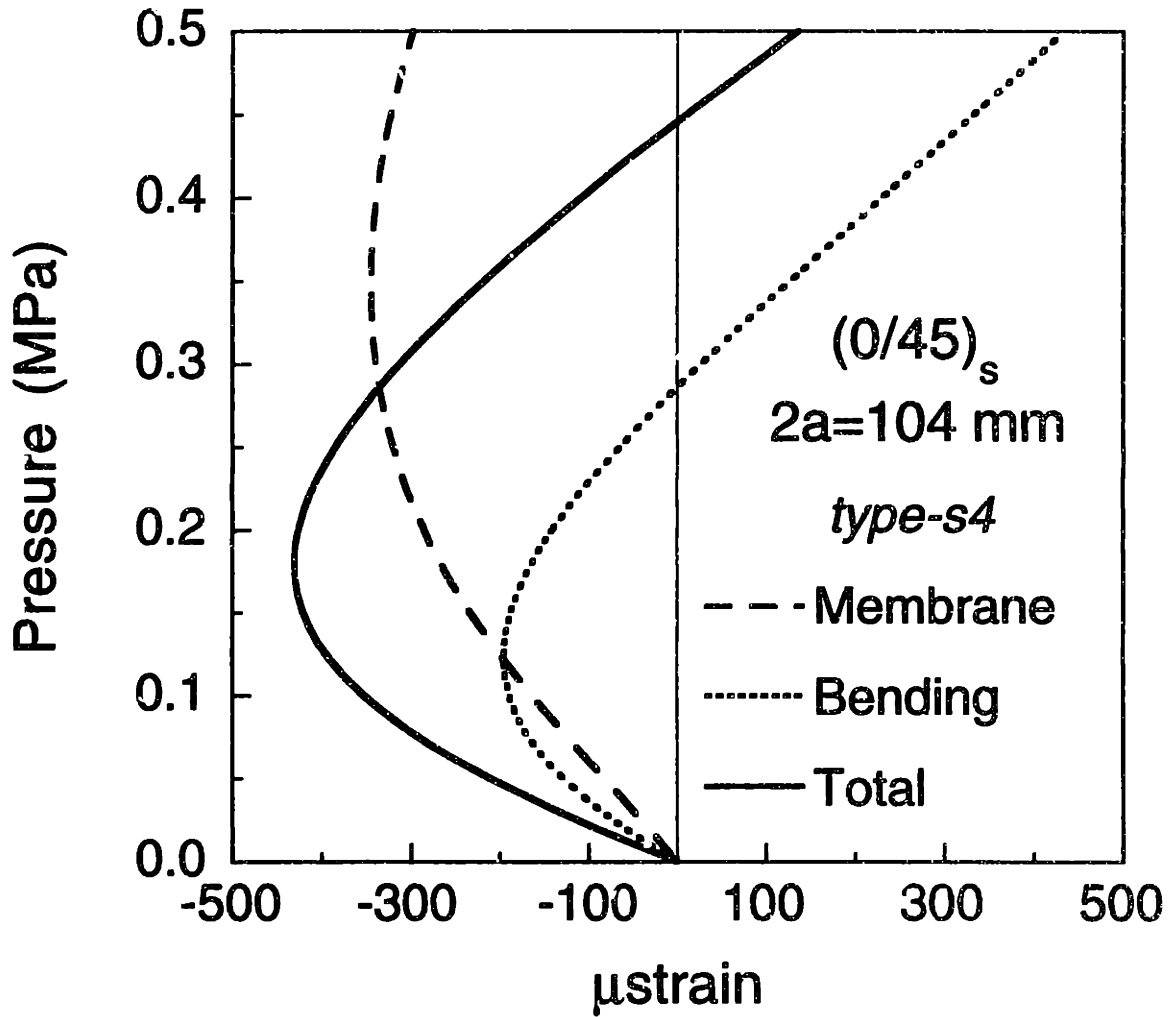


Figure 8.13 Contributions of the membrane and bending parts to the *type-s4* strain behavior.

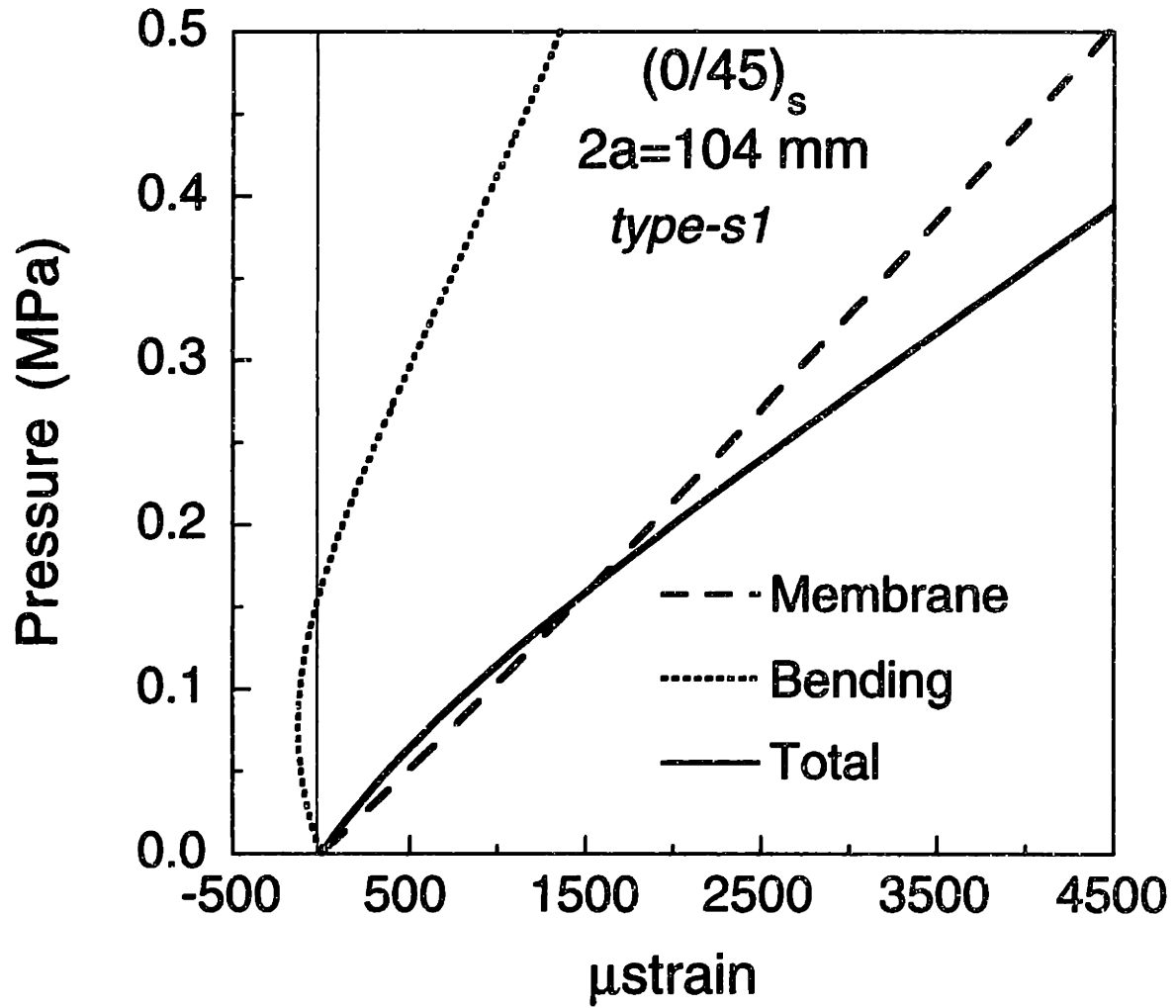


Figure 8.14 Contributions of the membrane and bending parts to the *type-s1* strain behavior.

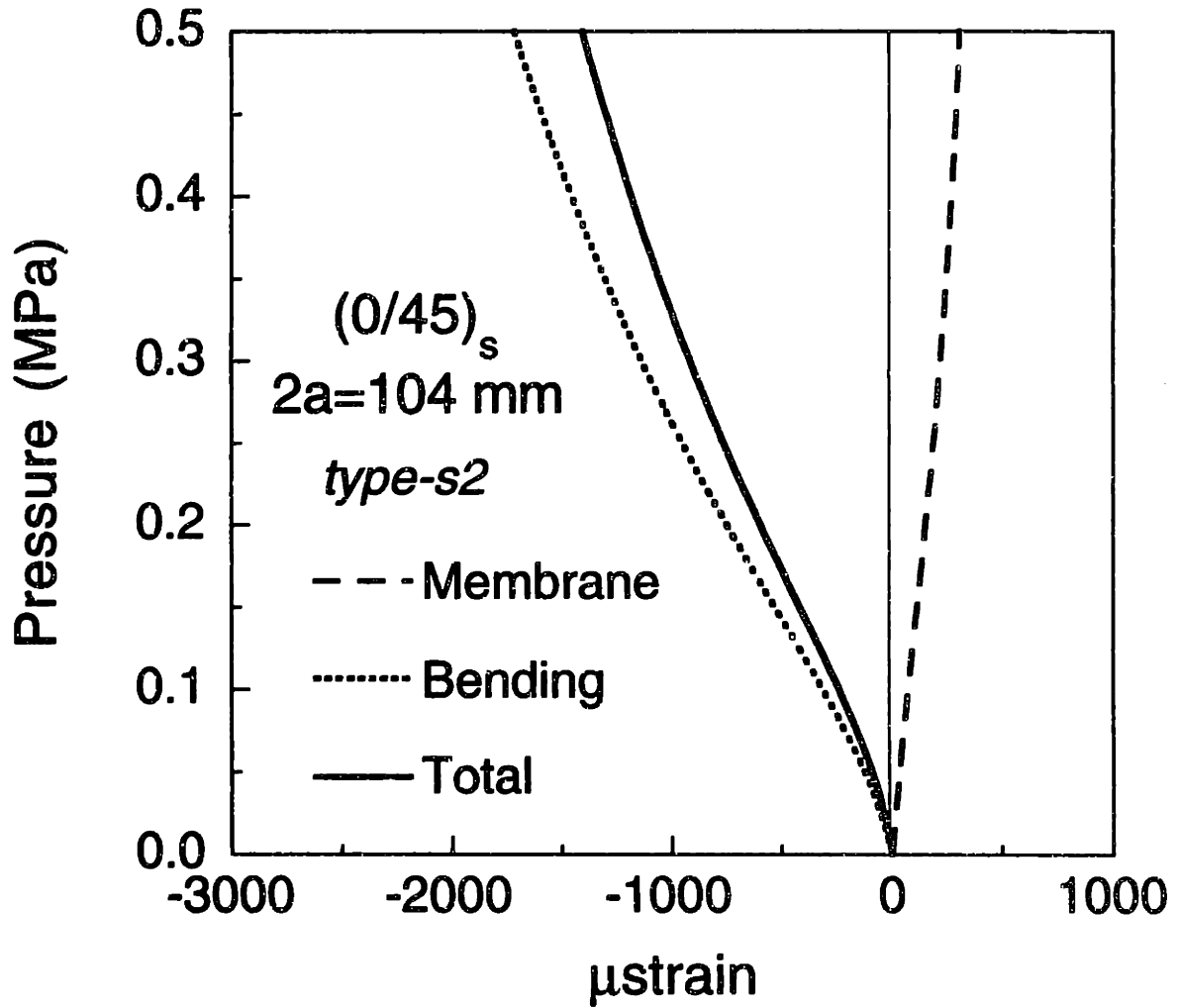


Figure 8.15 Contributions of the membrane and bending parts to the *type-s2* strain behavior.

appear "bilinear" and the "transition" point is not apparently obvious in this case. The shape of the bending strain computed on the top skin surface is similar to that of the total strain and shows a combination of "softening" and "stiffening". The membrane and bending strain values at a point can be of opposite sign as shown by the normalized membrane and bending longitudinal strain distributions in Figures 8.2 and 8.3 in the vicinity of the midslit region and in the region ahead, and in the vicinity of, the slit tip. Thus, there is a "trade off" between the bending and membrane actions. Since the nonlinear effects are greater in the bending distribution in this case, the overall (total) shape follows that of the bending response.

The separate contributions from the membrane and bending actions on a *type-s3* ("softening" followed by "linear") response, which is exhibited by the response of gage 4, are shown in Figure 8.16. Both the membrane and bending strains in this case show "stiffening" behavior with the bending component showing a somewhat higher degree of "stiffening" than the membrane strain. As in the *type-s2* case, the bending contribution in this case decreases the magnitude of the membrane strain as the two of them show different states of strain (i.e. compressive versus tensile). Thus, the total strain in a *type-s3* ("softening" followed by "linear") response is influenced by the "stiffening" responses in both the membrane and bending components.

All four strain characteristics discussed previously are all interplay of geometric nonlinearity effects on membrane and bending components. Note that the linear analysis predicts strain response that just scales linearly with loading and the shapes of the longitudinal and hoop strain distributions obtained from such an analysis do not change with loading. Therefore, if only

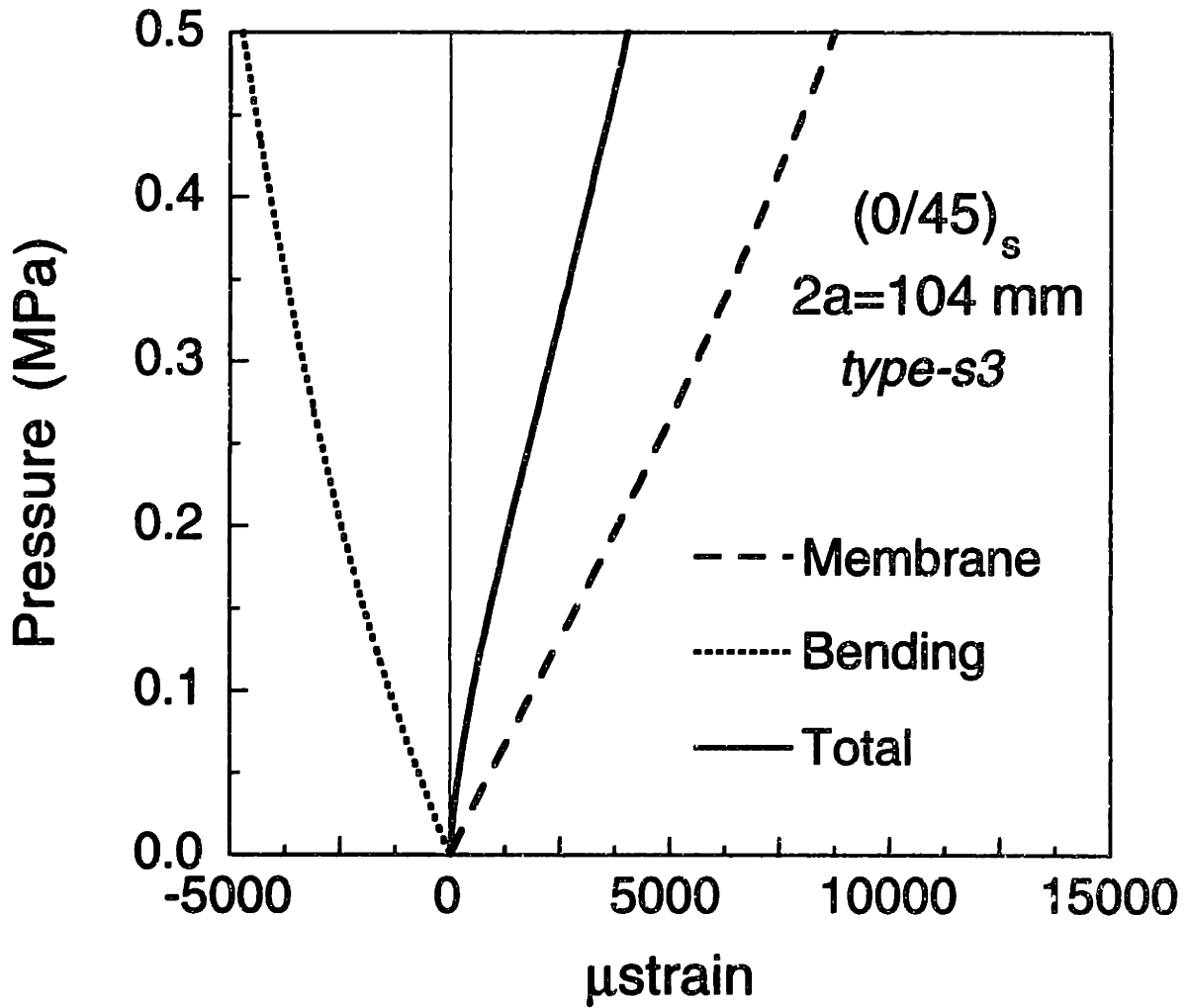


Figure 8.16 Contributions of the membrane and bending parts to the *type-s3* strain behavior.

linear analysis is performed, both the magnitudes and shapes of the strain responses will be incorrectly predicted.

Despite the general agreement in the trends between the predicted and measured strain responses, there does exist some disagreement in the magnitude of the predicted and measured strains. The discrepancies can be seen in the response of the hoop gage closest to the slit tip (gage 1) and in those of the two hoop gages located farthest from the slit axis in the midslit region (gages 8 and 9). For example, the analysis underpredicts the measured responses of gage 1 as shown in Figure 7.2 and of gage 9 as shown in Figure 7.4 by a factor of 2 or even greater in some cases. Gage 1 is located approximately 2.5 mm from the slit tip, and gage 9 is located at approximately 25.2 mm from the slit axis. Sensitivity studies on the placement of strain gages were performed up to approximately 2.0 mm from the measured center gage location. This distance was chosen for two main reasons. First, points on the cylinder surface located at distances greater than 2.5 mm from the measured center gage location are not realistic since such points are located behind, and not ahead of, the slit tip for this cylinder configuration. The second reason is that a strong gradient in the hoop strain distribution, as can be seen in Figure 8.7, occurs very close to the slit tip (within a few millimeters). Thus, the sensitivity range of 2.0 mm is chosen.

The predicted hoop strain responses at several locations near the slit tip are shown in Figure 8.17. The predicted reading is shown to be very sensitive to gage placement. A slight deviation from the measured center gage location, which is on the order 1.5 mm to 2.0 mm, makes the agreement between the predicted and measured responses better. Furthermore, as mentioned in Chapter 7, the use of strain gages to get the strain readings involves some kind of "averaging" over a finite region. The size of this finite

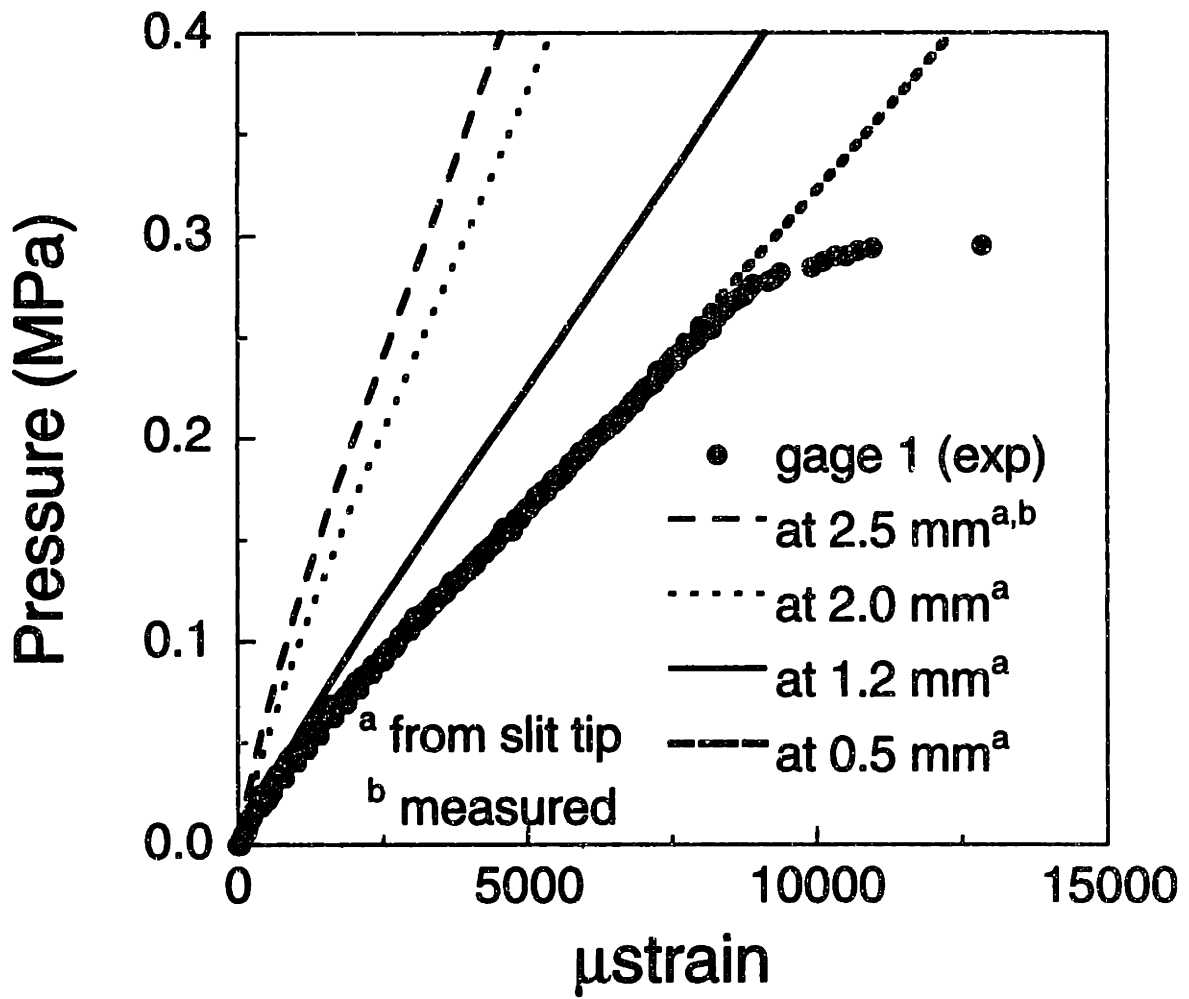


Figure 8.17 Sensitivity of gage placement on the predicted strain response of gage 1 (the closest hoop gage to the slit tip)

region is equal to the size of the active element in a gage (approximately 3.5 mm by 3.0 mm). Since the size of the finite element in this slit tip region is 1.3 mm, the "averaging" takes place in an area covered by approximately nine elements. The strain measurement technique, which involves "averaging" over a finite area, is therefore not expected to be accurate in a region where a significant strain gradient occurs. Thus, both the existence of strain gradient and the "averaging" technique used in the strain measurement technique utilized cause disagreement between the predicted and measured strain responses of gage 1.

The predicted hoop strain responses at several locations in the midslit region are shown in Figure 8.18. Sensitivity studies on the placement of strain gages were performed up to approximately 2.5 mm from the measured center gage location. Although the distance of 2.5 mm is somewhat arbitrary, such a distance is actually realistic and of roughly the same size as the length of an active gage element. Unlike the response of gage 1, however, the numerical responses obtained at different points are apparently insensitive to gage misplacement. Changing the locations of the gages does not seem to bring the experimental and predicted strain values any closer. To understand this, the hoopwise distributions of the total, membrane, and bending hoop strain in the midslit region (at $x/a = 0$) are shown in Figure 8.19, 8.20, and 8.21, respectively. The location of gage 9 is noted in each figure. Although this particular gage is located in the region of "mild" strain gradient due to the "bulging" (bending) phenomenon, the numerical response is not sensitive to gage misplacement. Apparently, the finite element mesh used in the present numerical modelling does not accurately capture the nonlinear strain gradient locally in this region.

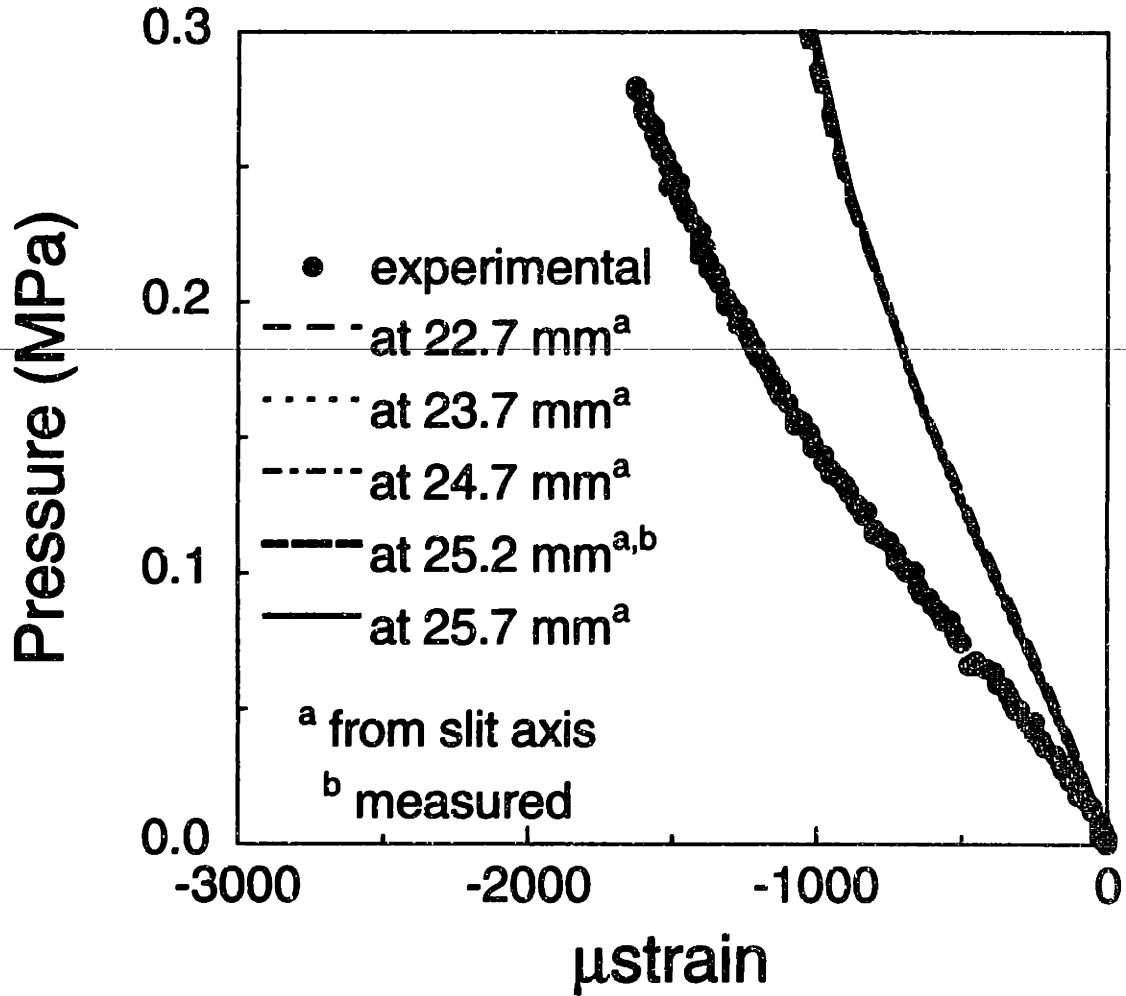


Figure 8.18 Sensitivity of gage placement on the predicted strain response of gage 9 (the farthest hoop gage to the slit axis in the midslit region).

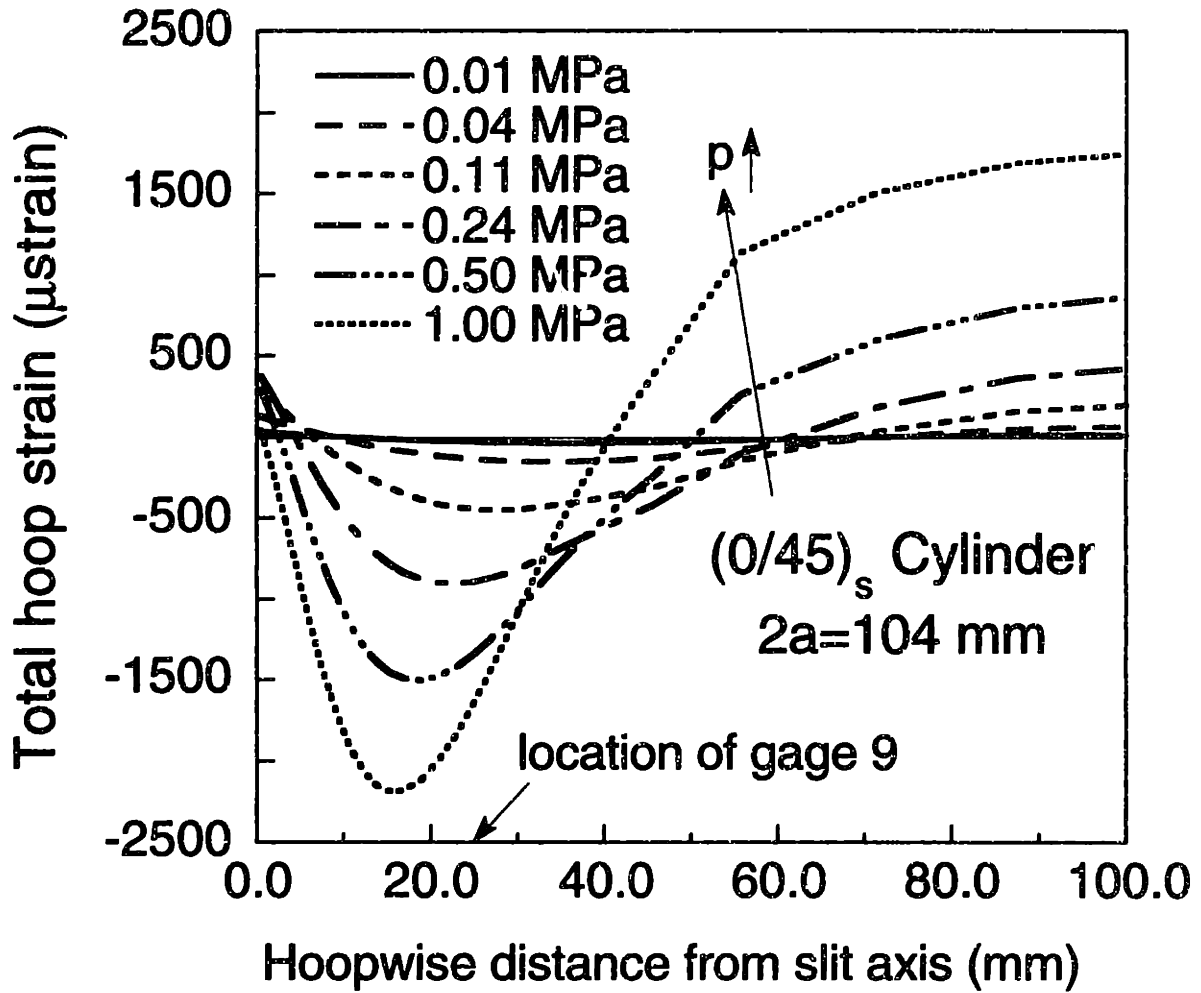


Figure 8.19 Evolution with increasing pressure of midslit hoop total strain distribution in the hoopwise direction computed on the top skin surface.

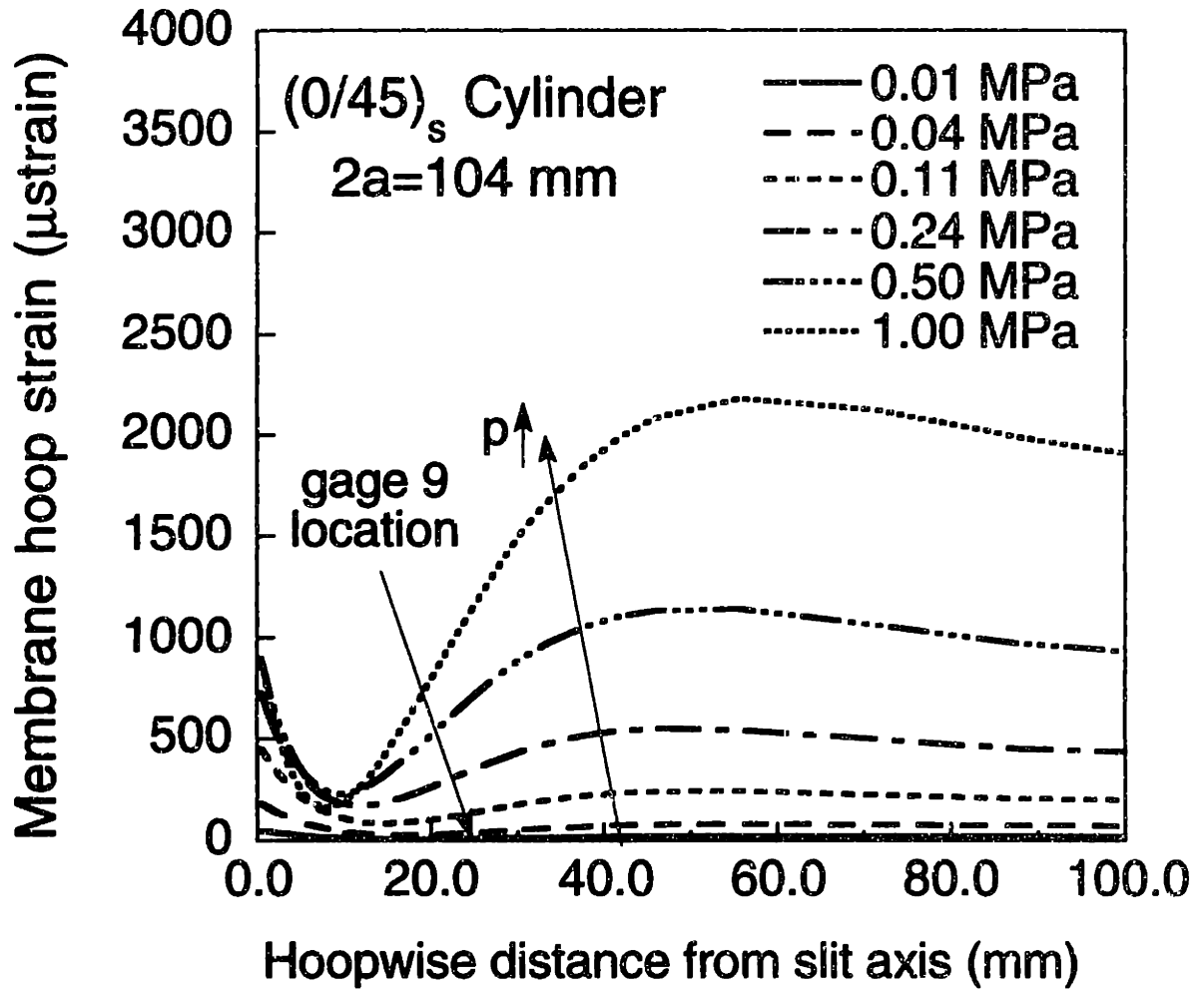


Figure 8.20 Evolution with increasing pressure of midslit hoop membrane strain distribution in the hoopwise direction.

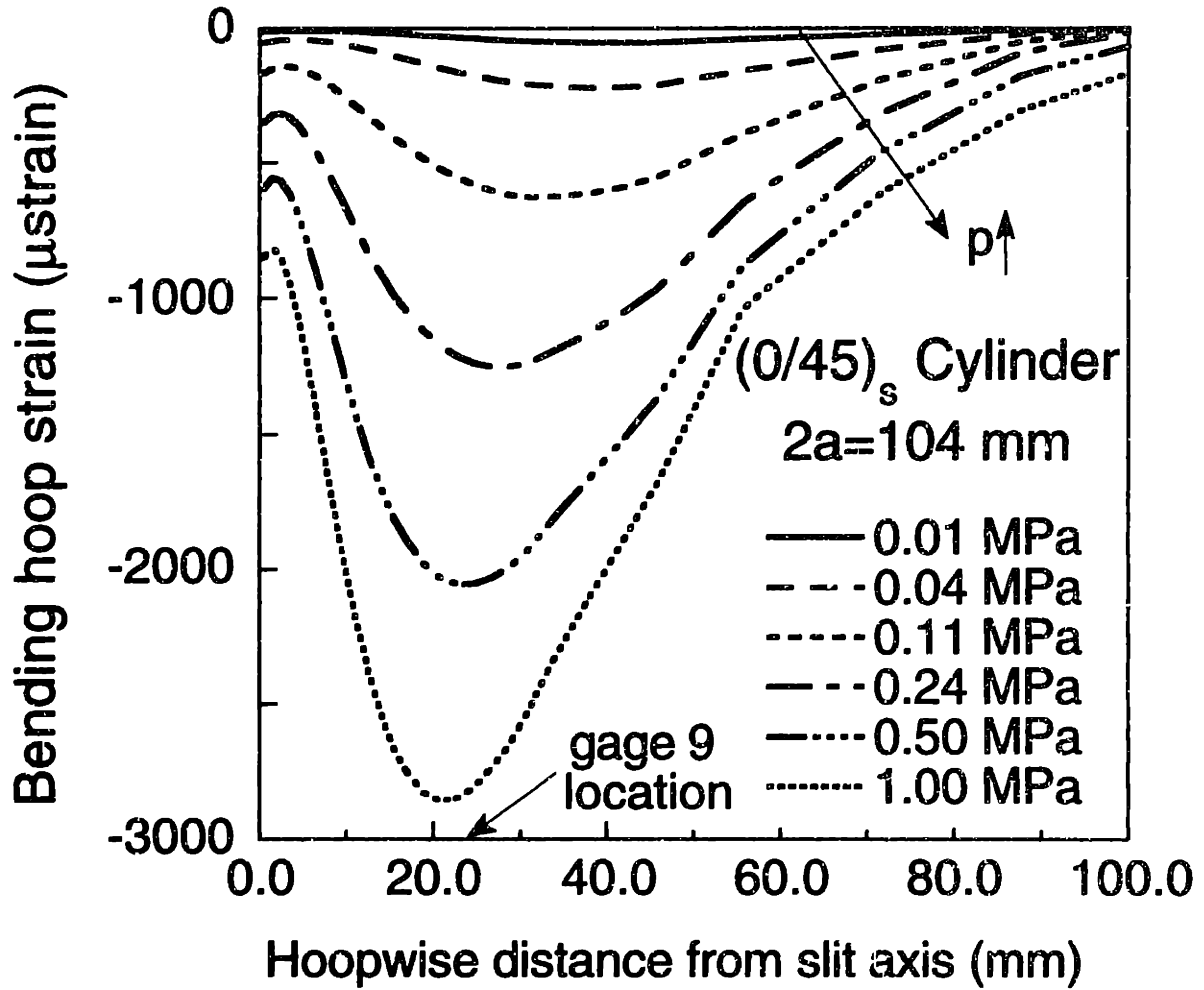


Figure 8.21 Evolution with increasing pressure of midslit hoop bending strain distribution in the hoopwise direction computed on the top skin surface.

The important point is that a mesh (refinement) created near a discontinuity (such as a slit) for a linear analysis may not be sufficient to capture the structural (membrane and bending) responses accurately when other higher order effects (such as geometric nonlinearity) are present. These higher order effects can have an influence in the regions which are relatively far from such a discontinuity. To capture these effects accurately, more refinement in the finite element mesh (i.e. more elements) is needed. The degree of refinement, however, is problem-specific and may not be known *a priori* in the nonlinear case and should be investigated further.

In general, the four (local) strain responses of a laboratory-scaled cylinder are well-predicted by the analysis and have been shown to be (local) manifestations of geometric nonlinear behavior. Furthermore, the disagreements between the predicted and measured strain responses have been explained. Note that all of the discussions on local strain responses presented herein deal with the unstiffened case. Discussion of the strain response in the stiffened case is presented in section 8.3.

8.2 Failure

The predicted failure pressures obtained using the linear and nonlinear methodologies along with the experimental values for the laboratory-scaled specimens tested in the present work are shown in Table 8.1. As a reminder, the linear methodology is based on the stress intensification formula proposed by Folias [16], which is a "curve-fit" to the more accurate numerical solution by Erdogan and Kibler [18]. As discussed by Folias, the accuracy of the formula is within approximately $\pm 6\%$. An iterative process, as described in Chapter 5, was utilized to obtain the

predicted failure pressure for the nonlinear methodology. The nonlinear effects, as seen in Table 8.1, are relatively insignificant in the laboratory-scaled cylinders tested. The differences between the predicted linear and nonlinear solutions for cylinders with slit lengths of 51 mm, 78 mm, and 104 mm are 1%, 7%, and 10%, respectively. The maximum difference occurs in the cylinder with the longest slit length. This is consistent with the numerical results presented in Chapter 5 which shows that the effects of nonlinearity are directly proportional to the slit size through the geometric parameter λ . The agreement between the prediction from the linear methodology and experimental failure pressures on the laboratory-scaled cylinders tested in the present investigation is generally good.

There are also numerous experimental data in the literature on the failure of laboratory-scaled pressurized cylindrical specimens with longitudinal cracks or slits. These experiments were performed on different cylindrical geometries and materials [22-24, 26, 36] as listed in Table 8.2. Similar failure prediction methodology as the one proposed for composite cylinders was developed and used to predict failure of metallic cylinders [16]. Again, good agreement between the predicted and experimental failure pressures was reported in those studies.

However, more recent numerical [27-31, 33] and experimental [27, 33] studies (fatigue crack propagation) on large metallic cylindrical shells that resemble a real aircraft fuselage show that the effects of nonlinearity are significant and cannot be ignored in predicting the failure and longevity (as studied in references [27] and [33]) of such a structure. The fundamental geometrical difference between a laboratory-scaled specimen and the cylinders investigated in [27, 33] is the radius-to-thickness (R/h) ratio. The

Table 8.1 Predicted and Experimental Failure Pressures of Cylinders Tested

Slit Size [mm]	Prediction		Average Experimental [MPa]
	Linear [MPa]	Nonlinear [MPa]	
51	1.04	1.05	0.86
78	0.65	0.68	0.57
104	0.46	0.51	0.46

Table 8.2 Characteristics of Cylinders Tested in Previous Work

Investigator	Radius [mm]	Thickness [mm]	Material
Anderson and Sullivan [23]	76	1.5	Al 2014 ^a
Getz, et. al. [22]	76	1.5	Al 2014-T6
Duffy [24]	381	9.5	X-52 C Steel
Graves & Sawicki [36]	152	1.4	(0/45) _s fabric composite
Ranniger, et. al. [26]	152	1.1	[90/±45/0] _s tape composite

^aDifferent heat treatments utilized.

typical (R/h) ratios of the two cylinder types (a full scale fuselage and a laboratory-scaled cylinder) differ by at least one order of magnitude. The "scale effects", which may be caused by different (R/h) ratios, need to be addressed using a general framework which can effectively assess the nonlinear effects in any cylindrical shell.

The proposed engineering estimation scheme, which uses the *iso-nonlinear plot* given in Figure 5.8, is utilized here to assess the nonlinear effects in both cylinder types (laboratory-scaled cylinder and full scale fuselage). As a reminder, the *iso-nonlinear plot* shows percentage differences between the linear (K_{linear}^{ext}) and nonlinear ($K_{nonlinear}^{ext}$) stress intensification factors as functions of the two proposed nondimensional parameters, λ and η . In order to use the *iso-nonlinear plot*, it is necessary to first normalize the experimental data from the previous experiments [22-24, 26, 36] conducted on different cylindrical configurations and materials by expressing the data in terms of λ and η . This is done in Tables 8.3 through 8.7.

When plotted on the *iso-nonlinear plot*, most of the normalized failure data of laboratory-scaled specimens fall in regions where the "error" is small (i.e. less than 5%) as shown in Figure 8.22. The maximum "error" predicted is around 15% when quasi-isotropic composite cylinders with large values of λ ($\lambda > 10$) were tested [36]. The implication is that the nonlinear effects, although they do exist in any cylindrical shell with a longitudinal slit or crack, do not significantly affect the failure of typical laboratory-scaled specimens.

The opposite is true in the larger cylinders that resemble an actual fuselage structure. Such cylinders have radius-to-thickness ratios (R/h) which are at least one order of magnitude higher than a laboratory-scaled

Table 8.3 Data for Al 2014 Cylinders [23]

Heat Treatment ^a	Crack Length [mm]	Geometrical Parameter λ	Failure Pressure [MPa]	Loading Parameter η ^b
1	1.3	0.21	10.7	0.38
	3.2	0.53	8.4	0.30
	6.5	1.10	5.3	0.19
	9.7	1.63	4.3	0.15
	12.9	2.17	2.9	0.11
	16.1	2.70	2.7	0.10
	22.3	3.73	1.7	0.06
	25.4	4.26	1.6	0.06
2	1.3	0.21	9.6	0.34
	1.9	0.32	9.3	0.33
	2.5	0.41	8.6	0.31
	3.2	0.51	7.9	0.28
	3.9	0.66	6.9	0.25
	5.1	0.85	6.3	0.23
	9.6	1.61	4.0	0.14
	12.8	2.14	3.1	0.11
	16.0	2.68	2.5	0.09
	22.5	3.78	1.8	0.06
	25.4	4.26	1.3	0.05
3	1.3	0.21	8.5	0.31
	6.5	1.08	4.5	0.16
	12.9	2.17	2.7	0.10
	25.4	4.26	1.3	0.05

^a Heat treatment gives different material properties: 1) $\sigma_y = 624 \text{ MPa}$ and $K_c = 56.7 \text{ MPa}\sqrt{\text{m}}$; 2) $\sigma_y = 566 \text{ MPa}$ and $K_c = 53.4 \text{ MPa}\sqrt{\text{m}}$; and 3) $\sigma_y = 469 \text{ MPa}$ and $K_c = 47.7 \text{ MPa}\sqrt{\text{m}}$.

^b Young's modulus for Al 2014 is 72 GPa.

Table 8.4 Data for Al 2014-T6 Cylinders [22]

Crack Length [mm]	Geometrical Parameter λ	Failure Pressure [MPa]	Loading Parameter η^a
1.5	0.34	19.1	0.17
1.5	0.34	19.7	0.17
1.5	0.34	20.4	0.18
3.6	0.86	16.0	0.14
3.6	0.86	16.6	0.14
3.9	0.93	15.2	0.13
5.1	1.21	12.2	0.11
5.1	1.21	13.6	0.12
6.4	1.51	10.5	0.09
6.4	1.51	11.3	0.10
9.7	2.30	7.83	0.07
12.9	3.06	6.34	0.06
25.4	6.03	2.53	0.02
25.4	6.03	3.11	0.03

^a Young's modulus for Al 2014-T6 is 72 GPa.

Table 8.5 Data for X-52 C Steel Cylinders [3]

Crack Length [mm]	Geometrical Parameter λ	Failure Pressure [MPa]	Loading Parameter η^a
43.7	1.31	5.9	0.047
74.7	2.24	5.4	0.043
80.5	2.42	4.6	0.037
158.0	4.74	2.6	0.021
234.2	7.03	1.8	0.014
304.9	9.15	1.3	0.010

^a Young's modulus used is 200 GPa

Table 8.6 Data for (0/45), AW370-5H/3501-6 Graphite/Epoxy Cylinders [36]

Slit Length [mm]	Geometrical Parameter λ	Failure Pressure [MPa]	Loading Parameter η^a
51	3.16	1.32	0.30
51	3.16	1.16	0.27
52	3.22	1.11	0.25
52	3.22	1.04	0.24
102	6.31	0.56	0.13
102	6.31	0.77	0.18
102	6.31	0.60	0.14
165	10.21	0.40	0.09
178	11.01	0.39	0.09

^a Young's modulus (from CLPT) is 51.6 GPa.

**Table 8.7 Data for [90/±45/0], AS4/3501-6 Graphite/Epoxy
Cylinders [26]**

Slit Length [mm]	Geometrical Parameter λ	Failure Pressure [MPa]	Loading Parameter η^a
12.7	0.90	2.42	0.13
25.4	1.80	1.34	0.14
38.1	2.69	0.96	0.09
50.8	3.59	0.79	0.09

^a Young's modulus (from CLPT) is 55.5 GPa.

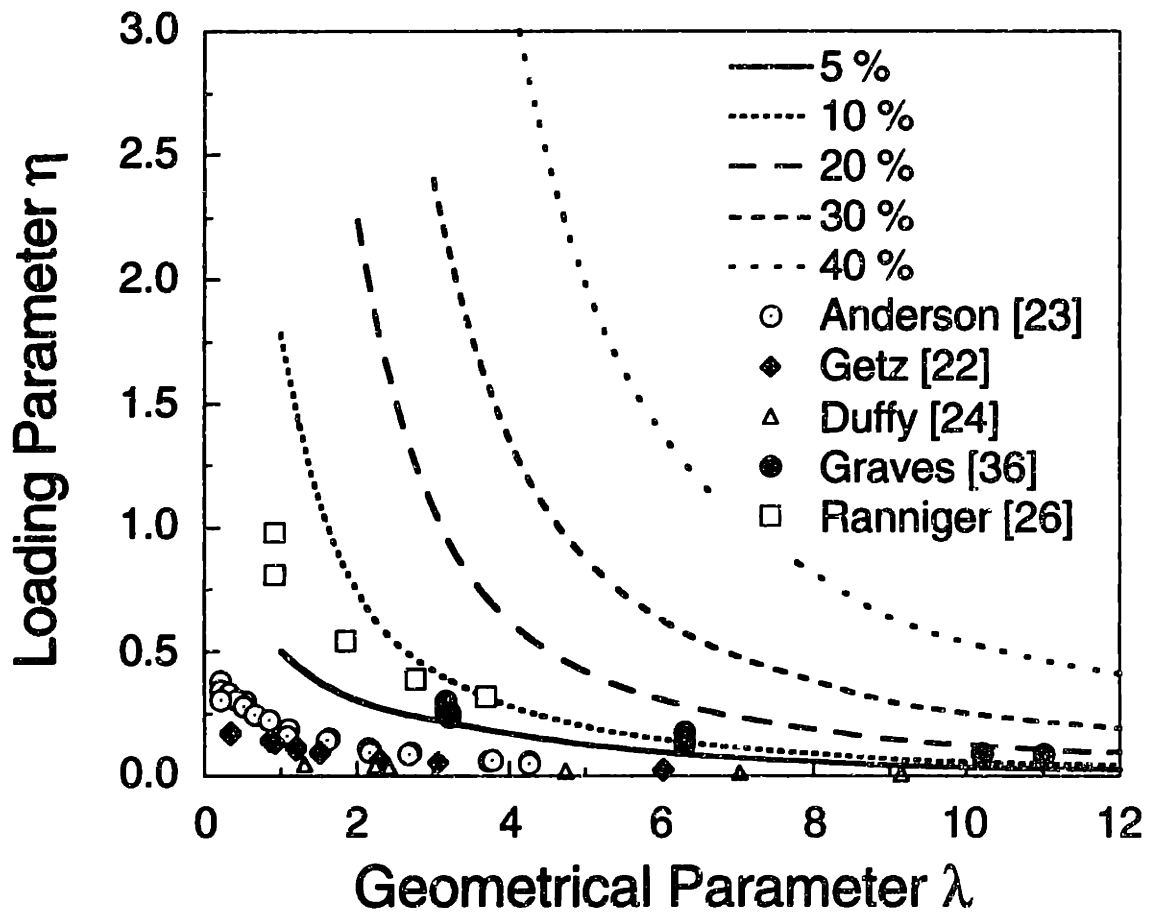


Figure 8.22 Iso-nonlinear plot with the reduced experimental failure results for metallic and quasi-isotropic cylinders with longitudinal cracks/slits.

cylinder. At operating or cruise condition at 30,000 feet (9.1 km), the cabin pressure differential is approximately 55 kPa. The radius-to-thickness ratios (R/h) of typical medium-range transport airplane ranges from 1000 to 2000. Assuming that the fuselage of an airplane is constructed from Al 2024 alloy with a stiffness (E) value of approximately 70 GPa, the loading parameter η can be shown to be of order 1 by using equation (4.10). The crack size to be considered in a typical aircraft fuselage (the so-called one-bay crack) can be as long as 500 mm (20 inches) [11]. Thus, depending on specific fuselage geometry (radius and thickness), this can result in a geometrical parameter λ that varies from 3 to 9. Using the *iso-nonlinear plot*, the predicted errors in an actual fuselage are large and can range from 20 to 40% or even greater. This error is the predicted percentage deviation from the linear and nonlinear stress intensification factors. The error in the predicted failure pressure is expected to be even higher.

To assess the nonlinear effects on the predicted failure pressures, an in-plane failure/fracture criterion along with the relevant fracture parameter(s) are needed. The *iso-error chart* shown in Figure 5.9 shows percentage differences between the predicted linear and nonlinear failure pressures of a (0/45)_s cylinder constructed from AW370-5H/3501-6 graphite/epoxy material system. The *iso-error chart* presented is based on the Mar-Lin composite fracture correlation [49]. The percentage differences are obtained as functions of the geometrical parameter, λ , and the shell ratio, R/h . All possible geometrical configurations for that particular material (given the fracture correlation and parameters) are considered in the *iso-error chart*. As shown in the *iso-error chart*, the difference between the linear and nonlinear predicted failure pressures depends strongly on the shell ratio, R/h . The effects on a laboratory-scaled specimen whose R/h ratio

is on the order of 100 ranges from 10 to 20%. The effects on a full scale fuselage, whose R/h ratios range from 1000 to 2000, can be 50% or even higher.

Using a similar procedure as the one described in Appendix D, an *iso-error chart* that is valid for Al 2024 (typical aluminum alloy used in the current fuselage design) is developed and presented in Figure 8.23. In constructing such a plot, the linear elastic fracture mechanics technique is used to replace the Mar-Lin composite fracture correlation. The "plane stress" toughness value depends on the thickness of the sheet. The plane stress fracture toughness, K_{Ic} , value of $120 \text{ MPa}\sqrt{\text{m}}$ used in the analysis was measured experimentally in [80] for a sheet thickness representative of that in a real fuselage (i.e. approximately 1 mm). The resulting *iso-error chart* for Al 2024 is very similar to the previous one developed for composite cylinders. Different degrees of nonlinearity are again predicted depending on the size of the structure. The difference between the linear and nonlinear predicted failure pressures depends strongly on the shell ratio, R/h . As in the composite cylinder case, the effects on a laboratory-scaled specimen with an R/h ratio on the order of 100 ranges from 10 to 20%. The effects on a full scale fuselage, whose R/h ratios range from 1000 to 2000, can be 50% or even higher.

By compiling the results from previous experiments and using the proposed estimation scheme, it has been shown that geometric nonlinearity affects the failure of full-scale fuselages and laboratory-scaled specimens differently. The effects on laboratory-scaled specimens are relatively minor and on the order of 15% or less. However, the effects on full-scale fuselages are much greater. Thus, linear scaling is not possible. The use of laboratory-scaled specimens in such a manner to predict failure of large structures can

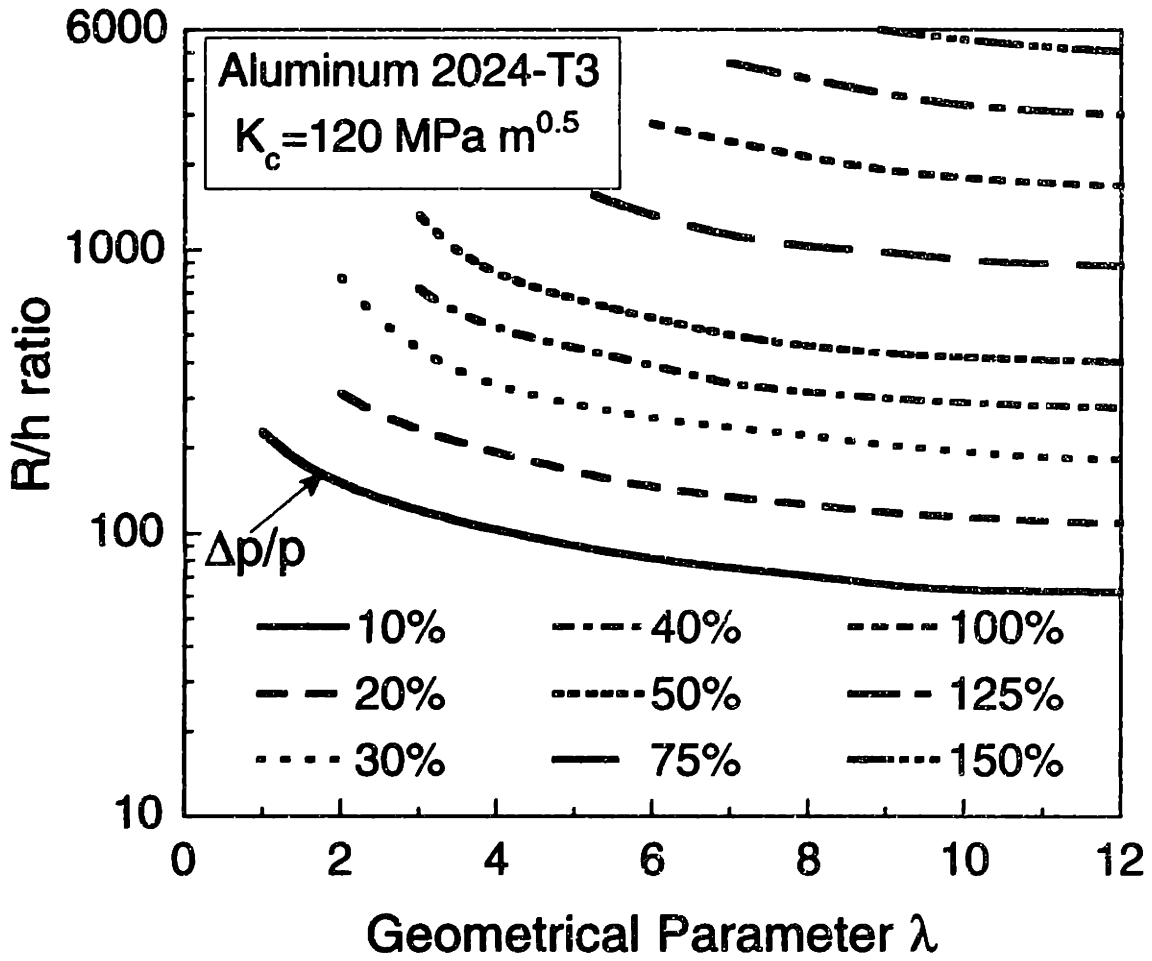


Figure 8.23 Iso-error plot showing the percentage error of the predicted failure pressures using linear and nonlinear methodologies for Aluminum 2024 cylinders with a thickness of 1.0 mm.

yield results which differ significantly due to the existence of different degrees of nonlinearity that operate at different scales.

In the present work, a relatively simple way to properly account for these nonlinear effects in the failure of any thin-walled pressurized cylindrical shell with a longitudinal crack or slit is presented. The methodology requires that the cylinder geometry and loading condition be normalized in terms of two nondimensional parameters λ and η . This methodology utilizes the so-called *iso-nonlinear plot* where differences between the linear and nonlinear stress intensification factors are presented as functions of the two parameters. Since this methodology takes into account different degrees of nonlinearity depending on the specific cylinder geometry, a one-to-one scaling between a laboratory-scaled specimen and a full scale fuselage is therefore possible.

8.3 Damage Arrest

The study of damage arrest in a pressurized cylindrical shell is very much related to that of damage bifurcation or turning in such a structure. Damage bifurcation in a pressurized cylinder can lead to other structural response (such as flapping) which can decrease the driving energy for damage propagation. When damage runs out of energy as a result of this structural response, a complete damage arrest is expected. This section on damage arrest is divided into two subsections. In the first subsection, the numerical and experimental results for both the *type-1* and *type-2* cylinders are discussed in the context of damage bifurcation. The implications of the results of the damage arrest experiments are discussed in the second subsection.

8.3.1 Damage Bifurcation

Several items are pursued in an effort to understand the observed phenomenon of damage growth in pressurized cylinders. First, the strain distributions obtained from the analysis are discussed in order to assess the nonlinear effects on the strain distribution, particularly near the slit tip and in the ligament region. Then, the combined effects of nonlinearity and stiffening bands on the nonlinear membrane stress intensification factors as damage approaches the stiffener are discussed.

As presented in Chapter 5, analyses of cylinders with the same ligament length of 20 mm but different ligament length to half-slit length ratios (ψ/a) were conducted to simulate damage growth in a stiffened cylinder. Both the strain distributions and the membrane stress intensification factors were obtained from such analyses.

The effects of the stiffening band can be seen clearly in the nonlinear longitudinal strain distribution shown in Figures 5.25 for a cylinder with a longitudinal slit length of 312 mm, resulting in a ψ/a ratio of 0.13 for the stiffened case. This strain, which attains a high value at the slit tip, initially decreases, reaches a minimum value, and then increases again near the edge of the stiffening band due to bending. Thus, a "well" in the longitudinal strain distribution occurs in the stiffened case, but not in the unstiffened case, with a concomitant rise in the strain level at the stiffener edge. This longitudinal strain may cause damage to turn 90° from its original propagation path. Although the linear solution also predicts the existence of a similar "well" in the distribution, the location of the minimum point and the magnitude differ greatly as shown in Figure 5.23 (i.e. in the nonlinear case, the lowest peak occurs much closer to the stiffening band and is smaller in magnitude than that from the linear solution). The measured strain response

of gage 5 (the longitudinal gage placed close to the edge of the stiffening band) in the stiffened case as reported in Chapter 7 is also higher than that in the unstiffened case. Thus, the existence of bending induced by the presence of the stiffening band has been indicated.

This bending behavior is caused by membrane and bending stiffness discontinuities between the unstiffened and stiffened regions. Such a bending response is expected to be proportional to the difference between the stiffnesses of the unstiffened and stiffened regions (i.e. an unstiffened cylinder does not show bending in the same location). Thicker stiffening bands with higher bending stiffnesses are expected to have more influence on this bending response than thinner ones. This bending response then alters the magnitude and orientation of strain in the ligament region. Thus, these numerical results provide a justification of the previously proposed (empirical) containment ratio [26], which is based on the bending stiffness ratio between the stiffened and unstiffened regions, in characterizing stiffener effectiveness in damage bifurcation.

In the current work, the damage did not bifurcate at the first set of hoop stiffeners in one of the *type-3* cylinders tested. This cylinder was stiffened with two layers of continuous (*type-B*) 0° fabric layers. This observed phenomenon can be explained using this proposed nondimensional containment ratio shown in equation (2.10). The empirical containment ratio depends on the slit size, cylinder radius, and ratio between the bending stiffnesses of the stiffened and unstiffened regions. Since all cylinders tested have the same slit length and radius, only the bending stiffness ratio needs to be considered.

The bending stiffnesses of the stiffened and unstiffened regions in the hoop direction are shown in Table 8.8. Although the hoop stiffeners in

Table 8.8 Bending stiffnesses of the *type-3* cylinders tested

Cylinder	Hoop Direction		Longitudinal Direction	
	Value ^a	Ratio ^b	Value ^a	Ratio ^b
1	89	5.6	33	2.1
2	74	4.6	74	4.6
3	232	14.5	232	14.5
4	144	9.0	144	9.0
5	232	14.5	1047	65.4

^a Bending stiffness in units of [GPa mm³]

^b Stiffened value/unstiffened value (unstiffened value = 16 GPa mm³)

cylinder 2 are actually thicker than that in cylinder 1 (0.70 mm for cylinder 2 versus 0.54 mm for cylinder 1), the in-plane stiffness of a fabric material is only roughly one-half of the value for unidirectional tape material. Thus, cylinder 2 has the lowest value of bending stiffness ratio and thus the lowest value of containment ratio. Therefore, the inability of the stiffening band in cylinder 2 has been explained using the proposed containment parameter. When more stiffening layers were added to the cylinder (as done in cylinders 3 through 5), the ratio of bending stiffnesses increased and damage bifurcation did take place.

In a real airplane, however, additional stiffening elements in the longitudinal and hoop directions are usually bonded on top of the "flat" tear straps. These stiffening elements are utilized to maintain the shape of the structure and to provide additional bending and buckling resistance to the main structure. Although the influence of such stiffeners on the strain distribution and damage propagation is not addressed in the present work, their effects may be significant and should be investigated further.

The previous discussion deals with the effects of nonlinearity on the longitudinal strain distribution as damage approaches the slit tip. It is also important to assess the interaction between the stiffening band and geometric nonlinearity on the magnitude of the nonlinear stress intensification factor, K^{ext} , as damage propagates and approaches the stiffening band. The effects on the stress intensification factor can actually be used to assess the same effects on the hoop stress distributions.

The effects of stiffening bands on the linear K^{ext} are shown in Tables 5.3 and 5.4. A maximum reduction ranging from 10-15% in the magnitude of the linear K^{ext} is predicted, depending on the specific layup, for cylinders with the smallest ψ/a ratio ($\psi/a = 0.13$). Thus, in the linear case, the difference

between the unstiffened and stiffened K^{III} values is relatively insignificant. The effects of geometric nonlinearity on the stiffened K^{III} values obtained from the linear and nonlinear solutions are shown in Figures 8.24 and 8.25 for cylinders with initial slit lengths of 51 mm and 78 mm, respectively. The simulation results shown in Figures 8.24 and 8.25 are to model the observed "self-similar" damage propagation in this fabric cylinder at rupture. The simulations are performed at different values of the ψ to a ratios ($\psi/a=0.78, 0.51, 0.38, 0.19,$ and 0.13) at their corresponding experimental failure pressures of 1 MPa internal pressure for a slit length of 51 mm and of 0.6 MPa for a slit length of 78 mm. The smallest ψ to a ratio corresponds to a situation in the *type-3* cylinder in which the simulated growing slit tip is at approximately 12 mm from the edge of the stiffening band. Note that the observed bifurcation point as described in Chapter 7 typically occurs at approximately 15 mm from the edge of the stiffening band.

The differences between the linear and nonlinear solutions are clearly seen in these two plots. The linear stress intensification factors keep increasing as damage approaches the stiffeners (i.e. as the ψ/a -ratio decreases for a fixed value of ψ). Although the nonlinear K^{III} in the stiffened case still increases as damage approaches the stiffener, its rate-of-increase actually decreases as damage grows further.

This reduction in the magnitude of the stress intensification further implies the same reduction in the hoop stress and strain close to the slit tip. This "stiffening" response due to nonlinear effects may therefore alter the magnitude and orientation of strain in the ligament region ahead of the slit tip and may be part of the mechanism which causes damage to turn.

The situation in an unstiffened cylinder constructed of the same fabric material is somewhat different. Damage initially propagates in a rather self-

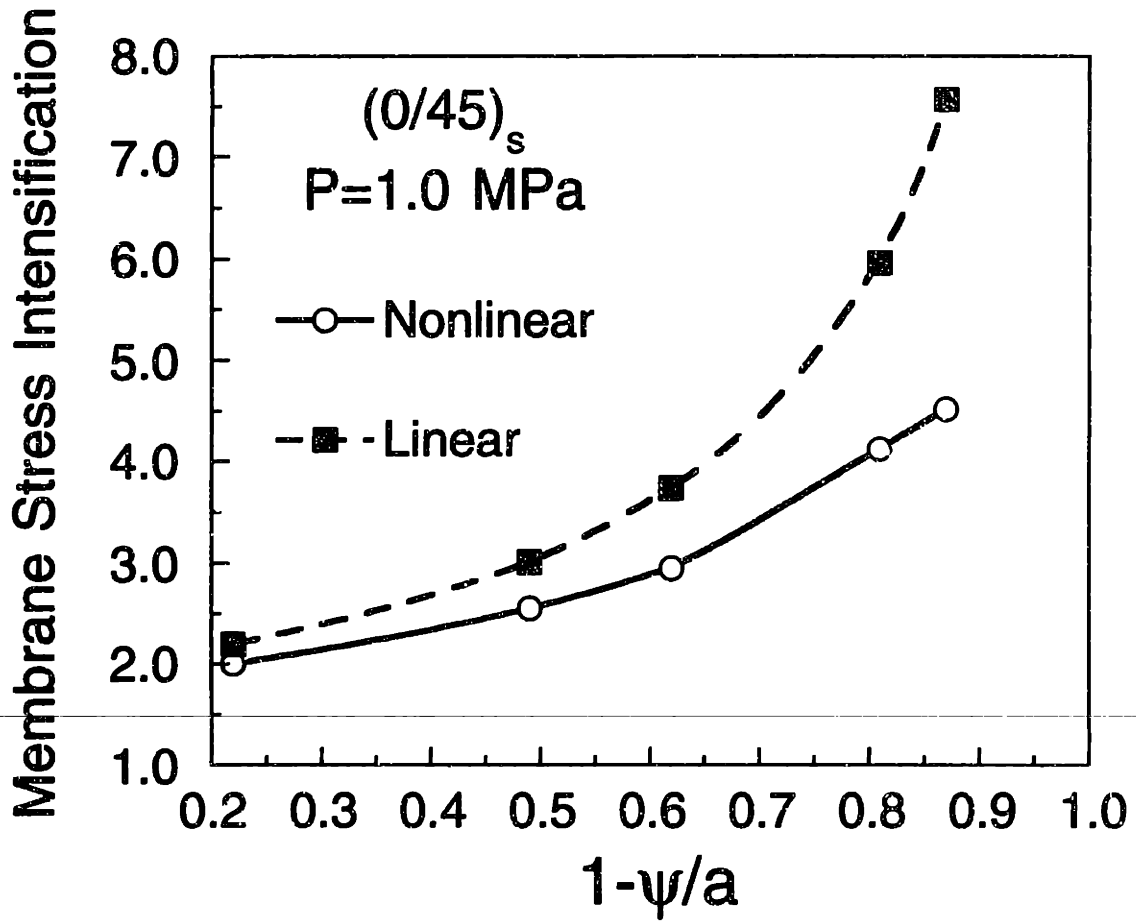


Figure 8.24 Membrane stress intensification plot for the simulation of damage growth in a stiffened (0/45)_s cylinder with an initial slit length of 51 mm which fails at an internal pressure of 1.0 MPa.

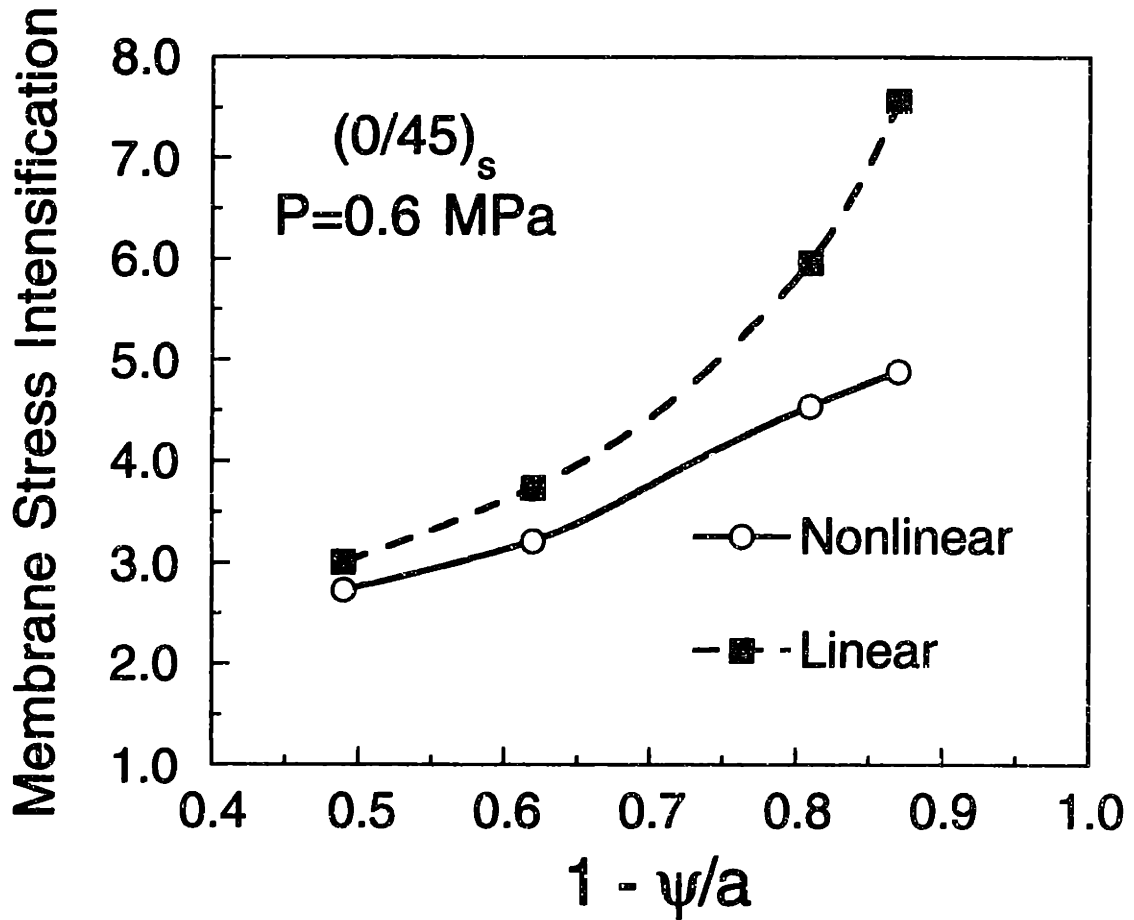


Figure 8.25 Membrane stress intensification plot for the simulation of damage growth in a stiffened (0/45)_s cylinder with an initial slit length of 78 mm which fails at an internal pressure of 0.6 MPa.

similar way and then bifurcates or branches at angles ranging from 40° to 50° from the longitudinal axis of the cylinder at approximately 200 mm from the cylinder ends [36] as depicted in Figure 8.26. Previous investigators [55] argued that such a bifurcation is induced by the "edge effects" from the cylinder ends that become significant as damage grows. However, the edge zone in a cylindrical shell is proportional to the square-root of the cylinder radius and thickness ($\sqrt{R h}$), which for the cylinders tested (radius of 153 mm and thickness of 1.4 mm) is only on the order of 15 - 20 mm from the cylinder ends. Thus, a mechanism other than the "edge effects" is likely operative in inducing damage bifurcation.

A similar fracture path is also observed in one of the *type-3* cylinders tested (cylinder 2) where damage bifurcation was observed within the first set of hoop stiffeners at approximately 200 mm from the ends of the cylinder. The triangular region in cylinder 2, formed by the two branches of damage, still contains all of the plies (a total of six plies including the stiffener). Such turning implies that the mechanism that causes bifurcation is related to the presence of a stiffener but is not the stiffener itself, since bifurcation can occur in an unstiffened cylinder. This requires further consideration.

Similar crack-turning phenomena as discussed for the composite cylinders have also been observed in metallic fuselages where a sharp ("saw-cut") longitudinal crack initially propagates in a stable manner along its original path and then turns and flaps [11, 81]. The actual mechanism for this turning is not well understood. Some crack-turning criteria based on the so-called *T-stress* concept have been proposed and applied to this problem. The *T-stress* is the nonsingular stress ahead of the crack tip that is parallel to the crack. This nonsingular stress has been shown to affect the stability of propagating cracks in metallic materials [82]. The crack stability criterion

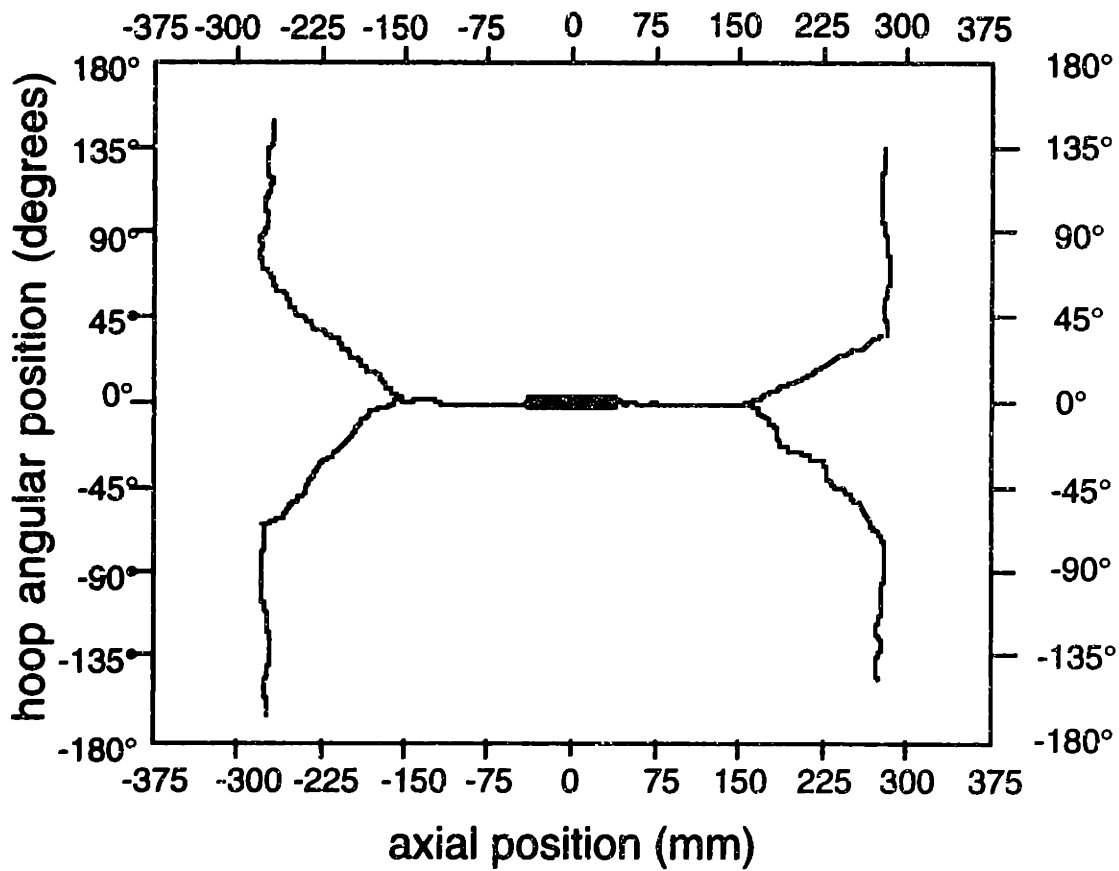


Figure 8.26 Typical fracture path of an unstiffened cylinder [36] (Note that bifurcation points are located approximately 200 mm from the cylinder ends).

proposed in [82], known as the *Cotterell and Rice* criterion, states that a propagating crack is stable and prefers to stay on its original propagation path if the *T-stress* is negative (compressive). The propagation becomes unstable and the crack tends to kink or deflect from its original path if the *T-stress* is positive (tensile). This crack stability criterion and its modified version [83] have been applied to many engineering applications ranging from multilayer designs in microelectronics components to problem of crack turning in metallic fuselage structures.

The application of the crack stability criteria in metallic material discussed previously ignores the nonlinear effects due to "bulging" [81]. It has been shown here that in a pressurized cylindrical shell, the response becomes more nonlinear as damage size becomes larger. The effects of nonlinearity on the longitudinal strain distribution in the unstiffened (0/45)_s cylindrical shell with a slit length of 104 mm are presented in Figure 5.14. A totally different distribution in the region very close to the slit tip is predicted in the nonlinear case due to different nonlinear effects on the membrane and bending components of the longitudinal strain. Since the strain in a material is related to the stress via a constitutive equation, the effects on the longitudinal strains also imply similar effects on the stress distribution in the same direction (i.e. parallel to the slit). It is suspected that nonlinearity alters the nature of the *T-stress* ahead of the slit tip and causes the damage to become unstable. However, more analytical and numerical work is needed to further study and explore the relationship between geometric nonlinear behavior and the nature of the *T-stress* and their combined roles in damage bifurcation.

8.3.2 Implications of the Results from Damage Arrest Experiments

In the experimental investigation of damage arrest using the *type-3* cylindrical configurations, the first set of hoop stiffeners was shown to be effective in inducing branching as damage turned and propagated near the edge of the hoop stiffeners in all but one case. No branching was observed in the damage path at the first set of hoop stiffeners of cylinder 2 as discussed previously. In cases where the first set of hoop stiffeners was effective in inducing damage redirection, damage continued its propagation in the hoop direction and, in general, cleanly ran through the longitudinal stiffening bands along the way. This can be seen in the fracture paths of cylinders 1, 3, and 4 shown in Figures 7.15, 7.21, and 7.22, respectively. Cylinder 1, which was reinforced with the *type-A* stiffener constructed from unidirectional material, suffered significant secondary damage in the form of delamination and stiffener debonding near the locations where the longitudinal and hoop reinforcements met. Thus, although damage may appear to have been diverted/turned in this case, it is more likely that it just found an "easier" path (via matrix cracking and associated delamination) along which to propagate.

In cylinders 3, 4, and 5, matrix crack initiation in the *type-A* stiffener configuration was prevented through the use of the *type-B* configuration as depicted in Figure 3.5. Unlike the *type-A* stiffener, the *type-B* stiffener was constructed from a fabric material and was cut in one piece with no discontinuities at the junction. Thus, this stiffener construction also reduces the potential for the formation of matrix cracking and delamination in the region where the longitudinal and hoop stiffeners meet. However, eliminating this matrix-crack path did not significantly increase the overall effectiveness of the longitudinal stiffeners closest to the slit in arresting

damage as can be seen in Figures 7.21 and 7.22 where damage continued its propagation across the first set of longitudinal stiffeners. The damage was arrested at the next set of longitudinal stiffeners which are located at angular locations of approximately $\pm 135^\circ$ from the slit. However, damage redirection by the first set of longitudinal stiffeners was indeed observed in cylinder 5, as depicted in Figure 7.21. This cylinder has more reinforcement in the longitudinal direction (up to 8 layers of 0° fabric). Despite the observed turning, damage, which now had split into four independent paths, continued to propagate and induced a considerable amount of secondary damage modes such as stiffener debonding, hoop and longitudinal stiffener breakage, as well as delamination of the unstiffened (base) region. As shown in its fracture path, one set of the bifurcated damage continued its propagation. This was caused by separation of one of the endcaps from the cylinder induced by the pressure at rupture. The other set of bifurcated damage was arrested at the next set of longitudinal stiffeners located at angular locations of approximately $\pm 135^\circ$ from the slit as in cylinders 1, 3, and 4.

Thus, it has been experimentally shown that the longitudinal stiffening bands are not as effective as the hoop stiffeners in inducing damage bifurcation. This has been confirmed by the analysis of Duncan and Sanders [43] for metallic cylinders. The geometrical parameters in their analytical solution that determine the stiffener effectiveness are the stiffener curvature and the stiffener thickness. It is shown that, under identical loading and stiffener configuration, the hoop stiffener in a cylinder, which has roughly the same radius of curvature as the cylinder, is more effective in reducing the stress intensity factor than the stiffener in a flat plate (with no curvature). Since the longitudinal stiffening bands in a cylinder are similar to those in a plate and are locally flat, the reduced effectiveness of the longitudinal

stiffeners is therefore expected. This is also important in considering scale effects and this is pursued subsequently.

In considering the relative effectiveness of hoop and longitudinal stiffeners to arrest/redirect damage, it is important to consider the driving force during different stages of damage propagation. The overall damage propagation can be separated into two stages: one, before the first bifurcation takes place during which damage propagates in the longitudinal direction and, two, after the first bifurcation during which the bifurcated damage continues its propagation in the hoop direction. In the first stage, damage propagates in a relatively self-similar way with the cylinder hoop stress as the scaling/driving parameter. This stage of damage propagation is the bulging phenomenon [13, 25]. The second stage of damage propagation is caused by the flapping phenomenon induced by internal pressure [11] as depicted in Figure 8.27.

The existence of two different driving forces that exist as damage propagates is proposed as one of the reasons why damage was not arrested by the first set of longitudinal stiffeners which were closest to the slit. To determine the proper scaling/driving parameter after flapping occurs, a first-cut engineering model is proposed based on dimensional argument. The cylindrical panel considered is shown in Figure 8.27. The initial damage is assumed to have bifurcated and split into four distinct parts. Due to internal pressure, bending and tearing of the top and bottom pieces are the relevant structural deformation of the slit region after bifurcation. If, after bifurcation has taken place, it is assumed that damage on the left and right edges propagates at the same rate and, thus, the left and right edges are of equal lengths, the symmetry of the problem is maintained and this physical

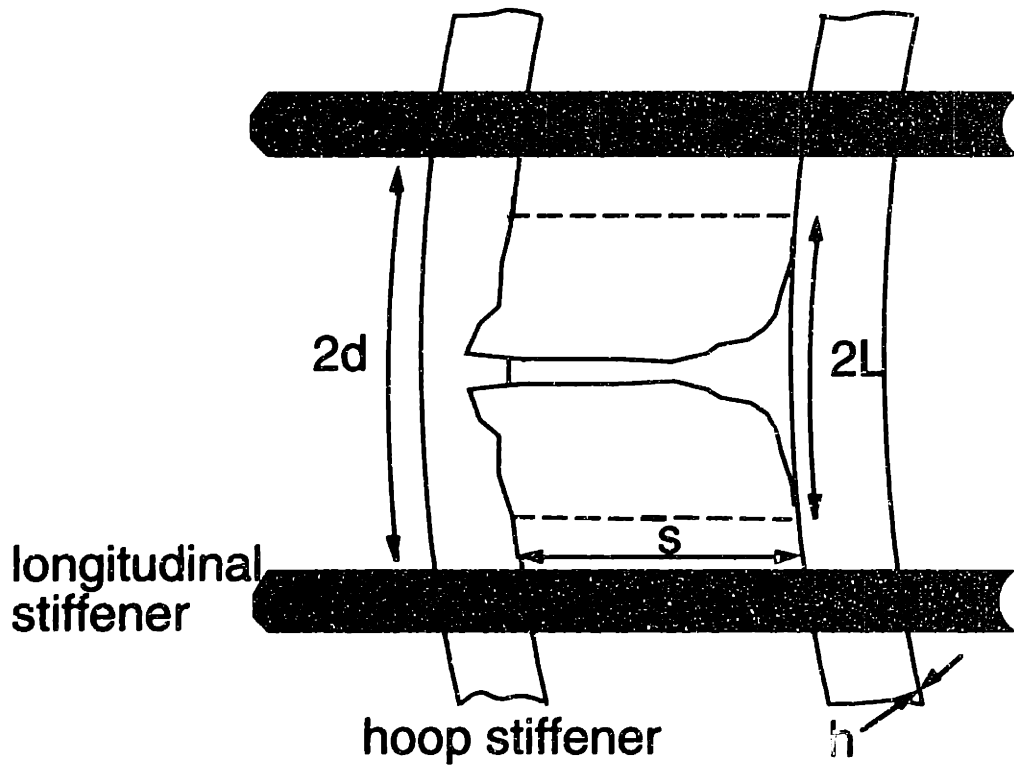


Figure 8.27 An illustration of flapping induced by damage bifurcation in a pressurized cylinder.

situation can be modelled as the bending of a free-free-free-clamped (i.e. cantilevered) plate under uniform pressure loading.

The moment taken at the tip of the damage (i.e. at the cantilevered edge) is proportional to the pressure, p , and the distance, L , the damage has run in the hoop direction

$$M \propto p L^2 \quad (8.1)$$

When the damage tip reaches the longitudinal stiffeners, this flapping distance is proportional to the spacing of the longitudinal stiffener denoted by $2d$ in Figure 8.27. Therefore, equation (8.1) can be rewritten as

$$M \propto p d^2 \quad (8.2)$$

Based on elementary beam/plate theory, the bending stress is proportional to the moment, M , the distance from the neutral axis of the cylinder, z_0 , and the area moment of inertia, I ,

$$\sigma_b \propto \frac{M z_0}{I} \quad (8.3)$$

By substituting equation (8.2) into equation (8.3) and noting that z_0 is proportional to the shell thickness, h , and I is proportional to the cube of the thickness, the bending stress becomes

$$\sigma_b \propto \frac{p d^2 h}{h^3} \quad (8.4)$$

which can be expressed as

$$\sigma_b \propto p \left(\frac{d}{h} \right)^2 \quad (8.5)$$

with the key parameters thus being the pressure at rupture, the longitudinal stiffener spacing, and the base cylinder thickness. It is also important to note from experiments in this work that as flapping occurs, the driving force

(pressure) decreases due to bending of the crack face which allows the pressurizing gas to leave the cylinder. This decrease in pressure is believed to be the reason for the observed damage arrest by the next set of longitudinal stiffeners located at angular locations of $\pm 135^\circ$ as seen in the fracture paths of cylinders 1, 3 and 4.

It has been shown that two driving or scaling parameters exist for damage propagation in a pressurized composite cylinder depending on the extent of damage progression. Before bifurcation takes place, the correct driving parameter is the hoop stress, which depends on the pressure, cylinder radius, and base cylinder thickness. After bifurcation, the proper driving parameter is the bending parameter, σ_b , shown in equation (8.5). To illustrate the potential pitfalls in using a subscale specimen to study damage growth initiation, bifurcation, and arrest, consider a full-scale fuselage and a potential laboratory-scaled specimen to simulate such. The geometries of the two cylinders (radius, thickness, longitudinal stiffener spacing) are shown in Table 8.9. The former is taken to have the same basic geometry as the fuselage of a Boeing 737 airplane with a radius of 2 meters, thickness of 1.4 mm, and tear strap spacing in the longitudinal direction of 240 mm [6]. The latter has the same geometry as the test specimens in the present study (radius of 150 mm, thickness of 1.4 mm, hoop stiffener spacing of 203 mm, and longitudinal stiffener spacing of 190 mm). The ultimate design pressure in a Boeing 737 airplane is on the order of 110 kPa, resulting in a hoop stress of approximately 160 MPa. Before bifurcation, the *hoop stresses* of the two cylinders are the proper scaling parameters and are set equal. Hence, to satisfy this criterion, the smaller cylinder must be pressurized up to approximately 1500 kPa. After bifurcation has taken place, the scaling/driving parameter of interest is the *bending parameter*, σ_b . Using the

Table 8.9 Effects of Different Cylinder Geometries on the Magnitude of the Bending Parameter

Radius [mm]	Thickness [mm]	Stiffener Spacing [mm]	Hoop Stress [MPa]	Bending Parameter [GPa]
150	1.4	203	160	~31.4
2000	1.4	240	160	~3.3

geometrical parameters shown in Table 8.9 in equation (8.5), it is shown that the magnitude of the *bending parameter* in the smaller cylinder is approximately 9.5 times that of the larger cylinder (i.e. almost one order of magnitude higher). This is one of the reasons why arrest by the longitudinal stiffener is more difficult to accomplish in a small-scaled specimen. Therefore, from this comparison, it is clear that it is unlikely to be able to simulate or scale both the bulging and flapping phenomena in a single experiment on one subscale specimen since different scaling parameters govern the two phenomena.

In addition to the scale effects induced by the existence of two different driving forces discussed previously, there is another possible scaling issue that may be important to consider in a damage arrest experiment. This is based on the observation of the fracture path of cylinder 5. As in cylinders 1, 3, and 4, damage bifurcation near the edge of the stiffening band occurred in cylinder 5. The bifurcated damage then grew in the hoopwise direction until it reached the first set of the longitudinal stiffeners. Since the "rectangular" piece, where the slit was located, was separated from the cylinder after the test was completed, it is hypothesized that damage was actually arrested and another bifurcation (now from the hoopwise to the longitudinal direction) took place at the edge of the first set of the longitudinal stiffeners. This hypothesized damage progression in cylinder 5 is shown in Figure 8.28. Thus, immediately after damage was arrested, the structure looked like a cylinder containing a stiffened rectangular cutout with "sharp" corners. Since nitrogen gas was used to pressurize the cylinder and, thus, the pressure was not quickly released at that instant, damage reinitiated at the corners due to the stress concentrations and then continued its propagation as depicted in Figure 8.28 and as can also be seen in the experimental results of Figure

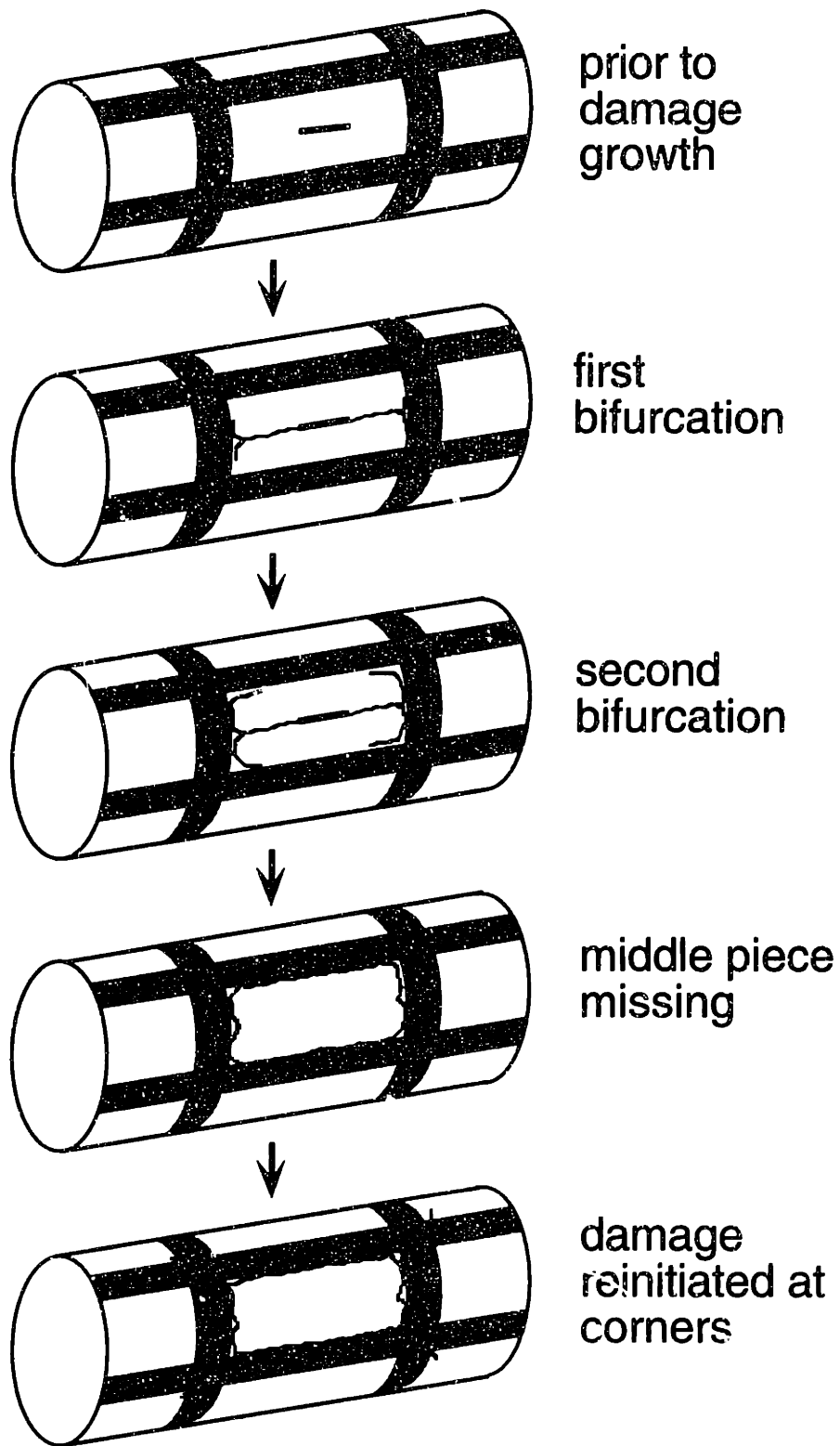


Figure 8.28 Hypothesized damage progression in cylinder 5.

7.23. Since cylinder 5 failed at approximately 0.6 MPa, it is believed that at such a pressure level, "new" damage initiation can take place at the corners of the rectangular cut-out.

Testing laboratory-scaled cylinders to show a complete damage arrest is therefore very challenging due to the existence of different driving forces depending on the extent of damage progression and the possibility of damage reinitiation in the event of a complete damage arrest. All of these factors make the condition in smaller, laboratory-scaled cylinders much more severe than that in a full-scale fuselage. Previous damage arrest experiments, such as the ones performed in the present work, were done by scaling the specimens based on the hoop stress alone. As shown by the experimental results, arrest is difficult, if not impossible, to achieve under this condition. It may therefore be necessary to scale the cylinder based on the proposed bending parameter and to keep the failure pressure sufficiently low to prevent other kinds of damage (such as matrix cracking and delamination) from reinitiating at the corners when the stiffened, rectangular cut-out is created by arrest at the edge of the longitudinal stiffener.

8.4 Final Notes

The present work has addressed two different, yet related, problems that are relevant in the damage tolerance of a fuselage structure: one, damage growth initiation and, two, damage arrest. The implications on both issues are addressed here.

As shown from results of the present investigation, the geometric nonlinear phenomenon in pressurized cylindrical shells containing longitudinal slits are induced by the existence of large deformation in the slit

region. This nonlinear phenomenon is manifested in both the local strain responses and in the failure process of such a structure. Failure of large cylindrical shells resembling an actual fuselage is affected strongly by nonlinearity (i.e. the effects can be 50% or even greater depending on the specific geometry). The failure of smaller, laboratory-scaled cylinders, however, are not significantly affected by nonlinearity (i.e. the effects are around 15% or lower).

Thus, analytical and numerical results of the present work have shown the limitation of "linear scaling" in predicting failure of laboratory-scaled specimens due to the existence of different degrees of nonlinearity that operate at different scales depending on the size of the structure. This further implies that, if a one-to-one scaling is desired between two structures of different sizes, such nonlinear effects must be taken into account. The proposed engineering estimation scheme presented herein can be used to provide the "correction" due to this nonlinear behavior.

The proposed methodology only deals with a through-thickness damage state oriented along the longitudinal direction and is strictly applicable only for quasi-isotropic and isotropic cases. The effects of anisotropy (i.e. bending-twisting coupling) on the linear and nonlinear stress intensification factors still need to be addressed. In addition, other in-service and accidental damage (such as those induced by low velocity impact events) can exist in the structure. Such damage states are very complex as they usually consist of multiple modes (i.e. delamination, matrix cracking, splitting) that may interact with each other. Thus, the damage tolerance of pressurized composite cylinders that contain other damage states (delamination, matrix cracking, splitting) also needs to be addressed before composites can be

utilized to their full potential in the design of primary, load-bearing aircraft structure.

Furthermore, an aircraft fuselage is loaded by bending and torsional loads from flight as well as by cabin pressurization. Thus, different parts of a fuselage are subjected to different primary loading conditions. The proposed design of a composite fuselage [5], where the main structure is divided into three major sections: the crown (the top), the side, and the keel (the bottom) sections, must take these different loading conditions into consideration as each of the three sections may be subjected to a combination of more than one loading type. Therefore, the effects of combined loading on the damage tolerance and growth initiation of an aircraft fuselage need to be understood.

Once growth initiation begins, it is also important to understand the subsequent propagation of damage. This includes bifurcation and subsequent arrest and the mechanisms associated with such need to be better understood. Hoop stiffening bands can be used to promote damage bifurcation. The presence of such hoop stiffening bands results in membrane and bending stiffness discontinuities between the unstiffened and stiffened regions. It has been shown in the present work that geometric nonlinearity and such stiffness discontinuities interact and can potentially change the magnitude of the strains in the ligament region between the slit tip and the edge of the stiffening bands. Due to such an interaction, the orientation of the maximum tensile strain can also change. Thus, damage turning or bifurcation in a stiffened construction is likely affected by this interaction between nonlinear effects and stiffening bands. It is also important to note that the experiments performed in the present study used a flat "tear strap" configuration. In an actual fuselage, stiffening elements of other geometry (such as top hat and Z-section stiffeners) are bonded to or placed on top of the

flat "tear straps" [6]. These additional stiffening members are used to provide additional membrane and bending stiffnesses against bending and buckling of the fuselage structure. The effects of additional stiffening elements on the damage propagation in such a structure are unclear at this time and should be investigated further.

Unlike the stiffened case, a different situation exists in the unstiffened case where damage bifurcation can still occur without the presence of stiffening bands. Preliminary numerical results of the strain distributions in such a cylinder show that the longitudinal strain level in the region close to, and ahead of, the slit tip is affected by nonlinearity. It can be shown, using a constitutive relation, that similar nonlinear effects are expected in the longitudinal stress distribution. In the isotropic case, the nature of the nonsingular component of stress which is parallel to the crack (i.e. the *T-stress*) has been shown to affect the stability of propagating crack. Although the preliminary numerical work presented here shows that the effects of geometric nonlinearity do have an influence in the nature of the longitudinal stress distribution, more analytical and numerical work is needed to further explore such effects on the stability of propagating damage in an unstiffened construction. Furthermore, the mechanisms in the unstiffened and stiffened cases are likely related and work needs to be done to pinpoint the underlying common mechanisms.

Once bifurcation occurs, damage arrest in the opposite direction becomes key. It has been shown, using a simple engineering method, that the damage growth initiation and arrest phenomena in pressurized composite cylinders are governed by two different, yet related, physical phenomena (bulging and flapping). The proper driving parameter for the bulging phenomenon is the *hoop stress* which depends on the pressure, cylinder

radius, and cylinder thickness. The *bending parameter* is the proper driving parameter for the flapping phenomenon and it depends on the pressure at rupture, longitudinal stiffener spacing, and base cylinder thickness. Thus, if a laboratory-scaled specimen is scaled for *hoop stress* consideration in an actual fuselage, then the magnitude of the *bending parameter* in such a specimen can be significantly different than that in a full scale fuselage. Thus, arrest is difficult, if not impossible, to accomplish in a smaller sized specimen scaled for initiation and bifurcation considerations. This is confirmed by the experimental work.

Another potential scaling problem is also identified in the event of a complete damage arrest by the longitudinal stiffeners. This additional complication arises if the pressure at rupture is sufficiently high such that other types of damage can reinitiate at the corners left by the rectangular blown-out piece bounded by the first sets of the longitudinal and hoop stiffeners. This hypothesis is supported by the observed damage path of a stiffened cylinder with significantly more reinforcement in the longitudinal direction.

Further experimental and modelling work that takes all of these scaling issues into consideration is needed to explore potential arrest in laboratory-scaled specimens. This should include the role of geometric nonlinearity in the flapping phenomenon in real and model fuselage structures as very limited numerical work is available that addresses this issue. Since flapping involves both bending and tearing actions, analysis based on the mechanics of flexible structure such as "paper mechanics" (e.g. [84, 85]) may provide more insights into the flapping mechanism and subsequent growth of damage. More detailed finite element and fracture analyses that include the mode-III (tearing) fracture mode may also be

needed in this case. Furthermore, an actual fuselage is also subjected to other types of loading (i.e. bending and torsional loads). The effects of combined loading on the damage propagation in such a structure are unclear at this time and should be investigated further.

Chapter 9

Conclusions and Recommendations

The present work was conducted with the objective to better understand the mechanisms of damage tolerance and arrest in pressurized composite cylinders. Two different, yet related, issues were addressed within this context: damage initiation and damage arrest. In the damage initiation area, a unified approach consisting of analytical, numerical, and experimental work was undertaken to study the general effects of geometric nonlinearity in the response and failure of pressurized composite cylinders. In the damage arrest area, numerical and experimental work was undertaken to assess the mechanisms of arrest in such a structure. In this chapter, conclusions are drawn from the results of the investigation and recommendations for future work are made.

9.1 Conclusions

The work conducted and the data and discussion presented herein lead to the following conclusions:

1. The nonlinear membrane stress intensification factor, K^{ext} , which is valid for isotropic and quasi-isotropic composite cylinders, depends only on two nondimensional parameters: a *geometrical parameter* λ , which depends on the cylinder radius, thickness, crack length, and

Poisson's ratio; and a *loading parameter* η , which depends on the pressure, material (structural) stiffness, and radius-to-thickness ratio.

2. The effects of nonlinearity on the failure of any isotropic or quasi-isotropic composite cylinder can be estimated via an engineering estimation scheme which utilizes the so-called *iso-nonlinear plot*. This plot shows the percentage differences between the linear and nonlinear K^{cr} as functions of the two nondimensional parameters λ and η . This can be extended to predict the failure pressure via the *iso-error plot* with the use of a pertinent failure criterion.
3. The apparent success of the failure prediction methodology based on the linear solution for metallic as well as quasi-isotropic composite, laboratory-scaled cylinders (with typical radius-to-thickness ratios on the order of 100 or smaller) is due to the fact that the nonlinear effects are not significant at that scale with the predicted error being less than 15% even for large values of λ (λ greater than 10).
4. The nonlinear effects in a real fuselage (with typical radius-to-thickness ratio on the order of 1000 or greater) are significantly more important than those in a laboratory-scaled specimen. In a real fuselage, the difference in the predicted failure pressures via linear and nonlinear methodologies can be 50% or greater, depending on the specific cylindrical configuration.

5. Nonlinear effects must be taken into account (for example, by using the proposed estimation scheme) if a laboratory-scaled specimen is to be used to predict failure of a full-scale (larger) cylinder.
6. The different types of nonlinear pressure-strain responses seen in the experiments and captured in the numerical analysis results are (local) manifestations of nonlinear effects on the membrane and bending strain components. In particular, such nonlinear strain responses are due to membrane stiffening.
7. The regions of a finite element model where mesh-refinement is needed to capture the stress or strain gradient accurately due to a discontinuity (such as a slit) are affected by the higher-order effects (i.e. geometric nonlinearity) and may require further refinement in areas not considered in a linear model.
8. The presence of hoop stiffening bands results in membrane and bending stiffness discontinuities between the unstiffened and stiffened regions which interact with the geometric nonlinearity to result in changes in the local strain field and the stress intensification factor. Such an interaction is a likely contributor to the observed damage bifurcation in a stiffened cylinder and is related to the ratio of the bending stiffnesses between the two regions.
9. For the same stiffener configuration, the stiffening bands in the longitudinal directions are not as effective as those in the hoop

direction in inducing damage bifurcation due to the difference in the radius of curvature between the two types of stiffeners.

10. There are two different scaling/driving parameters depending on the extent and direction of damage progression: the *hoop stress*, which depends on the pressure, cylinder radius, and cylinder thickness, is the proper driving parameter for longitudinal damage progression before bifurcation; while the *bending parameter*, which depends on the pressure at rupture, longitudinal stiffener spacing, and base cylinder thickness, is the proper driving parameter for hoopwise damage propagation after bifurcation.
11. The inability to satisfy both driving parameters in a single, laboratory-scaled specimen makes arrest very difficult, if not impossible, to accomplish in such a specimen properly scaled for damage initiation and bifurcation considerations.

9.2 Recommendations

Based on the work conducted, the following recommendations are made for future research:

1. Numerical analyses that can account for the structural anisotropic nature of composite cylinders are needed to assess the general effects of nonlinearity on the failure of such cylinders.

2. More directed analytical and numerical work, and associated experimental work, to explore the effects of geometric nonlinearity on the stability of propagating damage is needed to understand the mechanism(s) of bifurcation and turning that operate in the unstiffened and stiffened cases and potential commonality in both cases. Particularly, the local changes in strain field, K^{ext} , and T -stress due to nonlinear effects should be considered.
3. Experiments on laboratory-scaled specimens by performing scaling which is based on the proposed *bending parameter* are needed to study the possibility of arresting damage in flapping.
4. Due to significant bending and tearing actions during flapping, analytical modelling using the concepts from the *mechanics of flexible bodies* (such as paper mechanics) may provide more insights into the mechanisms of flapping and arrest.
5. The influence of higher-order effects (i.e. geometric nonlinearity) on the required mesh refinement in such a nonlinear structural problem needs to be investigated further.
6. The effects of additional stiffening elements (for example, Z-section or hat-section stiffeners) that are present in an actual fuselage on the damage propagation and arrest in such a structure need to be studied as well.

7. The effects of combined loading (pressure, axial, bending, and torsional loads) on the damage tolerance and arrest of composite cylinders need to be explored.

8. The damage tolerance of pressurized composite cylinders that contain other damage states (e.g. matrix cracking, delamination), such as those induced by low velocity impact, also needs to be addressed via analysis, numerical work, and experimentation.

References

1. "Damage Tolerance and Fatigue Evaluation of Structure", FAR Advisory Circular 25.571, Federal Aviation Administration, September, 1978.
2. "Military Specification: Airplane Damage Tolerance Requirements", MIL-A-83444, United States Air Force, July, 1974.
3. Lincoln, J. W., "Damage Tolerance - USAF Experience", *Proceeding of the 13th Symposium of the International Committee on Aeronautical Fatigue*, Pisa, Italy, 1985, pp. 265-295.
4. Gallagher, J. P., Giessler, F. J., Berens, A. P., and Engle, R. M., "USAF Damage Tolerant Design Handbook: Guidelines for the Analysis and Design of Damage Tolerant Aircraft Structures", AFWAL-TR-82-3073, Flight Dynamics Laboratory, USAF, May, 1984.
5. Ilcewicz, L. B., Smith, P. J., and Horton, R.E., "Advanced Composite Fuselage Technology", *Third NASA Advanced Composites Technology Conference*, Long Beach, CA, 1992, pp. 97-156.
6. Niu, C. Y. M., *Airframe Structural Design: Practical Design Information and Data on Aircraft Structures*, Conmilit Press, Ltd, Hong Kong, 1988, pp. 376-429.
7. Jozavi, H., Dupuis, C. W., and Sancaktar, E., "An Investigation of the Fracture Behavior of a Composite Crack Arrestor", *Journal of Composite Materials*, Vol. 22, No. 5, 1988, pp. 427-446.
8. Jones, R. M., *Mechanics of Composite Materials*, Hemisphere, Washington, D.C., 1975.
9. *Jane's All the World's Aircraft*, Sampson Low, Marston & Co., 1995.

10. Sabbagh, K., *21st Century Jet: The Making of the Boeing 777*, Macmillan, London, U.K., 1995.
11. Swift, T. L., "Damage Tolerance in Pressurized Fuselages", *Proceedings of the 14th Symposium of International Committee on Aeronautical Fatigue (ICAF)*, Ottawa, CA, 1987, pp. 1-78.
12. Flugge, W., "Stress Problems in Pressurized Cabins", NACA TN 2612, National Advisory Committee on Aeronautics, 1952.
13. Folias, E. S., "An Axial Crack in Pressurized Cylindrical Shell", *International Journal of Fracture Mechanics*, Vol. 1, 1965, pp. 20-46.
14. Folias, E. S., "On the Effect of Initial Curvature on Cracked Flat Sheets", *International Journal of Fracture Mechanics*, Vol. 5, No. 4, 1969, pp. 327-346.
15. Folias, E. S., "On the Predictions of Catastrophic Failures in Pressurized Vessels", in *Prospects of Fracture Mechanics*, ed. Sih, G. C., van Elst, H. C., and Broek, D., Noordhoff International, Leyden, 1974, pp. 405-418.
16. Folias, E. S., "Fracture in Pressure Vessels", in *Thin Shell Structures: Theory, Experiment, and Design*, ed. Fung, Y. C. and Sechler, E. E., Prentice Hall, 1974, pp. 483-518.
17. Folias, E. S., "Asymptotic Approximations to Crack Problems in Shells", in *Mechanics of Fracture - Plates and Shells with Cracks*, ed. Sih, G. C., Vol. 3, Noordhoff International Publishing, Leyden, 1977, pp. 117-160.
18. Erdogan, F. and Kibler, J. J., "Cylindrical and Spherical Shells with Cracks", *International Journal of Fracture Mechanics*, Vol. 5, No. 3, 1969, pp. 229-237.

19. Copley, L. G. and Sanders, J. L., "A Longitudinal Crack in Cylindrical Shell Under Internal Pressure", *International Journal of Fracture Mechanics*, Vol. 5, No. 2, 1969, pp. 117-131.
20. Barsoum, R. S., Loowis, R. W., and Stewart, B. D., "Analysis of Through Cracks in Cylindrical Shells by the Quarter-Point Elements", *International Journal of Fracture*, Vol. 15, No. 3, 1979, pp. 259-280.
21. Krenk, S., "Influence of Transverse Shear on Axial Crack in a Cylindrical Shell", *International Journal of Fracture*, Vol. 14, No. 2, 1978, pp. 123-143.
22. Getz, D. L., Pierce, W. S., and Calvert, H. F., "Correlations of Uniaxial Notch Tensile Data with Pressure Vessel Fracture Characteristics", ASME Paper 63-WA-187, 1963.
23. Anderson, R. D. and Sullivan, T. L., "Fracture Mechanics of Through-Cracked Cylindrical Pressure Vessels", NASA TN D-3252, 1963.
24. Duffy, A. R., "Studies of Hydrostatic Test Levels and Defect Behavior", *Symposium of Line Pipe Research, Pipeline Research Committee of American Gas Association*, Dallas, TX, November 17-18, 1965.
25. Graves, M. J. and Lagace, P. A., "Damage Tolerance of Composite Cylinders", *Composite Structures*, Vol. 4, No. 1, 1985, pp. 75-91.
26. Ranniger, C. U., Lagace, P. A., and Graves, M. J., "Damage Tolerance and Arrest Characteristics of Pressurized Graphite/Epoxy Tape Cylinders", *Composite Materials: Fatigue and Fracture - Fifth Volume, ASTM STP 1230*, ASTM, 1995, pp. 407-426.
27. Ansell, H., "Bulging of Cracked Pressurized Aircraft Structure", Department of Mechanical Engineering, Linkoping Institute of Technology, Sweden, Ph.D. Thesis, 1988.

28. Rankin, C. C., Brogan, F. A., and Riks, E., "Some Computational Tools for the Analysis of Through Cracks in Stiffened Fuselage Shells", *Computational Mechanics*, Vol. 13, 1994, pp. 143-156.
29. Riks, E. and den Rijier, P. J., "A Finite Element Analysis of Cracks in a Thin Walled Circular Cylinder Under Internal Pressure", NLR TR 87021 U, National Aerospace Laboratory, the Netherlands, 1987.
30. Riks, E., "Bulging Cracks in Pressurized Fuselages: a Numerical Study", NLR MP 87058 U, National Aerospace Laboratory, the Netherlands, 1987.
31. Riks, E., Brogan, F. A., and Rankin, C. C., "Bulging Cracks in Pressurized Fuselages: a Procedure for Computation", in *Analytical and Computational Models of Shells*, eds. Noor, A. K., Belytschko, T., and Simo, J., 1989, pp. 483-507.
32. Shenoy, V. B., Potyondy, D. O., and Atluri, S. N., "A Methodology for Computing Nonlinear Fracture Parameters for Bulging Crack in Pressurized Aircraft Fuselage", *Computational Mechanics*, Vol. 14, No. 6, 1994, pp. 529-548.
33. Chen, D. and Schijve, J., "Bulging of Fatigue Cracks in a Pressurized Aircraft Fuselage", *Proceeding of the 16th Symposium of International Committee on Aeronautical Fatigue (ICAF)*, Tokyo, Japan, 1991, pp. 277-315.
34. Sawicki, A. J., "Damage Tolerance of Integrally Stiffened Composite Plates and Cylinders", TELAC Report 90-17, Massachusetts Institute of Technology, September, 1990.
35. Sawicki, A. J., Graves, M. J., and Lagace, P. A., "Failure of Graphite/Epoxy Panels with Stiffening Strips", *Composite Materials: Fatigue and Fracture - 4th Volume, ASTM STP 1156*, ASTM, 1993, pp. 5-34.

36. Graves, M. J. and Sawicki, A. J., "The Failure of Integrally Stiffened Graphite/Epoxy Cylinders", *Composite Structures*, Vol. 27, 1994, pp. 269-282.
37. Ranniger, C. U., "Damage Tolerance and Arrest Characteristics of Pressurized Graphite/ Epoxy Tape Cylinders", TELAC Report 91-11, Massachusetts Institute of Technology, 1991.
38. Sanders, J. L., "Circumferential Through-Cracks in Cylindrical Shells under Tension", *Journal of Applied Mechanics*, Vol. 49, 1982, pp. 103-107.
39. Yamaki, N., *Elastic Stability of Circular Cylindrical Shells*, North-Holland Series in Applied Mathematics and Mechanics, ed. Becker, E., Budiansky, B., Koiter, W. T., and Lauwrier, H. A., Vol. 27, Elsevier Science Publishers, Amsterdam, 1984, pp. 1-18.
40. Amazigo, J. C., "On the J-Integral for an Internally Pressurized Cylindrical Shell with Longitudinal Crack", *International Journal of Fracture*, Vol. 9, 1973, pp. 492-494.
41. Nicholson, J. W. and Simmonds, J. G., "Sanders' Energy Release Rate Integral for Arbitrarily Loaded Shallow Shells and Its Asymptotic Evaluation for a Cracked Cylinder", *Journal of Applied Mechanics*, Vol. 47, June, 1980, pp. 363-369.
42. Nicholson, J. W., Bradley, M. R., and Carrington, C. K., "Asymptotic Evaluation of a Combined Stress Intensity Factor for a Pressurized Cylindrical Shell Containing a Longitudinal Crack", *Journal of Applied Mechanics*, Vol. 47, September, 1980, pp. 583-585.
43. Duncan, M. E. and Sanders, J. L., "The Effect of a Circumferential Stiffener on the Stress in a Pressurized Cylindrical Shell with Longitudinal Crack", *International Journal of Fracture Mechanics*, Vol. 5, No. 2, 1969, pp. 133-154.

44. Crichlow, W. J. and Wells, R. H., "Crack Propagation and Residual Static Strength of Fatigue-Cracked Titanium and Steel Cylinders", *Fatigue Crack Propagation, ASTM STP 415*, ASTM, 1967, pp. 25-70.
45. Hahn, G. T., Sarrate, M., and Rosenfeld, A. R., "Criteria for Crack Extension in Cylindrical Pressure Vessels", *International Journal of Fracture Mechanics*, Vol. 5, 1969, pp. 187-210.
46. Saeger, K. J. and Lagace, P. A., "Fracture of Pressurized Composite Cylinders with High Strain-to-Failure Matrix System", *Composite Materials: Fatigue and Fracture - 2nd Volume, ASTM STP 1012*, ASTM, 1989, pp. 326-337.
47. Awerbuch, J. and Madhukar, M. S., "Notched Strength of Composite Laminates: Predictions and Experiments - A Review", *Journal of Reinforced Plastics and Composites*, Vol. 4, 1985, pp. 3-159.
48. Whitney, J. M. and Nuismer, R. J., "Stress Fracture Criteria for Composite Laminates Containing Stress Concentrations", *Journal of Composite Materials*, Vol. 8, 1974, pp. 253-265.
49. Mar, J. W. and Lin, K. Y., "Fracture of Boron/Aluminum Composites with Discontinuities", *Journal of Composite Materials*, Vol. 11, 1977, pp. 405-421.
50. Lagace, P. A., "Notch Sensitivity and Stacking Sequence of Laminated Composites", *Composite Materials: Testing and Design - Seventh Conference, ASTM STP 893*, ASTM, 1986, pp. 161-176.
51. Fenner, D. N., "Stress Singularities in Composite Materials with an Arbitrarily Oriented Crack Meeting an Interface", *International Journal of Fracture*, Vol. 12, No. 5, 1976, pp. 705-721.
52. Brewer, J. C., "Tensile Fracture of Graphite/Epoxy with Angled Slits", TELAC Report 82-16, Massachusetts Institute of Technology, 1982.

53. Vaidya, R. and Sun, C. T., "Fracture Criterion for Notched Composite Laminates", *Proceeding of the 37th AIAA/ASME/ASCE/AHS/ASC Structures, Structural Dynamics, and Materials Conference*, Salt Lake City, Utah, 1996, pp. 331-338.
54. Chang, S. G. and Mar, J. W., "The Catastrophic Failure of Pressurized Graphite/Epoxy Cylinders with Slits at Various Angles", *Journal of Aircraft*, Vol. 22, No. 6, 1985, pp. 462-466.
55. Graves, M. J., "The Catastrophic Failure of Pressurized Graphite/Epoxy Cylinders", TELAC Report 82-10, Massachusetts Institute of Technology, 1982.
56. Priest, S. M., "Damage Tolerance of Uniaxial and Biaxial Loaded Composite Cylinders", TELAC Report 94-1, Massachusetts Institute of Technology, 1994.
57. Ranniger, C. U., "Effects of Cylinder Diameter on the Damage Tolerance of Graphite Epoxy Cylinders with Axial Notches", TELAC Report 91-10, Massachusetts Institute of Technology, May, 1991.
58. Trop, D. W., "Damage Tolerance of Internally Pressurized Sandwich Walled Graphite/Epoxy Cylinders", TELAC Report 85-3, Massachusetts Institute of Technology, 1985.
59. Saeger, K. J. and Lagace, P. A., "Effect of Localized Bending at Through-Flaws in Pressurized Graphite/Epoxy Tape Cylinders", *Journal of Aerospace Engineering*, Vol. 6, No. 4, 1993, pp. 381-393.
60. Saeger, K. J., "Damage Tolerance of Composite Cylinders with High Strain-to-Failure Matrix System", TELAC Report 86-11, Massachusetts Institute of Technology, Cambridge, MA, May, 1986.
61. Lagace, P. A. and Saeger, K. J., "Damage Tolerance Characteristics of Pressurized Graphite/Epoxy Cylinders", *Proceeding of the Sixth*

International Conference on Offshore Mechanics and Arctic Engineering, Houston, TX, 1987, pp. 31-37.

62. McGuire, P. A., Sampath, S. G., Popelar, C. H., and Kanninen, M. F., "A Theoretical Model for Crack Propagation and Crack Arrest in Pressurized Pipelines", *Crack Arrest Methodology and Applications*, ASTM STP 711, ASTM, 1980, pp. 341-357.
63. Kanninen, M. F., Mills, E., and Hahn, G., "A Study of Ship Hull Crack Arrester Systems", Technical Report SSC-265, Naval Systems Command, Department of the Navy, 1976.
64. Kanninen, M. F., Sampath, S. G., and Popelar, C., "Steady-State Crack Propagation in Pressurized Pipelines Without Backfill", *Journal of Pressure Vessel Technology*, Vol. 98, No. 1, 1976, pp. 56-65.
65. Sendeckyj, G. P., "Concepts for Crack Arrestment in Composites", *Fracture Mechanics of Composites*, 1975, pp. 215-226.
66. Bhatia, N. M. and Verette, R. M., "Crack Arrest of Laminated Composites", *Fracture Mechanics of Composites*, ASTM STP 593, ASTM, 1975, pp. 200-214.
67. Sanders, J. L., Jr., "Nonlinear Theories for Thin Shells", *Quarterly for Applied Mathematics*, Vol. 21, 1963, pp. 21-36.
68. Brogan, F. A., Rankin, C. C., and Cabiness, H. D., *STAGS User Manual*, LMSC P032594, Lockheed Palo Alto Research Laboratory, 1994.
69. Viz, M. J., Potyondi, D., Rankin, C. C., Riks, E., and Zehnder, A., "Computation of Membrane and Bending Stress Intensity Factors for Thin, Cracked Plates", *International Journal of Fracture*, November, 1995, pp. 21-38.

70. Simonds, R. A. and Stinchcomb, W. W., "Response of Notched AS4/PEEK Laminates to Tension/Compression Loading", *Advances in Thermoplastic Matrix Composite Materials, ASTM STP 1044*, ASTM, 1989, pp. 133-145.
71. Lagace, P. A., Bhat, N. V., and Gundogdu, A., "Response of Notched Graphite/Epoxy and Graphite/PEEK Systems", *Composite Materials: Fatigue and Fracture - 4th Volume, ASTM STP 1156*, ASTM, 1993, pp. 55-71.
72. Hutchinson, J. W., *Advanced Seminar in Solid and Structural Mechanics (Engineering Science 242 R Class Notes)*, Division of Applied Sciences - Harvard University, 1993.
73. Moran, B. and Shih, C. F., "Crack Tip and Associated Domain Integrals from Momentum and Energy Balance", *Engineering Fracture Mechanics*, Vol. 27, 1987, pp. 615-641.
74. Potyondy, D. O., Wawrzynek, P. A., and Ingraffea, A. R., "Discrete Crack Growth Analysis Methodology for Through-Cracks in Pressurized Fuselage Structures", *International Journal for Numerical Methods in Engineering*, Vol. 38, No. 10, 1995, pp. 1611-1633.
75. Rice, J. R., "A Path Independent Integral and the Approximate Analysis of Strain Concentration by Notches and Cracks", *Journal of Applied Mechanics*, Vol. 35, 1968, pp. 379-386.
76. Rice, J. R., "Mathematical Analysis in the Mechanics of Fracture", in *Fracture*, ed. Liebowitz, H., Vol. 2, Academic Press, 1968, pp. 191-311.
77. Press, W. H., Flannery, B. P., Teukolsky, S. A., and Vetterling, W. T., *Numerical Recipes: The Art of Scientific Computing*, Cambridge University Press, New York, 1990, pp. 86 - 89.

78. Ranniger, C. U. and Forbes, K., "Air Bladder Manufacturing Process for Cylindrical Graphite/Epoxy Pressure Vessels", Internal TELAC document, Massachusetts Institute of Technology, October, 1990.
79. Lagace, P. A., "Notch-Sensitivity of Graphite/Epoxy Fabric Laminates", *Composite Science and Technology*, Vol. 26, 1986, pp. 95-117.
80. Feddersen, C. E., Simonen, F. A., Hulbert, L. E., and Hyler, W. S., "An Experimental and Theoretical Investigation of Plane Stress Fracture of 2024-T351 Aluminum Alloy", Battelle Memorial Institute, 1970.
81. Zaal, K. J. J. M., "A Survey of Crack Path Stability Criteria and Their Application to Crack Flapping Phenomena in Stiffened Structures", Technical Report LR-681, Faculty of Aerospace Engineering, Technical University of Delft, the Netherlands, 1992.
82. Cotterell, B. and Rice, J. R., "Slightly Curved or Kinked Cracks", *International Journal of Fracture*, Vol. 16, 1980, pp. 155-169.
83. Sumi, Y., Nemat-Nasser, S., and Keer, L. M., "On Crack Path Stability in a Finite Body", *Engineering Fracture Mechanics*, Vol. 22, 1985, pp. 759-771.
84. Benson, R. C., "A Nonlinear Wound Roll Model Allowing for Large Deformation", *Journal of Applied Mechanics*, Vol. 62, No. 4, 1995, pp. 853-862.
85. Stolte, J. and Benson, R. C., "Dynamic Deflection of Paper Emerging from a Channel", *ASME Journal of Vibrations and Acoustics*, Vol. 114, No. 2, 1992, pp. 187-193.

Appendix A

Derivation of the Nondimensional Parameters Using the Sanders Nonlinear Shell Theory

In Chapter 4, the derivation of the nondimensional loading parameter η is presented based on the Donnell-Mushtari-Vlasov (DMV) nonlinear shallow-shell equations. The DMV theory is the simplest nonlinear shell theory. The nonlinearity assumed in the DMV theory includes large deformation and moderate rotation [39]. The moderate rotation kinematics imply that the maximum rotation that can be handled by such a theory should be less than 10° [72]. The kinematics or strain-displacement assumption inherent in the DMV theory is that of shell-shallowness. This shell-shallowness assumption implies that the shell geometry resembles that of a flat plate with small initial curvature. This implies that the ratio of the depth of the cylinder to the cylinder radius is small (much less than 1). To make sure that the parameters obtained previously in Chapter 4 using the DMV theory are universal, they are derived here from the more complicated nonlinear Sanders shell theory [67] which is valid to model non-shallow (deep) shells.

A.1 Governing Equations for Cylindrical Shells

The equilibrium equations based on Sanders shell theory [39, 67] for cylindrical geometries shown in Figure 3.1 can be written as

$$N_{xx,x} + N_{xy,x} + \frac{1}{2R}M_{xy,y} - \frac{1}{4}[(v_{,x} - u_{,y})(N_{xx} + N_{yy})]_{,y} = p_x \quad (\text{A.1})$$

$$N_{xy,x} + N_{yy,y} - \frac{3}{2R}M_{xy,x} - \frac{1}{R}M_{yy,y} - \frac{1}{R}\left[\left(w_{,y} + \frac{v}{R}\right)N_{yy} + w_{,x}N_{xy}\right] + \frac{1}{4}[(v_{,x} - u_{,y})(N_{xx} + N_{yy})]_{,x} = p_y \quad (\text{A.2})$$

$$M_{xx,xx} + 2M_{xy,xy} + M_{yy,yy} + \frac{1}{R}N_{yy} - \left[\left(w_{,y} + \frac{v}{R}\right)N_{xy} + w_{,x}N_{xx}\right]_{,x} + \left[\left(w_{,y} + \frac{v}{R}\right)N_{yy} + w_{,x}N_{xy}\right]_{,y} = p \quad (\text{A.3})$$

where u , v , and w are the displacements in the x -, y -, and z -directions, respectively, p_x and p_y are the edge loads, p represents the pressure loads, and the stress and moment resultants N_{ij} and M_{ij} are defined as

$$(N_{xx}, N_{xy}, Q_x) = \int_{-h/2}^{h/2} (\sigma_{xx}, \sigma_{xy}, \sigma_{xz}) dz \quad (\text{A.4})$$

$$(N_{yx}, N_{yy}, Q_y) = \int_{-h/2}^{h/2} (\sigma_{yx}, \sigma_{yy}, \sigma_{yz}) dz \quad (\text{A.5})$$

$$(M_{xx}, M_{xy}) = \int_{-h/2}^{h/2} (\sigma_{xx}, \sigma_{xy}) z dz \quad (\text{A.6})$$

$$(M_{yx}, M_{yy}) = \int_{-h/2}^{h/2} (\sigma_{yx}, \sigma_{yy}) z dz \quad (\text{A.7})$$

By performing integration through the thickness of the cylinder, the force and moment resultants (equations (A.4) through (A.7)) can be rewritten in the following standard matrix form:

$$\begin{Bmatrix} N_{xx} \\ N_{yy} \\ N_{xy} \\ M_{xx} \\ M_{yy} \\ M_{xy} \end{Bmatrix} = \begin{bmatrix} A_{11} & A_{12} & A_{16} & B_{11} & B_{12} & B_{16} \\ A_{12} & A_{22} & A_{26} & B_{12} & B_{22} & B_{26} \\ A_{16} & A_{26} & A_{66} & B_{16} & B_{26} & B_{66} \\ B_{11} & B_{12} & B_{16} & D_{11} & D_{12} & D_{16} \\ B_{12} & B_{22} & B_{26} & D_{12} & D_{22} & D_{26} \\ B_{16} & B_{26} & B_{66} & D_{16} & D_{26} & D_{66} \end{bmatrix} \begin{Bmatrix} \epsilon_{xx}^0 \\ \epsilon_{yy}^0 \\ \gamma_{xy}^0 \\ \kappa_{xx} \\ \kappa_{yy} \\ \kappa_{xy} \end{Bmatrix} \quad (\text{A.8})$$

The nonlinear kinematics considered in the Sanders shell theory are small strains and moderately large rotations. The moderate rotation kinematics implies that the maximum rotation that can be handled by this theory should be less than 10° [72]. The strain-displacement relations are manifested as

$$\varepsilon_{xx}^0 = u_{,x} + \frac{1}{2}w_{,x}^2 + \frac{1}{8}(v_{,x} - u_{,y})^2 \quad (\text{A.9})$$

$$\varepsilon_{yy}^0 = v_{,y} - \frac{w}{R} + \frac{1}{2}\left(w_{,y} + \frac{v}{R}\right)^2 + \frac{1}{8}(u_{,y} - v_{,x})^2 \quad (\text{A.10})$$

$$\gamma_{xy}^0 = u_{,y} + v_{,x} + w_{,x}\left(w_{,y} + \frac{v}{R}\right) \quad (\text{A.11})$$

$$\kappa_{xx} = -w_{,xx} \quad (\text{A.12})$$

$$\kappa_{yy} = -\left(w_{,yy} + \frac{1}{R}v_{,y}\right) \quad (\text{A.13})$$

$$\kappa_{xy} = -2\left[w_{,xy} + \frac{1}{4R}(3v_{,x} - u_{,y})\right] \quad (\text{A.14})$$

Also, based on Kirchhoff's hypothesis which states that lines normal to the neutral axis stay normal to that axis after deformation, the total strains can be written as the sum of the midplane strains and the bending contributions

$$\varepsilon_{xx} = \varepsilon_{xx}^0 + z\kappa_{xx} \quad (\text{A.15})$$

$$\varepsilon_{yy} = \varepsilon_{yy}^0 + z\kappa_{yy} \quad (\text{A.16})$$

$$\gamma_{xy} = \gamma_{xy}^0 + z\kappa_{xy} \quad (\text{A.17})$$

The constitutive equation shown (equation (A.8)) is general and is therefore not restricted to isotropic or quasi-isotropic materials only. For isotropic or homogenized quasi-isotropic composite cylinders, the terms in equations (A.8) can be further simplified to

$$N_{xx} = \frac{E h}{1 - \nu^2} (\varepsilon_{xx}^0 + \nu \varepsilon_{yy}^0) \quad (\text{A.18})$$

$$N_{yy} = \frac{E h}{1 - \nu^2} (\varepsilon_{yy}^0 + \nu \varepsilon_{xx}^0) \quad (\text{A.19})$$

$$N_{xy} = N_{yx} = \frac{E h}{2(1 + \nu)} \gamma_{xy}^0 \quad (\text{A.20})$$

$$M_{xx} = \frac{E h^3}{12(1 - \nu^2)} (\kappa_{xx} + \nu \kappa_{yy}) \quad (\text{A.21})$$

$$M_{yy} = \frac{E h^3}{12(1 - \nu^2)} (\kappa_{yy} + \nu \kappa_{xx}) \quad (\text{A.22})$$

$$M_{xy} = M_{yx} = \frac{E h^3}{24(1 + \nu)} \kappa_{xy} \quad (\text{A.23})$$

where h is the cylinder thickness, and E and ν are the material parameters.

A.2 Nondimensionalization Procedure

The following nondimensionalization procedures are performed:

$$u' = u_0 u \quad (\text{A.24})$$

$$v' = v_0 v \quad (\text{A.25})$$

$$w' = w_0 w \quad (\text{A.26})$$

$$x' = a x \quad (\text{A.27})$$

$$y' = a y \quad (\text{A.28})$$

where u_0 , v_0 , and w_0 are the normalization parameters to be determined shortly, and a is the crack half-length. Henceforth, the primed quantities correspond to the physical variables and the unprimed quantities are dimensionless.

To determine the u_0 , v_0 , and w_0 parameters, equations (A.24) through (A.28) are substituted into the nonlinear kinematics expressions (equations (A.9) through (A.14)), keeping in mind that

$$\frac{\partial}{\partial x'} = \frac{1}{a} \frac{\partial}{\partial x} \quad (\text{A.29})$$

and

$$\frac{\partial}{\partial y'} = \frac{1}{a} \frac{\partial}{\partial y}, \quad (\text{A.30})$$

Therefore, the strain-displacement equations become

$$\varepsilon_{xx}^0 = \left(\frac{u_0}{a}\right) u_{,x} + \left(\frac{w_0^2}{a^2}\right) \frac{1}{2} w_{,x}^2 + \left(\frac{v_0^2}{a^2}\right) \frac{1}{8} v_{,x}^2 + \left(\frac{u_0^2}{a^2}\right) \frac{1}{8} u_{,y}^2 - \left(\frac{v_0 u_0}{a^2}\right) \frac{1}{4} u_{,y} v_{,x} \quad (\text{A.31})$$

$$\varepsilon_{yy}^0 = \left(\frac{v_0}{a}\right) v_{,y} - \left(\frac{w_0}{R}\right) w + \left(\frac{w_0^2}{a^2}\right) \frac{1}{2} w_{,y}^2 + \left(\frac{v_0^2}{R^2}\right) \frac{1}{2} v^2 + \left(\frac{w_0 v_0}{a R}\right) w_{,y} v + \left(\frac{u_0^2}{a^2}\right) \frac{1}{8} u_{,x}^2 + \left(\frac{v_0^2}{a^2}\right) \frac{1}{8} v_{,y}^2 - \left(\frac{v_0 u_0}{a^2}\right) \frac{1}{4} u_{,x} v_{,y} \quad (\text{A.32})$$

$$\gamma_{xy}^0 = \left(\frac{u_0}{a}\right) u_{,y} + \left(\frac{v_0}{a}\right) v_{,x} + \left(\frac{w_0^2}{a^2}\right) w_{,x} w_{,y} + \left(\frac{w_0 v_0}{a R}\right) w_{,x} v \quad (\text{A.33})$$

$$\kappa_{xx} = -\left(\frac{w_0}{a^2}\right) w_{,xx} \quad (\text{A.34})$$

$$\kappa_{yy} = -\left(\frac{w_0}{a^2}\right) w_{,yy} - \left(\frac{v_0}{a R}\right) v_{,y} \quad (\text{A.35})$$

$$\kappa_{xy} = -2 \left(\frac{w_0}{a^2}\right) w_{,xy} - \left(\frac{v_0}{a R}\right) \frac{3}{4} v_{,x} - \left(\frac{u_0}{a R}\right) \frac{1}{4} u_{,y} \quad (\text{A.36})$$

The terms on the left hand side of equations (A.31) to (A.33) are strains and are therefore dimensionless and those of equations (A.34) to (A.36) are curvatures and have units of $(length)^{-1}$. Therefore, the terms in parentheses

in each equation are set "equal" (with reference to units) to each other (i.e. set $\left(\frac{w_0^2}{a^2}\right)$ equal to $\left(\frac{v_0}{a}\right)$ and $\left(\frac{w_0}{R}\right)$ from equation (A.32)). The expressions obtained are further simplified using the nondimensional parameter λ obtained from the linear solution (i.e. $\lambda = \frac{a}{\sqrt{Rh}} \sqrt{12(1-\nu^2)}$). Since the term containing the Poisson's ratio in the expression for λ is dimensionless, for purposes of nondimensionalization λ can be expressed as

$$\lambda = \frac{a}{\sqrt{Rh}} \quad (\text{A.37})$$

The results can then be used to determine the normalization parameters. For example, from equation (A.32), $\left(\frac{w_0^2}{a^2}\right)$ is set equal to $\left(\frac{w_0}{R}\right)$,

$$\frac{w_0^2}{a^2} = \frac{w_0}{R}, \quad (\text{A.38})$$

An expression for w_0 is then obtained in the form:

$$w_0 = \frac{a^2}{R} \quad (\text{A.39})$$

Equation (A.37) is used to express this as

$$w_0 = \lambda^2 h \quad (\text{A.40})$$

The normalization parameter w_0 is thereby obtained. Using the same procedure, the other normalization parameters u_0 and v_0 can be obtained in the forms

$$u_0 = \lambda^3 \left(\frac{h}{R}\right)^{1/2} h \quad (\text{A.41})$$

$$v_0 = \lambda^3 \left(\frac{h}{R}\right)^{1/2} h \quad (\text{A.42})$$

These expressions for u_0 , v_0 , and w_0 shown in equations (A.40), (A.41), and (A.42) are used to write the coefficients in the parentheses in equations (A.31) through (A.36) as

$$\frac{u_0}{a} = \lambda^2 \frac{h}{R} \quad (\text{A.43})$$

$$\frac{v_0}{a} = \lambda^2 \frac{h}{R} \quad (\text{A.44})$$

$$\frac{w_0}{R} = \lambda^2 \frac{h}{R} \quad (\text{A.45})$$

$$\frac{u_0^2}{a^2} = \left[\lambda^2 \frac{h}{R} \right]^2 \quad (\text{A.46})$$

$$\frac{v_0^2}{a^2} = \left[\lambda^2 \frac{h}{R} \right]^2 \quad (\text{A.47})$$

$$\frac{v_0^2}{R^2} = \left[\lambda^2 \frac{h}{R} \right]^3 \quad (\text{A.48})$$

$$\frac{w_0^2}{a^2} = \left[\lambda^2 \frac{h}{R} \right]^2 \quad (\text{A.49})$$

$$\frac{u_0 v_0}{a^2} = \left[\lambda^2 \frac{h}{R} \right]^2 \quad (\text{A.50})$$

$$\frac{w_0 v_0}{a R} = \left[\lambda^2 \frac{h}{R} \right]^2 \quad (\text{A.51})$$

$$\frac{u_0}{a R} = \left[\lambda^2 \frac{h}{R} \right] \frac{1}{R} \quad (\text{A.52})$$

$$\frac{v_0}{a R} = \left[\lambda^2 \frac{h}{R} \right] \frac{1}{R} \quad (\text{A.53})$$

$$\frac{w_0}{a^2} = \frac{1}{R} \quad (\text{A.54})$$

Substituting equations (A.43) through (A.54) into equations (A.31) through (A.36) yields the following nondimensional strain-displacement relations

$$\begin{aligned}\varepsilon_{xx}^0 &= \lambda^2 \left(\frac{h}{R} \right) \left[u_{,x} + \frac{1}{2} w_{,x}^2 + \frac{1}{8} \lambda^2 \left(\frac{h}{R} \right) (v_{,x} - u_{,y})^2 \right] \\ &= \lambda^2 \left(\frac{h}{R} \right) [\Omega]\end{aligned}\tag{A.55}$$

$$\begin{aligned}\varepsilon_{yy}^0 &= \lambda^2 \left(\frac{h}{R} \right) \left[v_{,y} - w + \frac{1}{2} w_{,y}^2 + \lambda^2 \left(\frac{h}{R} \right) \left\{ \lambda^2 \left(\frac{h}{R} \right) \frac{1}{2} v^2 + w_{,y} v + \frac{1}{8} (u_{,y} - v_{,x})^2 \right\} \right] \\ &= \lambda^2 \left(\frac{h}{R} \right) [\Xi]\end{aligned}\tag{A.56}$$

$$\begin{aligned}\gamma_{xy}^0 &= \lambda^2 \left(\frac{h}{R} \right) \left[u_{,y} + v_{,x} + w_{,x} w_{,y} + \lambda^2 \left(\frac{h}{R} \right) w_{,x} v \right] \\ &= \lambda^2 \left(\frac{h}{R} \right) [\Psi]\end{aligned}\tag{A.57}$$

$$\begin{aligned}\kappa_{xx} &= -\frac{1}{R} w_{,xx} \\ &= -\frac{1}{R} [\Theta]\end{aligned}\tag{A.58}$$

$$\begin{aligned}\kappa_{yy} &= -\frac{1}{R} \left[w_{,yy} + \lambda^2 \left(\frac{h}{R} \right) v_{,y} \right] \\ &= -\frac{1}{R} [\Pi]\end{aligned}\tag{A.59}$$

$$\begin{aligned}\kappa_{xy} &= -\frac{2}{R} \left[w_{,xy} + \frac{1}{4} \lambda^2 \left(\frac{h}{R} \right) (3v_{,x} - u_{,y}) \right] \\ &= -\frac{2}{R} [\Phi]\end{aligned}\tag{A.60}$$

where the capitalized Greek symbols are used in equations (A.55) to (A.60) in order to simplify the algebraic expressions. These nondimensional strain-displacement equations are substituted into the equations for force and moment resultants (equations (A.18) through (A.23)), resulting in

$$N_{xx} = \frac{E h}{1 - \nu^2} \frac{h}{R} \lambda^2 \{ \Omega + \nu \Xi \}\tag{A.61}$$

$$N_{yy} = \frac{E h}{1 - \nu^2} \frac{h}{R} \lambda^2 \{ \Xi + \nu \Omega \}\tag{A.62}$$

$$N_{xy} = \frac{E h}{2(1+\nu)} \frac{h}{R} \lambda^2 \{ \Psi \} \quad (\text{A.63})$$

$$M_{xx} = -\frac{E h^3}{12(1-\nu^2)} \frac{1}{R} \{ \Theta + \nu \Pi \} \quad (\text{A.64})$$

$$M_{yy} = -\frac{E h^3}{12(1-\nu^2)} \frac{1}{R} \{ \Pi + \nu \Theta \} \quad (\text{A.65})$$

$$M_{xy} = -\frac{E h^3}{24(1+\nu)} \frac{1}{R} \{ 2 \Phi \} \quad (\text{A.66})$$

By substituting the force and moment resultants (equations (A.61) to (A.66)) into the equilibrium equations (equations (A.1) to (A.3)), the following equilibrium equation is obtained

$$\frac{E}{1-\nu^2} \frac{h^2}{R \sqrt{R h}} \lambda \left\{ \begin{array}{l} (\Omega + \nu \Xi)_{,x} + \frac{(1-\nu)}{2} \Psi_{,x} - \\ \left(\frac{h}{R} \right) \frac{(1-\nu)}{24 \lambda^2} (\Phi)_{,y} - \\ \frac{1+\nu}{4} \left(\frac{h}{R} \right) \lambda^2 [(v_{,x} - u_{,y}) (\Omega + \Xi)]_{,y} \end{array} \right\} = p_x \quad (\text{A.67})$$

or

$$\frac{E}{1-\nu^2} \frac{h^2}{R \sqrt{R h}} \lambda \{ F(\Omega, \Xi, \Phi, \nu, u, v) \} = p_x \quad (\text{A.68})$$

Similarly, the second and third equilibrium equations can be written as

$$\frac{E}{1-\nu^2} \frac{h^2}{R \sqrt{R h}} \lambda \left\{ \begin{array}{l} \frac{(1-\nu)}{2} \Psi_{,x} + (\Xi + \nu \Omega)_{,y} + \left(\frac{h}{R} \right) \frac{(1-\nu)}{8 \lambda^2} \Phi_{,x} + \\ \left(\frac{h}{R} \right) \frac{1}{12 \lambda^2} (\Pi + \nu \Theta)_{,y} - \\ \lambda^2 \left(\frac{h}{R} \right) \left[\left(w_{,y} + \lambda^2 \left(\frac{h}{R} \right) \nu \right) (\Xi + \nu \Omega) + \frac{(1-\nu)}{2} w_{,x} \Psi \right] + \\ \frac{1+\nu}{4} \left(\frac{h}{R} \right) \lambda^2 [(v_{,x} + u_{,y}) (\Omega + \Xi)]_{,x} \end{array} \right\} = p_y \quad (\text{A.69})$$

or

$$\frac{E}{1-\nu^2} \frac{h^2}{R\sqrt{Rh}} \lambda \{ G(\Omega, \Xi, \Phi, \Psi, \Pi, \Theta, \nu, u, v, w) \} = p_y \quad (\text{A.70})$$

$$-\frac{E}{12(1-\nu^2)} \left(\frac{h}{R}\right)^2 \frac{1}{\lambda^2} \left\{ \begin{array}{l} (\Theta + \nu \Pi)_{,xx} + \Phi_{,yy} + (\Pi + \nu \Theta)_{,yy} + \\ 6 \lambda^4 \left[(1-\nu) \left(w_{,y} + \lambda^2 \frac{h}{R} \nu \right) \Psi + 2(\Omega + \nu \Xi) w_{,x} \right]_{,x} \\ 6 \lambda^4 \left[(1-\nu) w_{,x} \Psi + 2 \left(w_{,y} + \lambda^2 \frac{h}{R} \nu \right) (\Xi + \nu \Omega) \right]_{,y} \end{array} \right\} = p \quad (\text{A.71})$$

or

$$\frac{E}{12(1-\nu^2)} \left(\frac{h}{R}\right)^2 \frac{1}{\lambda^2} \{ H(\Omega, \Xi, \Phi, \Psi, \Pi, \Theta, \nu, u, v, w) \} = p \quad (\text{A.72})$$

where F , G , and H are functions of the variables in the parentheses. For symmetrically-loaded cylinders under internal or external pressure only (without edge loads),

$$p_x = p_y = 0 \quad (\text{A.73})$$

Therefore, the first two normalized equilibrium equations shown in equations (A.68) and (A.70) are trivially satisfied. For this case, the nondimensional loading parameter can thus be obtained from the third equilibrium equation (equation (A.72)). Since the parameters of the function H are nondimensional, the function H is also nondimensional. The last set of dimensional parameters are therefore combined to yield:

$$\eta = \frac{p}{E \left(\frac{h}{R}\right)^2} \quad (\text{A.74})$$

This is the same result as from the DMV theory shown in equation (4.10) and is, indeed, nondimensional.

It has therefore been shown that the same nondimensional loading parameter for an axially-cracked cylindrical shell can be obtained using the more complicated Sanders nonlinear shell theory. This is expected as the length of the crack oriented in the longitudinal direction does not affect the shallowness condition in a shell structure. It is worth noting that the derivation of the nondimensional loading parameter η shown using the Sanders theory only requires the existence of symmetric loading and, therefore, does not distinguish whether the crack is oriented in the longitudinal or circumferential direction as the symmetry of the problem is still maintained by those two cases. However, for the case of the crack in the circumferential direction, the Donnell theory should not be used to obtain the solution as the shallowness assumption inherent in the Donnell theory can be easily violated depending on the crack length. This has been shown to be the case in [38] where the results from the two theories diverge as crack length increases.

Appendix B

Derivation of the Iso-Error Chart

The numerical results for the nonlinear membrane stress intensification factors K^{ext} discussed in Chapter 5 are also presented in the form of percentage difference of the predicted failure pressure in order to allow a better assessment of the nonlinear effects on the failure of such structures. Unlike the *iso-nonlinear plot*, this *iso-error chart* depends on the specific fracture correlation and fracture parameter(s). This chart is therefore *material-* and *laminare-dependent*. The percentage errors of the predicted failure pressures due to neglecting the nonlinear effects are plotted with respect to two nondimensional parameters: the geometrical parameter λ and the shell ratio R/h . The second parameter (R/h) is chosen since it is the key geometrical term in the loading parameter, η , given in equation (4.10). This means that all possible geometrical configurations for that particular material (given the fracture correlation and parameters) are considered. The derivation of the *iso-error chart* for the AW370-5H/3501-6 fabric cylinders with (0/45)_s stacking sequence, which is based on the Mar-Lin composite fracture correlation [49], is presented here.

The stiffness, E , and Poisson's ratio, ν , of this laminate computed using CLPT [8] are 51.6 GPa and 0.33, respectively. In the Mar-Lin correlation [49], the measured composite fracture parameter, H_C , is $698 \text{ MPa mm}^{0.28}$ [57] and the exponent m , which is a measure of a singularity of a crack terminating perpendicular to a bimaterial interface [51], is analytically determined for the graphite/epoxy bimaterial to be 0.28 [50]. The

predicted failure pressure, p^{linear} , based on the linear solution can be written as (see equation (2.9))

$$p^{linear} = \frac{h H_c (2 a)^{-0.28}}{R K_{lin}^{ex}(\lambda)} \quad (B.1)$$

where h is the cylinder thickness, R is the cylinder radius, $2 a$ is the slit size, K_{lin}^{ex} is the linear membrane stress intensification factor, and λ is the geometrical parameter given in equation (4.7). Similarly, the failure pressure predicted using the nonlinear solution, p^{NL} , can be written as

$$p^{NL} = \frac{h H_c (2 a)^{-0.28}}{R K_{nonlinear}^{ex}(\lambda, \eta)} \quad (B.2)$$

where $K_{nonlinear}^{ex}$ is the nonlinear membrane stress intensification factor and η is the loading parameter given in equation (4.10). In general, the magnitudes of p^{linear} and p^{NL} are different.

To construct the *iso-error chart*, an "inverse" problem needs to be solved. In this "inverse" problem, the known quantities are the cylinder thickness, fracture parameter(s), geometrical parameter λ , and percentage differences between the linear and nonlinear predicted failure pressures. The only unknown to be determined from this analysis is the cylinder radius R . The iso-error levels are predetermined *a priori* to be 10, 20, 30, 40, 50, 75, 100, 125, and 150%. Errors of 10% or lower imply that nonlinear effects are basically not important.

Let the difference between the nonlinear and linear solutions normalized with respect to the linear solution at a specified value of λ be defined as e

$$e(\lambda) = \frac{p^{NL} - p^{linear}}{p^{linear}} \quad (B.3)$$

In other words, the predicted pressure from the nonlinear solution, p^{NL} , can be written as

$$p^{NL} = (1 + e) p^{linear} \quad (B.4)$$

Substituting equations (B.1) and (B.2) into equation (B.4) yields

$$\frac{h}{R} \frac{H_c (2a)^{-0.28}}{K_{nonlinear}^{exi}(\lambda, \eta)} = (1 + e) \frac{h}{R} \frac{H_c (2a)^{-0.28}}{K_{lin}^{exi}(\lambda)} \quad (B.5)$$

Equation (B.5) can be simplified as

$$K_{no.linear}^{exi}(\lambda, \eta) = \frac{K_{lin}^{exi}(\lambda)}{(1 + e)} \quad (B.6)$$

The linear stress intensification factor, K_{lin}^{exi} , is only a function of λ . Since this is a given quantity for a particular case, K_{lin}^{exi} can be found from the numerical solution. Since the iso-error level, e , is also given, then the nonlinear stress intensification factor, $K_{nonlinear}^{exi}$, can be found using equation (B.6).

The nonlinear stress intensification factor, $K_{nonlinear}^{exi}$, is a function of the two nondimensional parameters (λ and η). Thus, for a fixed value of λ , the loading parameter, η , can be found once the nonlinear stress intensification factor, $K_{nonlinear}^{exi}$, is known (i.e. there is a one-to-one correspondence between $K_{nonlinear}^{exi}$ and η for a fixed value of λ from the numerical solutions used to construct the *iso-nonlinear plot*). The loading parameter, η , is shown in equation (4.10) as:

$$\eta = \frac{p^{NL}}{E \left(\frac{h}{R} \right)^2} \quad (B.7)$$

Substituting equations (B.1), (B.2) and (B.4) into equation (B.7) yields

$$\eta = \frac{(1+e) \frac{h}{R} \frac{H_c (2a)^{-0.28}}{K_{lin}^{ext}(\lambda)}}{E \left(\frac{h}{R}\right)^2} = \frac{(1+e) R}{E} \frac{H_c (2a)^{-0.28}}{h K_{lin}^{ext}(\lambda)} \quad (B.8)$$

Note that the loading parameter, η , shown in equation (B.8) is determined from the numerical solution (i.e. η is a function of the nonlinear stress intensification factor, $K_{nonlinear}^{ext}$, for a fixed value of λ).

The slit size, $2a$, is related to the cylinder radius, R , and thickness, h , via the geometrical parameter, λ (from equation (4.7)),

$$\lambda = \frac{a}{\sqrt{R h}} \sqrt[4]{12(1-\nu^2)} \quad (B.9)$$

and can thus be expressed as:

$$2a = \frac{2 \lambda \sqrt{R h}}{\sqrt[4]{12(1-\nu^2)}} \quad (B.10)$$

Thus, by substituting equation (B.10) into equation (B.8), the following expression is obtained

$$\eta = \frac{(1+e) R}{E} \frac{H_c \left(\frac{2 \lambda \sqrt{R h}}{\sqrt[4]{12(1-\nu^2)}} \right)^{-0.28}}{h K_{lin}^{ext}(\lambda)} \quad (B.11)$$

Equation (B.10) can be rewritten as

$$\eta = \Xi R^{0.86} \quad (B.12)$$

where Ξ is defined as

$$\Xi = \frac{(1+e) 1}{E} \frac{H_c \left(\frac{2 \lambda \sqrt{h}}{\sqrt[4]{12(1-\nu^2)}} \right)^{-0.28}}{h K_{lin}^{ext}(\lambda)} \quad (B.13)$$

Since η and all of the terms in Ξ are known quantities, the cylinder radius that corresponds to the specified percentage error can be determined using equation (B.12).

The same computation is performed for different values of λ and different iso-error levels. The results are depicted in Figure 5.9.

Appendix C

Predicted and Measured Strain Responses for Cylinders with Longitudinal Slit Lengths of 51 and 78 mm

Comparison between the predicted and measured strain responses for the *type-1* and *type-2* cylinders with longitudinal slit lengths of 51 and 78 mm are presented in this appendix. The comparisons for cylinders with a longitudinal slit length of 104 mm are presented in Chapter 7 for both the *type-1* and *type-2* cylinders. The contents of this appendix are summarized in Table C.1.

Table C.1 Appendix C Contents

Figure Descriptions	Figure Numbers
Predicted and measured strain responses for the unstiffened (0/45), cylinder with a longitudinal slit length of 51 mm	C.1 - C.4
Predicted and measured strain responses for the unstiffened (0/45), cylinder with a longitudinal slit length of 78 mm	C.5 - C.8
Predicted and measured strain responses for the unstiffened (45/0), cylinder with a longitudinal slit length of 51 mm	C.9 - C.12
Predicted and measured strain responses for the unstiffened (45/0), cylinder with a longitudinal slit length of 78 mm	C.13 - C.16
Predicted and measured strain responses for the stiffened (0/45), cylinder with a longitudinal slit length of 51 mm	C.17 - C.18
Predicted and measured strain responses for the stiffened (0/45), cylinder with a longitudinal slit length of 78 mm	C.19 - C.20
Predicted and measured strain responses for the stiffened (45/0), cylinder with a longitudinal slit length of 51 mm	C.21 - C.22
Predicted and measured strain responses for the stiffened (45/0), cylinder with a longitudinal slit length of 51 mm	C.23 - C.24

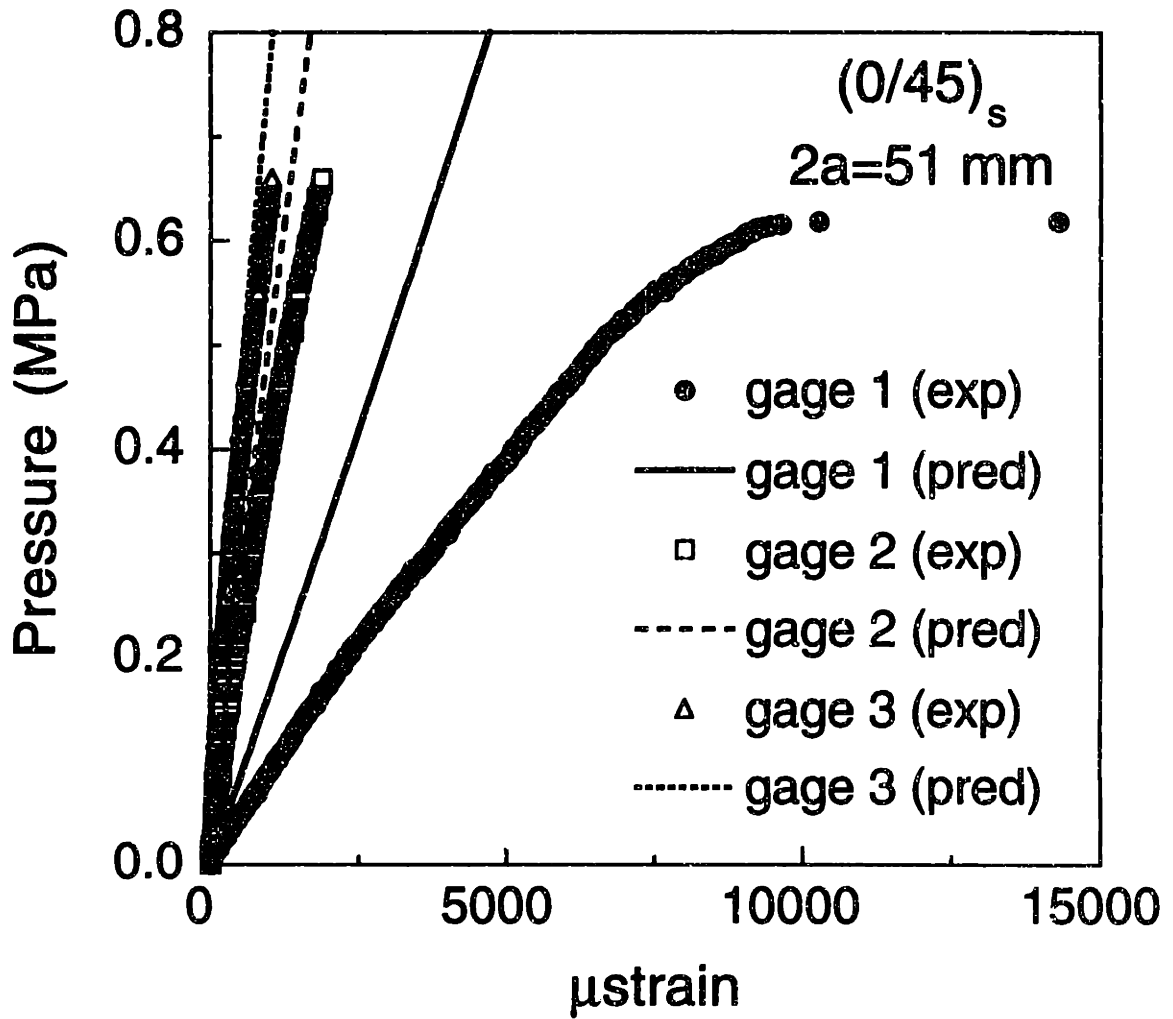


Figure C.1 Predicted and experimental strain responses for gages 1 to 3 in the unstiffened (0/45)_s cylinder with a longitudinal slit length of 51 mm.

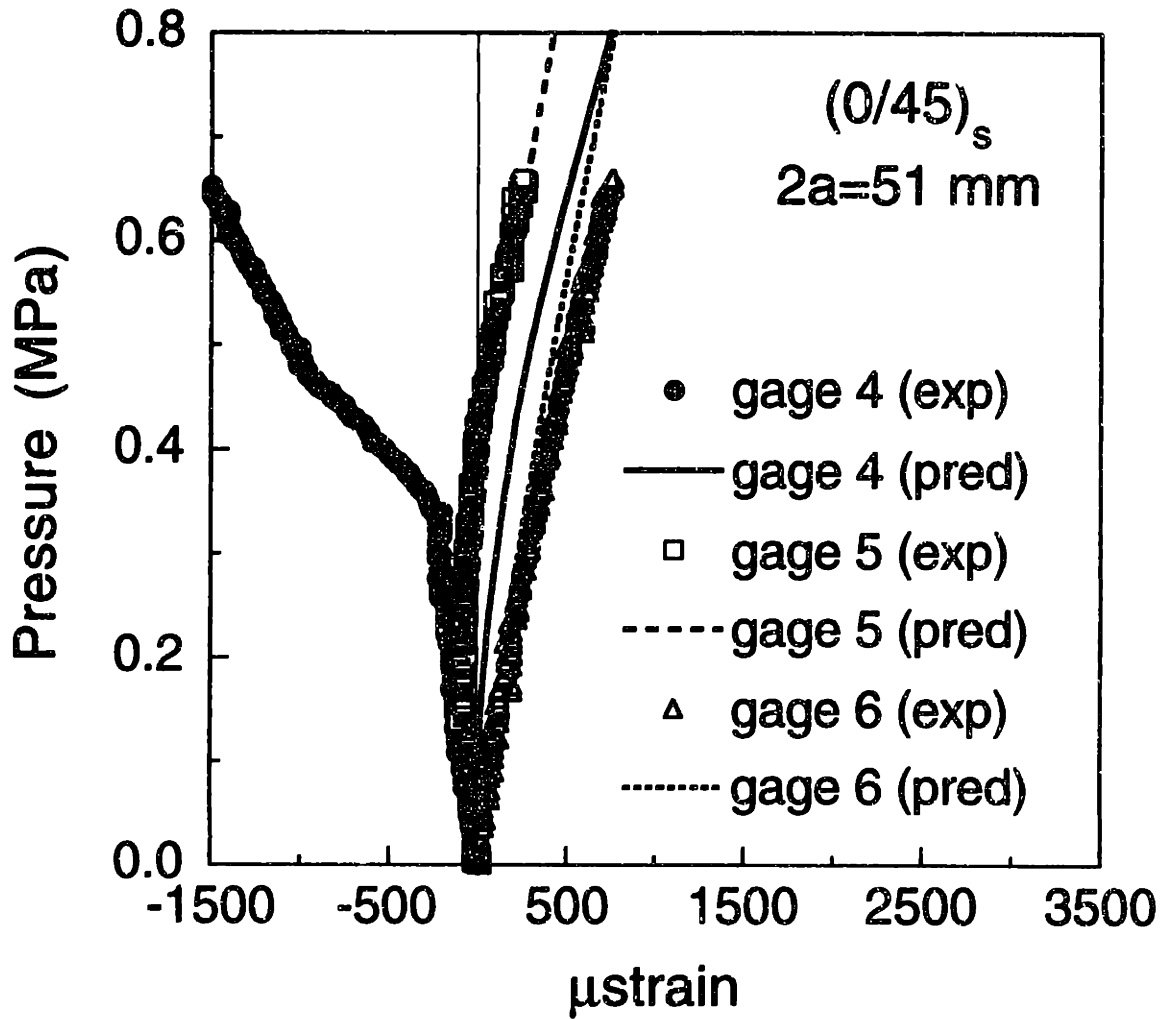


Figure C.2 Predicted and experimental strain responses for gages 4 to 6 in the unstiffened $(0/45)_s$ cylinder with a longitudinal slit length of 51 mm.

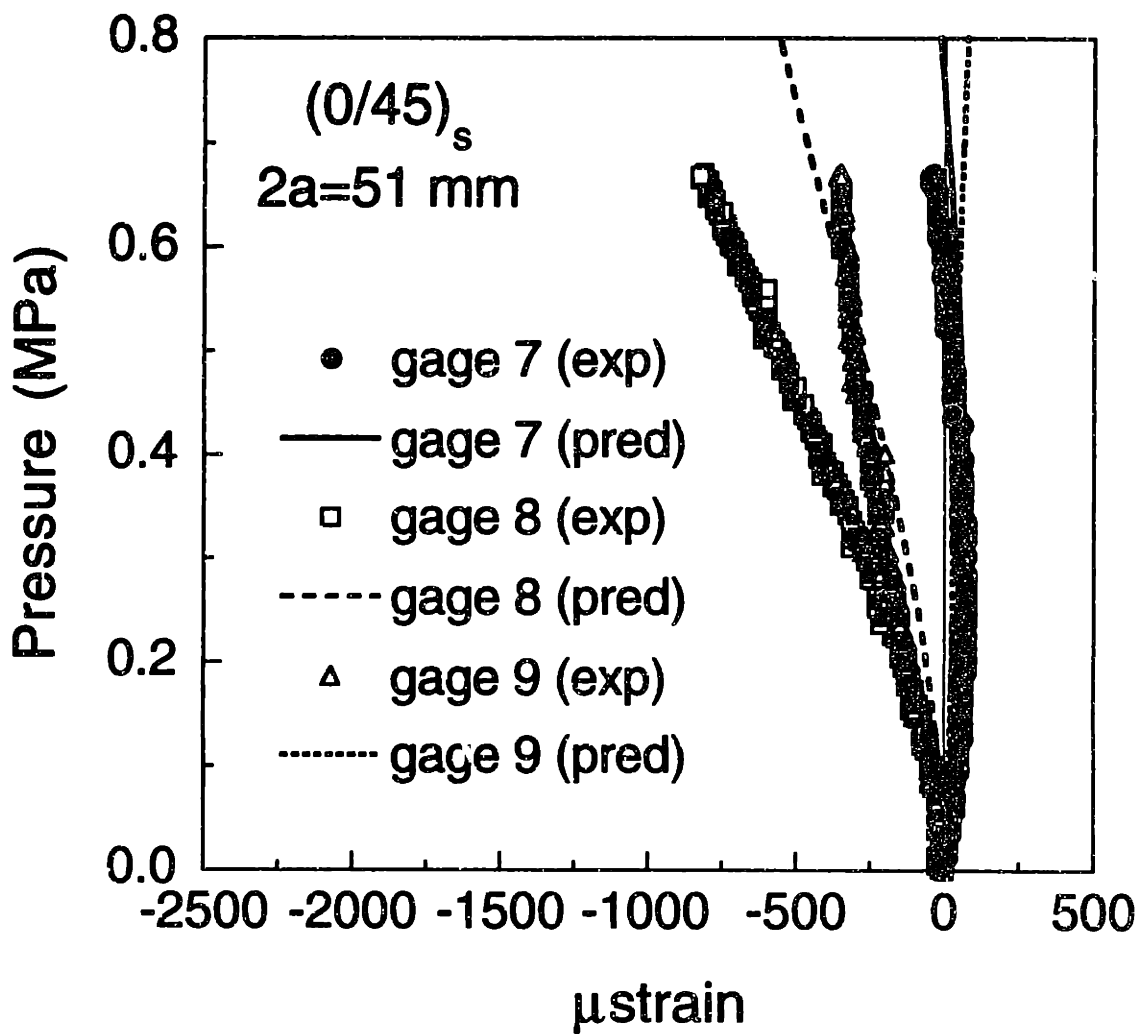


Figure C.3 Predicted and experimental strain responses for gages 7 to 9 in the unstiffened (0/45)_s cylinder with a longitudinal slit length of 51 mm.

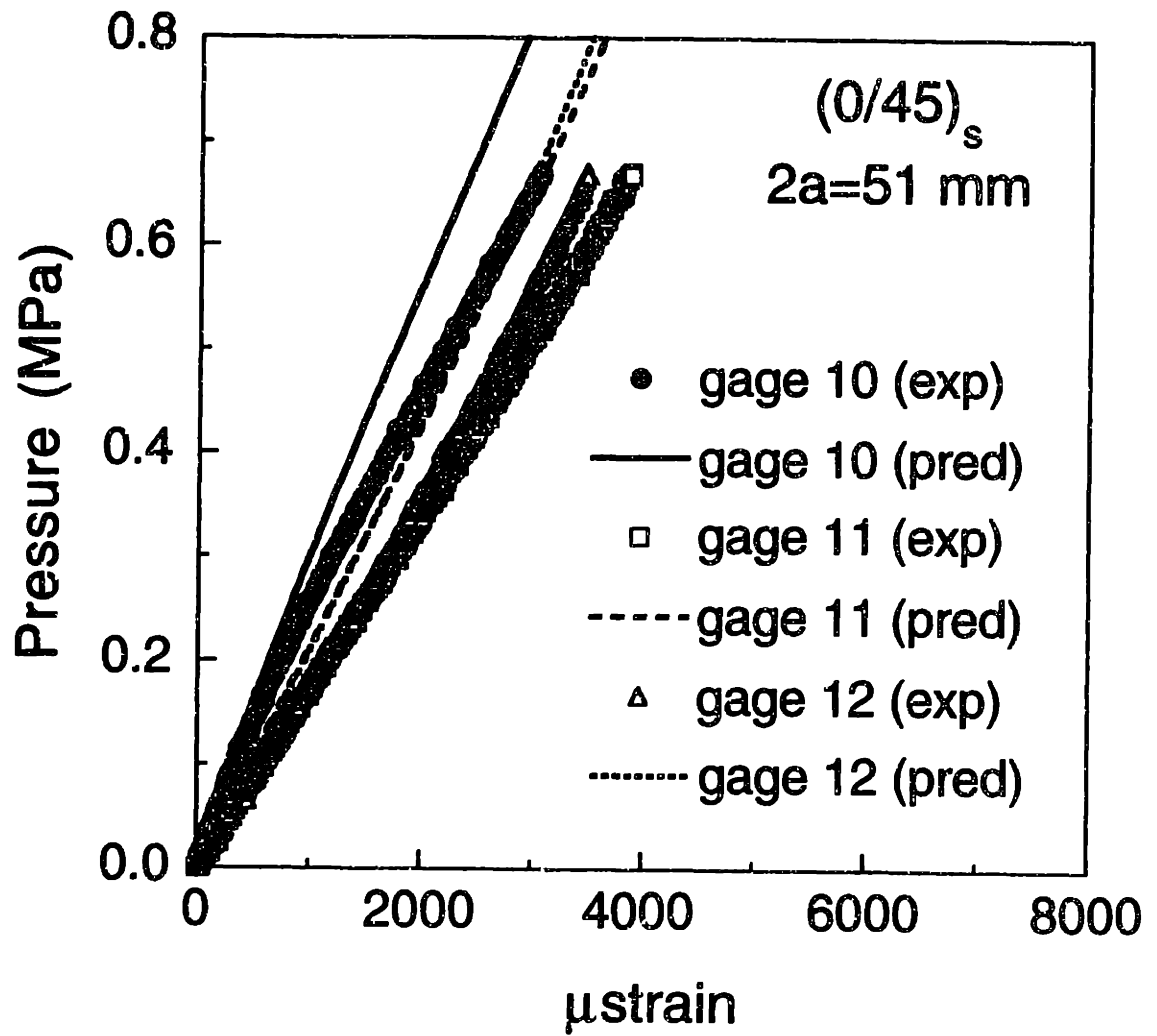


Figure C.4 Predicted and experimental strain responses for gages 10 to 12 in the unstiffened (0/45)_s cylinder with a longitudinal slit length of 51 mm.

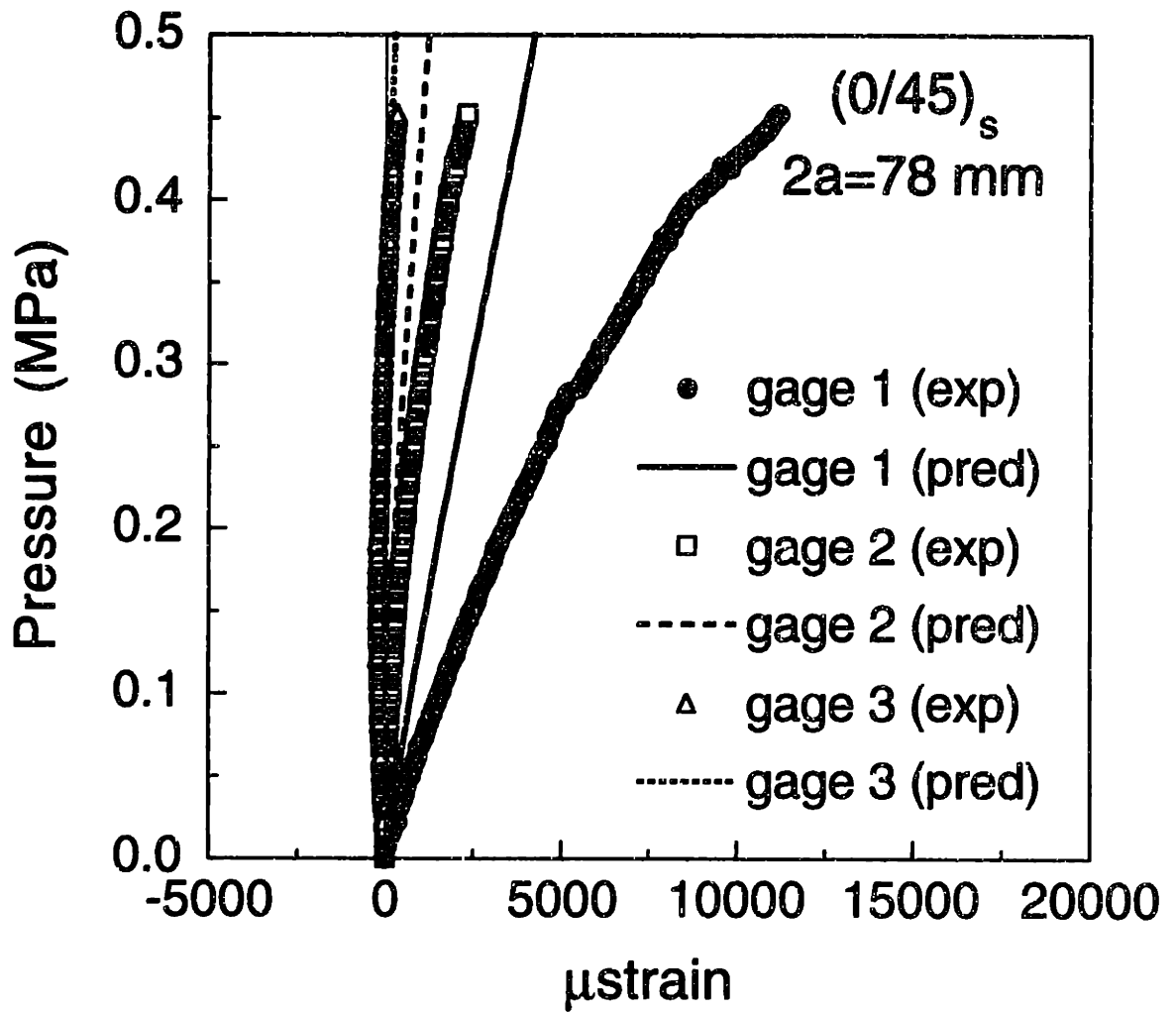


Figure C.5 Predicted and experimental strain responses for gages 1 to 3 in the unstiffened $(0/45)_s$ cylinder with a longitudinal slit length of 78 mm.

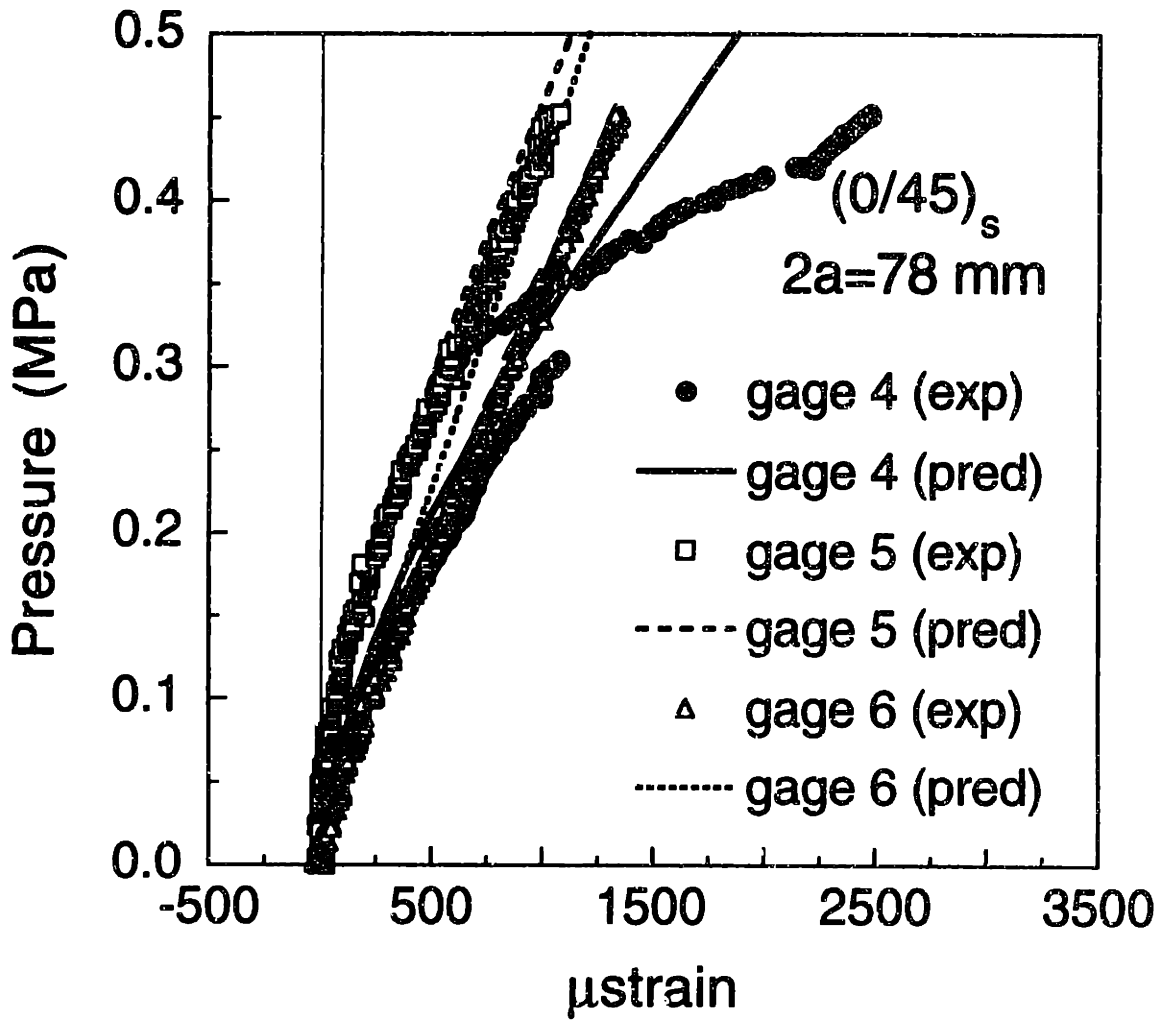


Figure C.6 Predicted and experimental strain responses for gages 4 to 6 in the unstiffened $(0/45)_s$ cylinder with a longitudinal slit length of 78 mm.

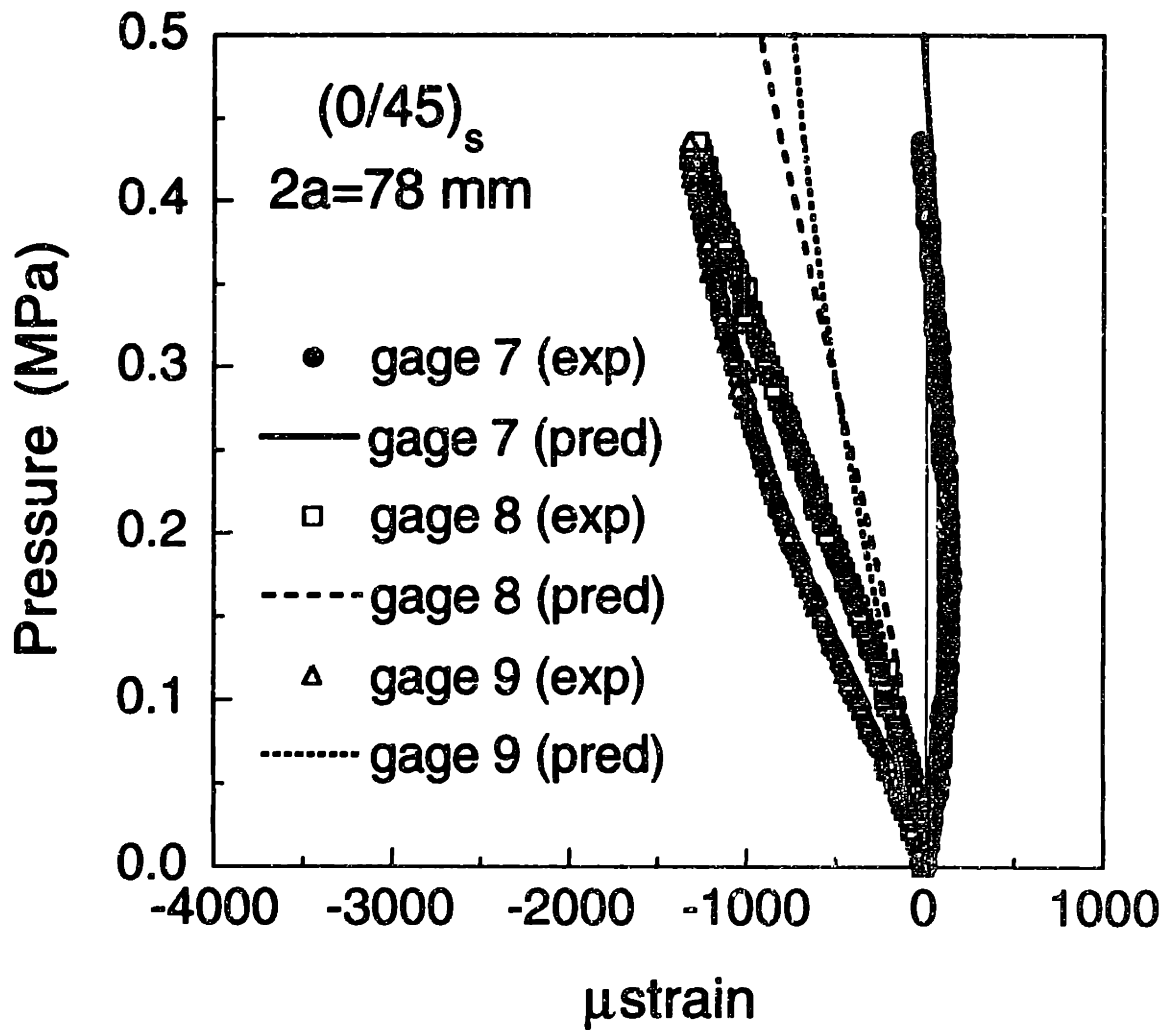


Figure C.7 Predicted and experimental strain responses for gages 7 to 9 in the unstiffened (0/45)_s cylinder with a longitudinal slit length of 78 mm.

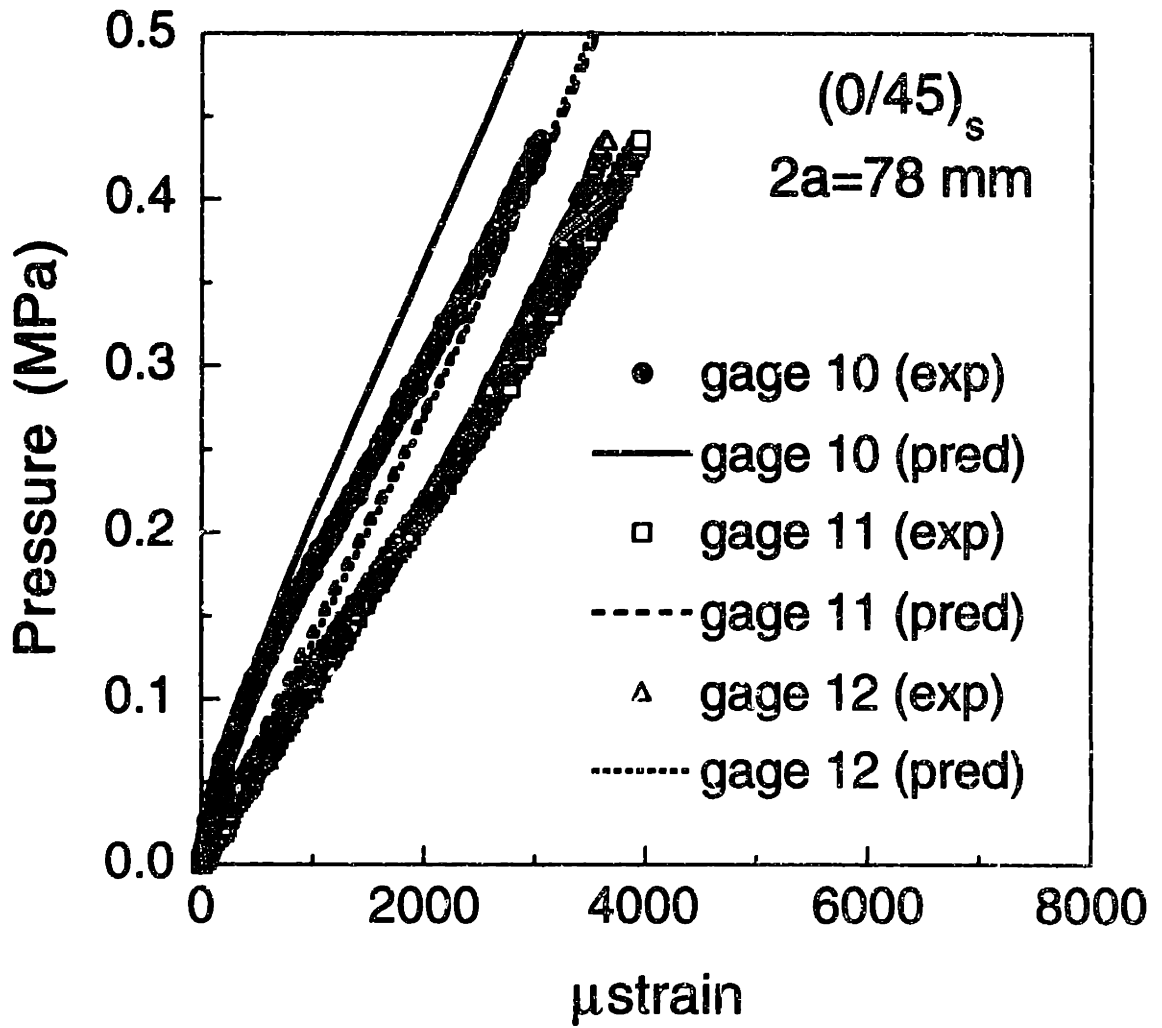


Figure C.8 Predicted and experimental strain responses for gages 10 to 12 in the unstiffened $(0/45)_s$ cylinder with a longitudinal slit length of 78 mm.

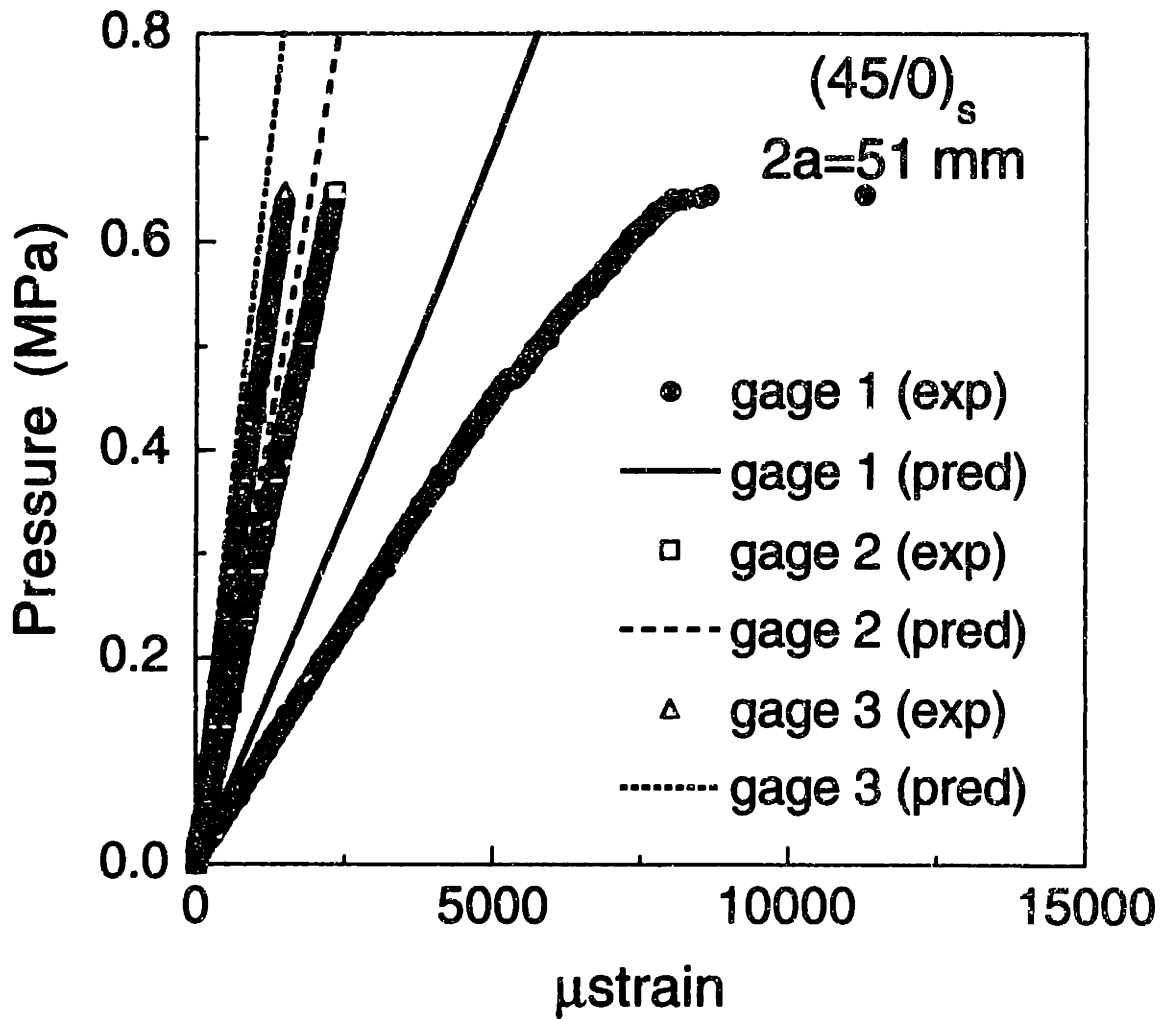


Figure C.9 Predicted and experimental strain responses for gages 1 to 3 in the unstiffened (45/0)_s cylinder with a longitudinal slit length of 51 mm.

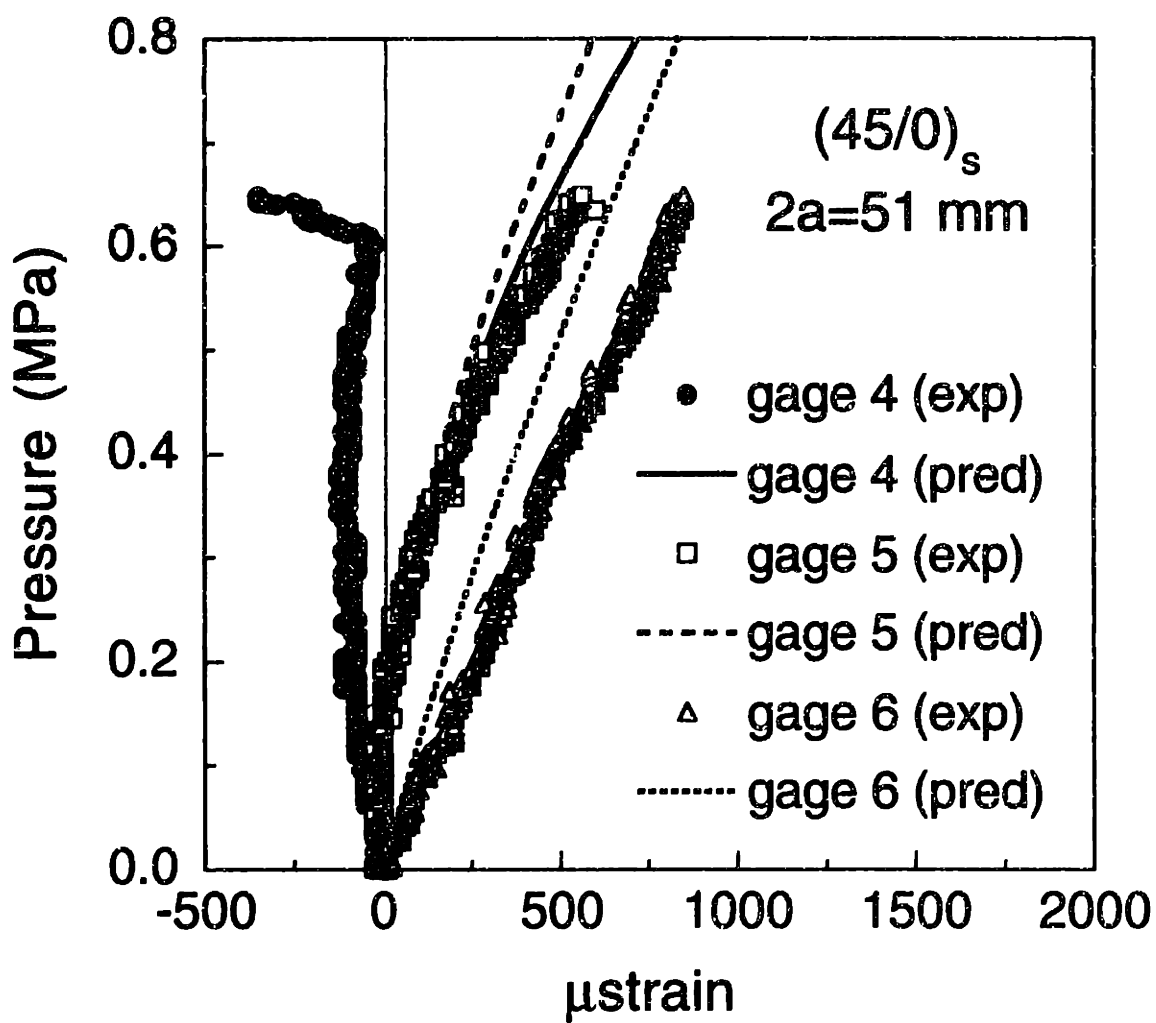


Figure C.10 Predicted and experimental strain responses for gages 4 to 6 in the (45/0)_s cylinder with a longitudinal slit length of 51 mm.

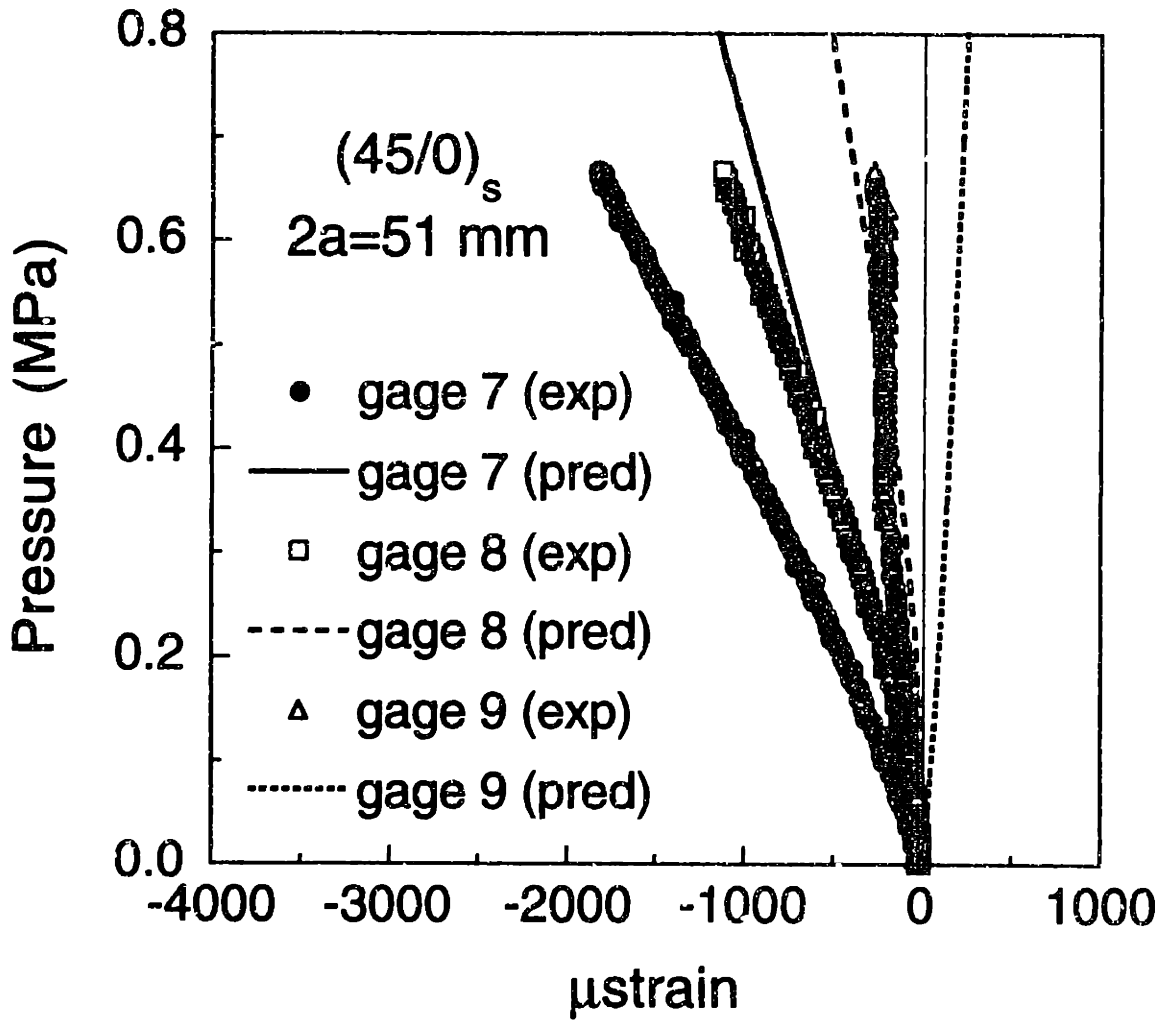


Figure C.11 Predicted and experimental strain responses for gages 7 to 9 in the unstiffened (45/0)_s cylinder with a longitudinal slit length of 51 mm.

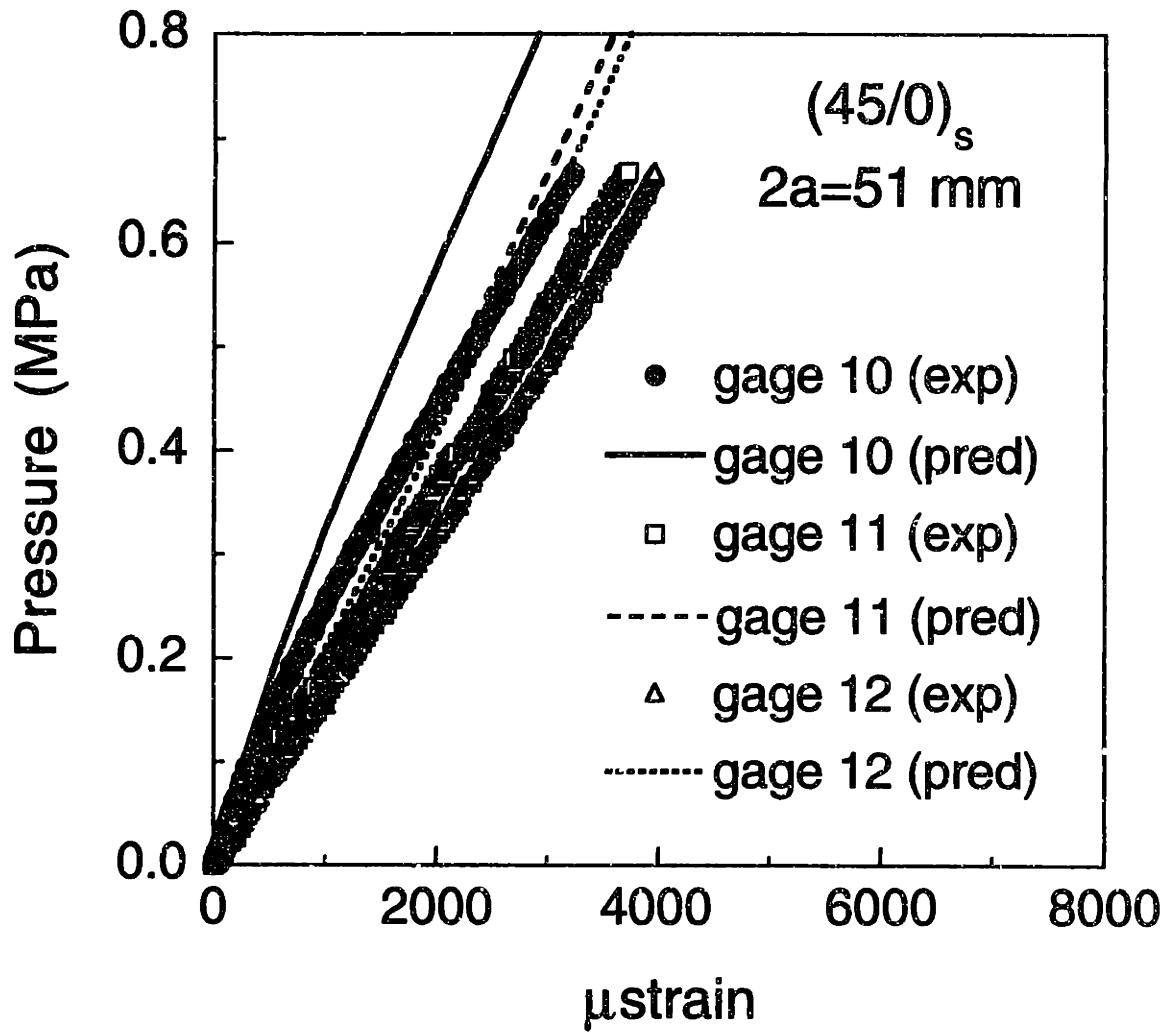


Figure C.12 Predicted and experimental strain responses for gages 10 to 12 in the unstiffened (45/0)_s cylinder with a longitudinal slit length of 51 mm.

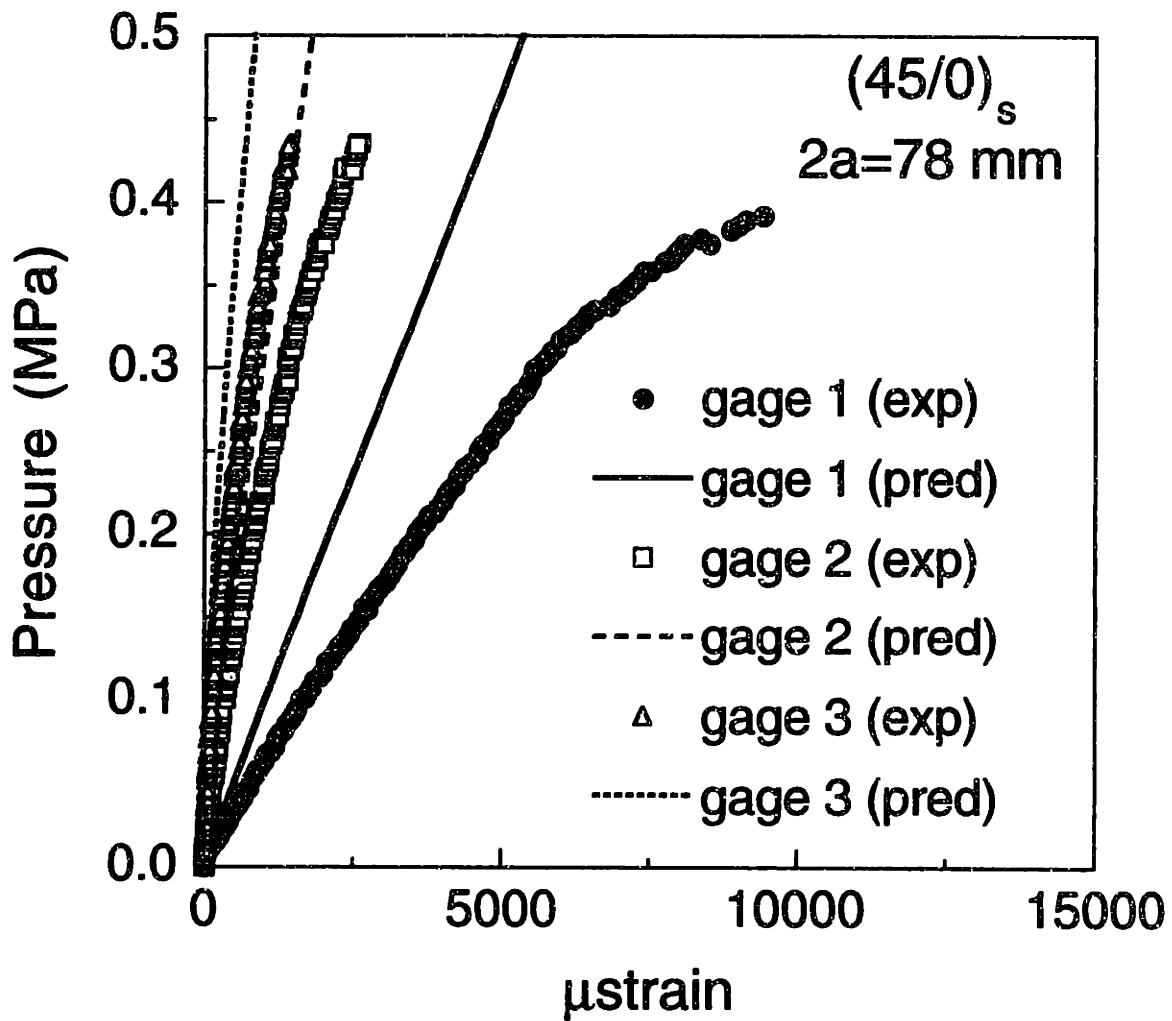


Figure C.13 Predicted and experimental strain responses for gages 1 to 3 in the unstiffened (45/0)_s cylinder with a longitudinal slit length of 78 mm.

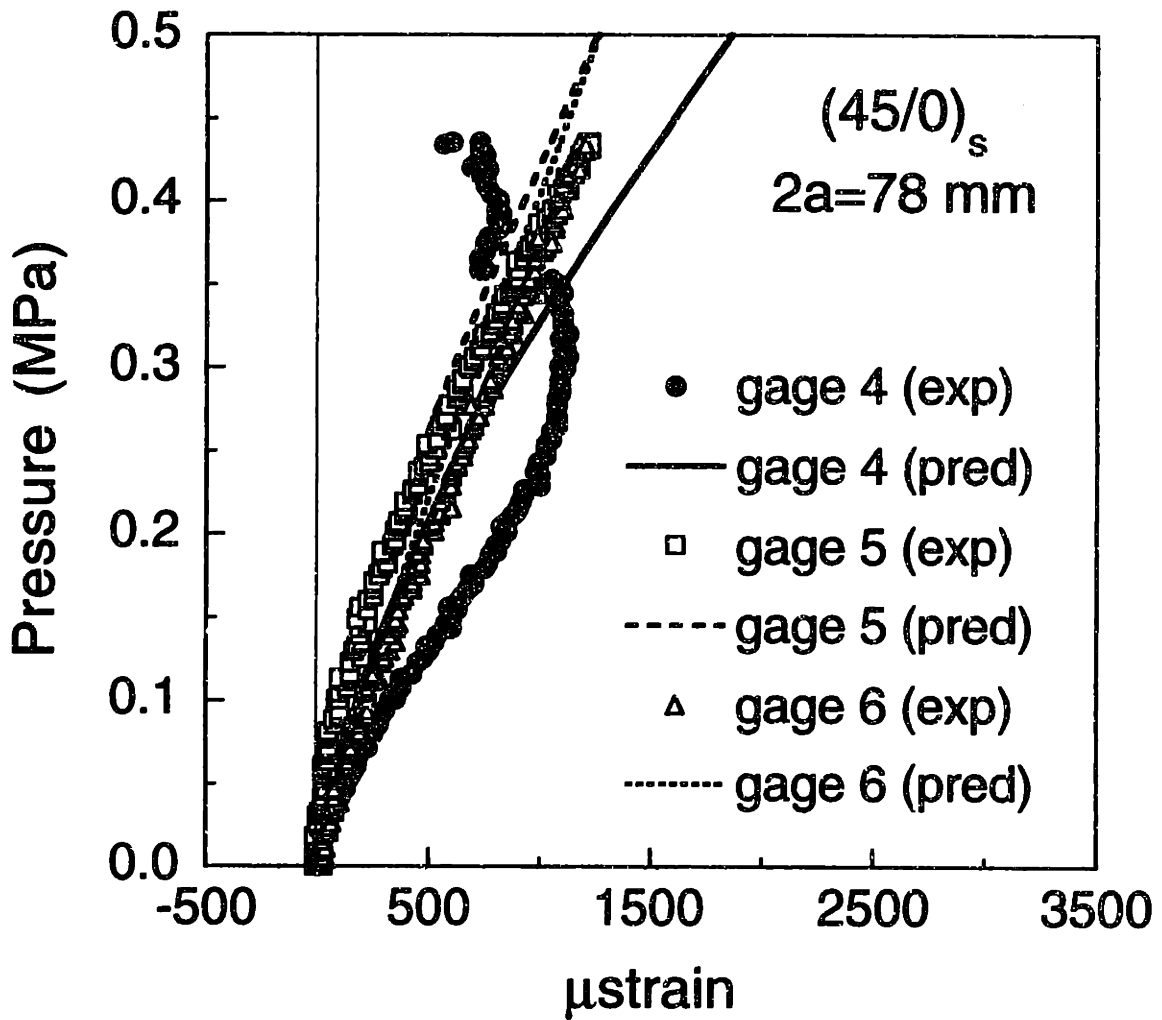


Figure C.14 Predicted and experimental strain responses for gages 4 to 6 in the unstiffened (45/0)_s cylinder with a longitudinal slit length of 78 mm.

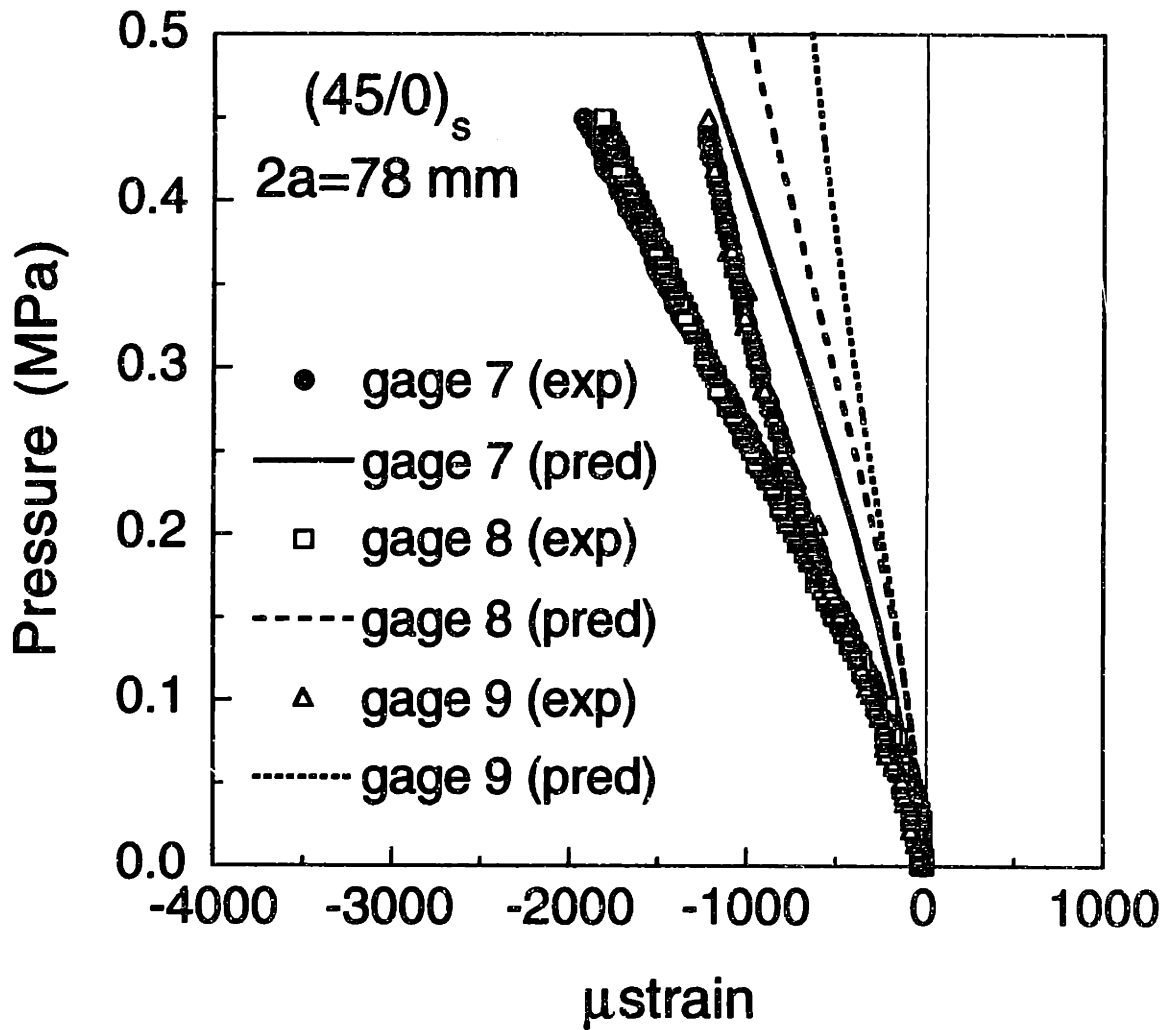


Figure C.15 Predicted and experimental strain responses for gages 7 to 9 in the unstiffened (45/0)_s cylinder with a longitudinal slit length of 78 mm.

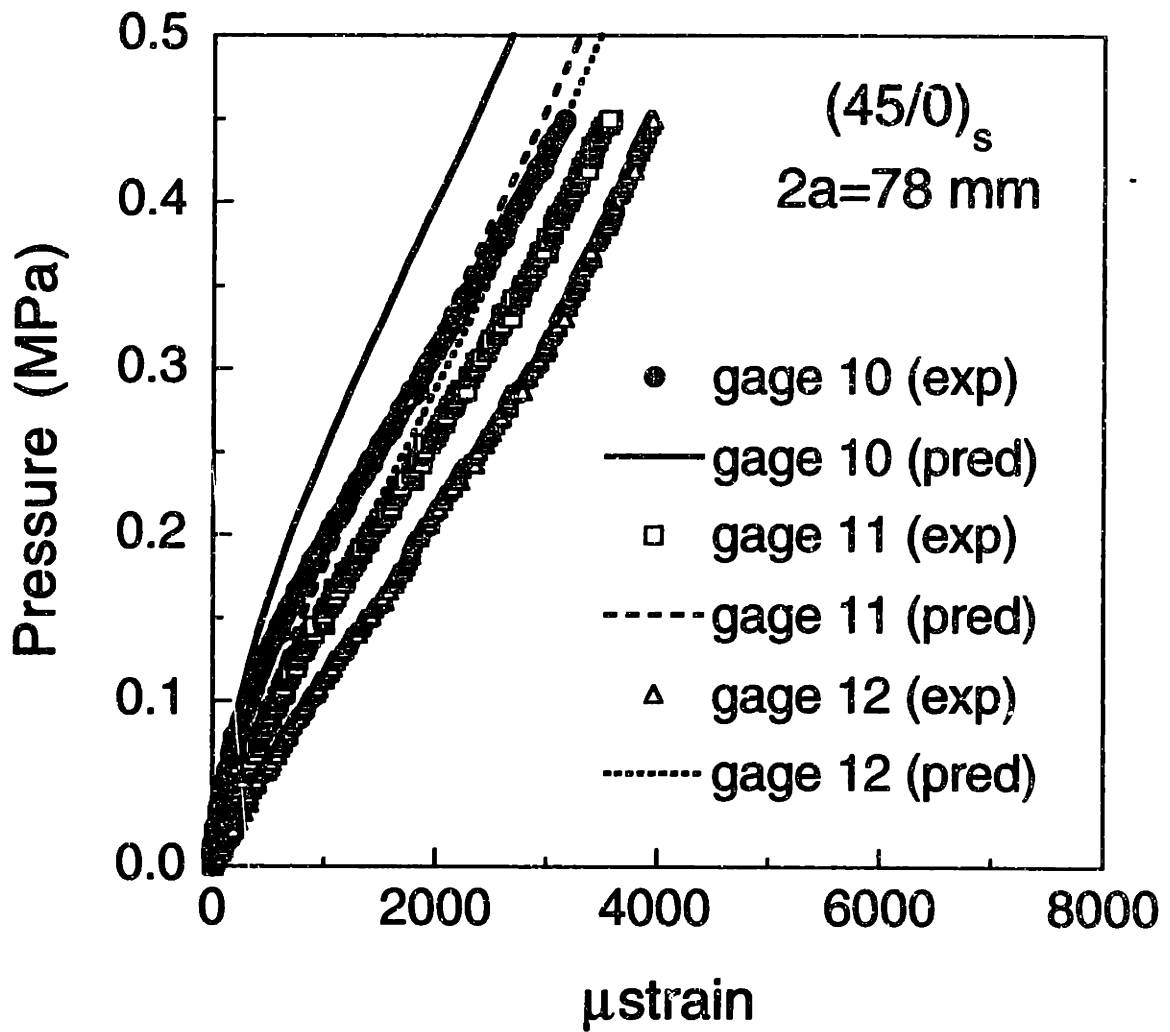


Figure C.16 Predicted and experimental strain responses for gages 10 to 12 in the unstiffened $(45/0)_s$ cylinder with a longitudinal slit length of 78 mm.

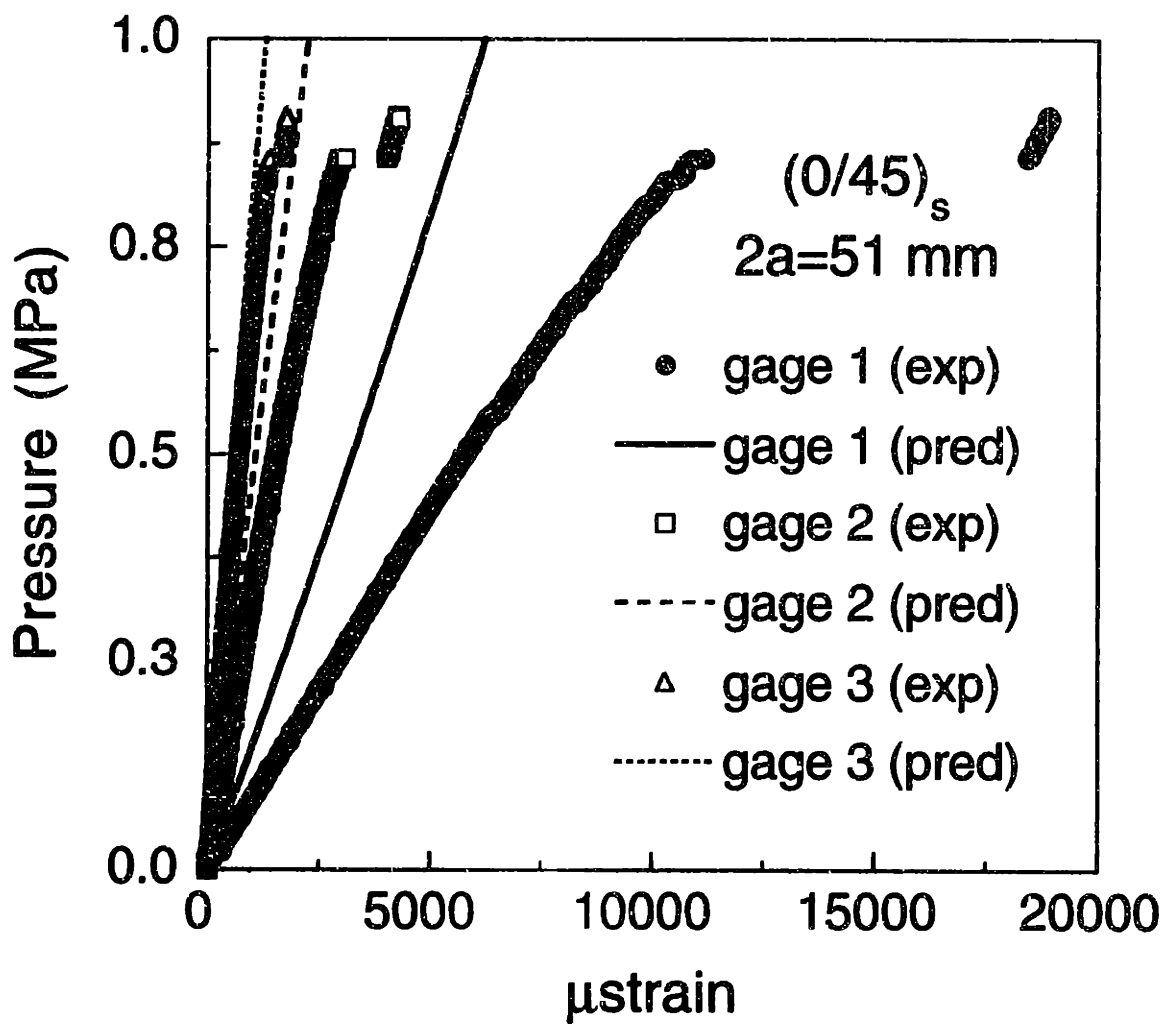


Figure C.17 Predicted and experimental strain responses for gages 1 to 3 in the stiffened $(0/45)_s$ cylinder with a longitudinal slit length of 51 mm.

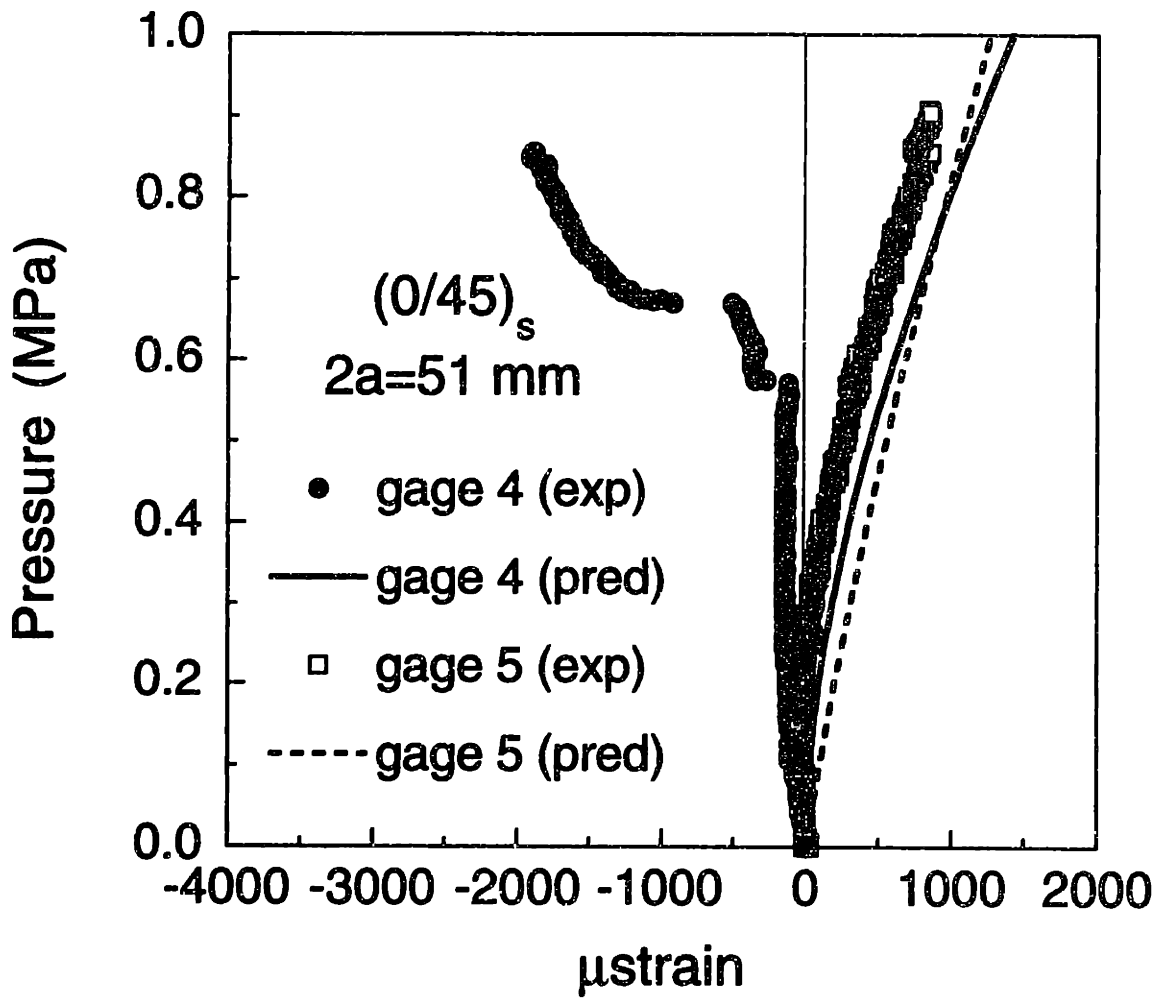


Figure C.18 Predicted and experimental strain responses for gages 4 and 5 in the stiffened (0/45)_s cylinder with a longitudinal slit length of 51 mm.

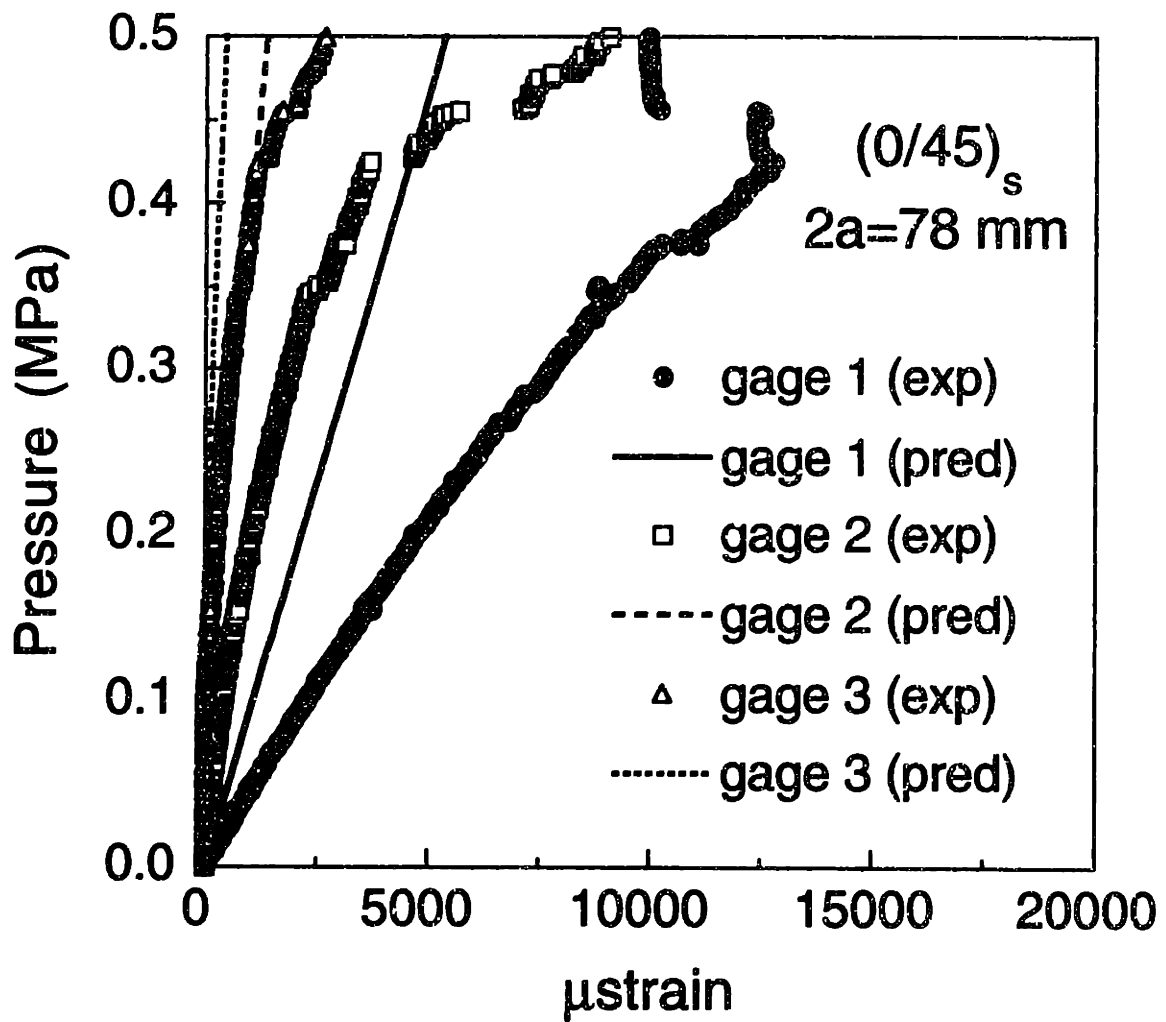


Figure C.19 Predicted and experimental strain responses for gages 1 to 3 in the stiffened (0/45)_s cylinder with a longitudinal slit length of 78 mm.

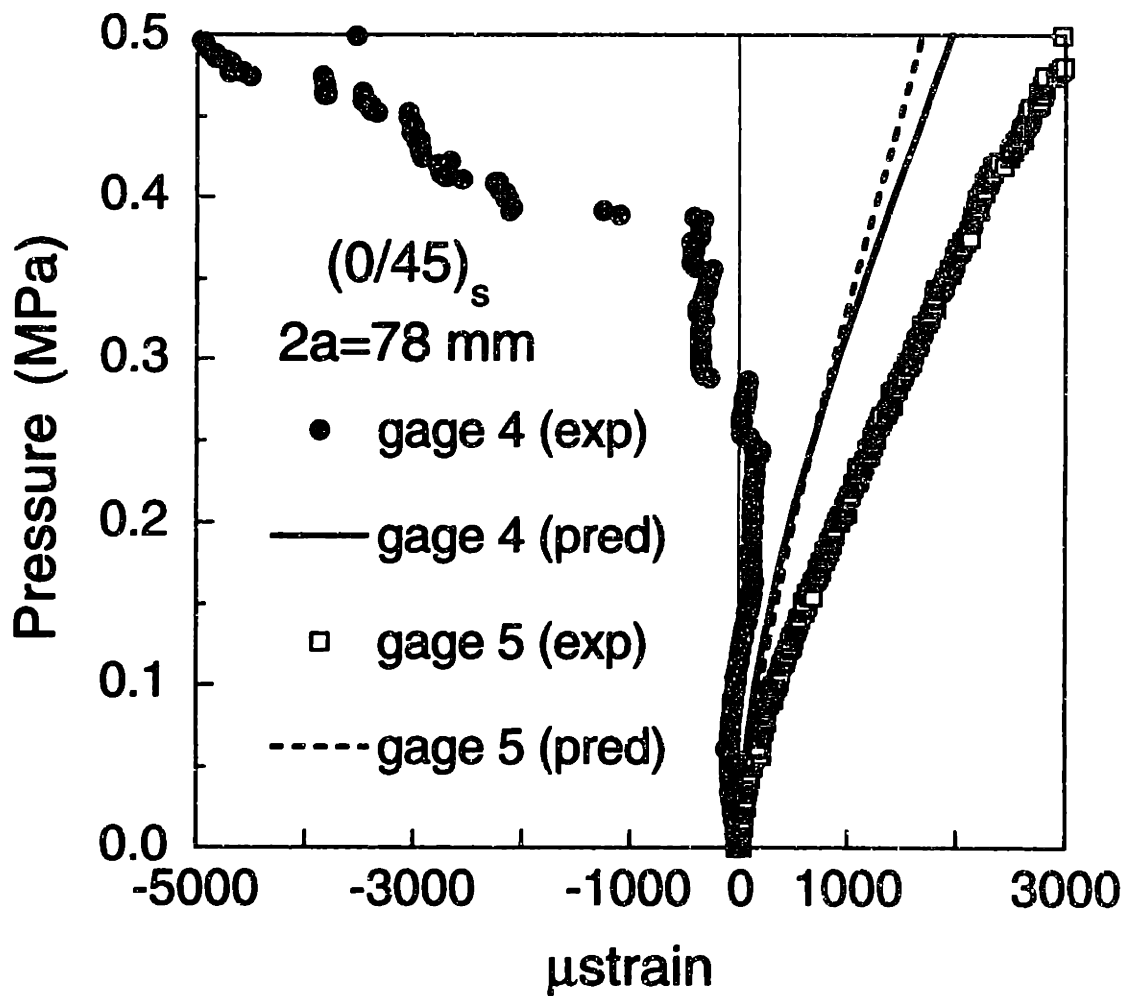


Figure C.20 Predicted and experimental strain responses for gages 4 and 5 in the stiffened (0/45)_s cylinder with a longitudinal slit length of 78 mm.

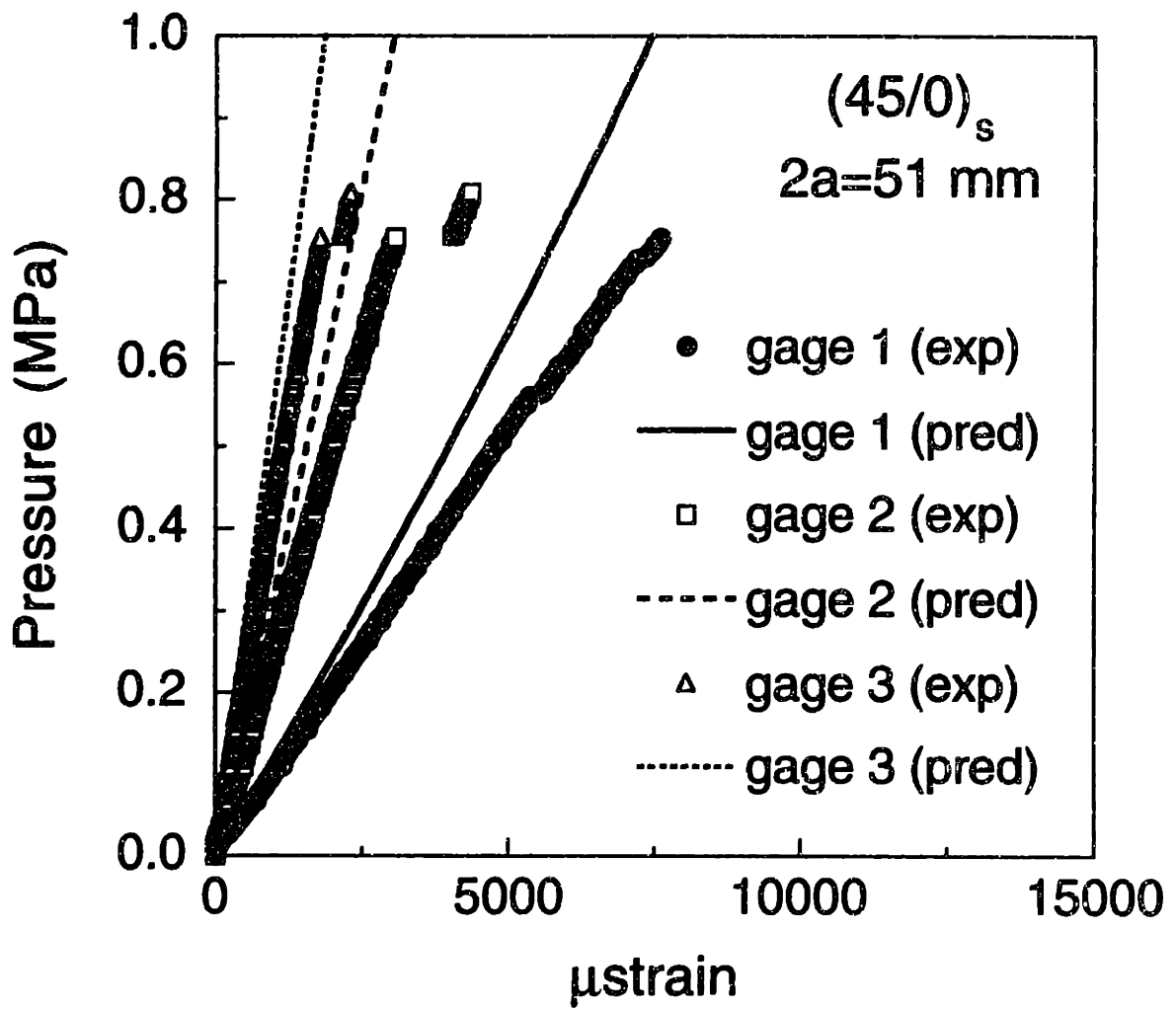


Figure C.21 Predicted and experimental strain responses for gages 1 to 3 in the stiffened $(45/0)_s$ cylinder with a longitudinal slit length of 51 mm.

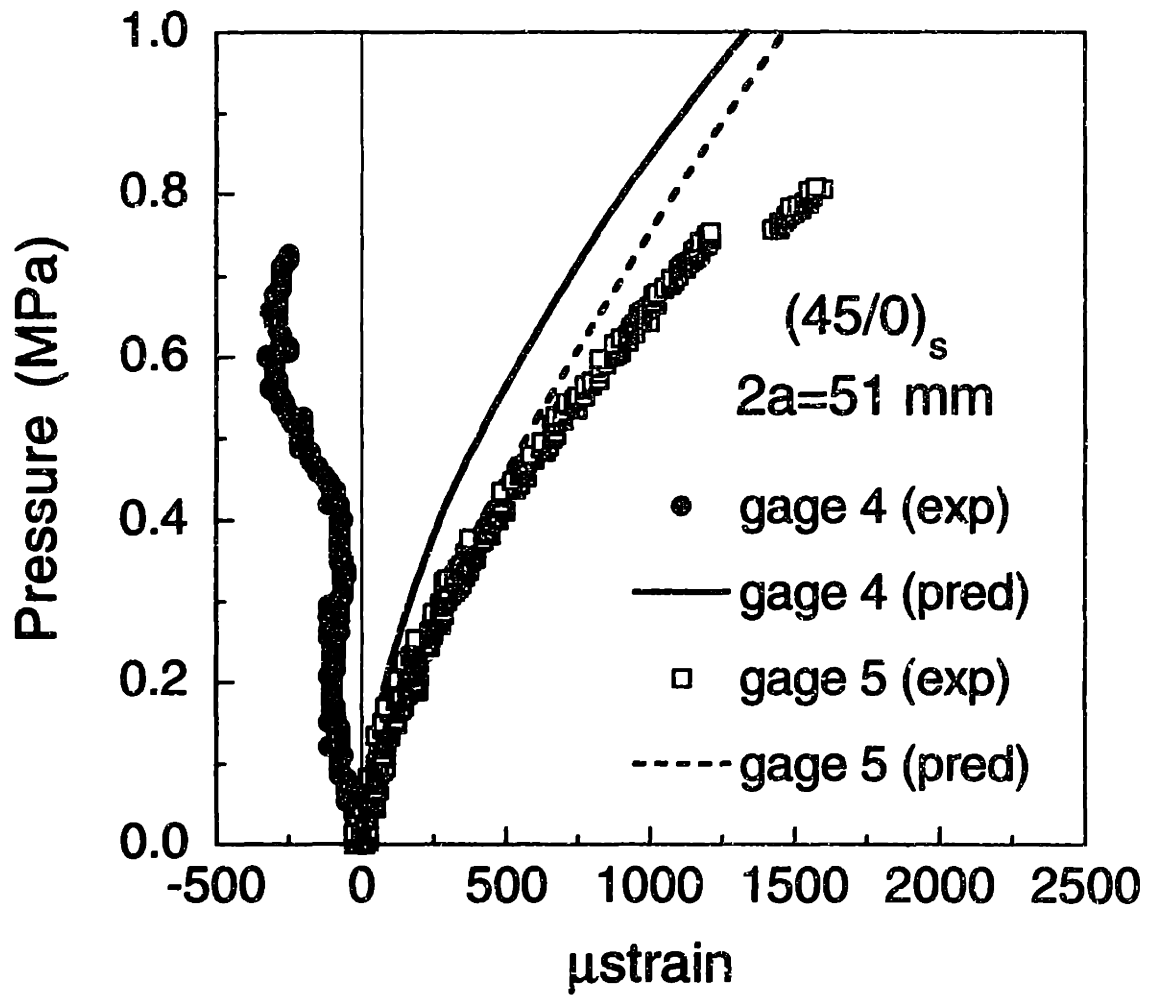


Figure C.22 Predicted and experimental strain responses for gages 4 and 5 in the stiffened $(45/0)_s$ cylinder with a longitudinal slit length of 51 mm.

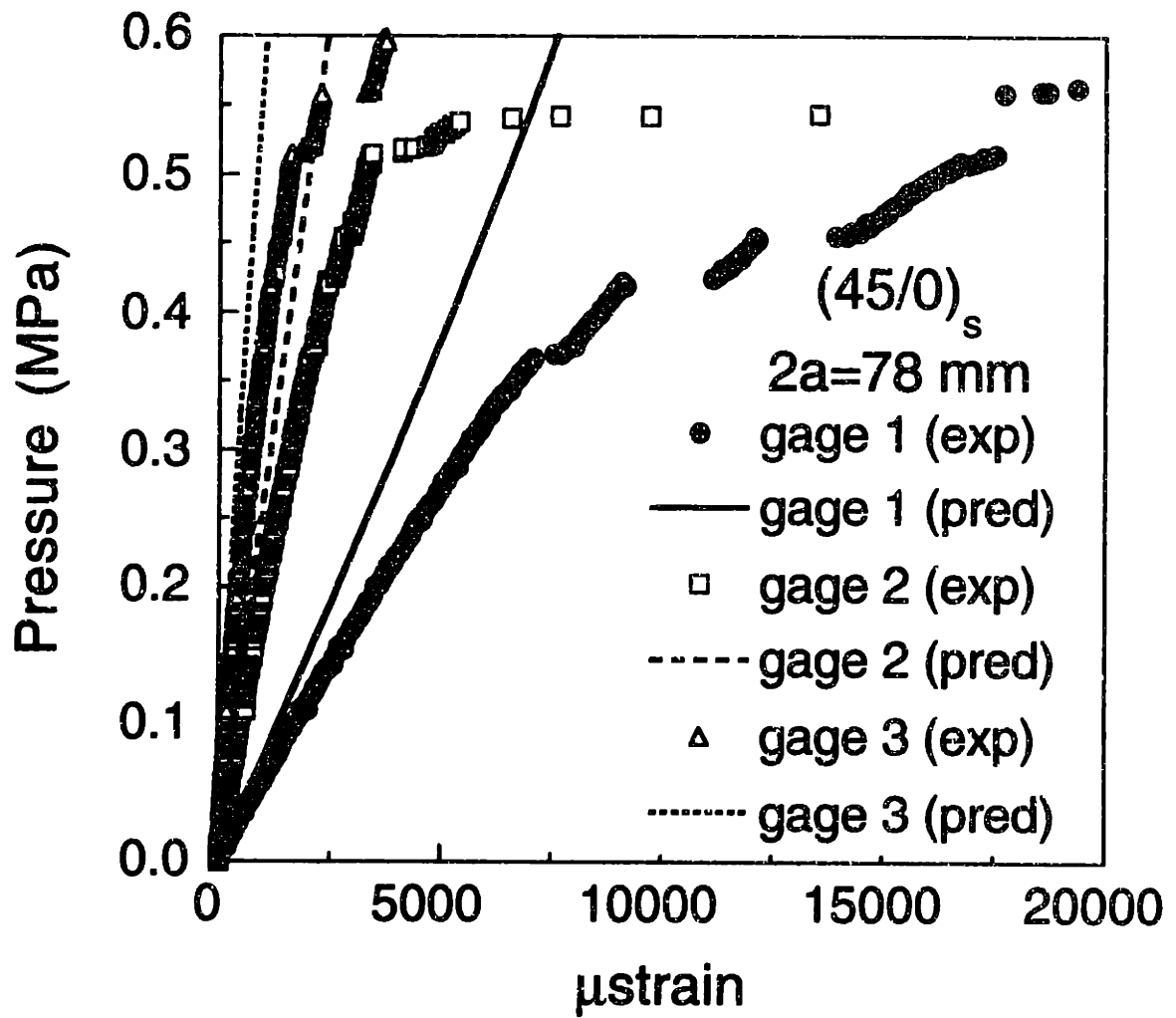


Figure C.23 Predicted and experimental strain responses for gages 1 to 3 in the stiffened $(45/0)_s$ cylinder with a longitudinal slit length of 78 mm.

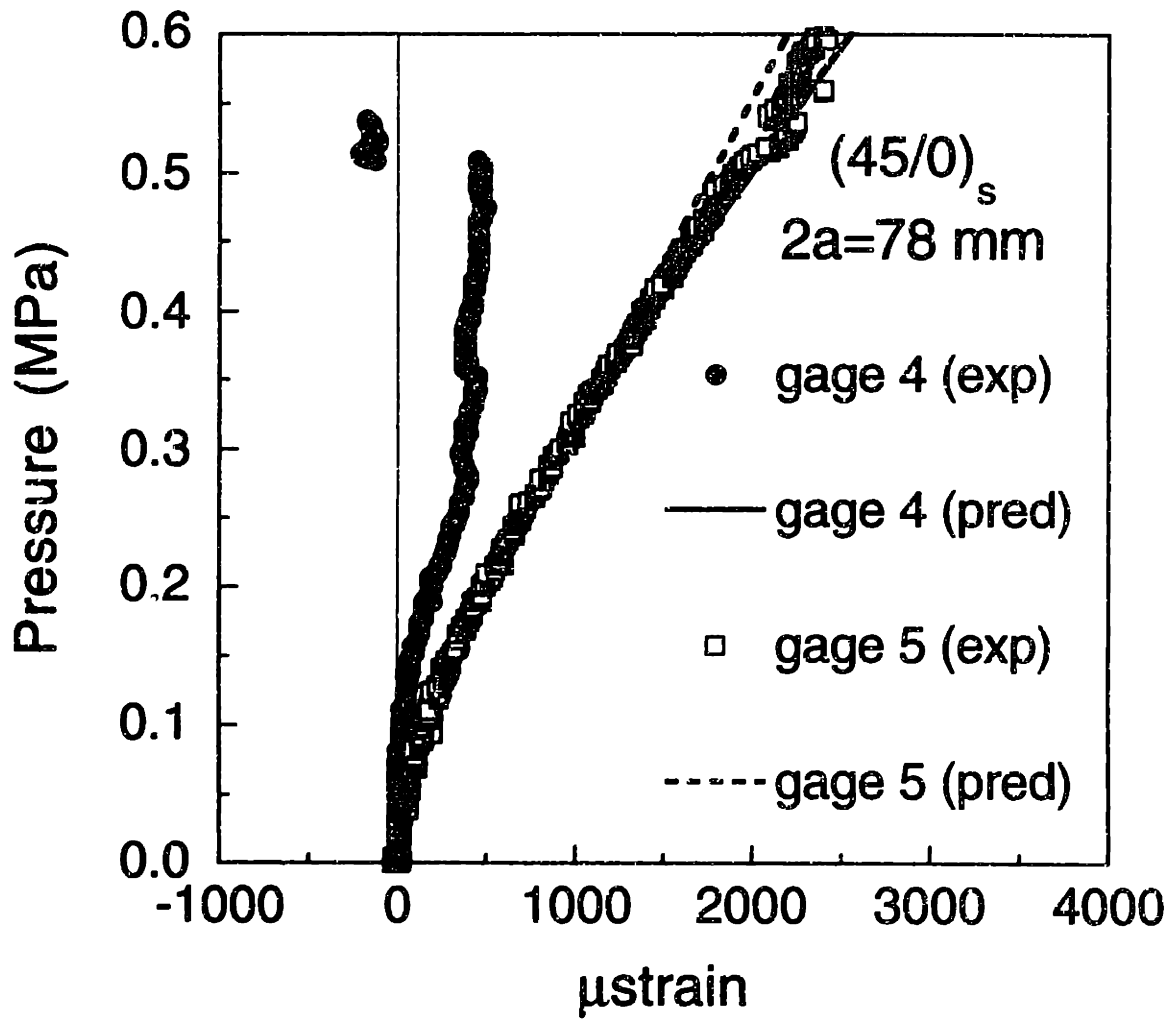


Figure C.24 Predicted and experimental strain responses for gages 4 and 5 in the $(45/0)_s$ stiffened cylinder with a longitudinal slit length of 78 mm.

Vita

Haryanto T. Budiman was born in Jakarta, Indonesia on May 27, 1968, the first son of Mr. and Mrs. Hendra Budiman. He was educated in the United States after he finished his high school education in Jakarta in 1987. He was first enrolled at Texas A&M University, majoring in Aerospace Engineering. He graduated with a Bachelor of Science degree in May 1990. He was then awarded the Presidential Fellowship by the Virginia Polytechnic Institute & State University in Blacksburg, VA, to enroll in the Master of Science program in Engineering Mechanics. He studied under the mentorship of Prof. John Morton. After receiving his Master of Science degree from Virginia Tech, Haryanto was awarded the Richard D. DuPont Fellowship by the Department of Aeronautics and Astronautics at MIT to enroll in the Ph.D. program in the area of Structures Technology under the mentorship of Professor Paul A. Lagace. While at MIT, he also cross-registered at Harvard University studying Solid and Structural Mechanics. He was the Jerome C. Hunsaker Teaching Fellow in Structural Mechanics at MIT in the Fall semester of 1993. Haryanto has accepted an offer to join the McKinsey & Company as a management consultant starting September 1, 1996.